Investigations of Open-Shell Open-Shell Van der Waals Complexes

George Economides
St Peter's College, Oxford

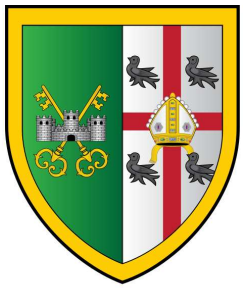

Thesis submitted in fulfilment of the requirements
for the degree of Doctor of Philosophy

University of Oxford, Trinity Term 2013

Investigations of Open-Shell Open-Shell Van der Waals Complexes

George Economides,
St Peter's College, Oxford

Thesis submitted in fulfilment of the requirements
for the degree of Doctor of Philosophy.

University of Oxford, Trinity Term 2013

Abstract

The question posed in this work is how one would model and predict the rotational spectrum of open-shell open-shell van der Waals complexes. There are two secondary questions that arise: the nature of radical-radical interactions in such systems and the modelling of the large amplitude motion of the constituent molecules. Four different systems were studied in this work, each providing part of the answer to the main question.

Starting with the large amplitude motion, there are two theoretical approaches that may be adopted: to either model the whole complex as a semi-rigid molecule, or to perform quantum dynamical calculations. We recorded and analysed the rotational spectrum (using Fourier transform microwave spectroscopy) of the molecule of tertiary butyl acetate (TBAc) which exhibits a high degree of internal rotation; and of the weakly-bound complex between a neon atom and a nitrogen dioxide molecule (Ne-NO_2). We used the semi-rigid approach for TBAc and the quantum dynamical approach for Ne-NO_2. We also explored the compatibility of these two approaches. Moreover, we were able to predict and analyse the fine and hyperfine structure of the Ne-NO_2 spectrum using spherical tensor operator algebra and the results of our dynamics calculations.

To explore the nature of the interactions in an radical-radical van der Waals complex we calculated the PESs of the possible states that the complex may be formed in, when an oxygen and a nitrogen monoxide molecule meet on a plane using a number of high level *ab initio* methods. Finally, our conclusions were tested and applied when we performed the angular quantum dynamics to predict the rotational spectrum of the complex between an oxygen and a nitrogen dioxide molecule, and account for the effect of nuclear spin statistics in that system.

This thesis was typeset with LaTeX.

Published at the University of Oxford, Oxford, United Kingdom.

"*The most incomprehensible thing about the universe is that it is comprehensible*"

Albert Einstein

Thanks

First and foremost, I wish to thank my supervisor Prof. Brian J. Howard. He has been a true inspiration and a pleasure to work with. I was very fortunate to have someone with so much experience, patience and pure interest in this project to learn from, and I am very proud to have been a member of his group these last years.

Next, I wish to thank my family, especially my loving parents Demetres and Naya, grant-parents George, Mary, Antonis and Iro, my aunt Filio and my nanny, Litsa. Being far from them has been the hardest part of my studies. Their love and support was always felt, no matter the distance.

Moreover, I wish to thank the Alexander S. Onassis Public Benefit Foundation for their generous scholarship to support my studies. Furthermore, I wish to thank St Peter's College and the Department of Chemistry, for their generous awards which allowed me to attend very educational and stimulating conferences. I also wish to thank the people that have been very significant to me these years: Vera Mystaka, Ian Preston, Christos Papanikas, Joanna Bagniewska, Alexander Tsimbanoulis, and their families. Our interactions have forged who I am today and I count myself lucky to have them close to me. Jonas Muir Wood has been an extraordinary generous and kind person, and the least I can do is thank him for his help in various times.

I wish to thank all the previous members of the group, starting with the previous Part II students: Edward Steer, Felicia Crossley, Harry Richards, Lee Dyer, Chris Essex, Jeremy Wu, Markus Frise, Mike Newsome and Thomas Smith. They made the lab a fun, creative place to work. Also the previous D. Phil. canditate, Dr. Bin Oyang and the post-doctoral researcher Dr. Sarandis Marinakis. From fixing spectrometers, analysing results and reading thesis drafts to sharing coffee and cakes, each and every one of these people have been a significant part of my time in Oxford.

I also wish to acknowledge the support of lab services, electronics and IT teams, especially Paul Mitchell, Pete Biggs, Kevin Valentine, Neville Baker and John Adams. Many a time I have run to ask for their help or advice and they always obliged. Moreover, I wish to thank Eleni Aliferi for being such a nice and friendly presence over all these years.

Dancing has been a major part of my life in Oxford. Firstly I wish to thank Tamasin Graham and Alex Gray, for welcoming me into Featherwaits, and giving me their trust and support. I also wish to thank these extraordinary teachers whose lessons have extended beyond the ballroom: Hans Peter Stokkebroe, Kristina Juel Stokkebroe and Ekaterina Lapaeva. They have given me new ways to perceive and act, in dance and in life. I also wish to thank Gillie McNeil and the NCHP group: Maria Xucla-Lerma, Joy Shakespeare, Alison Leverett-Morris and Su Ricks-McPherson for opening new horizons to my understanding of people.

Finally, I wish to thank all my friends over the years. They have all contributed to me reaching this point today.

Contents

List of Figures

List of Tables

Chapter 1

Introduction

"*The underlying physical laws necessary for the mathematical theory of a large part of physics and the whole of chemistry are thus completely known, and the difficulty is only that the exact application of these laws leads to equations much too complicated to be soluble.*"

-PAM Dirac

1.1 Overview

In the effort to explain the natural world, the first approximation made (in high school science) is to divide the natural phenomena into two extreme categories: the physical and the chemical phenomena. These differ in that in the former, the participating species (these may be atoms, ions, radicals, molecules etc.) retain their identity, while in the latter they do not. Thus, in the first case the interactions between species may be approximated as separate to their internal structure, while in the second the participating species may be divided into reactants and products. To a gross level, these define the domains of physics and chemistry, and although as our understanding of the world developed subsequent approximations have moved these two domains towards each other, the basic distinction remains. Physical chemistry however, lies in the common ground between these two domains, and thus can examine physical phenomena, while

a chemical reaction may take place. In that sense, physical chemistry is uniquely positioned in the natural sciences not only to examine both kinds of phenomena, but more importantly, cases that do not fall clearly in either category.

1.2 Van der Waals Complexes

In the case of gases, an extreme "physical phenomenon" perspective is the ideal gas law which predicts molecules to co-inhabit the same space but with no interaction taking place between them, as if they had no internal structure (i.e. nuclei and electrons arranged in a specific way):

$$pV = nRT \tag{1.1}$$

where p is the pressure, V the volume, n the number of moles, R the ideal gas constant and T the temperature. Introducing the concept of intermolecular forces is the first deviation from a "purely" physical perspective, where while the particles do maintain their identities, there is a perturbation of the bulk properties of the gas due to their internal structure. The ideal gas law was modified by J. D. van der Waals in 1873 as to describe "real" gases with the equation [1]:

$$\left(p + a\left(\frac{n}{V}\right)^2\right)(V - nb) = nRT \tag{1.2}$$

where a and b are the van der Waals coefficients, which are characteristic of each gas. a accounts for a long-range attractive force, which brings the gas particles together and thus reduces the pressure on the container walls, while b accounts for the non-zero size of the gas particles. Equivalently, we can view b as accounting for a short-range repulsive force, which introduces a limit to how close two gas particles may get. Although at the time that J. D. van der Waals proposed his equation, these parameters were derived semi-empirically using classical (rather than quantum) reasoning, it is remarkable that these two contributions (a long-range attraction and a short-range repulsion) are still the basis of all intermolecular[1] forces considerations. In-

[1]These forces are called intermolecular even between a pair of atoms, as for example in the case of the interaction between two argon atoms.

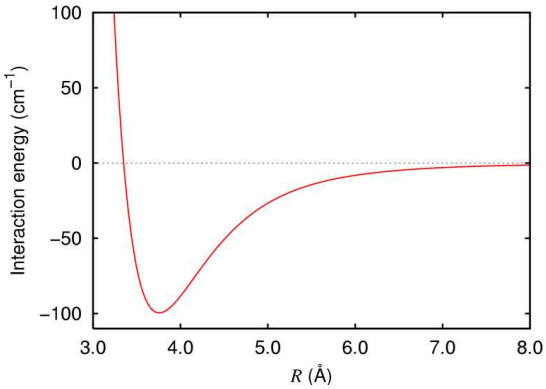

Figure 1.1: A typical intermolecular potential energy curve [4]

termolecular forces are present in all real systems and are the origin of the condensed phases of matter. Yet, it should be emphasised that that these are non-bonding interactions, and their strength is approximately $\approx 1\%$ that of a chemical bond [2, 3].

Figure 1.1 shows the overall effect of these contributions on the intermolecular potential energy as two Ar atoms approach [4]. At the vertical axis is the interaction energy between the two atoms, while at the horizontal the interatomic distance R. At short R the repulsive interaction dominates, while at longer R there is an attractive force bringing the atoms together which decays with distance. In the intermediate R there is a point, R_0, that the two effects counterbalance and close to it, a potential energy well is formed. If this well is deep enough, it is able to support a weakly bound complex, called a van der Waals complex. Another perspective is to view this molecular complex as a weakly-bound diatomic, and the large amplitude motion of the atoms in the potential well as a low-energy vibration [5].

If instead of atoms we had considered molecules, there would be two major changes: the first one is that there would be an angle dependence in the corresponding figure 1.1 and the value of R_0 would change according to the relative orientation of the molecules[2]. One way this is can be modelled is by mapping the variation of the potential energy with respect to the inter- and intra-molecular coordinates. If only one coordinate (such as the intermolecular distance in figure 1.1) is varied then this is called a Potential Energy Curve (PEC), while if more coordinates (such as angles) are also varied, this gives rise to a Potential Energy Surface

[2]Assuming a potential well is still formed in that orientation.

(PES). The potential energy between groups of atoms in specific geometries may be calculated using computer software, which will be explored in detail in chapter 4. Indeed, theoretical investigations of van der Waals complexes have gained a lot of interest in the recent years, thanks to the rapid increase of computational power.

The second effect is that each of the molecules (colloquially called "monomers") may now exhibit internal motion. The rotation of each monomer would correspond to a low-energy vibrational mode of the complex, if the potential energy well is sufficiently deep to sustain it. These monomer rotations are quenched due to the presence of the intermolecular potential [6].

Therefore, there are two approaches to study such complexes: either as a cluster of the monomers, where each monomer retains their identity but its motions are quenched due to the presence of its partner, or as an extremely weakly-bound molecule with pronounced large amplitude motion of its components. When these two approaches meet and what is the optimal way to model such complexes remains an open question.

Thus, van der Waals complexes can be viewed as intermediate species, positioned between isolated molecules and strongly bonded compounds. Their structure and properties depend very sensitively on the intermolecular forces holding them together. Apart from pure scientific curiosity, the study of such complexes expands our understanding of intermolecular interactions, which itself may find applications to other research areas, for example in collisional dynamics, in atmospheric chemistry, interstellar chemistry, catalysis and biological systems [2, 3, 7, 8, 9, 10].

1.3 Open-shell Open-shell Complexes

While van der Waals complexes may be regarded as species positioned between strongly bound molecules and independent monomers, their intermolecular interaction is clearly very weak. Characteristically, the van der Waals forces are often called "non-covalent forces" to emphasize the absence of strong chemical bonding. However, this simple picture becomes unclear when one, or both, of the monomers are open-shell species. Open-shell molecules (or "free radicals")

contain unpaired electrons and when two of them meet, chemical intuition would expect them to form strong chemical bonds. In fact one of the reasons that so few open-shell species van der Waals complexes have been studied to-date is the difficulty of obtaining and sustaining a significant population of free radicals without them reacting to form other products.

Yet, there are a handful of small radical species, namely NO, NO_2, ClO_2 and O_2 [11], that defy this trend and are relatively stable at room temperature. In the case of open-shell open-shell van der Waals complexes, the bonding may be expected to be "intermediate between van der Waals and chemical bonding" [12], but exactly what does that mean and how one would model it, remains unclear. We also currently have no established way of treating the interactions in such complexes, or predicting and explaining why some radicals react to form strong molecular bonds and some do not. Given the abundance and importance of these species in atmospheric chemistry [13] and biological systems [14], investigating these complexes may not only reveal some fundamental chemistry, but also provide useful conclusions and pathways to future research.

Therefore, there are two main challenges in the cases of open-shell open-shell van der Waals complexes: understanding the nature of open-shell open-shell interactions in such systems, and also the large amplitude motion of the monomers. Moreover, there are two approaches to analyse such complexes: either by performing a quantum dynamical analysis of how the monomers interact as they come together or by approximating the complex as a molecule with pronounced internal rotation. In this work, we used both approaches to examine a range of systems. Furthermore, we performed extensive experimental investigations as to compare our theoretical results against "hard" data.

1.4 Thesis Outline

In this thesis, our work in investigating four separate systems is presented. If one thinks of the question of open-shell open-shell van der Waals complexes as a two-axis problem, one of the degree of large amplitude motion and one of the degree of radical-radical interaction, then each

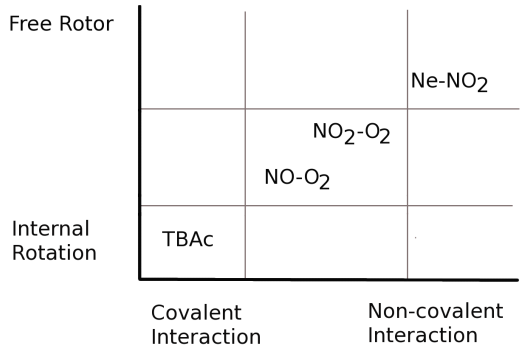

Figure 1.2: The four systems studied

of these systems targets a different part of the problem: Tertiary-butyl acetate is the simple case of a covalently bound molecule, which nevertheless demonstrates a high degree of quenched internal rotation[3]. On the diametric opposite is the case of the van der Waals complex of an atom of neon (Ne) with a nitrogen dioxide molecule (NO_2), which is held by a very weak intermolecular interaction, barely perturbing the internal structure of NO_2. The study of these two systems examines the effect of large amplitude motion in either extreme. To target the question of the nature of the intermolecular forces when two radicals form a van der Waals complex, we studied the complex between a molecule of nitrogen oxide (NO) with a molecule of oxygen (O_2). Then, all the elements of the problem were combined to analyse the complex between nitrogen dioxide and oxygen (NO_2-O_2).

All systems, except the NO-O_2 complex, were also studied experimentally, as well as theoretically. This was done using microwave spectroscopy, as the high resolution of this method is capable of probing some of the weakest interactions that arise due to presence of unpaired electrons in radical species (characteristically named “fine” and “hyperfine” interactions).

The main investigation of this thesis is done in terms of rotational energy levels and rotational spectroscopy and in the second chapter the theory needed to investigate and predict the pure rotational spectra of a species is presented. In the third chapter, a short survey of the angular momentum and spherical tensor operator algebra that was used in this work is given. In the fourth chapter, the *ab initio* computational methods used in this thesis are presented. Then, in

[3] Although it is clearly not the standard way of looking at it, one could potentially view this species as a very strongly bound complex between a t-butyl acid radical and a methyl radical.

the fifth chapter, the practical and theoretical aspects of the experimental work performed are given. Following this, in the sixth chapter, our work to record and analyse the rotational spectra of tertiary-butyl acetate is shown. In the seventh chapter, we present the theory used to describe intermolecular forces, which will be used in chapter eight, where the NO-O_2 complex is investigated. In chapter nine we present the theory of fine and hyperfine interactions, which is then used in chapter ten where the Ne-NO_2 complex is investigated, and chapter eleven, where we look at the NO_2-O_2 complex. Finally, in chapter twelve, we present our collective conclusions from this work.

Chapter 2

Pure Rotational Spectra Theory

"This all sounds fairly complicated, and so it is! It is not difficult to follow, however, and this logical development is the only alternative to pulling terms out of a hat"

- Alan Carrington [15]

2.1 Introduction

In this thesis, the rotational spectra of various species, mostly weakly bound van der Waals complexes, are being predicted, recorded and analysed. Another way to view this work is as the examination of the rotational spectra as we systematically deviate from the ideal rigidly-bound rotating molecule, to a strongly-bound molecule with pronounced internal rotation to complexes which are hardly bound at all. In either case, it is crucial to establish the standard theory to treat a rotating species in a quantum mechanical way, before we discuss how this is challenged by the different kinds of bonding.

There are two main approaches to analysing rotational spectra: The first is a rather analytical approach which emphasises the reasons different terms come into play, and how these relate to the rotational Hamiltonian and the perturbations of its energy levels. The second, more practical, approach is by including corrections to an approximate Hamiltonian as a series expansion to

its terms. This second approach has been of great use to spectroscopists over the years as allows fitting empirical parameters directly related to observed spectra. The limitations of the first approach are due to the extent that the required theoretical calculations may be practically performed. These often require extensive knowledge of the excited states of a molecule or complex, which is hard (if possible) to calculate. The limitations of the second approach is that it assumes a physical reality (in our case of a semi-rigid molecule) which is a prerequisite in order for the correction series to be convergent. For many of the complexes in this thesis, neither approach is perfectly suited. For this reason both approaches are presented here, as both will be used in later chapters. We will start with the more analytical approach before presenting the practical one.

For the purposes of this chapter, the only source of angular momentum considered is that of rotation, i.e. nuclear, orbital and electron spin angular momenta are all assumed zero. How these effect the appearance of a rotational spectrum will be described in chapter 9. Moreover, for the following discussion, space is considered isotropic. Finally, the motion of a molecule is considered as the motion of its nuclei only[1].

2.2 The Hamiltonian For A Rotating Molecule

Initially one can use the Cartesian coordinates of the atoms in the molecules, with respect to some laboratory-fixed frame of reference.

2.2.1 The rotational Hamiltonian

If we start from the classical equivalent of rotational kinetic energy:

$$E_{rot} = \frac{1}{2} I \omega^2 \tag{2.1}$$

[1]This is the Born-Oppenheimer approximation, which will be presented analytically in chapter 4.

This is the moment of inertia (I) times the square of the angular velocity, ω. The moment of inertia matrix is defined as:

$$I = \sum_{\eta}^{N} \sum_{i,j=x,y,z} r_{ij\eta} m_{\eta} \tag{2.2}$$

where m_η is the mass of particle η and r_η its distance from the origin. This becomes a quantum mechanical operator:

$$\hat{H}_{rot} = \frac{1}{2} \sum_{\eta=1}^{N} m_\eta (\omega \times \mathbf{r}_\eta) \cdot (\omega \times \mathbf{r}_\eta) = \frac{1}{2} \omega^T \mathbf{I} \omega \tag{2.3}$$

where now $\mathbf{I}$ is the moment of inertia tensor. In the case that the atoms are in their equilibrium position, then the moment of inertia tensor is noted as $\mathbf{I}_{eq}$. The axes system that gives a diagonal $\mathbf{I}_{eq}$ is called the principal axes system, and the axes are labeled a, b and c. In this case the rotational kinetic energy operator becomes:

$$\hat{H}_{rot} = \frac{1}{2} \omega^T \mathbf{I}_{eq} \omega = \frac{1}{2} \left(I_{aa} \omega_a^2 + I_{bb} \omega_b^2 + I_{cc} \omega_c^2 \right) \tag{2.4}$$

Following the Mulliken [16] convention, this is taken so that:

$$I_{aa} \leq I_{bb} \leq I_{cc} \tag{2.5}$$

Finally, we can use the classical expression for angular momentum [1], as the product of the moment of inertia of a body times its angular velocity:

$$L = I\omega \tag{2.6}$$

which in quantum mechanics can be written in tensor notation as:

$$\hat{J} = \mathbf{I}\omega \tag{2.7}$$

Therefore, we can re-write equation 2.4 as

$$\hat{H}_{rot} = A\hat{J}_a^2 + B\hat{J}_b^2 + C\hat{J}_c^2 \tag{2.8}$$

where

$$A = \frac{1}{2I_{aa}} \qquad B = \frac{1}{2I_{bb}} \qquad C = \frac{1}{2I_{cc}} \tag{2.9}$$

are the definitions of the rotational constants[2] around each principle axis. It should be remembered that the expression (2.8) is only valid for the atoms being fixed in their equilibrium position. The assumption that this "instantaneous" arrangement remains constant during rotation (in other words that the rotational constants are constants) is called the *rigid rotor approximation*.

The eigenstates of $\hat{H}_{rot}$ may be characterised in Dirac notation using their rotational angular momentum quantum number (J) and its projections. Although the projection may be taken with respect to any axes system, usually the rigid rotor states are written as:

$$|\phi_{rot}(\theta,\phi,\chi)\rangle = |J,M,K\rangle \tag{2.10}$$

where M is the projection to the space/laboratory-fixed axes system and K to the molecule/body-fixed axes system. The matrix elements therefore are, according to standard angular momentum theory [1]:

$$\hat{J}^2|J,M_J\rangle = J(J+1)|J,M_J\rangle \tag{2.11}$$

$$\hat{J}_z|J,M_J\rangle = M_J|J,M_J\rangle \tag{2.12}$$

where $\hat{J}_z$ is the projection along the axis of quantisation and depending on axes system chosen, gives M or K. The projections of an angular momentum on different axis of the same frame do not commute[3]:

$$[\hat{J}_x,\hat{J}_y] = -\imath\hat{J}_z \tag{2.13}$$

[2] For frequency units one has to simply multiply by $\frac{\hbar}{2\pi}$.

[3] We use $\imath = \sqrt{-1}$ to distinguish this from i which is often used as an index.

so only one projection may be specified per frame of reference, although all commute with the total angular momentum operator squared, $\hat{J}^2$:

$$[\hat{J}^2, \hat{J}_x] = [\hat{J}^2, \hat{J}_y] = [\hat{J}^2, \hat{J}_z] = 0 \tag{2.14}$$

and projections on different frames also commute. The angles (θ, ϕ, χ) that appear in equation 2.10 and called the Euler angles and specify the orientation of the rotor with respect to the laboratory-fixed frame. As the rotation of the molecule changes the relative orientation of the molecule-fixed to the laboratory-fixed frame, these angles can be used as rotational coordinates for the molecule. We will discuss the Euler angles in more detail in chapter 2.

A special note has to be made for linear rotors, whose eigenfunction strictly speaking only depends on two Euler angles. This problem was solved by Hougen [16, 17], who introduced an additional angle χ, for which all the standard equations apply, and the eigenstates of the Hamiltonian (which will now have an artificial degree of freedom) are the same as before the angle was introduced. This Hamiltonian is not strictly speaking the same as before the extra angle was introduced, but is isomorphic to it. The way that Hougen's *isomorphic Hamiltonian* manages to alleviate this problem is beyond the scope of this thesis and for all practical purposes we can simply regard the diatomic Euler angles as $(\theta, \phi, 0)$.

2.3 Classification Of Rotors

Under the rigid rotor approximation, it is possible to categorise the different rotating molecules (called "rotors" or "tops") according to their moments of inertia as:

2.3.1 Linear rotors

This group includes all diatomic molecules and polyatomic linear molecules, e.g. NO or OCS. As the moment of inertia around the principle axis is zero and the other two axes are connected

via a symmetry operation[4]:

$$I_{aa} = 0 \qquad I_{bb} = I_{cc} \tag{2.15}$$

In this case $B = C$, the rotational Hamiltonian becomes:

$$\hat{H}_{rot} = B(\hat{J}_B^2 + \hat{J}_C^2) = B\hat{J}^2 \tag{2.16}$$

and the energy levels simply are

$$E_{linear}(J) = BJ(J+1) \tag{2.17}$$

The degeneracy of the levels depends on their M quantum number, and in absence of any fields is $(2J+1)$.

2.3.2 Symmetric tops

In this case, two of the moments of inertia are the same. Therefore, there are two possibilities:

1. *Prolate tops*: where

$$I_{aa} < I_{bb} = I_{cc} \tag{2.18}$$

Examples include NH_3 and CH_3CN. In this case, a is the "special" axis, which will be used for the quantisation in the molecule, thus $K = K_A$. The rotational Hamiltonian and energy levels expressions now become:

$$\hat{H}_{rot} = A\hat{J}_a^2 + B(\hat{J}_b^2 + \hat{J}_c^2) = A\hat{J}_a^2 + B(\hat{J}^2 - \hat{J}_a^2) = B\hat{J}^2 + (A-B)\hat{J}_a^2 \tag{2.19}$$

$$E_{prolate}(J,K) = BJ(J+1) + (A-B)K^2 \tag{2.20}$$

As $A > B$, the energy rises with $|K|$. All levels are degenerate with respect to the M projection, i.e. they have a $(2J+1)$ degeneracy. Additionally, as the energy only depends on K^2, all but the $K = 0$ levels also have a double $(\pm K)$ degeneracy.

[4]It is traditional if two or more rotational constants are the same, for them to be noted as B.

2. *Oblate tops*: where

$$I_{aa} = I_{bb} < I_{cc} \tag{2.21}$$

These molecule have a pancake-like shape, and examples include C_6H_6 and BH_3. In this case the unique axis is c, and this will be used for quantizing the rotational angular momentum in the molecular frame, so now $K = K_C$:

$$\hat{H}_{rot} = B\hat{J}^2 + (C-B)\hat{J}_c^2 \tag{2.22}$$

$$E_{oblate}(J,K) = BJ(J+1) + (C-B)K^2 \tag{2.23}$$

The main difference is that as $C < B$, now the energy of the levels decreases with $|K|$.

2.3.3 Asymmetric tops

In this case no two moments of inertia are the same ($I_{aa} < I_{bb} < I_{cc}$). This is the largest group of molecules and examples include NO_2 and C_4H_5N. As there is not a single unique axis, there is no possible rearrangement as to obtain a Hamiltonian matrix diagonal in J and K. As only one projection may be specified at any one time, we will use the axes system x, y, z, where z is the axis of quantization which is to be decided what principle axis it corresponds to. The rotational constants around axes x, y, z are noted as X, Y, Z respectively.

The rearrangement that allows us to evaluate the Hamiltonian matrix elements is using the creation and annihilation (or raising and lowering) operators:

$$\hat{J}_\pm = \hat{J}_x \pm \imath \hat{J}_y \tag{2.24}$$

with matrix elements [1]:

$$\hat{J}_\pm |J, J_z\rangle = \sqrt{[J(J+1) - J_z(J_z \mp 1)]}\,|J, J_z \mp 1\rangle \tag{2.25}$$

Therefore, the rotational Hamiltonian becomes:

$$\hat{H}_{rot} = X\hat{J}_x^2 + Y\hat{J}_y^2 + Z\hat{J}_z^2 = \frac{1}{2}(x+y)(\hat{J}_x^2 + \hat{J}_y^2) + Z\hat{J}_z^2 + \frac{1}{2}(x-y)(\hat{J}_x^2 - \hat{J}_y^2) \quad (2.26)$$

$$= \alpha\hat{J}^2 + \beta\hat{J}_z^2 + \gamma(\hat{J}_+^2 + \hat{J}_-^2) \quad (2.27)$$

where the rotational constants in the last line are defined as:

$$\alpha = \frac{1}{2}(X+Y) \qquad \beta = C - \frac{1}{2}(X+Y) \qquad \gamma = \frac{1}{4}(X-Y) \quad (2.28)$$

According to whether the molecule is closer to a prolate or oblate top, the corresponding representation may be chosen and K is defined. Evaluating the Hamiltonian matrix using equation 2.27, we find there are diagonal elements:

$$\langle J,K|\hat{H}_{rot}|J,K\rangle = \alpha J(J+1) + \beta K^2 \quad (2.29)$$

and non-diagonal terms that link states with $K' = K \pm 2$:

$$\langle J,K\pm 2|\hat{H}_{rot}|J,K\rangle = \gamma\sqrt{(J\mp K)(J\pm K+1)(J\mp K-1)(J\pm K+2)} \quad (2.30)$$

Moreover, the asymmetric top Hamiltonian has the property that remains unchanged by any 180 degree rotation[5] around the axes x,y,z, so two-fold rotations around any of the symmetry axis ($C_2(i)$, where $i = a,b$ or c) are symmetry operations.

When fitting an asymmetric top spectrum it is useful to gain an understanding by comparing it to a symmetric top. One useful way to measure the asymmetry of the top is by Ray's asymmetry parameter, κ:

$$\kappa = \frac{2B - A - C}{A - C} \quad (2.31)$$

where A,B,C are the principle axes rotational constants. This quantity equals -1 in the case of the prolate top and $\kappa = 1$ for oblate tops. Therefore, plotting a correlation diagram of κ versus the energy, one covers all the possible cases for asymmetric tops, with the energy diagrams

[5]Therefore, the Hamiltonian belongs to the D_2 symmetry group, also called *Viergruppe* (V).

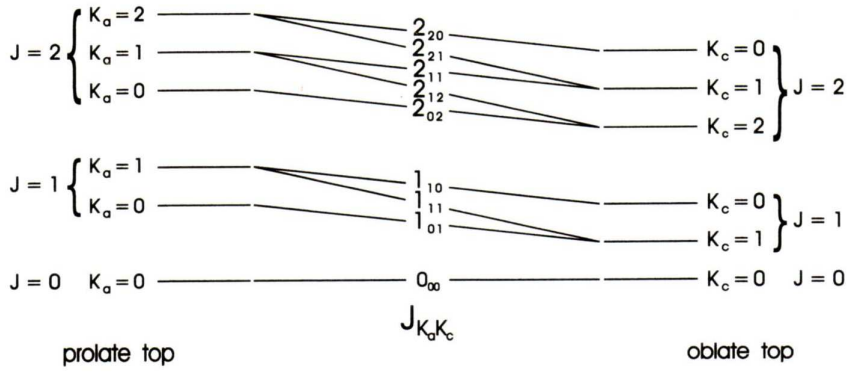

Figure 2.1: The energy levels of symmetric and asymmetric tops [18]

Table 2.1: Symmetry species of asymmetric top energy levels

i.r.		$K_A K_C$
A	$\leftrightarrow$	*ee*
B_c	$\leftrightarrow$	*oe*
B_b	$\leftrightarrow$	*oo*
B_a	$\leftrightarrow$	*eo*

for a prolate and oblate top at the ends. While the meaning of K is clear at either end of this correlation diagram, in the intermediate stages it is unknown, but it may be labeled by the prolate and oblate states it links. This notation is J_{K_A,K_C}, where J is the principle rotational quantum number, K_A is the prolate top projection and K_C the oblate top projection. This way the levels are labeled uniquely, although the K_i numbers do not actually correspond to any projections in the molecule. Also, as both prolate and oblate top energies depend on $|K|$, only positive values of K are used. Such a correlation diagram is given in figure 2.1 [18]. Now we can link this rotation to the symmetry operations of the asymmetric top Hamiltonian. The following correspondence between the D_2 irreducible representation (i.r.) and whether K_A and K_C are even (e) or odd (o) can be made, which is given in table 2.1. This symmetry characterisation will be useful when later on we deduce the selection rules for transitions between the energy levels.

2.4 Non-Rigid Rotation

The rigid rotor approximation introduced in the previous section is reasonable for tightly-bound molecules, and in these cases it may be enough to predict the energy levels (and their splittings) at low J values. However, as more flexible molecules are examined, its limitations become apparent and the first step to correct this is to treat the molecules as semi-rigid. That is, to still assume that the rigid rotor provides a good first approximation and then correct it by including either additional terms (usually via perturbation theory) or by expanding the terms used in the rigid rotor expressions in order to account for the effects of non-rigidity and from the so-far neglected vibration and Coriolis operators. Coriolis forces couple the rotational and vibrational motion as they depend on both rotational and vibrational coordinates[6]

The first step is to admit that the nuclei will not stay clamped into place during rotation. To illustrate this point we can simply consider the moment of inertia of a diatomic molecule, as the distance from between the atoms changes by displacement x from the reference distance r_e:

$$I = \mu r^2 = \mu(r_e + x)^2 = I_e \left(1 + \frac{2x}{r_e} + \left(\frac{x}{r_e}\right)^2\right) \tag{2.32}$$

which when substituted in the expression

$$\hat{H}_{rot,diatomic} = \frac{\hat{J}^2}{2I} = \frac{\hat{J}^2}{2I_e \left(1 + \frac{2x}{r_e} + \left(\frac{x}{r_e}\right)^2\right)} \tag{2.33}$$

yields terms dependent on $\hat{J}^2$. If treated via perturbation theory [1], these terms become the perturbing Hamiltonian $\hat{H}'$ and their first order contribution will be a correction to the rotational constant as it has the same J dependency:

$$\langle \psi | \hat{H}' | \psi \rangle \propto J(J+1) \tag{2.34}$$

[6]Vibrational coordinates are distinguished from rotational ones, as they are subject to an interatomic potential [9].

At second order, the correction will be via matrix elements:

$$-\frac{\langle\psi|\hat{H}'|\psi'\rangle\langle\psi'|\hat{H}'|\psi\rangle}{\Delta E} \propto \langle\psi|\hat{J}^2|\psi'\rangle\langle\psi'|\hat{J}^2|\psi\rangle \quad (2.35)$$

$$\propto J^2(J+1)^2 \quad (2.36)$$

where the $|\psi\rangle$ is the ground state of the molecule, $|\psi'\rangle$ is an excited state and ΔE is the energy difference between the two states. As in order to analytically evaluate the above matrix elements one needs to know all the excited states and therefore it is simpler to fit the proportionality constant, called the centrifugal distortion constant (D), to experimental data. Thus, the expression for energy levels of a diatomic molecule, including a second order perturbative centrifugal distortion correction, is:

$$E_{rot,diatomic} = BJ(J+1) - DJ^2(J+1)^2 \quad (2.37)$$

However, as the rotational frequencies are typically of the order of $10^9 - 10^{12}$ Hz, while vibrational frequencies are typically $10^{13} - 10^{14}$ Hz, there is at least one order of magnitude difference between the two motions. This means that the spectroscopic constants (i.e. the fitted rotational and centrifugal distortion constants) are averaged over the vibrational state.

Moving to polyatomic molecules, the situation becomes more complex, as there are possible degeneracies (which could cause a breakdown of the perturbative approach due to the $\frac{1}{\Delta E}$ dependence) and many more terms to be considered. The same procedure that gave expression 2.37, in the polyatomic case will give terms not dependent on the square of the total angular momentum operator but on the product of different projections[7], i.e. the operators will be of the sort

$$-C\frac{\hat{J}_\alpha\hat{J}_\beta}{2I_{\alpha\alpha}I_{\beta\beta}}$$

where the Greek letters can be any of the principle axes. These terms taken in second order

[7]Clearly in the case of linear rotors the two are equivalent.

perturbation theory will yield a dependence as

$$-\frac{\langle\psi|\hat{H}'|\psi'\rangle\langle\psi'|\hat{H}'|\psi\rangle}{\Delta E} \propto \left\langle \psi \left| \frac{\hat{J}_\alpha \hat{J}_\beta}{2I_{\alpha\alpha}I_{\beta\beta}} \right| \psi' \right\rangle \left\langle \psi' \left| \frac{\hat{J}_\gamma \hat{J}_\delta}{2I_{\gamma\gamma}I_{\delta\delta}} \right| \psi \right\rangle \tag{2.38}$$

Each set of axes $(\alpha,\beta,\gamma,\delta)$ may be assigned a proportionality constant $(\tau_{\alpha\beta\gamma\delta})$. Kivelson and Wilson [19] showed that the asymmetric top centrifugal distortion Hamiltonian with second order perturbation theory can be written as:

$$\begin{aligned}\hat{H}_{rot,CD} &= (X-4R_6)\hat{J}_x^2+(Y-4R_6)\hat{J}_y^2+(Z-4R_6)\hat{J}_z^2 \\ &\quad -D_J\hat{J}^4-D_{JK}\hat{J}^2\hat{J}_z-\delta\hat{J}^2\left(\hat{J}_+^2+\hat{J}_-^2\right) \\ &\quad +R_5[\hat{J}_z^2\left(\hat{J}_+^2+\hat{J}_-^2\right)+\left(\hat{J}_+^2+\hat{J}_-^2\right)\hat{J}_z^2]+R_6\left(\hat{J}_+^4+\hat{J}_-^4\right)\end{aligned} \tag{2.39}$$

where x,y,z are the axes used where z is the quantization axis, XYZ are the corresponding rotational constants and all the other terms are centrifugal distortion terms which are connected to the various values of τ. These terms are called quartic centrifugal distortion constants. However, it has been shown that at most only five quartic terms may be determined from experimental data [16, 20]. Therefore, there are two ways to represent the Hamiltonian: a "first principles" way and a "reduced" Hamiltonian, which can be fitted from the spectra.

The most used reduced Hamiltonian for an asymmetric top was provided by Watson [21], the "A-reduced Hamiltonian". In his reduction, he eliminated the R_6 terms. The Hamiltonian may be separated to different contributions: the rigid rotor $(\hat{H}_r)$ and the quartic centrifugal distortion Hamiltonian $(\hat{H}_{D,a}^{(4)})$. The rigid rotor Hamiltonian is analogous to the first-principles Hamiltonian presented earlier:

$$\hat{H}_r = X'\hat{J}_x^2+Y'\hat{J}_y^2+Z'\hat{J}_z^2 \tag{2.40}$$

$$\begin{aligned}&= \frac{1}{2}(X+Y)\hat{J}^2+\left(Z-\frac{1}{2}(X+Y)\right)\hat{J}_z^2 \\ &\quad +\frac{1}{4}(X-Y)\left(\hat{J}_+^2+\hat{J}_-^2\right)\end{aligned} \tag{2.41}$$

The quartic centrifugal distortion A-reduced Hamiltonian is:

$$\begin{aligned}\hat{H}^{(4)}_{cd,A} &= -\Delta_J \hat{J}^4 - \Delta_{JK}\hat{J}^2\hat{J}_z^2 - \Delta_K \hat{J}_z^4 \\ &\quad -\delta_j \hat{J}^2\left(\hat{J}_+^2 + \hat{J}_-^2\right) - \delta_k\left[\hat{J}_z^2\frac{\left(\hat{J}_+^2+\hat{J}_-^2\right)}{2} + \frac{\left(\hat{J}_+^2+\hat{J}_-^2\right)}{2}\hat{J}_z^2\right]\end{aligned} \tag{2.42}$$

In the case of a symmetric top, another reduction is more useful, the so-called S-reduced Hamiltonian. This is derived from a first principles Hamiltonian by eliminating R_5 contribution. Its difference from the A-reduced form starts at the quartic terms:

$$\begin{aligned}\hat{H}^{(4)}_{cd,S} &= -D'_J \hat{J}^4 - D'_{JK}\hat{J}^2\hat{J}_z^2 - D'_K \hat{J}_z^4 \\ &\quad -d_1 \hat{J}^2\left(\hat{J}_+^2 + \hat{J}_-^2\right) - d_2(\hat{J}_+^4 + \hat{J}_-^4)\end{aligned} \tag{2.43}$$

The coefficients appearing on equations 2.43 and 2.42 are linear combinations of the ones appearing on equation 2.39. Finally, as we will be using mainly the S-reduced Hamiltonian, it is worth mentioning the next order centrifugal distortion terms, which are related to the third order perturbation theory terms in a first principles Hamiltonian. These are the so-called sextic terms:

$$\begin{aligned}\hat{H}^{(6)}_{cd,S} &= H_J \hat{J}^6 + H_{JK}\hat{J}^4\hat{J}_z^2 + H_{KJ}\hat{J}^2\hat{J}_z^4 + H_K \hat{J}_z^6 \\ &\quad +h_1 \hat{J}^4\left(\hat{J}_+^2 + \hat{J}_-^2\right) + h_2\hat{J}^2(\hat{J}_+^4 + \hat{J}_-^4) + h_3(\hat{J}_+^6 + \hat{J}_-^6)\end{aligned} \tag{2.44}$$

So, for a symmetric top, the overall rotational Hamiltonian with centrifugal corrections up to sextic terms is:

$$\hat{H}_{rot-s} = \hat{H}_r + \hat{H}^{(4)}_{cd,S} + \hat{H}^{(6)}_{cd,S} \tag{2.45}$$

2.5 Selection Rules and Rotational Transitions

The strongest interaction linking different states, and therefore allowing a transition, is that between the electric field gradient and the dipole moment of the molecule. This will be examined

in more detail in chapter 5 (more information are also provided in the appendix section C.2), and for our purposes here it is enough to note that the intensity of a transition between two states is proportional to the corresponding matrix element squared:

$$I \propto |\langle J', M', K'|\mu \cdot \mathbf{E}|J, M, K\rangle|^2 \tag{2.46}$$

where J', M' and K' are the quantum numbers for the excited rotational state and J, M, K are the quantum numbers for the ground rotational state. From this we can already conclude that only polar molecules are expected to have a rotational spectrum.

As the transitions between the rotational levels are accompanied by emission or absorption of a photon, and since a photon has only a single unit of angular momentum, due to the law of conservation of angular momentum we can conclude that:

$$J' = J \pm 1 \tag{2.47}$$

However, there is no corresponding restriction on the orientation of the change of the angular momentum operator. Therefore, the change on the projection quantum number may take all three possible (quantised) values for both the body-fixed (K) and space-fixed (M) axes systems:

$$\Delta M = M' - M = 0, \pm 1 \tag{2.48}$$

$$\Delta K = K' - K = 0, \pm 1 \tag{2.49}$$

These selection rules may now be applied to determine the transition frequencies from the corresponding energy levels for different rotors.

2.5.1 Linear and spherical tops

As there is no M dependence in the energy level expression, the transition energies are simply:

$$\nu(J+1 \leftarrow J)_{linear} = 2B(J+1) - 4DJ^2(J+1)^2 \tag{2.50}$$

Consequently, the spectrum is composed by lines with approximately equal spacing of $2B$.

2.5.2 Symmetric tops

For a symmetric top, according to symmetry arguments, the matrix element allowing a transition on the unique axis (i.e. the quantization axis) can be non-zero only if there is a non-zero zeroth component of dipole moment (μ_0). Therefore only $\Delta K = 0$ transitions are observed. This results in both oblate and prolate tops having the same transition energy expressions:

$$\nu(J+1 \leftarrow J)_{symmetric} = 2(J+1)(B - D_{JK}K^2) - 4D_J(J+1)^3 \tag{2.51}$$

where $K = K_A$ for prolate and $K = K_C$ for oblate tops. Therefore the general appearance of the spectrum is close to that of linear rotors, but now different K levels are slightly separated due to the centrifugal distortion.

2.5.3 Asymmetric tops

In the case of an asymmetric top now all three components of the dipole moment are potentially non-zero. Moreover, as was seen in an earlier section, it is not possible to characterise the states of an asymmetric top by a single projection quantum number. Therefore, attempting to write out the transition energy expression simply by the so-far stated selection rules will be very complicated if indeed possible. Instead, we can try to use symmetry arguments to obtain specific (instead of gross) selection rules for a transition along each dipole moment component.

As the $|J,K\rangle$ basis is not sufficient to describe an asymmetric top wavefunction, this will be expressed as a linear combination of oblate and prolate top functions, collectively indicated as J_{K_A,K_C}. The symmetry of each level may be determined from the irreducible representation it corresponds to found in the D_2 (V) representation. By restricting the even/odd K_A/K_C combination between the initial and final states, the correct symmetry may be achieved to satisfy the symmetry requirement for $\Gamma^{\psi_f} \otimes \Gamma^{\psi_i}$. This has to be antisymmetric, so when the direct product

Table 2.2: Asymmetric top selection rules according to transition type

Transition Type	Dipole Component	$K_A, K_C \leftrightarrow K'_A, K'_C$	ΔK_A	ΔK_C
a-type	$\mu_a \neq 0$	$ee \leftrightarrow eo$	$0, \pm 2, \ldots$	$\pm 1, \pm 3 \ldots$
		$oe \leftrightarrow oo$		
b-type	$\mu_b \neq 0$	$ee \leftrightarrow oo$	$\pm 1, \pm 3 \ldots$	$\pm 1, \pm 3 \ldots$
		$oe \leftrightarrow eo$		
c-type	$\mu_c \neq 0$	$ee \leftrightarrow oe$	$\pm 1, \pm 3 \ldots$	$0, \pm 2, \ldots$
		$eo \leftrightarrow oo$		

with Γ^{μ} is taken, this would contain a final symmetric product, which is a prerequisite for the integral in equation 2.46 to be non-zero.

In table 2.2, the restrictions on the changes in K_A and K_C are tabulated, depending on which projection of the dipole moment induces the transition. An odd $K_{A/C}$ number is indicated as o and an even one as e. As the state is a linear combination of functions with a $K_{A/C}$ value, rather than a single one, the total $K_{A/C}$ may change by more than one unit each time.

2.6 Flexible Species And Internal Rotations

In this final section we are moving even further from our initial assumption of a rigid rotor, into the domain of flexible molecules. To define what we mean by *flexible molecules*, and how these are different from a rigid, or a semi-rigid molecule can use the instantaneous position vector ($\mathbf{d}_\eta$) for atom η. This is defined as:

$$\mathbf{d}_\eta = \mathbf{r}_\eta - \mathbf{a}_\eta \tag{2.52}$$

where $\mathbf{r}_\eta$ is the equilibrium position vector and $\mathbf{a}_\eta$ the vector deviation from it [9]. Now we can categorise the different types of molecules depending on the relative magnitude of the instantaneous displacement $\mathbf{d}_\eta$ to the reference vectors $\mathbf{r}_\eta$, [16]:

- Rigid rotor: $\mathbf{d}_\eta = \mathbf{r}_\eta - \mathbf{a}_\eta = 0$
- Semi-rigid molecule: $\mathbf{d}_\eta << \mathbf{r}_\eta$

- Flexible molecule: $\mathbf{d}_\eta \approx \mathbf{r}_\eta$

Although there are obvious differences between these categories, the flexible molecules may be seen as semi-rigid molecules with large amplitude motion. These large amplitude motions are may be equivalently regarded as low-lying vibrations of the molecule, or internal rotations of parts of the molecule. As was mentioned earlier, the mixing of vibrational and rotational degrees of freedom is caused by the Coriolis interactions.

2.6.1 Internal vibration angular momentum

One approach capable of accounting for the effects of vibration is to introduce a "vibrationally-induced" angular momentum, $\hat{l}$. This now can be used to represent the Coriolis forces, thus modeling the overlap of rotation and vibration. This angular momentum, $\hat{l}$ will depend on both the rotational and the vibrational degrees of freedom. It can be shown [16] that, if we define the total rotational angular momentum (analogous to the classical angular momentum) as $\hat{J}$ and the vibrational angular momentum as $\hat{P}$, then Hamiltonian for the energy dependence of the molecule with respect to both the vibrational and rotational degrees of freedom ($\hat{H}'_{rv}$) for a polyatomic rotor becomes:

$$\hat{H}_{rv} = \hat{T}_{rot} + \hat{T}_{vibr} + \hat{T}_{cor} + V \tag{2.53}$$

$$= \hat{H}'_{rot} - \hat{T}'_{vibr} + V \tag{2.54}$$

where

$$\hat{T}'_{vibr} = \frac{1}{2}\sum_r P_r^2 \tag{2.55}$$

is the vibrational Hamiltonian based only on the pure vibrational angular momenta (no dependence on the rotational coordinates). Now, following the same argument as in the beginning of this chapter, we can re-define the modified rotational Hamiltonian:

$$\hat{H}'_{rot} = A(\hat{J}_a - \hat{l}_a) + B(\hat{J}_b - \hat{l}_b) + C(\hat{J}_c - \hat{l}_c) \tag{2.56}$$

which includes a Coriolis contribution due to internal rotation.

2.6.2 Internal rotation Hamiltonian

Thankfully, for all of the categories outlined at the beginning of this section, the approach just described can be used, so that large-amplitude motion causing the deviation from the rigid rotor picture can be considered as a separate source of angular momentum.

Considering the effects of internal rotation will also come useful when we later consider van der Waals complexes: In the case of van der Waals complexes, the rotation of the constituent molecules ("monomers") may be quenched during complexation, but usually continues in various degrees depending on the intermolecular potential. Therefore, we can distinguish two extreme cases for the monomers: when the intermolecular potential is very strong thus heavily hindering their motion and when the intermolecular potential is very weak thus barely limiting their range of movement. The latter case is also called the "free-rotor" limit. Similarly to the flexible molecules' case, the monomers' rotation corresponds to a vibration or an internal rotation when the complex as a whole is considered.

Yet, although we are mostly interested in the rotation of monomers within a complex, most of the theory of internal rotations has been developed with respect to organic group rotations and for this reason, the approach presented here may seem "organic"-oriented. Actually in chapter 6, we will consider the methyl group internal rotation, where the following is directly applicable. For this reason, we will use the methyl group internal rotation in an organic molecule as an example here and will concentrate on that from now on. The molecule is considered rigid except for one torsional angle, τ. If ω_τ, the angular velocity around the torsional angle, is zero, then the expressions derived earlier are accurate, as the molecule is rigid. When $\omega_\tau \neq 0$, then we can separate the internal rotor from the rest of the molecule, and the latter is referred to as the "frame". From the frame's perspective, the internal rotor is collapsed to a point with mass equal to the sum of the masses of the rotor, but without any structure.

Now we can make the connection with the theory presented earlier in this section: at equa-

tion 2.56, $\hat{J}$ is the frame rotation and $\hat{l}$ the angular momentum for the internal rotation. Respectively, we can define the rotational constants of the frame only as:

$$A \to A_f \qquad B \to B_f \qquad C \to C_f$$

Ignoring the purely vibrational Hamiltonian $\hat{T}'_{vibr}$ in equation 2.55, and taking into account all principle axes, the Hamiltonian may be expanded as[8]:

$$\begin{aligned} \hat{H}_{rot,int} &= \underbrace{A_f\hat{J}_a^2 + B_f\hat{J}_b^2 + C_f\hat{J}_c^2}_{\hat{H}_{frame}} \\ &\quad \underbrace{-2A_f\hat{J}_a\hat{l}_a - 2B_f\hat{J}_b\hat{l}_b - 2C_f\hat{J}_c\hat{l}_c}_{\hat{H}_{Cor}} \\ &\quad \underbrace{+b_{eff}\hat{l}^2 + V(\tau)}_{\hat{H}_{tor}} \end{aligned} \tag{2.57}$$

where all the terms depending only on the internal rotor angular momentum are collected in $b_{eff}\hat{l}^2$. Using the directional cosines λ_i, which indicate the cosine of the angle between the axis of the internal rotation and the principle axis of the frame:

$$b_{eff} = b_0 + A_f\lambda_A^2 + B_f\lambda_B^2 + C_f\lambda_C^2 \tag{2.58}$$

where b_0 is the rotational constant of the internal rotor. b_{eff} practically projects the Hamiltonian of the internal rotor to the principle axis system. The Hamiltonian for the internal rotor along with the potential that hinders its motion is called the *torsional* Hamiltonian.

The eigenstates of $\hat{H}_{rot,int}$, noted as $|\Psi\rangle$, can be taken as the product of the wavefunctions for $\hat{H}_{frame}$, noted as $|\psi_r\rangle$, with the wavefunctions of $\hat{H}_{tor}$, noted as $|\psi_\tau\rangle$:

$$|\Psi\rangle = |\psi_r\rangle|\psi_\tau\rangle \tag{2.59}$$

and $\hat{H}_{Cor}$ mixes the two subsets of eigenstates. Both $|\psi_r\rangle$ and $|\psi_\tau\rangle$ are symmetric top wavefunctions.

[8]This Hamiltonian is the same as the one used by the programs SPFIT and SPCAT by Picket [22, 23].

2.6.3 Perturbative correction to molecular energy levels

If we are interested in solving the Schrödinger equation for a molecule with internal rotation, using the Hamiltonian in equation 2.57, we can do this by taking $\hat{H}_{frame}$ as the reference Hamiltonian and $\hat{H}_{Cor}$ as a perturbation. Then, the terms arising due to the Coriolis interaction can be taken as effective centrifugal distortion terms in a least-squares fitting program, corresponding to their dependence on $\hat{J}_A, \hat{J}_B$ and $\hat{J}_C$.

The first order correction according to standard perturbation theory [1] is:

$$\langle 0|\hat{H}_{Cor}|0\rangle = \underbrace{-2A_f\lambda_A\langle 0|\hat{l}|0\rangle}_{D_a}\hat{J}_a - \underbrace{2B_f\lambda_B\langle 0|\hat{l}|0\rangle}_{D_b}\hat{J}_b - \underbrace{2C_f\lambda_C\langle 0|\hat{l}|0\rangle}_{D_c}\hat{J}_c \tag{2.60}$$

The assignment of the operators here follows the assignment in the SPFIT program. Practically, this enables us to fit a molecule with internal rotation as if it simply had a very large centrifugal distortion. Moreover, it allows us to detect a large degree of internal rotation if the centrifugal distortion constants are unphysically large.

The second order correction is:

$$\begin{aligned}
-\sum_{n\neq 0}\frac{\langle 0|\hat{H}_{Cor}|n\rangle\langle n|\hat{H}_{Cor}|0\rangle}{E_n - E_0} \quad = \quad & -4A_f^2\lambda_A^2\sum_{n\neq 0}\frac{\langle 0|\hat{l}|n\rangle\langle n|\hat{l}|0\rangle}{E_n - E_0}\hat{J}_a^2 \\
& -4B_f^2\lambda_B^2\sum_{n\neq 0}\frac{\langle 0|\hat{l}|n\rangle\langle n|\hat{l}|0\rangle}{E_n - E_0}\hat{J}_b^2 \\
& -4C_f^2\lambda_C^2\sum_{n\neq 0}\frac{\langle 0|\hat{l}|n\rangle\langle n|\hat{l}|0\rangle}{E_n - E_0}\hat{J}_c^2 \\
& -4A_fB_f\lambda_A\lambda_B\sum_{n\neq 0}\frac{\langle 0|\hat{l}|n\rangle\langle n|\hat{l}|0\rangle}{E_n - E_0}\hat{J}_a\hat{J}_b \\
& -4B_fC_f\lambda_B\lambda_C\sum_{n\neq 0}\frac{\langle 0|\hat{l}|n\rangle\langle n|\hat{l}|0\rangle}{E_n - E_0}\hat{J}_b\hat{J}_c \\
& -4A_fC_f\lambda_A\lambda_C\sum_{n\neq 0}\frac{\langle 0|\hat{l}|n\rangle\langle n|\hat{l}|0\rangle}{E_n - E_0}\hat{J}_a\hat{J}_c
\end{aligned} \tag{2.61}$$

Here some of the corrections depend on $\hat{J}_A^2, \hat{J}_B^2$ and $\hat{J}_C^2$, so these terms may be absorbed in the rotational constants. The final three terms give off-diagonal elements with respect to the

principle axis.

Finally, Ouyang [24] has derived the following expressions for the third order perturbation theory corrections, W_i^3, for each of the principle axes, i. For $i = A$ and A being the quantisation axis, the correction is:

$$\begin{aligned} W_A^3 &= -\Bigg(\underbrace{8A_f^3\lambda_A^3\Xi}_{D_A^A}\hat{J}_a^3 + \underbrace{8A_fB_f^2\lambda_A\lambda_B^2\Xi}_{D_A^B}\left(\hat{J}_b^2\hat{J}_a + \hat{J}_b\hat{J}_a\hat{J}_b + \hat{J}_a\hat{J}_b^2\right) \\ &\quad + \underbrace{8A_fC_f^2\lambda_A\lambda_C^2\Xi}_{D_A^C}\left(\hat{J}_c^2\hat{J}_a + \hat{J}_c\hat{J}_a\hat{J}_c + \hat{J}_a\hat{J}_c^2\right)\Bigg) \end{aligned} \tag{2.62}$$

where

$$\Xi = \sum_{(n,m\neq 0)} \frac{\langle 0|\hat{l}|n\rangle\langle n|\hat{l}|m\rangle\langle m|\hat{l}|0\rangle}{(E_n - E_0)(E_m - E_0)} - \sum_{(m\neq 0)} \frac{\langle 0|\hat{l}|m\rangle\langle m|\hat{l}|0\rangle\langle 0|\hat{l}|0\rangle}{(E_m - E_0)^2} \tag{2.63}$$

Equation 2.62 may be rearranged using the raising and lowering operators, in an analogous way that the asymmetric top Hamiltonian was rearranged, in terms of J and J_a (K) as:

$$W_A^3 = -\left[\underbrace{\left(D_A^A - \frac{D_A^B + D_A^C}{2}\right)}_{D_A^K}\hat{J}_A^2 + \underbrace{\left(\frac{D_A^B + D_A^C}{2}\right)}_{D_A^J}\hat{J}^2 + \underbrace{\left(\frac{D_A^B - D_A^C}{4}\right)}_{D_A^1}\left(\hat{J}_+^2 + \hat{J}_-^2\right)\right]\hat{J}_A \tag{2.64}$$

2.6.4 The solutions of the torsional Hamiltonian

Going back to equation 2.57, in order to have the complete picture, we also need to concern ourselves with the energy levels coming from the purely torsional Hamiltonian, $\hat{H}_{tor}$.

So far, we have considered the case that the Coriolis interaction was a perturbation to the molecular Hamiltonian, i.e. the main energy level splittings came from $\hat{H}_{frame}$. We now consider the reverse case where the bonding between the frame and the internal rotor is so weak that what would be an internal vibration then slows down enough that it occurs in the microwave region and can be classified as an internal rotation. Furthermore, in this case the torsional

Hamiltonian gives rise to the main energy level splittings [16].

Moving this case to extreme, it would correspond to a no-barrier (i.e. $V(\tau) = 0$) free-rotor case where the frame and rotor rotate freely and independently. We will actually start with that and then come all the way back to the high barrier case where the internal rotation is again a vibration.

If the internal rotor has a C_n symmetry axis around the torsional τ angle, then this will be reflected in the potential, as rotation by $\frac{2\pi}{n}$ should not change the energy. This means [9, 25]:

$$V(\tau) = V\left(\tau \pm \frac{2\pi}{n}\right) \tag{2.65}$$

Therefore any one-dimensional potential can be expanded in the Fourier form:

$$V(\tau) = \frac{1}{2}\sum_{m=1}^{\infty} V_{nm}(1 - \cos mn\tau) \tag{2.66}$$

This is applicable to any C_n axis, but for an example let us consider the case when $n = 3$, which is the case for the methyl radical. Then, expanding the series we get:

$$V(\tau) = \frac{1}{2}V_3(1 - \cos 3\tau) + \frac{1}{2}V_6(1 - \cos 6\tau) + \ldots \tag{2.67}$$

Usually, this can be truncated after the first (V_3) term to a good approximation. This can then be used to solve the Schrödinger equation for the internal rotor:

$$\hat{H}_{rot,int}|\psi_\tau\rangle = E_{rot,int}|\psi_\tau\rangle \tag{2.68}$$

directly[9], or may be used as a perturbative Hamiltonian.

In the case of very low barrier (free rotor limit) the Schrödinger equation becomes simply:

$$-b_0\frac{\partial^2\psi_\tau}{\partial^2\tau} = E\psi_\tau \tag{2.69}$$

[9]The details of this approach may be found in reference [16].

Table 2.3: The C_3 point group character table [17]

C_3	E	C_3	C_3^2
A	1	1	1
E	1	$e^{\frac{2\imath\pi}{3}}$	$e^{\frac{-2\imath\pi}{3}}$
	1	$e^{\frac{-2\imath\pi}{3}}$	$e^{\frac{2\imath\pi}{3}}$

which is analogous to the equation for a particle in a ring. The eigenstates and eigenvalues for this are:

$$|\psi_\tau\rangle = |l,m\rangle = \frac{e^{\imath m\tau}}{\sqrt{2\pi}} \tag{2.70}$$

$$E_m = b_0 m^2 \quad ; \quad m = 0, \pm 1, \pm 2, \ldots, \pm l \tag{2.71}$$

where l is the principal quantum number for the rotational angular momentum of the internal rotor and m its projection to its unique axis. What this means is that in the free rotor limit, the contribution of the internal rotor in energy is equivalent to adding the energy levels of another independent rotating species.

Moreover, these eigenfunctions have to be invariant with respect to the C_3 operation, and thus can be categorised by the irreducible representations of the C_3 character table [26]: That is, the eigenvectors may either transform as the totally symmetric A irreducible representation, or as part of the doubly degenerate E representation. If the m projection is any multiple of 3 or 0, then the irreducible representation of that state is A. Otherwise, the state transforms as one of the degenerate E irreducible representations. Thus, $m = \pm 3 * n$ levels are the only ones that do not have to be degenerate for an C_3 asymmetric top, while any other $\pm m$ value belongs to an E and therefore is degenerate by symmetry.

Increasing the barrier from the free rotor limit to low barrier, the larger energy difference still comes from the internal rotor splittings. The reference Hamiltonian matrix has elements:

$$\langle m|\hat{H}_{rot,int}|m\rangle = b_{eff} m^2 + \frac{V_3}{2} \tag{2.72}$$

$$\langle m \pm 3|\hat{H}_{rot,int}|m\rangle = -\frac{V_3}{4} \tag{2.73}$$

Diagonalising this Hamiltonian matrix would give the torsional ground ($|0\rangle$) and excited ($|n\rangle$; $n \neq 0$) states. The symmetry of the torsional energy levels alternates as "*AEEAA*...".

At the high barrier limit on the other hand, the V_3 potential becomes impenetrable. Now, the wavefunctions are localised at each minima, and the situation resembles a harmonic oscillator in each energy well. As they are not mixed, the states in identical minima are the same, and therefore degenerate.

The potential function may be further expanded using a Taylor series:

$$1-\cos 3\tau = 1-\left(1-\frac{(3\tau)^2}{2!}+\frac{(3\tau)^4}{4!}-\ldots\right)\approx\frac{(3\tau)^2}{2!} \tag{2.74}$$

Then, the torsional Hamiltonian has the form of Harmonic oscillator:

$$\hat{H}_{rot,int} = b_{eff}l^2+\frac{9V_3\tau^2}{4} \tag{2.75}$$

Now, if we approximate the potential around the minimum as a parabolic harmonic oscillator potential with force constant k:

$$V=\frac{1}{2}k\tau^2 \tag{2.76}$$

the frequency of the torsional oscillation, ω_t, is:

$$\omega_t=\frac{1}{2\pi}\sqrt{\frac{k}{I_r}} \tag{2.77}$$

The force constant may be related to the potential with C_n symmetry as:

$$k=\left(\frac{\partial^2 V}{\partial\tau^2}\right)_{\tau=0}=\frac{n^2V}{2} \tag{2.78}$$

Finally, the contribution of the internal rotation to the energy levels expression now is a harmonic oscillator:

$$E_{\text{internal}\quad\text{rotation}}=\omega_t(v+\frac{1}{2}) \tag{2.79}$$

where v is the torsional vibration quantum number. At this case, there is no distinction between

A and E states. Therefore, it has been demonstrated how moving from a free rotor to a high barrier case, the energy levels change with respect to the effect of internal rotation.

2.6.5 The methyl group rotation

As was demonstrated in the previous section, the internal rotation around a C_3 barrier in a low barrier (but not free-rotor) case gives rise to states with symmetry A and E. Normally, this would increase the number of transitions recorded. However, internal rotation may also be considered as a tunnelling motion between energy minima. As the hydrogen nucleus has an angular momentum $I_H = \frac{1}{2}$, for the rotation of the methyl group we also need to make sure it obeys the Pauli Exclusion Principle. Since there are three indistinguishable spin $\frac{1}{2}$ particles, each with an $m_s = \pm\frac{1}{2}$, there are eight possible spin states. By following an approach outlined by Wilson [19], we can get the character table for the nuclear spin wavefunction. These can be reduced to $4A \oplus 2E$ irreducible representations.

The total wavefunction needs to be antisymmetric with respect to the interchange between two of the protons. Interestingly, a C_3 rotation (and similarly a C_3^2 rotation) is equivalent to two successive interchanges of two protons. Therefore, the wavefunction needs to be symmetric with respect to such a rotation, i.e. the direct product of the nuclear spin and the tunnelling wavefunctions needs to contain the A representation.

From the direct product tables [26], we can see that for this to be the case, each irreducible representation must be multiplied by itself. This means that the A and E tunnelling/internal rotation states will have to be combined with the A and E nuclear spin states respectively. As there are $4A$ and $2E$ nuclear spin functions and the direct product tables dictate:

$$A \otimes A = A \tag{2.80}$$

$$E \otimes E = 2A + E \tag{2.81}$$

there is in total an equal number (4) of A states from the combination of the $4A$ nuclear spin states with the A tunnelling state and the combination of $2E$ nuclear spin states with the E

internal rotation state. Therefore, the A and E tunnelling states have equal statistical weight, although A states are lower in energy. Moreover, a transition between A and E states would require a change of the nuclear spin, which is not feasible in our experimental setup. Therefore, the two states do not mix and each produces a separate spectrum.

Unfortunately, as the separation between A and E transition frequencies is not a simple analytical form of the rotational quantum numbers, their spectra cannot easily give information about the internal rotation in the molecule. One way to obtain such information is presented in chapter 6.

Chapter 3

Angular Momentum and Tensor Algebra

"*The simplicities of natural laws arise through the complexities of the language we use for their expression.*"

- Eugene Wigner

3.1 Introduction

The aim of this chapter is to present some key results of angular momentum theory and spherical tensor algebra, that will be useful for the reader in the following chapters. However, both of the mentioned topics are vast. Therefore, the presentation here is not meant to be exhaustive, and many results unfortunately are quoted without their derivation. Derivations and more detail than provided here may be found in the references, although special care needs to be taken with notation as it is not shared in all books.

In classical mechanics, the linear momentum vector $\mathbf{p}$ is defined by:

$$\mathbf{p} = m\mathbf{v} \tag{3.1}$$

where m is the mass of the particle and $\mathbf{v}$ is its velocity. The angular momentum $\mathbf{l}$ is defined as

the vector cross product between the position vector of the particle **r** and its linear momentum:

$$\mathbf{l} = \mathbf{r} \times \mathbf{p} \tag{3.2}$$

By analogy to these expressions, the quantum mechanical operator for angular momentum can be constructed from equation 3.2 by substituting the operator for linear momentum, $\hat{p}$. The Cartesian components of $\hat{p}$ have the form:

$$\hat{p}_j = -\imath \frac{\partial}{\partial j} \tag{3.3}$$

where j is the corresponding Cartesian axis. The corresponding angular momentum operators in a Cartesian system are labelled ℓ_j, and the angular momentum operator squared is [27]:

$$\ell^2 = \ell_x^2 + \ell_y^2 + \ell_z^2 \tag{3.4}$$

It is often more practical to use spherical polar rather than Cartesian coordinates. The standard transformation between them is:

$$x = r\sin\theta\cos\phi; \quad y = r\sin\theta\sin\phi; \quad z = r\cos\theta$$

where r is the distance of the from the origin of the Cartesian axes, θ is the (polar) angle from the z axis and ϕ the (azimuthal) angle on the xy plane. Perhaps the best way to define angular momentum operators is by their commutation relations:

$$[\ell_x, \ell_y] = \imath\ell_z; \quad [\ell_y, \ell_z] = \imath\ell_x; \quad [\ell_z, \ell_x] = \imath\ell_y; \quad \left[\ell^2, \ell_j\right] = 0$$

where j may again be any of the Cartesian axes.

3.2 Legendre Polynomials and Spherical Harmonics

The eigenstates that satisfy the equations:

$$\ell^2|\ell,m\rangle = \ell\hbar^2(\ell+1)|\ell,m\rangle \tag{3.5}$$

$$\ell_z|\ell,m\rangle = m\hbar|\ell,m\rangle \tag{3.6}$$

are the spherical harmonics[1]:

$$|\ell,m\rangle = \mathscr{Y}_m^\ell(\theta,\phi) \tag{3.7}$$

where ℓ is an integer greater or equal to zero, and m takes the values $\ell,\ell-1,\ldots,-\ell$. Conventionally, the symbol ℓ is reserved for the orbital angular momentum operator, and general angular momentum is written as j. However, spherical harmonics are also the eigenstates of the Schrödinger equation for a particle on a sphere, and have the same functional form as the hydrogenic atomic orbitals. For this reason, the (ℓ,m) notation is often used instead of the (j,m_j) [28]. The spherical harmonics are a product of two functions, each corresponding to a different angle dependence:

$$\mathscr{Y}_m^\ell(\theta,\phi) = \Theta_{\ell m}(\theta)\Phi_m(\phi) \tag{3.8}$$

where:

$$\Phi_m(\phi) = (2\pi)^{-1/2}\exp(\imath m\phi) \tag{3.9}$$

$$\Theta_{\ell m}(\theta) = \frac{(-1)^m}{(2^\ell)\ell!}\left[\frac{2\ell+1}{2}\frac{(\ell-m)!}{(\ell+m)!}\right]^2 \sin^m(\theta)\left[\frac{d}{d\cos\theta}\right]^{\ell+m}(\cos^2\theta-1)^\ell \tag{3.10}$$

Spherical harmonics form a complete set of functions for the two angles they depend on. Therefore, a theoretical infinite weighted combination of them can represent any function with a (θ,ϕ) dependence. The $\Theta_{\ell m}(\theta)$ function may also be connected to another complete set of functions, now with a single angle dependence, the associated Legendre functions [27]:

$$\mathscr{P}_m^\ell(\cos\theta) = \sin^m\theta\left[\frac{d}{d\cos\theta}\right]^m \mathscr{P}^\ell(\cos\theta) \tag{3.11}$$

[1] For clarity from here on we set $\hbar = 1$ for the rest of this chapter.

where

$$\mathscr{P}^{\ell}(\cos\theta) = \frac{1}{2^{\ell}\ell!}\left[\frac{d}{d\cos\theta}\right]^{\ell}(\cos^2\theta - 1)^{\ell} \tag{3.12}$$

are called the ordinary Legendre polynomials. The relation to the $\Theta_{\ell m}(\theta)$ function is:

$$\Theta_{\ell m}(\theta) = (-1)^m\left[\frac{2\ell+1}{2}\frac{(\ell-m)!}{(\ell+m)!}\right]^{1/2}\mathscr{P}_m^{\ell}(\cos\theta) \tag{3.13}$$

for $m \geq 0$. For $m < 0$, the following symmetry relationship may be used:

$$\Theta_{\ell-|m|}(\theta) = (-1)^m\Theta_{\ell|m|}(\theta) \tag{3.14}$$

which, in conjunction with equation 3.9, gives:

$$\mathscr{Y}_m^{\ell *}(\theta,\phi) = (-1)^m\mathscr{Y}_{-m}^{\ell}(\theta,\phi) \tag{3.15}$$

Spherical harmonics are normalised so that:

$$\int_0^{2\pi}\int_0^{\pi}\mathscr{Y}_m^{\ell,*}(\theta,\phi)\mathscr{Y}_{m'}^{\ell'}(\theta,\phi)\sin\theta d\theta d\phi = \delta_{\ell'\ell}\delta_{m'm} \tag{3.16}$$

For some applications it is convenient to use Racah harmonics, which are defined as:

$$\mathscr{C}_m^{\ell}(\theta,\phi) = \sqrt{\frac{4\pi}{2\ell+1}}\mathscr{Y}_m^{\ell}(\theta,\phi) \tag{3.17}$$

Racah harmonics have the additional property:

$$\mathscr{C}_m^{\ell}(0,0) = \delta_{m,0} \tag{3.18}$$

These may now be used to define the regular ($\mathscr{R}_{\ell,m}$) and irregular ($\mathscr{I}_{\ell,m}$) spherical harmonics:

$$\mathscr{R}_{\ell,m} = r^{\ell}\mathscr{C}_m^{\ell}(\theta,\phi) \tag{3.19}$$

$$\mathscr{I}_{\ell,m} = r^{\ell-1}\mathscr{C}_m^{\ell}(\theta,\phi) \tag{3.20}$$

Finally, we can use the spherical harmonics to define the *real spherical harmonics*. These are similar functions that will prove useful later on in this work, especially in relation to intermolecular forces:

$$\mathscr{S}_0^\ell(\theta,\phi) = \mathscr{Y}_0^\ell(\theta,\phi) \tag{3.21}$$

$$= \sqrt{\frac{2\ell+1}{4\pi}}\mathscr{P}^\ell(\cos\theta) \tag{3.22}$$

$$\mathscr{S}_m^\ell(\theta,\phi) = \begin{cases} \left.\begin{aligned} &= \tfrac{1}{\sqrt{2}}\left(\mathscr{Y}_m^\ell(\theta,\phi) + (-1)^m\mathscr{Y}_{-m}^\ell(\theta,\phi)\right) \\ &= \sqrt{\tfrac{(2\ell+1)(1-m)!}{2\pi(1+m)!}}\mathscr{P}_m^\ell(\cos\theta)\cos(m\phi) \end{aligned}\right\} & \text{for} \quad m>0 \\ \\ \left.\begin{aligned} &= \tfrac{\imath}{\sqrt{2}}\left((-1)^{|m|}\mathscr{Y}_{|m|}^\ell(\theta,\phi) - \mathscr{Y}_{-|m|}^\ell(\theta,\phi)\right) \\ &= \sqrt{\tfrac{(2\ell+1)(1+|m|)!}{2\pi(1-|m|)!}}\mathscr{P}_{-|m|}^\ell(\cos\theta)\sin(-|m|\phi) \end{aligned}\right\} & \text{for} \quad m<0 \end{cases} \tag{3.23}$$

3.3 Addition Of Angular Momenta

3.3.1 Coupling of two angular momenta

If we consider two separate but interacting sources of angular momenta, j_1 and j_2, with projections m_1 and m_2, then there are two possible representations of the system: the "coupled" and the "uncoupled" representation. In the uncoupled (also called "decoupled") representation, the eigenstates are characterised by the angular momenta and projections of the components:

$$|j_1,m_1,j_2,m_2\rangle = |j_1,m_1\rangle|j_2,m_2\rangle \tag{3.24}$$

However, the states of this representation are not eigenstates of the total angular momentum of the system (which classically would be the vector sum of j_1 and j_2). This becomes more problematic as the interaction becomes stronger.

If there is just a single interaction that couples the two angular momenta, then they are no longer eigenfunctions of the complete system and the coupled representation is the natural

choice[2]. This is characterised by the total angular momentum j and its projection m. If the latter one is stronger, then the uncoupled representation may be preferred.

The coupled eigenstates are written as:

$$|j, j_1, j_2, m\rangle$$

The two are linked by the fact that the projection of the total angular momentum on an axis has to equal the sum of the projections of the constituent momenta on that same axis:

$$m = m_1 + m_2 \tag{3.25}$$

and by the so-called triangle condition:

$$|j_1 + j_2| \geq j \geq |j_1 - j_2| \tag{3.26}$$

This is also written as $\Delta(j_1, j_2, j)$. Choosing between these representations, one practically chooses what quantum numbers will be good, and therefore which interactions will appear on the diagonal terms of an angular-momentum operator Hamiltonian matrix, and which in the off-diagonal terms. Although if a complete basis set is used, the final numerical results will be the same (the physical reality is the same in both representations), computationally this is often difficult or impossible to do. Therefore, one often relies to the understanding of the underlying physical interaction in order to choose the representation that will give the optimum combination of the smallest basis set without neglecting any important effects. Since both representations are complete, one can be expressed as a linear combination of the states of the other. This is called the Clebsch-Gordan series:

$$|j, j_1, j_2, m\rangle = \sum_{m_1, m_2} \langle j, m | j_1, m_1, j_2, m_2 \rangle |j_1, m_1, j_2, m_2\rangle \tag{3.27}$$

where $\langle j, m | j_1, m_1, j_2, m_2 \rangle$ are called the Clebsch-Gordan coefficients and are the overlap in-

[2]However, it is often the case that more than one interaction is present, one that couples j_1 and j_2 and another one that uncouples, e.g. by only involving one of them.

tegrals between the two states: the closer to unity a specific coefficient is, the more alike the two states it links are. Clebsch-Gordan coefficients add up to one. A more symmetric way to express them is using 3-j symbols:

$$\langle j_1, m_1, j_2, m_2 \mid j, m\rangle = (-1)^{j_1 - j_2 + m}(2j+1)^{1/2} \begin{pmatrix} j_1 & j_2 & j \\ m_1 & m_2 & -m \end{pmatrix} \tag{3.28}$$

This way, the symmetries of the 3-j symbols are easier to see:

$$\begin{pmatrix} j_1 & j_2 & j \\ m_1 & m_2 & m_3 \end{pmatrix} = (-1)^{j_1+j_2+j} \begin{pmatrix} j_1 & j_2 & j \\ -m_1 & -m_2 & -m_3 \end{pmatrix} \tag{3.29}$$

Moreover, they are symmetric to even and antisymmetric to odd permutations:

$$\begin{pmatrix} j_1 & j_2 & j \\ m_1 & m_2 & m_3 \end{pmatrix} = \begin{pmatrix} j_2 & j & j_1 \\ m_2 & m_3 & m_2 \end{pmatrix} = \begin{pmatrix} j & j_1 & j_2 \\ m_3 & m_1 & m_2 \end{pmatrix} \tag{3.30}$$

$$\begin{pmatrix} j_1 & j_2 & j \\ m_1 & m_2 & m_3 \end{pmatrix} = (-1)^{j_1+j_2+j} \begin{pmatrix} j_2 & j_1 & j \\ m_2 & m_1 & m_3 \end{pmatrix} \tag{3.31}$$

A useful formula if one of the angular momenta is zero is:

$$\begin{pmatrix} j & j & 0 \\ m & -m & 0 \end{pmatrix} = (-1)^{j-m}\sqrt{2j+1} \tag{3.32}$$

3.3.2 Coupling of more than two angular momenta

If more than two angular momenta need to be added, then the order that the addition occurs is important, as different quantum numbers are maintained. For example, consider the case of three interacting sources of angular momenta, j_1, j_2 and j_3. The first possibility is to couple j_1

to j_2 to give j_{12}, and then couple j_{12} to j_3 to give j. In this case, the final eigenfunctions are:

$$\begin{aligned} |j_{12},j_3,j,m\rangle &= \sum_{m_{12},m_3} \langle j_{12},m_{12},j_3,m_3|j,m\rangle |j_{12},m_{12},j_3,m_3\rangle \\ &= \sum_{m_1,m_2,m_{12},m_3} \langle j_{12},m_{12},j_3,m_3|j,m\rangle \langle j_1,m_1,j_2,m_2|j_{12},m_{12}\rangle \\ &\quad \times |j_1,m_1,j_2,m_2,j_3,m_3\rangle \end{aligned} \tag{3.33}$$

Another possibility is to couple j_2 to j_3 to give j_{23}, which is then coupled to j_1 to give j. In that case, the final eigenstates now are:

$$\begin{aligned} |j_{23},j_1,j,m\rangle &= \sum_{m_{23},m_1} \langle j_{23},m_{23},j_1,m_1|j,m\rangle |j_{23},m_{23},j_1,m_1\rangle \\ &= \sum_{m_2,m_3,m_{32},m_1} \langle j_{23},m_{23},j_1,m_1|j,m\rangle \langle j_2,m_2,j_3,m_3|j_{23},m_{23}\rangle \\ &\quad \times |j_1,m_1,j_2,m_2,j_3,m_3\rangle \end{aligned} \tag{3.34}$$

These representations are related by a unitary transformation:

$$|j_{23},j_1,j,m\rangle = \sum_{j_{12}} \langle j_{12},j_3,j|j_1,j_{23},j'\rangle |j_{12},j_3,j',m'\rangle \tag{3.35}$$

In equation 3.35 $j' = j$ and $m' = m$ due to orthogonality. The $\langle j_{12},j_3,j|j_1,j_{23},j'\rangle$ coefficients are called re-coupling coefficients as they link different coupling schemes. In an analogous relationship to the one between Clebsch-Gordan coefficients and 3-j symbols, re-coupling coefficients are linked to the 6-j symbols:

$$\left\{ \begin{array}{ccc} j_1 & j_2 & j_{12} \\ j_3 & j & j_{23} \end{array} \right\} = \frac{(-1)^{j_1+j_2+j_3+j}}{\sqrt{(2j_{12}+1)(2j_{23}+1)}} \langle j_{12},j_3,j|j_1,j_{23},j\rangle \tag{3.36}$$

One reason for using the 6-j symbols is that their symmetries are easier to see. 6-j symbols are invariant to interchange of any two columns and also to the interchange of the upper and lower

argument in any two columns:

$$\left\{ \begin{array}{ccc} j_1 & j_2 & j_3 \\ j_4 & j_5 & j_6 \end{array} \right\} = \left\{ \begin{array}{ccc} j_1 & j_3 & j_2 \\ j_4 & j_6 & j_5 \end{array} \right\} = \left\{ \begin{array}{ccc} j_4 & j_2 & j_3 \\ j_1 & j_5 & j_6 \end{array} \right\} \tag{3.37}$$

One may expand the 6-j symbol in terms of 3-j symbols:

$$\begin{aligned} \left\{ \begin{array}{ccc} j_1 & j_2 & j_3 \\ j_4 & j_5 & j_6 \end{array} \right\} &= \sum_{\text{All } m_i} (-1)^{j_1-m_1+j_2-m_2+j_3-m_3+j_4-m_4+j_5-m_5+j_6-m_6} \\ &\times \left(\begin{array}{ccc} j_1 & j_2 & j_3 \\ -m_1 & -m_2 & -m_3 \end{array} \right) \left(\begin{array}{ccc} j_1 & j_5 & j_6 \\ m_1 & -m_5 & m_6 \end{array} \right) \\ &\times \left(\begin{array}{ccc} j_2 & j_6 & j_4 \\ m_2 & -m_6 & m_4 \end{array} \right) \left(\begin{array}{ccc} j_3 & j_4 & j_5 \\ m_3 & -m_4 & m_5 \end{array} \right) \end{aligned} \tag{3.38}$$

There are four triangle conditions in order for a 6-j symbol to be non-zero. Using the notation of equation 3.38, these are $\Delta(j_1, j_2, j_3), \Delta(j_1, j_5, j_6), \Delta(j_4, j_2, j_6)$ and $\Delta(j_4, j_5, j_3)$.

As all but two indices (m_i) are related to another, if a projection (for example m_5) is not summed over, then the following equality between a 6-j and 3-j symbols is true:

$$\begin{aligned} \left\{ \begin{array}{ccc} j_1 & j_2 & j_3 \\ j_4 & j_5 & j_6 \end{array} \right\} &= \sum_{m_1,m_2,m_3,m_4,m_6} (2j_5+1)(-1)^{j_1+j_2-j_3+j_4+j_5+j_6-m_1-m_6} \\ &\times \left(\begin{array}{ccc} j_1 & j_2 & j_3 \\ m_1 & m_2 & -m_3 \end{array} \right) \left(\begin{array}{ccc} j_4 & j_5 & j_3 \\ m_4 & m_5 & m_3 \end{array} \right) \\ &\times \left(\begin{array}{ccc} j_2 & j_4 & j_6 \\ m_2 & m_4 & -m_6 \end{array} \right) \left(\begin{array}{ccc} j_5 & j_1 & j_6 \\ m_5 & m_1 & m_6 \end{array} \right) \end{aligned} \tag{3.39}$$

Finally, if one of the j_i component is zero, then the 6-j symbol collapses to

$$\left\{ \begin{array}{ccc} j_1 & j_2 & 0 \\ j_4 & j_5 & j_6 \end{array} \right\} = \frac{(-1)^{j_1+j_4+j_6}}{\sqrt{(2j_1+1)(2j_4+1)}} \delta_{j_1 j_2} \delta_{j_4 j_5} \tag{3.40}$$

As the coupling of two angular momenta has led us to a 3-j symbol and the coupling of three to a 6-j symbol, unsurprisingly, the coupling of four angular momenta is best handled with the use of a 9-j symbol. Similar to the 6-j symbol case, a 9-j symbol takes into account all possible coupling schemes by linking their unitary transformations. To illustrate the point, consider the interacting angular momenta j_1, j_2, j_3 and j_4. One case is that j_1 and j_2 couple to give j_{12}, while j_3 and j_4 couple to give j_{34}. The final coupling is then between j_{12} and j_{34} to give j. This coupling scheme may be denoted as $|(j_1,j_2)j_{12},(j_3,j_4)j_{34},j,m\rangle$.

One alternative coupling scheme is to couple j_1 to j_4 to give j_{14}, and j_2 to j_3 to give j_{23}. Then j_{14} and j_{23} couple to give j, and the eigenstates can now be characterised as $|(j_1,j_4)j_{14},(j_2,j_3)j_{23},j,m\rangle$.

Then, the transformation between these two schemes is again simply:

$$\begin{aligned}|(j_1,j_2)j_{12},(j_3,j_4)j_{34},j,m\rangle \;=\; & \sum_{j_{14},j_{23}} \langle(j_1,j_2)j_{12},(j_3,j_4)j_{34},j,m|(j_1,j_4)j_{14},(j_2,j_3)j_{23},j,m\rangle \\ & \times|(j_1,j_4)j_{14},(j_2,j_3)j_{23},j,m\rangle \end{aligned} \tag{3.41}$$

Now the 9-j symbol may be seen as simply one normalised expression of the re-coupling coefficient above. One thing to note is that, in contrast to the 3-j symbols, in 6-j and 9-j symbols there is no reference to the m projection. This is simply due to the implicit summation.

$$\begin{aligned}&\langle(j_1,j_2)j_{12},(j_3,j_4)j_{34},j,m|(j_1,j_4)j_{14},(j_2,j_3)j_{23},j,m\rangle = \\ &\qquad = \sqrt{(2j_{12}+1)(2j_{23}+1)(2j_{34}+1)(2j_{14}+1)} \quad \begin{Bmatrix} j_1 & j_2 & j_{12} \\ j_3 & j_4 & j_{34} \\ j_{14} & j_{23} & j \end{Bmatrix}\end{aligned} \tag{3.42}$$

9-j symbols are unchanged by even permutations of rows and columns, but in the case of an odd permutation they are multiplied by the following phase factor:

$$(-1)^{j_1+j_2+j_3+j_4+j_{12}+j_{23}+j_{14}+j_{34}}$$

As a 9-j symbol takes into account the coupling of four different sources of angular momenta,

it may be expanded in different combinations of coupling between three angular momenta, i.e. 6-j symbols:

$$\begin{Bmatrix} j_1 & j_2 & j_{12} \\ j_3 & j_4 & j_{34} \\ j_{14} & j_{23} & j \end{Bmatrix} = \sum_k (-1)^{2k}(2k+1) \begin{Bmatrix} j_1 & j_4 & j_7 \\ j_8 & j_9 & k \end{Bmatrix} \times \begin{Bmatrix} j_2 & j_5 & j_8 \\ j_4 & k & j_6 \end{Bmatrix} \begin{Bmatrix} j_3 & j_6 & j_9 \\ k & j_1 & j_2 \end{Bmatrix} \tag{3.43}$$

Moreover, when one j_i is zero, the 9-j symbol collapses to:

$$\begin{Bmatrix} j_1 & j_2 & j_3 \\ j_4 & j_5 & j_6 \\ j_7 & j_8 & 0 \end{Bmatrix} = \frac{(-1)^{j_2+j_3+j_4+j_7}}{\sqrt{(2j_3+1)(2j_7+1)}} \begin{Bmatrix} j_1 & j_2 & j_3 \\ j_5 & j_4 & j_7 \end{Bmatrix} \tag{3.44}$$

3.4 Rotation Transformations

There are two ways to specify the rotation of a function or point with respect to some axis:

1. Active Rotation: In this case the function or object rotates with respect to the axis
2. Passive Rotation: In this case the axis rotates with respect to the point or function

The sense of the rotation reverses between an active and a passive rotation: an active rotation by an angle (α), is equivalent to a passive rotation by ($-\alpha$). The operation of rotating (right-hand corkscrew) by α around the positive direction of the unit vector $\mathbf{n}$, can be written as $\hat{P}_R(\alpha\mathbf{n})$. Conventionally[3] this is reserved for an active rotation. $\mathbf{P}_R(\alpha\mathbf{n})$ is related to the angular momentum projected on the $\mathbf{n}$ axis as:

$$\hat{P}_R(\alpha\mathbf{n}) = \exp\left(-\imath\alpha\hat{J}\cdot\mathbf{n}\right) = \exp\left(-\imath\alpha\hat{J}_n\right) \tag{3.45}$$

[3]It is important to note that the convention in angular momentum books is notoriously controversial, differing even between the most commonly-used ones as Brink and Satchler [17], Edmonds [29], Rose [30], etc. The notation used here is following that of Zare [27] and of Brown and Carrington [17].

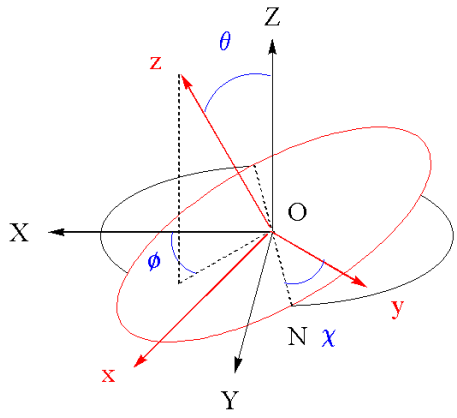

Figure 3.1: The three Euler angle rotations [31]

where $\hat{J}$ is the total angular momentum operator and $\hat{J}_n$ is the angular momentum operator around the axis of rotation. However, in the case of a three-dimensional molecule, three different angles are required to describe a rotation, known as the Euler angles[4]: ϕ, θ and χ.

The first two are used to define the orientation of an axis internal to the rotating molecule (also called the "figure" axis) and the axis that the species rotates with respect to, while the third is used to measure the rotation. Therefore, any rotation might be defined as the rotation between two axis systems: the one molecule-fixed axis system (denoted xyz) and the external, or space-fixed axis system (denoted XYZ). For this transformation, we need to define the line of nodes, ON, as the line of intersection between the xy and the XY planes.

If these are defined as to have the same origin, O, then the Euler angles are defined as the necessary values to rotate between the two axis systems in the following systematic way. There are three successive finite rotations that can make the axis systems to coincide:

1. A counterclockwise rotation by ϕ around the Z axis, aligning Y to ON.

2. A counterclockwise rotation by θ around ON, which would carry Z into z.

3. A counterclockwise rotation χ around z/Z which would carry N into y.

[4] Another common way is to write the Euler angles as α, β and γ.

These are illustrated in figure 3.1 [31]. The overall rotation to make the two axis systems coincide can be written as a product of the three rotations:

$$\hat{P}_R(\phi,\theta,\chi) = \exp(-\imath\phi J_Z)\exp(-\imath\theta J_Y)\exp(-\imath\chi J_Z) \tag{3.46}$$

The range of the Euler angles is defined as:

$$0 \leq \phi \leq 2\pi \qquad 0 \leq \theta \leq \pi \qquad 0 \leq \chi \leq 2\pi$$

As all operators in the above equation are angular momentum operators in the same frame of reference (in this case the space-fixed frame) $|J,M\rangle$ can be used to charactise these states. Moreover, a rotation cannot physically alter the angular momentum of the system, therefore only M (and not J) may change. This can be written as:

$$\hat{P}_R(\phi,\theta,\chi)\,|J,M\rangle = \sum_{M'} \mathscr{D}^J_{M',M}(\phi,\theta,\chi)\,\left|J,M'\right\rangle \tag{3.47}$$

where M' is the projection after the rotation and $\mathscr{D}^J_{M,M'}(\phi,\theta,\chi)$ is called the Wigner rotational matrix (or D-matrix). Post-multiplying by a specific final (after-rotation) state gives:

$$\mathscr{D}^J_{M',M}(\omega) = \left\langle J,M'\right|\hat{P}_R(\phi,\theta,\chi)\,|J,M\rangle \tag{3.48}$$

where ω is an abbreviation for all three Euler angles. So the D-matrix may be thought of a Clebsh-Gordan coefficient between the states before and after the rotation. Substituting in the expression from equation 3.46 in equation 3.48:

$$\begin{aligned}\mathscr{D}^J_{M',M}(\phi,\theta,\chi) &= \left\langle J,M'\right|\exp(-\imath\phi J_Z)\exp(-\imath\theta J_N)\exp(-\imath\chi J_Z)\,|J,M\rangle \\ &= \exp(-\imath\phi M')d^J_{M',M}(\theta)\exp(-\imath\chi M)\end{aligned} \tag{3.49}$$

where $d^J_{M',M}$ is the "reduced" or "little" d-matrix, and practically corresponds to the operation of making the z and Z axis coincide. Wigner showed that [27]:

$$\begin{aligned} d^J_{M',M}(\theta) &= \langle J,M'|e^{-\imath\theta J_Y}|J,M\rangle \\ &= \left[(J+M)!(J-M)!(J+M')!(J-M)!\right]^{1/2} \\ &\quad \times\sum_\nu \frac{(-1)^\nu(\cos(\frac{\theta}{2}))^{2J+M-M'-2\nu}(-\sin\frac{\theta}{2})^{M'-M+2\nu}}{(J-M'-\nu)!(J+M-\nu)!(\nu+M'-M)!\nu!} \end{aligned} \tag{3.50}$$

where ν takes all possible values for which the factorials are not negative. The following symmetry relationships have proved useful [29]:

$$d^J_{M',M}(\theta) = (-1)^{M'-M}d^J_{-M',-M}(\theta) \tag{3.51}$$

$$d^J_{M',M}(\theta) = (-1)^{M'-M}d^J_{M,M'}(\theta) = (-1)^{M'-M}d^J_{-M',-M}(\theta) \tag{3.52}$$

$$d^J_{M',M}(0) = \delta_{M',M} \tag{3.53}$$

These may be used to derive the following symmetry relationship [32]:

$$\mathscr{D}^J_{M',M}(\omega) = (-1)^{M-M'}\mathscr{D}^{J*}_{-M',-M}(\omega) \tag{3.54}$$

The complex conjugate of a D-matrix is simply the reverse transformation, and naturally the angle sense is reversed:

$$\mathscr{D}^J_{M',M}(\phi,\theta,\chi)^* = \mathscr{D}^J_{M,M'}(-\phi,-\theta,-\chi) \tag{3.55}$$

Wigner D-matrices form a complete set of functions for angles they depend on, and if one of them is zero, they simplify to Racah or spherical harmonics:

$$\mathscr{D}^J_{M,0}(\phi,\theta,0) = \mathscr{C}^{J*}_M(\phi,\theta) = \left[\frac{4\pi}{2J+1}\right]^{1/2}\mathscr{Y}^{J*}_M(\phi,\theta) \tag{3.56}$$

$$= (-1)^M\left[\frac{4\pi}{2J+1}\right]^{1/2}\mathscr{Y}^J_{-M}(\phi,\theta) \tag{3.57}$$

$$= (-1)^M\mathscr{D}^J_{0,M}(0,\theta,\phi) \tag{3.58}$$

Actually, their similarity to spherical harmonics runs deeper: just as spherical harmonics can be used as wavefunctions for a particle on a sphere (which requires two degrees of freedom), D-matrices can be used to express the wavefunction of a rigid symmetric top [27]:

$$|J,K,M\rangle = \left[\frac{2J+1}{8\pi^2}\right]^{1/2} \mathscr{D}^{J*}_{M,K}(\phi,\theta,\chi) \tag{3.59}$$

$$= (-1)^{M-K}\left[\frac{2J+1}{8\pi^2}\right]^{1/2} \mathscr{D}^{J}_{-M,-K}(\phi,\theta,\chi) \tag{3.60}$$

Moreover, a rigid asymmetric top may be expressed as a linear combination of symmetric top wavefunctions, and thus a linear combination of D-matrices.

One of the reasons that equation 3.59 is useful is due to the integration properties of D-matrices. If these are integrated over all space (i.e. $d\Omega = \sin\theta d\phi d\theta d\chi$), the following formulæ apply:

$$\int \mathscr{D}^{J}_{M',M}(\omega)d\omega = \delta_{J,0}\delta_{M,0}\delta_{M',0} \tag{3.61}$$

$$\int \mathscr{D}^{J_1*}_{M'_1,M_1}(\omega)\mathscr{D}^{J_2}_{M'_2,M_2}(\omega)d\omega = \left[\frac{8\pi^2}{2J_1+1}\right]\delta_{J_1,J_2}\delta_{M_1,M_2}\delta_{M'_1,M'_2} \tag{3.62}$$

$$\int \mathscr{D}^{J_3}_{M'_3,M_3}(\omega)\mathscr{D}^{J_2}_{M'_2,M_2}(\omega)\mathscr{D}^{J_1}_{M'_1,M_1}(\omega)d\omega = (8\pi^2)\begin{pmatrix} J_1 & J_2 & J_3 \\ M'_1 & M'_2 & M'_3 \end{pmatrix} \times \begin{pmatrix} J_1 & J_2 & J_3 \\ M_1 & M_2 & M_3 \end{pmatrix} \tag{3.63}$$

3.4.1 Anomalous commutation relationships

A special note needs to be made about considering the rotation of a body from within its rotating frame. When one examines the commutation relationships for the angular momentum operators within the rotating frame, instead of the standard formulæ shown below:

$$[j_x, j_y] = j_x j_y - j_y j_x = \iota j_z \tag{3.64}$$

$$[j_z, j_\pm] = \pm j_\pm \tag{3.65}$$

the curious result of the anomalous commutation relationships is met:

$$[j_x, j_y] = -\imath j_z \tag{3.66}$$

$$[j_z, j_\pm] = \mp j_\pm \tag{3.67}$$

Perhaps the neatest solution [17, 28] is re-defining the raising and lowering operators within the rotating frame:

$$J^\pm = J_x \mp \imath J_y \tag{3.68}$$

which then gives the expected result

$$\left[j_z, j^\pm\right] = \pm j^\pm \tag{3.69}$$

It should be made very clear that this "anomaly" only occurs for the rotational angular momentum operators only, and all other angular momentum operators (such as orbital angular momentum) obey normal commutation rules in both body-fixed[5] and space-fixed axis systems.

3.5 Spherical Tensor Operators Algebra

So far the discussion has been centred around the eigenfunction part of the eigenvalue equation. However, the same principles can be applied to operators that are expressed in spherical polar coordinates. A generic (spherical) tensor operator of rank k and projection q can be defined as one whose unitary transformation between different frames of reference is:

$$\hat{P}_R(\omega) T_q^k \hat{P}_R(\omega)^{-1} = \sum_{q'} \mathscr{D}^k_{q',q}(\omega) T_{q'}^k \tag{3.70}$$

where both q and q' can take values $k, k-1, \ldots, 1-k, -k$, and each T_q^k transforms as an irreducible representation of a $(2k+1)$ space. The spherical tensor of an operator $\hat{\Xi}$ will be noted as $T_q^k(\Xi)$, but if the argument is applicable for all cases, the operator sign may be ignored. An-

[5] The body-fixed frame is also often referred to as the "molecule"-fixed frame. Here both are used interchangeably.

other way to define spherical tensor operators is via their commutation relations with standard angular momentum operators:

$$\left[J_z, T_p^k\right] = pT_p^k \tag{3.71}$$

$$\left[J_\pm, T_p^k\right] = \sqrt{k(k+1)-p(p\pm 1)}T_{p\pm 1}^k \tag{3.72}$$

In the special case where $k=0$, then T_0^0 is invariant to rotation and it is a scalar operator. In the case of $k=1$, the operator is a vector. The spherical tensor operators are related to the Cartesian operators as:

$$T_{\pm 1}^1(J) = \mp\frac{J_x \pm \imath J_y}{\sqrt{2}} = \mp\frac{J_\pm}{\sqrt{2}} \tag{3.73}$$

$$T_0^1(J) = J_z \tag{3.74}$$

When moving between body-fixed and space-fixed frames of reference, the rank of the tensor cannot change by a rotation, so we only need to consider its projections: q for the body-fixed frame and p for the space fixed one. From equation 3.70, moving from molecule (body) to space can be written as [27]:

$$T_q^k = \sum_p \mathscr{D}_{p,q}^k(\omega) T_p^k \tag{3.75}$$

The reverse transformation, requires the complex conjugate of the D-matrix:

$$T_p^k = \sum_q \mathscr{D}_{p,q}^{k*}(\omega) T_q^k \tag{3.76}$$

The above equations allow us to transform any operators (as well as the basis set) from the body-fixed frame to the space-fixed frame:

$$\hat{P}_R(\omega)\left[T_q^k\left|j,m\right\rangle\right] = \hat{P}_R(\omega)T_q^k\hat{P}_R^{-1}(\omega)\hat{P}_R(\omega)\left|j,m\right\rangle \tag{3.77}$$

$$= \sum_{q'}\sum_{m'} T_{q'}^k\left|j,m'\right\rangle D_{q',q}^k(\omega)D_{m',m}^j(\omega) \tag{3.78}$$

From equation 3.78, it can be seen that the eigenequation is defined in the space $\Gamma^k \otimes \Gamma^j$. However, this is reducible, and we can define an irreducible space Γ^K. Therefore, we can write an eigenstate ensemble in the Γ^K with projection Q as $|K,Q\rangle$. This will be related to the product of equation 3.78 via a Clebsch-Gordan series as:

$$|K,Q\rangle = \sum_{q,m} \langle kq, jm \mid kj, KQ\rangle \, T^k_q \, |jm\rangle \tag{3.79}$$

Post-multiplying by $\langle j'm'|$, gives:

$$\left\langle j'm' \mid K,Q\right\rangle = \sum_{q,m} \langle kq, jm \mid kj, KQ\rangle \left\langle j'm' \middle| T^k_q \middle| jm\right\rangle \tag{3.80}$$

Which may be rearranged to:

$$\left\langle j'm' \middle| T^k_q \, |jm\right\rangle = \sum_{K,Q} \langle kq, jm \mid kj, KQ\rangle \left\langle j'm' \mid KQ\right\rangle \tag{3.81}$$

However the right-hand side of the above equation is a scalar and due to orthogonality vanishes unless $j' = K$ and $m' = Q$. Under these conditions, this is independent of m'. Therefore, this can be written as:

$$\left\langle j'm' \middle| T^k_q \middle| jm\right\rangle = \langle kq, jm \mid kj, KQ\rangle \left\langle j' \middle|\middle| T^k \middle|\middle| j\right\rangle$$

where $\left\langle j \middle|\middle| T^k \middle|\middle| j'\right\rangle$ is called the "reduced matrix element". Practically, this separates the evaluation of the tensor matrix element to a physical part (the reduced matrix element) and a geometrical part (the Clebsch-Gordan coefficient). This is called the Wigner-Eckart theorem and is usually expressed using a 3-j symbol as:

$$\left\langle j'm' \middle| T^k_q \middle| jm\right\rangle = (-1)^{j'-m'} \begin{pmatrix} j' & k & j \\ -m' & q & m \end{pmatrix} \left\langle j' \middle|\middle| T^k \middle|\middle| j\right\rangle$$

One way to evaluate the reduced matrix element is to evaluate the right-hand side expression of equation 3.82, using a known matrix element. One such example is to evaluate for $T_0^1(J) = J_z$:

$$\begin{aligned} \langle j'm' | J_z | jm \rangle &= \delta_{j',j}\delta_{m',m} m & (3.82) \\ &= (-1)^{j'-m'} \begin{pmatrix} j' & 1 & j \\ -m' & 0 & m \end{pmatrix} \langle j' || T^1(J) || j \rangle & (3.83) \end{aligned}$$

It is worth noting that the $T_p^1(J)$ operator cannot link different j eigenstates, i.e. $j' = j$. From above it can be concluded that:

$$\langle j' || T^1(J) || j \rangle = \delta_{j',j} \sqrt{j(j+1)(2j+1)} \tag{3.84}$$

The reduced matrix element for the second rank angular momentum tensor may be found the same way, by simply coupling the first rank tensor to itself:

$$\begin{aligned} \langle j'm' | T_0^2(J,J) | jm \rangle &= \left\langle j'm' \left| \frac{\left[3J_z^3 - J^2\right]}{\sqrt{6}} \right| jm \right\rangle & (3.85) \\ &= \delta_{j',j}\delta_{m',m} \frac{3m^2 - j(j+1)}{\sqrt{6}} & (3.86) \\ &= (-1)^{j'-m'} \begin{pmatrix} j' & 2 & j \\ -m' & 0 & m \end{pmatrix} \langle j' || T^2(J,J) || j \rangle & (3.87) \end{aligned}$$

which shows that:

$$\langle j' || T^2(J,J) || j \rangle = \delta_{j',j} \frac{\sqrt{(2j-1)(2j)(2j+1)(2j+2)(2j+3)}}{2\sqrt{6}} \tag{3.88}$$

For any higher rank angular momentum spherical tensor reduced matrix elements, the following result of Smith and Thornley [17] may be used:

$$\left\langle j' \left|\left| T^k(J,\ldots,J) \right|\right| j \right\rangle = \delta_{j'j} k! \sqrt{\frac{(2j+k+1)!}{2^k (2k)! (2j-k)!}} \tag{3.89}$$

Although the Wigner D-matrices are not strictly speaking spherical tensor operators, and one may not simply apply the Wigner-Eckart theorem, an analogous expression may be derived:

$$\begin{aligned}\left\langle j'm'\mu' \left| \mathscr{D}^{k*}_{p,q}(\omega) \right| jm\mu \right\rangle &= (-1)^{m'-\mu'}\sqrt{(2j+1)(2j'+1)} \\ &\quad \times \begin{pmatrix} j' & k & j \\ -\mu' & q & \mu \end{pmatrix} \begin{pmatrix} j' & k & j \\ -m' & p & m \end{pmatrix} \qquad (3.90) \\ &= (-1)^{j'-m'} \begin{pmatrix} j' & k & j \\ -m' & q & m \end{pmatrix} \left\langle j'\mu' \left|\left| \mathscr{D}^{k*}_{\cdot,q}(\omega) \right|\right| j\mu \right\rangle \qquad (3.91)\end{aligned}$$

where m, m' are the projections to the space-fixed axis system and μ, μ' the projections to the body-fixed one. Using equation 3.63, we can define the reduced rotation matrix element [17]:

$$\left\langle j'\mu' \left|\left| \mathscr{D}^{k*}_{\cdot,q}(\omega) \right|\right| j\mu \right\rangle = (-1)^{j'-\omega'}\sqrt{(2j+1)(2j'+1)} \begin{pmatrix} j' & k & j \\ -\mu' & q & \mu \end{pmatrix} \qquad (3.92)$$

where the dot represents the subscript of the projection that has been reduced.

3.5.1 Products of spherical tensor operators

Just as in the case of interacting angular momenta from different sources, spherical tensors may transform between a coupled and an uncoupled representation via an expansion similar to a Clebsch-Gordan series. In the case of angular momenta $\hat{A}$ and $\hat{B}$ coupling to give $\hat{J}$, in spherical tensor notation we can write:

$$T^k_q(J) = \sum_{q_1,q_2} \langle k_1, q_1, k_2, q_2 | k, q \rangle T^{k_1}_{q_1}(A) T^{k_2}_{q_2}(B) \qquad (3.93)$$

The direct product $T^{k_1}_{q_1}(A) \otimes T^{k_2}_{q_2}(B)$ will give rise to tensors with rank $k = |k_1 + k_2|, |k_1 + k_2 - 1|, \ldots, |k_1 - k_2|$. Selecting the tensor with rank k and projection q may also be written as:

$$\begin{aligned} T^k_q(J) &= \left[T^{k_1}(A) \otimes T^{k_2}(B)\right]^k_q && (3.94) \\ &= \sum_{q_1} (-1)^{k_2 - k_1 - q} T^{k_1}_{q_1}(A) T^{k_2}_{q-q_1}(B) \\ &\times \sqrt{2k+1} \begin{pmatrix} k_1 & k_2 & k \\ q_1 & q-q_1 & -q \end{pmatrix} && (3.95) \\ &= \sum_{q_1} \langle k_1, q_1, k_2, q-q_1 | j, q \rangle T^{k_1}_{q_1}(A) T^{k_2}_{q-q_1}(B) && (3.96) \end{aligned}$$

In the special case where $k = 0$, i.e. where a scalar product (or "dot" product) is being computed, according to equation 3.32, $k_1 = -k_2$:

$$\left[T^{k_1} \otimes T^{k_1}\right]^0_0 = \sum_m \langle k_1, m, k_1, -m | 0, 0 \rangle T^{k_1}_m T^{k_1}_{-m} \tag{3.97}$$

which means that only tensors of the same order can combine to give a scalar product. For two tensors of the same rank but different operators represented as $T^{k_1}(A)$ and $T^{k_1}(B)$, two useful equalities are:

$$\begin{aligned} T^{k_1}(A) \cdot T^{k_1}(B) &= (-1)^{k_1} (2k_1 + 1)^{\frac{1}{2}} \left[T^{k_1}(A) \otimes T^{k_1}(B)\right]^0_0 && (3.98) \\ &= \sum_q (-1)^q T^{k_1}_q(A) T^{k_1}_{-q}(B) && (3.99) \end{aligned}$$

Now combining the above equations with:

$$\begin{aligned} |j_1, j_2, j, m\rangle &= \sum_{m_1, m_2} \langle j, m | j_1, m_1, j_2, m_2 \rangle |j_1, m_1\rangle |j_2, m_2\rangle && (3.100) \\ &= \sum_{m_1, m_2} (-1)^{j_1 - j_2 + m} \sqrt{2j+1} \begin{pmatrix} j_1 & j_2 & j \\ m_1 & m_2 & -m \end{pmatrix} |j_1, m_1\rangle |j_2, m_2\rangle && (3.101) \end{aligned}$$

allows us to evaluate the matrix elements between tensors acting on different parts of the system, moving between coupled and uncoupled representations.

More specifically, consider the tensor operators $T^{k_1}_{q_1}(A)$ and $T^{k_2}_{q_2}(B)$, acting on $|j_1,m_1\rangle$ and $|j_2,m_2\rangle$. Coupling the two tensors may form a composite tensor $T^k_q(J)$, which would act on the coupled representation of the eigenstates $|j,m\rangle$. In this case, using equations 3.93 and 3.28, the composite tensor may be expressed as:

$$\begin{aligned} T^k_q(J) &= \sum_{q_1,q_2} (-1)^{k_1-k_2+q}\sqrt{2k+1}\,T^{k_1}_{q_1}(A)T^{k_2}_{q_2}(B) \\ &\quad \times \begin{pmatrix} k_1 & k_2 & k \\ q_1 & q_2 & -q \end{pmatrix} \end{aligned} \tag{3.102}$$

and, using the Wigner-Eckart theorem of equation 3.82, its reduced matrix element as:

$$\begin{aligned} \langle j'_1, j'_2, j', m'|T^k_q(J)|j_1, j_2, j, m\rangle &= (-1)^{j'-m'} \left\langle j'_1, j'_2, j' \middle|\middle| T^k(J) \middle|\middle| j_1, j_2, j \right\rangle \\ &\quad \times \begin{pmatrix} j' & k & j \\ -m' & q & m \end{pmatrix} \end{aligned} \tag{3.103}$$

Then, using equations 3.102 and 3.101 this reduced matrix element can be evaluated by the reduced matrix elements of its component tensors:

$$\begin{aligned} \left\langle j'_1, j'_2, j' \middle|\middle| T^k(J) \middle|\middle| j_1, j_2, j \right\rangle &= \sqrt{(2j+1)(2j'+1)(2k+1)} \begin{Bmatrix} j'_1 & j_1 & k_1 \\ j'_2 & j_2 & k_2 \\ j' & j & k \end{Bmatrix} \\ &\quad \times \left\langle j'_1 \middle|\middle| T^{k_1}(A) \middle|\middle| j_1 \right\rangle \left\langle j'_2 \middle|\middle| T^{k_2}(B) \middle|\middle| j_2 \right\rangle \end{aligned} \tag{3.104}$$

In the special case of $k = 0$, using equation 3.44, the 9-j symbol collapses to a 6-j symbol:

$$\begin{aligned} \left\langle j'_1, j'_2, j' \middle|\middle| T^{k_1} \cdot T^{k_2} \middle|\middle| j_1, j_2, j \right\rangle &= (-1)^{j_1+j'_2+j'} \sqrt{(2j'+1)} \begin{Bmatrix} j'_1 & j'_2 & j' \\ j_2 & j_1 & k_1 \end{Bmatrix} \\ &\quad \times \left\langle j'_1 \middle|\middle| T^{k_1} \middle|\middle| j_1 \right\rangle \left\langle j'_2 \middle|\middle| T^{k_2} \middle|\middle| j_2 \right\rangle \end{aligned} \tag{3.105}$$

Finally, two very useful relations are when a tensor operator acts only on one of the component

angular momenta. As in all cases, special care should be taken in the order of coupling, which is well-illustrated by the difference between the phase factors in the two relations:

$$\begin{aligned}\left\langle j_1', j_2', j' \left|\left| T^{k_1} \right|\right| j_1, j_2, j \right\rangle &= \delta_{j_2,j_2'}\sqrt{(2j+1)(2j'+1)}(-1)^{j_1'+j_2'+j+k_1} \\ &\times \left\{ \begin{array}{ccc} j_1' & j' & j_2' \\ j & j_1 & k_1 \end{array} \right\} \left\langle j_1' \left|\left| T^{k_1} \right|\right| j_1 \right\rangle \qquad (3.106) \\ \left\langle j_1', j_2', j' \left|\left| T^{k_2} \right|\right| j_1, j_2, j \right\rangle &= \delta_{j_1,j_1'}\sqrt{(2j+1)(2j'+1)}(-1)^{j_1'+j_2+j'+k_2} \\ &\times \left\{ \begin{array}{ccc} j_2' & j' & j_1' \\ j & j_2 & k_2 \end{array} \right\} \left\langle j_2' \left|\left| T^{k_2} \right|\right| j_2 \right\rangle \qquad (3.107)\end{aligned}$$

3.5.2 Evaluating body-fixed rotational tensor operators

The anomalous commutation relationships mentioned earlier in the chapter means that the tensor representation of the rotational angular momentum ($\hat{N}$) in the body-fixed axis of the rotation it represents needs to be treated with special care.

This problem usually arises when an interaction between the rotational angular momentum operator is coupled to another angular momentum operator in the molecule. To illustrate the point, let us consider a spin-rotation interaction, $T^1(N)\cdot T^1(S)$. Brown and Howard [28] showed that these may be handled with tensor algebra as long as the matrix elements for the operators are evaluated in the space-fixed axis system. The issue causing the problem becomes obvious when one attempts to use equation 3.75 to transform the rotation operator of the molecule to space. For our example, using equation 3.99:

$$\begin{aligned}T^1(N)\cdot T^1(S) &= \sum_q (-1)^q T^1_{-q}(N) T^1_q(S) \qquad (3.108) \\ &= \sum_{p,q} (-1)^q \mathscr{D}^{1*}_{p,-q}(\omega) T^1_p(N) T^1_q(S) \qquad (3.109)\end{aligned}$$

while the matrix elements of $T^1_q(S)$ can be clearly evaluated with the expressions presented in the previous section, in $\mathscr{D}^{1*}_{p,-q}(\omega)T^1_p(N)$, the rotation operator modifies the Euler angles that the D-matrix depends on. Therefore the rotation D-matrix does not commute with the tensor

operator and their product is not Hermitian.

The easiest to solve this problem is:

1. Antisymmetrise the product of the D-matrix with the tensor operator. This can be done by substituting:

$$\frac{1}{2}\left(\mathscr{D}^{1*}_{p,-q}(\omega)T^1_p(N)+T^1_p(N)\mathscr{D}^{1*}_{p,-q}(\omega)\right)$$

   This makes the operator Hermitian[6].

2. Now that the operator is Hermitian, in order to evaluate the matrix elements we can introduce a resolution of the identity between the D-matrix and the spherical tensor operator. Each one of them refer to a different eigenstate, and we can make use of the folmuæ presented earlier. Therefore, the corresponding matrix element would be:

$$\begin{aligned}\sum_p \langle j'm'\mu'|\mathscr{D}^{1*}_{p,-q}(\omega)T^1_p(N)|jm\mu\rangle &= \sum_p \sum_{j''m''\mu''} \langle j'm'\mu'|\mathscr{D}^{1*}_{p,-q}(\omega)|j''m''\mu''\rangle \\ &\quad \times\langle j''m''\mu''|T^1_p(N)|jm\mu\rangle \qquad (3.110)\end{aligned}$$

   Although in equation 3.110 in theory an infinite sum is taken, the rotational angular momentum can only link states of the same j, therefore $j''=j$. Also, as $\mu''=\mu+p$ and $m''=m$, the sum collapses to a single surviving state.

[6] In the special case that both the rotation matrix and the rotation operator have the same index but with different sign, Howard [33] has shown that this is unnecessary. However, it is demonstrated here for all the other cases where it still is necessary.

Chapter 4

Ab Initio Calculations

> "*Creativity is allowing oneself to make mistakes, art is knowing which ones to keep.*"
>
> -Scott Adams

4.1 Introduction

Ab initio methods aim to calculate the energy of a system of electrons and nuclei by solving an appropriate Schrödinger equation for that system. However, although for the hydrogen atom this may be done analytically, as soon as one tries to calculate the energy levels of the helium (He) atom, which is a three-particle system, approximations have to be used. Different *ab initio* methods use different sets of approximations to calculate the energy of systems of nuclei and electrons.

As different approximations are used, the numerical result of the calculations is not directly comparable between different methods. The "art" of this kind of calculation is for the researcher to select the method offering the best result accuracy for minimum computational effort.

The aim of this chapter is to provide an outline of methods used in this project. From our point of view, *ab initio* calculations are mainly used to either find the minimum energy geometry of a system (which directly influences the value of its rotational constant), or to calculate how the potential energy between the constituent species of a complex varies as they rotate with respect to each other. In the latter case, the steepness of the potential around an energy well, as well as the depth of that minimum, will determine the range of large amplitude motions these species will be able to perform and therefore the effective rotational constants of the system.

In the following section the method that forms the basis of all *ab initio* calculations used in this work, namely the Self-Consistent Field (SCF), is presented. The greatest omission of this method is the so-called "electron correlation", i.e. how the electron-electron repulsion affects the relative motion of electrons with respect to each other. The various methods developed to compensate for this omission (post-SCF methods) are presented in the third section. In the fourth section, different approaches to approximate the wavefunction of the system are investigated as a combination of what are called "basis-set functions". Finally, in the fifth section the computer systems used for the work presented in this thesis are discussed.

4.2 Self-Consistent Field Calculations

Ab initio methods are mathematical methods used to approximate the solutions of the time-independent Schrödinger equation:

$$\widehat{H}|\Psi\rangle = E|\Psi\rangle \tag{4.1}$$

where $\widehat{H}$ in this case is the Hamiltonian for the molecular system, $|\Psi\rangle$ is the wavefunction of the system and E the energy for that wavefunction. To achieve this, there are some commonly used approximations. In the next section two of the most fundamental ones, namely the Born-Oppenheimer and the Adiabatic approximations, are presented.

4.2.1 Born-Oppenheimer and Adiabatic approximations

The full molecular Hamiltonian can be written as [34]:

$$\widehat{H}_{tot} = \widehat{T}_n + \widehat{T}_e + \widehat{V}_{ne} + \widehat{V}_{ee} + \widehat{V}_{nn} \tag{4.2}$$

where $\widehat{T}_n$ is accounting for the kinetic energy of nuclei, $\widehat{T}_e$ for the kinetic energy of electrons, $\widehat{V}_{ne}$ for the potential energy between nuclei and electrons, $\widehat{V}_{ee}$ for the potential energy between electrons and $\widehat{V}_{nn}$ for the potential energy between nuclei. This may be re-arranged in a centre-of-mass axis system as

$$\widehat{H}_{tot} = \widehat{T}_n + \widehat{H}_e \tag{4.3}$$

where now the first term is still the kinetic energy of the nuclei and the second term is:

$$\widehat{H}_e = \widehat{T}_e + \widehat{V}_{ne} + \widehat{V}_{ee} + \widehat{V}_{nn} \tag{4.4}$$

The reason behind writing the Hamiltonian this way is to make a first approximation, which is to assume that the total wavefunction of the system may be written out as a product of an electron and a nuclear wavefunction:

$$|\Psi(R,r)\rangle = \sum_{i,j} |\phi_{e,i}(r;R)\rangle |\phi_{n,j}(R)\rangle \tag{4.5}$$

Now the electron wavefunction $|\phi_e(r;R)\rangle$ depends on the coordinates of the electrons (r) and parametrically on the position of the nuclei (R), while the nuclear wavefunction $|\phi_n(R)\rangle$ depends only on the nuclear coordinates. By assuming such a product is sufficient, the time-independent Schrödinger equation for the electronic Hamiltonian may be solved, yielding the electronic energy levels, as a function of the nuclear coordinates (R). Plotting the energy of an electronic state against one or more structural coordinates (for example the distance between nuclei) gives a Potential Energy Surface (PES). If only one electronic energy surface is considered (one solution of the electronic Hamiltonian), and all terms linking it to other surfaces are ignored, this is called the *adiabatic approximation*. The next important approximation is the Born-

Oppenheimer Approximation (BO) [35]. The logical argument for this approximation is that the masses and timescale of the movement of electrons is of a different order of magnitude to that of the nuclei, therefore the two motions may be separated to a good approximation.

There are two main uses of *ab initio* calculations: either to calculate a PES or to perform an optimisation calculation, in which the nuclear coordinates are changed (within limits) to find the energy minimum of the system. In both cases, some coordinates might be "frozen" to reduce the computational cost. The description below applies equally for both PES and optimization uses of *ab initio* calculations.

The next approximation is the "*orbital approximation*": each electron may be assigned to its own orbital, $|\phi_e\rangle$ [36]. Moreover, we need to include the effect of spin of the electron. This is done in an *ad hoc* manner by multiplying the orbital wavefunction of an electron with a spin wavefunction, $|\phi_s\rangle$, The $|\phi_s\rangle$ is a spin-eigenstate, namely either $|\alpha\rangle$ or $|\beta\rangle$. This creates a "*spinorbital*" which is a combined spin-space state of an electron. Then, we can approximate the total electronic wavefunction as a linear combination of individual spinorbitals.

According to the Pauli Exclusion Principle, the total wavefunction has to be antisymmetric with respect to the permutation of two indistinguishable half-integer spin particles (fermions, e.g. electrons). One way to construct such an electronic wavefunction is to represent it as a Slater determinant. This is a normalised determinant where every possible spinorbital is occupied by every electron. Different columns correspond to different spinorbitals (ϕ_i) while different rows to different electron coordinates. The Slater determinant for a system of N electrons with N spin-orbit functions is

$$\Phi_{SD} = \frac{1}{\sqrt{N!}} \begin{vmatrix} \phi_1(1) & \phi_2(1) & \dots & \phi_N(1) \\ \phi_1(2) & \phi_2(2) & \dots & \phi_N(2) \\ \vdots & & \ddots & \vdots \\ \phi_1(N) & \phi_2(N) & \dots & \phi_N(N) \end{vmatrix} \tag{4.6}$$

4.2.2 Self-consistent field calculations and supermolecular approximation

In Hartree-Fock theory, the trial wavefunction for electrons is a single Slater determinant, which is optimised variationally to get the lowest energy. To achieve this, the potential energy between the electrons and the nuclei of the system is calculated, using the operators in equation 4.4. These can be re-grouped according to how many electron coordinates are required. V_{nn} is the only one with no electron coordinate-dependency, while:

$$\widehat{h}_i = -\frac{1}{2}\nabla_i^2 + \frac{Z_a}{|\mathbf{R}_a - \mathbf{r}_i|} \tag{4.7}$$

depends on the position of one electron and practically describes the motion of an electron in the field created by the nuclei. R_a refers to the coordinates of nucleus a, r_i refers to the coordinates of electron i and Z_a to the charge of nucleus a, and all operators are expressed in atomic units. Also:

$$\widehat{g}_{ij} = \frac{1}{|\mathbf{r}_i - \mathbf{r}_j|} \tag{4.8}$$

depends on the positions of two electrons. It is also useful to define the diagonal product of a Slater determinant, Π:

$$\Pi = \phi_1(1)\phi_2(2)\ldots\phi_N(N) \tag{4.9}$$

and a two-particle permutation operator $\hat{P}_{ij}$, which when applied interchanges the electron coordinates i and j. Yet, for Π, the indices for electron coordinates are the same as the indices for the spinorbitals. Using Π we can evaluate the expectation value of the potential energy between electrons as:

$$\left\langle \Pi_{SD} \left| \sum_{i}^{N_{electrons}} \sum_{j>i}^{N_{electrons}} \widehat{g}_{ij} \right| \Pi_{SD} \right\rangle = \sum_{i}^{N_{electrons}} \sum_{j>i}^{N_{electrons}} J_{ij} - K_{ij} \tag{4.10}$$

where J_{ij} is called the Coulomb integral and it corresponds to the classic repulsion between two electrons. For example, between electrons p and q this would correspond to:

$$J_{ij} = \langle \Pi | \widehat{g}_{ij} | \Pi \rangle = \langle \phi_i(i)\phi_j(j) | \widehat{g}_{ij} | \phi_i(i)\phi_j(j) \rangle \tag{4.11}$$

K_{ij} is called the exchange integral and corresponds to the interaction between the non-diagonal terms in the Slater determinant. To generate these from the diagonal product, we can apply the permutation operator $\widehat{P}_{ij}$ successively applied on the diagonal product. This will generate all the other possible occupancies:

$$K_{ij} = \langle \Pi | \widehat{g}_{ij} | \widehat{P}_{ij} \Pi \rangle = \langle \phi_i(j)\phi_j(i) | \widehat{g}_{ij} | \phi_i(i)\phi_j(j) \rangle \tag{4.12}$$

The exchange integral has no classical counterpart and its effect is to lower the energy of the system. So far, the energy of the electronic wavefunction is given by:

$$E = \langle V_{nn} \rangle + \sum_{i}^{N_{\text{electrons}}} \langle h_i \rangle + \frac{1}{2} \sum_{i}^{N_{\text{electrons}}} \sum_{j}^{N_{\text{electrons}}} (J_{ij} - K_{ij}) \tag{4.13}$$

where the factor of $\frac{1}{2}$ is to avoid counting the interaction of electrons twice. The nuclear-nuclear repulsion is constant in each molecular geometry and, given the position of the nuclei, the nuclear-electron interaction can be optimised without any problems. The main issue occurs at the electron-electron repulsion, which depends on two electron coordinates. Yet, if one assumes that the positions and functions of all but one electron are known, then the following one-electron energy operator, called the Fock operator, may be used to find the optimum function for that last electron:

$$\widehat{F}_i = \widehat{h}_i + \sum_{j \neq i}^{N_{\text{electrons}}} (\hat{J}_j - \hat{K}_j) \tag{4.14}$$

where the $\hat{J}_j$ and $\hat{K}_j$ now are the Coulomb and exchange operators defined as:

$$\hat{J}_i |\phi_j(2)\rangle = \langle \phi_i(1) | \widehat{g}_{12} | \phi_i(1) \rangle | \phi_j(2) \rangle \tag{4.15}$$

$$\hat{K}_i |\phi_j(2)\rangle = \langle \phi_i(1) | \widehat{g}_{12} | \phi_j(1) \rangle | \phi_i(2) \rangle \tag{4.16}$$

It is worth noting that the sum of the Fock energies will be double-counting the interaction between electrons. Performing an Hartree-Fock calculation is an iterative procedure: The coordinates of all electrons but one are guessed initially and using the Fock operator, the optimum space function is calculated for that one electron and saved. Then the calculation is repeated for

all electrons, one by one, until the change in energy is below a pre-set threshold. A set of functions that fits these criteria are called Self-Consistent Field (SCF) orbitals. These are organised in energy order and filled according to the Aufbau principle, thus giving occupied and virtual orbitals.

As the eigenstate of an electron's motion is optimised in an average field (also referred to as the "mean field" approximation), this means there is no direct electron correlation. Moreover, as only occupied orbitals are included in a Slater determinant, only one electronic configuration is included. For this reason, transition states, bi-radical species, or generally any species that cannot be adequately described by a single electron configuration[1], will not be well represented.

Moreover, the calculation may be restricted so that the each spatial orbital has two electrons of opposite spin, which is called the "Restricted Hartree-Fock" (RHF). Similar to that is the "Restricted Open-Shell Hartree Fock" (ROHF) where the restriction is applied on all closed-shell orbitals. If no such restriction is applied, then the method is called "Unrestricted Hartree-Fock" (UHF) and since there is practically one more degree of freedom per electron pair to be variationally optimised, the energy of UHF is typically lower than for RHF. Yet, the final wavefunction is no longer an eigenstate of the spin operator as the linear combinations for the spatial wavefunctions of paired electrons differ and therefore are no longer necessarily orthogonal. This is termed "spin-contamination" and results in the spin quantum number of the calculated state no longer being well defined. This effect increases with the size of the basis set.

One problem of HF calculations that is especially important when dealing with radical dimers is the dissociation problem. If a pair of electrons is shared between two nuclei, e.g. in the case of H_2, and the nuclei are pulled apart, this should physically result in a homolytic bond cleavage. However, if the two electrons are sharing the same spatial wavefunction (as in the case of RHF) they will have an equal chance to be found both around either nucleus. Therefore half of the wavefunction represents an ionic bond which, when propagated to long distance gives a 50% chance of heterolytic bond dissociation. This causes the energy of the complex to increase too rapidly as a function of distance between the centres which raises the

[1] In this context, a configuration is a specific Slater determinant. As only occupied orbitals are used in a Slater determinant, selecting which spinorbital to include is equivalent to selecting an electron configuration.

bond stretching vibrational frequencies and may shift the minimum. This problem is somewhat avoided in the case of UHF, as orbitals are allowed to "localise".

Finally an important approximation to be noted is the supermolecular approximation: The energy of a system of molecular species is taken as the energy of the system minus the energy of each species separately.

$$\Delta E_{A-B} = E_{AB} - E_A - E_B \tag{4.17}$$

4.3 Electron Correlation Methods

The main omission of HF methods is the neglect of electron correlation: the ability of electrons to avoid each other. To some extent, the UHF calculations, by not restricting electron pairs to have the same spatial orbital, include correlation in an average way: this is termed static correlation. This is mainly the case of electrons having an averaged position shifted with respect to each other.

The second type of correlation is "dynamic correlation": this is the case where the electron densities are the same, but electrons move away from each other and thus can minimise their Coulomb repulsion. Although this interaction is neglected in HF calculations, they still offer about 99% [34] of the total energy of the system. Therefore, the HF calculations' results are used as initial guesses for the more expensive correlation calculations. Usually, the ground state wavefunction for an electron correlation method is taken as a linear combination of the HF solution plus excited states,

$$\Psi = a_0 \psi_{HF} + \sum_{i=1} a_i \psi_i \tag{4.18}$$

where ψ_{HF} is the Hartree-Fock solution. The excited determinants ψ_i represent excited configurations: in their Slater determinants, one or more of the spinorbitals from the HF ground state are replaced by one of higher energy. It is useful to characterise these determinants according to the number of single (one electron moved to an unoccupied orbital) excitations required to achieve their configuration from the ψ_{HF} ("ground state"): therefore there are the single (S),

double (D), triple (T), quadruple (Q) etc. excited states.

If all possible excited states could be included[2], then the motion of electrons could be described precisely and all electron correlation would have been recovered. However, such a calculation is not possible, and the larger the system and the number of nuclear geometries that need to be calculated, the grosser the assumptions that have to be made. Limiting the number of excitations leads to a "truncation error" in the correlation method.

A common assumption is to neglect the excitation (and therefore the electron correlation) of the inner electrons ("frozen core"). This is not strictly speaking correct, but since most of the chemically important interactions occur with the valence shell electrons, this will simply provide a mainly systematic error.

4.3.1 Multi-Configuration SCF

In Multi-Configuration SCF (MCSCF), the wavefunction is taken as a linear combination of the HF eigenstates, but both the coefficients of the linear combination as well as the HF states themselves are variationally optimised. The wavefunctions now are called Configuration State Functions (CSF).

By taking the appropriate combination of HF solutions, the use of CSFs predicts correctly homolytic bond breaking. Moreover, as many HF electron configurations are taken into account in each CSF, this method is appropriate for cases when more than one electron configurations ("multireference" cases, MR) is required to describe the ground state.

Convergence in this method is much slower than in HF, however it is essential for systems that cannot be accurately described by a single electron configuration. Although it could also be used as a way to regain some of the electron correlation, and indeed some non-dynamical correlation is recovered, it is very expensive and inefficient. The configuration space used at

[2]Here implicitly we assume that we are also using enough functions to represent numerically the ground and excited states accurately. This assumption is usually wrong as for practical reasons we only use a limited number of functions, leading to what is called "basis set incompleteness error". This will be explored in more detail later in this chapter.

each calculation is called the "active space".

In MCSCF, the orbitals are distinguished to active and spectator orbitals, with the active being the ones that undergo substantial change in the process of interest. All CSFs are optimised variationally, but only for the active orbitals there is some static electron correlation calculation. Choosing which are the active orbitals is the main difficulty of this method. A calculation that takes into account all possible electron configurations (called Complete Active Space Self Consistent Field-CASSCF) becomes unmanageable very soon with increasing system size.

A quicker method is the Restricted Active Space SCF (RASSCF), where the active orbitals are further split to RAS1, RAS2 and RAS3. RAS1 are usually doubly occupied (or with limited vacancies), RAS3 are usually empty (or with limited occupation) and RAS2 are the orbitals whose occupancy changes between important configurations ("fully active"). Then the full calculation is run for RAS2, while interactions between RAS1-RAS2 and RAS2-RAS3 are included to allow for orbital relaxation.

The problem of choosing the appropriate chemically important MOs unfortunately does not have a standard solution. This is not aided by the fact that convergence to a value for any CAS state is very rarely practically met [37]. Usually RHF calculations are performed before the MCSCF as to indicate the important orbitals, their symmetry and occupancy.

4.3.2 Configuration Interaction

In Configuration Interaction (CI) calculations, the final wavefunction is a variationally optimised linear combination of HF eigenstates, taken so that the overall spin of the final state is the same as the ground state. In theory, a full CI calculation will take into account all possible excitations and would recover all electron correlation for that basis set. However, this is too expensive and usually CI calculations are truncated to the most important excitations.

According to Brillouin's theorem [34], the single excitations by themselves cannot offer any improvement to the HF solution, so the minimum excitation level that has to be included is D (in which case the method is named CID). This theorem holds true for any post-HF method that

uses the same ground state as HF (i.e. not MR methods). Qualitatively, CID can be thought of representing the electron correlation between pairs of electrons while Q excitations represent the products of CID. S excitations allow relaxation between the pairs of electrons after an excitation, and therefore are important. CI is a variational method, so the calculated energy is always higher than the true energy and the lower the energy, the better the calculation[3].

As in the CI calculations the RHF eigenstates are combined, the dissociation problem is resolved. Unfortunately, another problem arises: at long distances, the energy of a dimer should be the same as the sum of the two monomers. Yet, this is not true for CI calculations. To see why, we may consider a supermolecule AB: a CISD calculation would calculate a D excitation of the supermolecule and then relax it with an S excitation. However, at a large distance between A and B, the same calculation would be equivalent to a S excitation of A plus a D excitation on B, giving an overall CISDT term. Therefore the order of excitations taken into account changes with distance between the molecules. This gives an extra artificial binding energy and the method is characterised as *size inconsistent*. Practically, the Size Consistency Error (SCE) is assumed to be a constant that may be calculated at large distances and then subtracted from everywhere, although there is no clear theoretical justification for it.

CI calculations can also be combined with MCSCF calculations. In these cases, Multireference CI (MRCI) calculations are performed where the excitations are taken out of all states combined in a CSF.

4.3.3 Møller-Plesset Perturbation Theory

In this method perturbation theory (PT) is used between the HF ground state and excited state. As PT is applied to a system of interacting bodies assuming they are independent, this is a many-body perturbation theory (MBPT) method. In all perturbation theory approaches there is the assumption that the ground state (the HF solution) is well-separated from any other (excited) state. Therefore, this method is unsuitable for any cases of possible multireference character.

[3]Yet, it is important to note that if a supermolecular calculation is performed, although the energy of the complex and each monomer is variational, there is no strict requirement for their difference to be.

According to standard PT [36], the Hamiltonian of the system is separated as a reference ($\widehat{H}^0$) and a perturbative ($\widehat{H}'$) operator:

$$\widehat{H}_{Total} = \widehat{H}^0 + n\widehat{H}' \tag{4.19}$$

where n is a parameter indicating the order of perturbation. The ($\widehat{H}^0$) is taken as the sum of the Fock operators

$$\widehat{H}^0 = \sum_{i}^{N_{electrons}} \widehat{F}_i \tag{4.20}$$

However this means that the zeroth-order results would count all the interactions between the electrons twice, and is actually worst than the HF result. The perturbation Hamiltonian is the potential caused by the electrons. This is expressed as the difference between the true electron-electron repulsion, minus twice the averaged repulsion:

$$\widehat{H}' = \widehat{V}_{ee,true} - 2 \times \langle \widehat{V}_{ee} \rangle \tag{4.21}$$

$$\langle \Phi_0 | \widehat{H}' | \Phi_0 \rangle = \widehat{V}_{ee} - 2 \times \langle \widehat{V}_{ee} \rangle = -\langle \widehat{V}_{ee} \rangle \tag{4.22}$$

It may be noticed that the basic assumption of the perturbation being small compared to the reference Hamiltonian is not really satisfied. The first order correction ($n = 1$) simply gives back the HF solution. It is only from $n = 2$ that one improves the result. In honour of C. Møller and M. S. Plesset that formulated the approach, this method is called Møller-Plesset Perturbation theory of n-th order, or MPn.

Unfortunately, this is not a variational method: the energy calculated at a given order is not necessarily higher than the true energy, as the importance of perturbation might be over or under estimated. Moreover, the even n MPn methods tend to over-estimate binding energies, while the odd ones tend to underestimate it. It is also generally thought better to perform even MPn calculations as they have been found consistently closer to the full-CI solution [34].

One advantage of MPn methods is that they are size-consistent and also relatively inexpensive to perform. If the system explored has no important MR contributions, the MP3 method can

account for $90-95\%$ of the correlation energy and MP4 typically accounts for $95-98\%$ [38]. Although there are MP5 and MP6 methods available, these are rarely used in practice, due to computational cost.

4.3.4 Coupled Cluster methods

In MPn methods, all possible excitations are included at n-th order. In the Coupled-Cluster (CC) methods, on the other hand, the emphasis is placed on the specific excitations that link the HF solution to the final wavefunction. The interactions then resulting from a specific kind of excitation, are included precisely, which would correspond to infinite order correction in MPn. It is useful to define the excitation operator $\widehat{T}$:

$$\widehat{T} = \widehat{T}_1 + \widehat{T}_2 + \widehat{T}_3 + \dots \tag{4.23}$$

where $\widehat{T}_i$ is the operator causing an i-th excitation. Relating back to CI methods, the excited states can be constructed by acting on a ground state by the excitation operator:

$$(1+\widehat{T})|\Psi_0\rangle = (1+\widehat{T}_1+\widehat{T}_2+\widehat{T}_3+\dots)|\Psi_0\rangle \tag{4.24}$$

while in CC methods, the Taylor series of an exponential excitation operator is used:

$$\Psi_{cc} = e^{\widehat{T}}\Psi_{HF} = (1+\widehat{T}+\widehat{T}^2/(2!)+\dots)\Psi_{HF} = (1+\underbrace{\widehat{T}_1}_{\text{S}}+\underbrace{(\widehat{T}_2+(1/2)\widehat{T}_1^2)}_{\text{D}}+\dots)\Psi_{HF} \tag{4.25}$$

In the last form of the equation, all operators leading to the same order final excitation are grouped together. This way, both connected (here $\widehat{T}_2$ indicates the double excitation of a single electron) and disconnected ($\widehat{T}_1^2$ indicates two separate single excitations) are taken in the D contribution. Then to calculate the energy of the system is calculated by:

$$E_{CC} = \langle\Phi_0|\widehat{H}e^{\widehat{T}}|\Phi_0\rangle \tag{4.26}$$

where Φ_0 is taken as the HF solution. For CCD methods, only the D excitations are included[4], for CCSD both S and D excitations are included and so on. As both connected and disconnected excitations are included, this method is size consistent.

However, although precise, this method becomes expensive (computationally) very fast, so the "golden standard" that is thought to give the optimum accuracy for effort is CCSD(T), where the parenthesis indicates that the triplet excitations are included non-iteratively, by perturbation theory on the CCSD results.

Like MPn methods, CC is a single-reference method, although more forgiving in close-degeneracies. The most common test for MR character is the so-called T1 diagnostic: the contribution of S excitation over the square root of the number of electrons in the system. If that is large (over 0.02 [34]) then this indicates that the energy of the system changes significantly if electron pairs relax with respect to each other, so another configuration is important. Also, like MPn methods, CC are not variational.

4.3.5 Multireference perturbation theory

Arguably the most successful method to include dynamic correlation to MCSCF wavefunction has been the use of second order perturbation theory [39]. The usual approach consists of applying a MBPT theory on either CAS (or RAS) wavefunctions, produced by an MCSCF calculation.

The most widely applied method is the CASPT2 (also referred to as Rayleigh-Schrödinger Second Order Perturbation Theory-RSPT2), which has also been extended to CASPT3 [40]. Practically it is MPn theory applied to a CASSCF wavefunction and this method is suitable for near-degenerate states. There is also a way to truncate the number of CSFs taken into account, thus speeding up the calculation, by using a RAS-PT: i.e. restricting occupation numbers for specific orbitals in the same way as for RAS-SCF.

[4] Again, due to the Brillouin principle, S excitations by themselves cannot improve on the HF solution.

CASPT3 also contains the perturbative Hamiltonian interaction between excited states that practically means relaxation of the orbitals in the excited state. This has been shown to be very important at some cases, although there is evidence that the oscillatory behaviour of MPn results may be found at CASPTn as well, in which case CASPT2 might be closer to the solution[5]. Also, a big change between the CASPT2 and CASPT3 results would indicate that the CSF taken as the reference is inadequate.

One problem of CASPT methods is that they are not size consistent. Moreover, there is the problem of intruder states: the cases where the degeneracies of the excited and ground state cause a singularity in the calculation. One way to alleviate that problem is by shifting the energy of the virtual orbital with respect to the active orbitals by a specific amount, however this is not physically justified, especially in cases where the geometry changes and this can lead to non-systematic errors. It has been found that for states separated by a small amount in energy, choosing a shift parameter (σ) that is too small, can lead to CASPT2 predicting a false ground state [41]. This has again been attributed to intruder states and selection of active space [42]. Furthermore, it has been argued that CASPT predictions overestimate the dissociation energy, and actually deteriorate at very large basis sets [43].

Another method is the CI-PT Method [43], which treats excitation only from the active space with CI and the rest with PT. This eliminated the intruder state issue, however, as a CI method, is not size consistent (even less size consistent than CASPT2). Along the same lines, the active space interaction, which is the main contributor in terms of energy, is treated by a variational method. Thus, CIPT2 is usually considered a variational method. In contrast to CASPT2, CIPT2 usually underestimates the dissociation energy and the anisotropy of the Potential Energy Surface (PES) with respect to a MRCI calculation.

Finally, the third method to be discussed in this section is the *n*-electron valence state second order perturbation theory approach-NEVPT2. The big difference for this method is that it uses a different zeroth order Hamiltonian, the Dyall Hamiltonian [44]. Dyall noticed that the use of a one-electron Hamiltonian to build the reference function meant that, once post-HF corrections

[5]This also highlights another shortcoming of CASPT: that it is not a variational method.

were applied, the ground state was allowed to include bielectronic interactions but the excited states were not. This created an energy bias to the ground state, and to correct it, he proposed a partly bielectronic Hamiltonian. All NEVPT2 theory is based on this work although there are variants depending on the contraction of states, separating Strongly Contracted (SC) and Partly Contracted (PC) methods. All work presented in this thesis is done with the most precise of the two, the Partly Contracted method. The functional space of NEVPT2 is distinguished in the same way as CASPT2, so a comparison between them is valid [45].

There are two big advantages in using NEVPT2: firstly, the method is size-consistent and secondly, the states produced by NEVPT2 are so well separated, that the chance of an intruder state is practically insignificant [46]. The results of NEVPT2 calculations tend to overestimate the dissociation energy. Work on heterodimers comparing the CASPT2 with NEVPT2 methods suggests that NEVPT2 is preferable, not only due to lack of intruder states and size inconsistency, but also because of the accuracy of the final energy [47].

In the case of a closed-shell single-reference problem, all CASPT2, NEVPT2 and CIPT2 are equivalent to MP2, while CASPT3 is equivalent to MP3.

4.3.6 Combinations of methods

The "gold standard" method for computational effort to results is CCSD(T). However, this method cannot handle multireference cases and as a result, a lot of innovative work has gone into combining different *ab initio* methods. The main idea is that CC methods are used for one state and another one is then derived as the difference from that first state with an MR-able method. This way CC would "guarantee" a reasonable representation of the state it can describe. Perhaps the most common combination is that of CC and MRCI methods [48, 49]. By approximating the size extensivity as the same in the two states, the difference in energy between the ground and an excited state (ΔE_{MRCI}) can be added to the CC calculations. As any corrections relating to the supermolecular approximation[6] for the two states are the same, they cancel at ΔE_{MRCI}.

[6]For example, the counterpoise correction discussed in detail in the next section.

A similar approach is to add the differences from CASPT calculations between different states, again on CCSD(T) calculations [50]. This method is also more economical, and thus can be used for larger systems or when more than one excited state is required. Some studies [51, 52], suggest that this method produces slightly better agreement with experimental results than the MRCI combination with RCCSD(T), at a lower cost. One major advantage is that CASPT2 has a significantly smaller[7] size inconsistency error and therefore, the approximation that this cancels between the two states or produces a constant shift, is more valid.

However, there is a point to be made about combining different techniques both at the level of operators used and of the wavefunctions representing these states. As CC methods will be operating on a SCF state and MRCI or CASPT methods on a MCSCF state, the latter will be operating not on the same state as the former, but on a weighted linear combination of the ground and excited states. Even if one argues that the MCSCF ground state is predominantly one SCF state, it is not clear how true that is for the excited states. Also, it goes against the previous assumption that most of the potential between these states is the same and they are close in energy. Moreover, applying excitations on a MCSCF state would be different than on a SCF state, as the excitations to produce the states within the MCSCF wavefunction would be automatically of higher order. There is also the comment that CC operators and CI operators are not strictly speaking compatible [54].

4.4 Basis Sets

In this section the basis sets commonly used for *ab initio* calculations, emphasizing on the ones used in this project, are presented. In theory, any complete set of functions with the appropriate angle dependencies could be used as a basis set to describe the system's wavefunction. However, such a calculation is impossible and the basis sets have to be truncated, leading to the "basis set truncation", or "basis set incompleteness" error. The theoretical extreme where an infinite basis

[7] This is noted to be one order of magnitude difference, while in reference [53] the size inconsistency error is noted to be "*very small*".

set is used is called the Complete Basis Set (CBS) limit. Using a CBS, the calculated energy would be the best possible given the limitations of the method (e.g. HF) used.

Usually the coordinates of the electron are represented in spherical coordinates, where a spherical harmonic ($\mathscr{Y}_l^m(\theta,\phi)$) is used to represent the angle dependence and the radial coordinate is commonly represented by either a Slater-type or a Gaussian-type function. Slater-type function (or Slater-type orbitals, STO) have the general form:

$$\chi_{\mathrm{STO}} = N_{n\ell m} r^{n-1} e^{-\zeta r} \mathscr{Y}_m^{\ell}(\theta,\phi) \tag{4.27}$$

where n is similar to the principal quantum number used to describe atomic orbitals, $N_{n\ell m}$ is a normalisation constant and ζ is called the orbital exponent. Gaussian-type functions (or Gaussian-type orbitals, GTOs) have the form:

$$\chi_{\mathrm{GTO}} = N_{n\ell m} e^{-\zeta r^2} \mathscr{Y}_m^{\ell}(\theta,\phi) \tag{4.28}$$

The "true" orbital is approximated by a combination of functions in the calculation, and these functions are called the basis set. The larger the basis set, the better the description of the orbital (according to the variational principle), but the longer each calculation takes. Linear combinations of STOs are better in modeling molecular (or atomic orbitals) and represent especially the "tail" of the orbitals and the area near the nuclei more physically[8]. However, the integrals of GTOs are far quicker to calculate and cheaper to store (mainly due to the property that sums or differences of Gaussians is another Gaussian).

For this reason, in small systems STOs can offer good precision with fairly small basis sets, but for larger systems (more than two to three atoms), larger basis sets of GTOs can offer the same precision quicker. STOs and GTOs are routinely used to model atomic orbitals and these are then used in calculations. The GTOs/STOs before any other modification are called the "primitive" orbitals.

[8]The GTOs fall too quickly on the long and short extremes thus misrepresenting the electron cusp at the nucleus and the long-distance overlap with other orbitals.

It should be noted that the concept of "orbital" is not as easy to define as is in the hydrogen atom. Linear combinations of GTOs/STOs are used, that are modelled to Atomic Orbitals (AO), but then a number or features are added. Here, an "orbital" is a set of functions that is aimed to describe the motion of one electron.

A minimal basis set is one that only contains enough orbitals to accommodate all electrons in a single configuration, so for example, for H atom it would be only the 1s orbital. A Double Zeta (DZ) basis includes twice the number of orbitals of the minimal basis set, and so on. However, as this increases computational effort it is common to "split" the basis set, so only Valence (V) electrons have more than the minimal basis; for DZ this is noted as VDZ.

Following the same line of thought, the valence orbitals can be enhanced in order to represent better any deviations between atomic (after which they are modelled) and molecular environments. Considering a single bond formed by s-atomic orbitals one can see the benefit of including higher angular momentum functions (in this case p-orbitals) to replicate the effect that in Valence Bond theory (VB) would be described as hybridisation, although in VB no extra functions are introduced. These higher momentum functions offer a faster convergence in electron correlation calculations. Usually, $(l-1)$ polarisation functions of l angular momentum are included, eg. 3s2p1d. This is denoted with a p- in the name of the basis set, e.g. pVDZ.

Moreover, as in an *ab initio* calculation threshold is (usually) set in terms of energy, the core-orbitals are far more significant than the valence, even though the orbitals of chemical interest are the other way round. Thus, to emphasise on the valence electrons, the GTOs/STOs used to express the core orbitals is fixed to a linear combination of the primitive GTOs/STOs, called contracted GTOs/STOs. Once a specific Zeta contracted basis set has been computed for an element, it can be used to speed up calculations. Segmented basis sets use a combination of contracted and primitive functions. Example of such GTO basis sets are the most commonly used Pople and Dunning basis sets [55]. The main practical difference between same-zeta basis sets is that the Dunning ones do not have the restriction of s- and p- orbitals having the same exponents, which applies to Pople Basis sets. This extra degree of freedom allows better precision but comes at a computational cost.

However, the main reason that Dunning basis sets were used in this project was that they can be chosen to be Correlation-Consistent (cc-). This means that the basis set is designed so functions that contribute on a similar magnitude to the electron correlation are included in the same stage, independently of the function type. That allows for a more monotonic convergence to the CBS energy as basis set size increases. cc- functions can be "augmented" (aug-) by diffuse functions, e.g. adding a p function of small exponent to an s function. Therefore, a split-shell polarised-valence correlation-consistent augmented X zeta Dunning basis set can be written as: aug-cc-pVXZ, where X=D,T,Q etc.

4.4.1 Basis set related errors and CBS extrapolation

If one could perform the calculation with a complete set of functions (CBS), then the energy of the system would be described as well as possible for the level of theory applied. Unfortunately, this is practically impossible and the error caused by the inadequacy of the basis set used is called the basis set incompleteness error.

In the case of a molecular complex, calculated by the supermolecular approximation, the assumption is that the basis set of each molecule (monomer) will be used to describe the orbitals of that monomer only, so when the energy of individually calculated monomers is subtracted, only the interaction energy remains. However, basis set functions that are not used by the molecule they are intended for, may be used to describe another one. Since these will not be available when the energy of each molecule is computed individually, this creates an artificially stronger binding energy and it is called the Basis Set Superposition Error (BSSE).

The usual way to correct for the BSSE in a supermolecular system with monomer A and B, is by the Counterpoise Procedure (CP) by Boys and Bernardi [56]: For the supermolecular calculation of the binding energy of the system A-B, we can define the basis sets a and b as the basis sets used to calculate the energy of the individual molecules, and ab as the basis set used for the complex calculation. The binding energy is now given as:

$$E_{\text{binding}} = E_{AB,ab} - (E_{A,ab} + E_{B,ab} - E^*_{A,a} - E^*_{B,b} + E_{A,a} + E_{B,b}) \tag{4.29}$$

where A, B show that the calculation is carried out with the nuclei and electrons of species A or B, while a, b indicate that the calculation used the basis set of A or B. The starred terms allow for the possibility that the geometry of the molecules changes upon complexation. Therefore, they are the respective energies in the changed geometry.

As the CP correction practically accounts for all the energy lowering of one molecule due to the presence of a completely empty basis set of the other species (and not just the functions that are free in the basis set of the other species), it over-compensates for the BSSE. Still, it is considered a better estimate than the uncorrected energy. If the basis set used for each molecule was sufficiently large (called a saturated basis set), then no extra functions from the other molecule would be required and no BSSE would be noted. One side effect of the CP overestimation is that it removes any charge transfer between the molecules[9] that might be occurring [58]. Therefore, CP is best regarded as an indication of the severity of the BSSE.

Especially when using cc- basis sets, one can extrapolate the energy to the CBS, based on the assumptions that firstly, it is a converging series and secondly, the convergence is monotonic. Halkier, Klopper *et al.* [59] argued for an exponential expression and also used much larger basis sets.

$$E_X^{HF} = E_{cbs}^{HF} + A^{HF} e^{-\beta' X} \tag{4.30}$$

$$E_X^{Corr} = E_{cbs}^{Corr} + A^{Corr} e^{-\beta X} \tag{4.31}$$

The higher the zeta of the calculations used for extrapolation, the more accurate the result, as the error limits with respect to the CBS result decrease. Adding diffuse functions ("aug-") also improves the extrapolation.

A previous member of the group, Kevin Back [60], agreed with Klopper's scheme by noticing that the ratio between energies of adjacent zeta is almost the same, and then improved on that by adding a quadratic term on the exponential. This significantly improved the results,

[9] Another related issue that may arise here is that induction might be overestimated due to functions located on the "inducing" partner. These basis functions are sometimes called the "far-bond" functions, and may lead to unphysically large induction which could even be partly a charge-transfer effect [57]. A more detailed discussion of the charge-transfer effect is given in chapter 7.

which, using Klopper's data, were closer extrapolated to the "CBS" limit with cc-DZ and cc-TZ calculation than by cc-QZ and cc-5Z with Klopper's formula. The formula Back suggested is:

$$E_X^{Corr} = E_{cbs}^{Corr} + A^{Corr} e^{-\beta' X + \gamma' X^2} \tag{4.32}$$

with $\beta = 1.201634, \gamma = 0.06154717$ for MP2 and $\beta = 1.302213, \gamma = 0.061319381$ for CCSD. More recently, another member of the group, Starkey [2], also expanded that for the HF calculations, with the values $\beta = 0.6154$ and $\gamma = -0.1474$ and for RSPT2 energies with $\beta = 1.2184, \gamma = 0.0629$. This scheme is intuitive and also calibrated to the basis sets used here (AVDZ and AVTZ) and therefore preferred. The assumption that CCSD and CCSD(T) energies [58] can be extrapolated with the same scheme is also assumed here.

4.5 The Computers Used

As a significant amount of *ab initio* calculations were performed, a combination of group, departmental and national machines were used to make this possible. All machines described here have 64 bit processor architecture. There are two main limiting factors for *ab initio* calculations: the number of processors (as the speed of the calculation scales linearly for at least up to 8 processors, for some programs and calculations even more) and the amount of memory (mainly RAM as ideally where all pre-calculated integrals would be stored at, rather than having to be retrieved from hard disk memory, which slows the calculation down by an order of magnitude).

Firstly, the group machines: The first machine used was BJH3, a single core, AMD Athlon 64 3500 machine with 2 GB of memory. That was actually the only machine available to perform MRPT calculations during the first year of this study. The following year, BJH5 became available, which has a 4 core processor (Intel Quad Core Q9550, each with a processing speed of 2.83 GHz), and 4 GB of memory. Finally, the year after that BJH10 was introduced, with 8 cores (two Intel E5530 Xeon processors, each running up to 2.40 GHz) and 32GB of RAM.

In addition to these, it was fortunate to have access to the Espresso departmental machine,

a multi-blade machine, each blade having a dual- core Intel Xeon processor, each operating at 2.40 GHz with 2 GB of memory. Moreover, via MPLS, access was granted to the Oxford Electronic Research Center (OeRC) supercomputers: HAL, SAL and Arcus. HAL has 8 2.8GHz Xeon cores per blade and 16 GB of Memory, while SAL also has 8 cores of 2.53GHz and 24 GB of memory. Arcus is the latest machine with 16 cores per blade and 64 GB of memory. Unfortunately, due to the cost of using these machines, only limited calculations were performed there until the end of the last year. Furthermore, the EPSRC UK National Service for Computational Chemistry Software (NSCCS) was approached and a very productive trial period was agreed upon. The Columbus cluster that was used has 8 cores per node, each operating at 2.66GHz with 2TB of memory accessible by all 64 nodes.

Chapter 5

Experimental

"*It doesn't matter how beautiful your theory is. It doesn't matter how smart you are. If it doesn't agree with experiment, it's wrong.*"

- Richard P. Feynman

5.1 Introduction

The true test of any theory or prediction is the comparison with experimental data and the weaker the interaction investigated, the greater the precision required. We are interested in ways to measure the intermolecular forces in van der Waals complexes at the greatest feasible precision.

As was noted in chapter 1, the study of van der Waals complexes is largely the study of intermolecular forces. There is a plethora of methods available to experimentally study the intermolecular forces in the gas phase: On the one end, there are methods that determine the interaction between molecules in a sample based on its bulk properties and on the other end, there are the spectroscopic techniques, such as Infra-Red (IR) and Microwave (MW) spectroscopy. Spectroscopic methods detect the way a sample interacts with radiation and MW radiation experiments specifically probe the rotational transitions. In these techniques, the quantum mechanical structure and the energy level separations of the complexes is probed directly. As

the energy scale of the transitions decreases, weaker effects can be observed. To put that into perspective, one may consider that the results of *ab initio* calculations are usually quoted in Hartrees, of photoelectron spectroscopy in electron volts (eV), of IR in wavenumbers (cm^{-1}) and of MW in MHz:

$$1 \quad \text{hartree} \approx 27.2107 \quad \text{eV} \approx 219,474.63 \quad \text{cm}^{-1} \approx 6.57966 \times 10^{9} \quad \text{MHz} \tag{5.1}$$

Thus, the reason that MW spectroscopy has been preferred is for its accuracy, as the errors in the measurement (in our setup) are in the kHz scale. The experimental work undertaken in this project was carried out using two pulsed-nozzle Fourier Transform Microwave Spectrometers (FTMS), both constructed in the group according to the specifications given by Balle and Flygare [61]. These specifications have also been modified to enhance sensitivity and automate signal detection as well as target specific cases of species. Before going in detail about each part of the experimental setup, it is helpful to have the general idea in mind: A gas sample containing the species[1] to be studied is introduced to a sealed high-vacuum chamber (the "cavity") through a pulsed nozzle. Next, a MW frequency pulse is released through an antenna, co-linear to the nozzle. If the energy of the radiation corresponds to the energy of a rotational transition of the sample, then this is absorbed. The chamber is then left for the input radiation to decay ("ring down") and the same antenna is used to collect the emitted radiation as the sample relaxes back to its previous state. The collected signal (called the Free Induction Decay, FID) is then amplified, digitised and Fourier transformed. The final spectrum displays both the frequency of the emitted radiation and its intensity. A single data collection cycle like the one described is referred to a "shot". The cavity is constantly held in high vacuum by a pump system.

The most common problem for weakly-bound complexes is that the intensity of the emitted radiation is very weak, and therefore difficult to differentiate from noise. This is quantified by the Signal-to-Noise ratio (S/N) and many techniques, that will be explored below, are used to optimise this. One way is to perform many shots in the same frequency, and add their signal, which will increase the S/N as the signal will add proportionally to the number of shots (M)

[1] This could be a molecule or a van der Waals complex. As both cases were studied in this work, we use the term "species".

while random noise will add as the square root of M. Therefore, the S/N increases with the square root of the number of shots. Each shot has a length of approximately 1 MHz. It is possible to change stepwise the MW frequency and then add the resulting spectra as to both further reduce noise and to obtain a more collective picture. Setting the frequency of the experiments, number of shots as well as the processing of the signals (including adding the spectra) is done via the FTMS program written in C++ by a previous member of the group, Ben Watson [62]. The final spectrum usually has resolution greater than 5 kHz. Two different spectrometers were used for these experiments and their combined range covers from 2 GHz to 18 GHz.

In the following sections, each part of the experiments will be presented in detail. Firstly, the ways to create the sample and how this is introduced into the cavity are discussed. Secondly, the microwave components that create and regulate the excitation radiation as well as collect the emitted radiation are presented. Thirdly, the signal itself and the practical aspects of recording and displaying it are analysed. Finally, all the components are again considered collectively.

5.2 The Sample

5.2.1 The supersonic expansion

When a high-pressure gas is released into a lower pressure environment through a small hole (in our case a nozzle orifice), this creates a directional gas beam. If the diameter of the hole is much larger than the mean free path (λ) of the gas in the high pressure environment, then a large number of collisions will take place as molecules go through it.

These collisions have a double effect to the molecules: on the one hand they serve to transfer energy between molecules, thus resulting in a nearly-homogeneous distribution of energy. On the other hand, via collisional relaxation, the internal energy of each molecule is converted to its translational degrees of freedom. Therefore, the resulting forward beam has a narrow velocity spread. Moreover, as all molecules are moving in the same direction at the same speed, the relative motion between the molecules is significantly reduced, thus effectively cooling the

sample. In a typical nozzle beam, 50% of the gas molecules will have a velocity which is within 5% of the average, which is clearly a non-equilibrium distribution. In such an expansion, the mean free path of the molecules may be calculated as:

$$\lambda = \frac{k_B T}{\sqrt{2}\sigma P} \tag{5.2}$$

where k_B is the Boltzmann factor, T is the temperature, P is the pressure and σ is the collision diameter of the gas. The nozzle used in our experiments has an orifice diameter of 0.5 mm and e.g. for a He expansion at 293 K and with 1.5 bar backing pressure, λ is about 140 nm. Therefore, the condition for a supersonic expansion ($\lambda \ll d$) is satisfied [62].

If the speed of the molecules in the forward beam is greater than the local speed of sound, the expansion of the gas is called "supersonic". Using a supersonic expansion creates a very low temperature (only a few Kelvin) collision-free environment in the axis system of the beam [63].

The distribution of molecules with specific velocity ($N(v)$) in a supersonic expansion is:

$$N(v) \propto e^{-\frac{m(v-\overline{v})^2}{2k_B T}} \tag{5.3}$$

where $\overline{v}$ is the mean flow velocity.

A useful quantity to describe the behaviour of the expansion is the Mach number (M) which is defined as the ratio of the speed of the flow to the local speed of sound (α) [64]:

$$M = \frac{\overline{v}}{\alpha}; \quad \alpha = \sqrt{\frac{\gamma k_B T}{m}} \tag{5.4}$$

where γ is the ratio of the heat capacities at constant pressure and volume:

$$\gamma = \frac{C_p}{C_v} \tag{5.5}$$

For a circular orifice, the Mach number can be written as a function of distance in nozzle diameters (d) away from the beginning of the expansion. A more precise expression can be

obtained by expanding this dependence as a Taylor series:

$$M = \left(\frac{x}{d}\right)^{\gamma-1}\left(C_1 + C_2\left(\frac{d}{x}\right) + C_3\left(\frac{d}{x}\right)^2 + \ldots\right) \tag{5.6}$$

where, for a monoatomic gas, $C_1 = 3.232$, $C_2 = -0.7563$ and $C_3 = 0.3937$. The local pressure, temperature and density (ρ) of the flow are related to the Mach number as:

$$\frac{T}{T_0} = \left(1 + \frac{\gamma-1}{2}M^2\right)^{-1}; \quad \frac{P}{P_0} = \left(1 + \frac{\gamma-1}{2}M^2\right)^{-\frac{\gamma}{\gamma-1}}; \quad \frac{\rho}{\rho_0} = \left(1 + \frac{\gamma-1}{2}M^2\right)^{-\frac{1}{\gamma-1}} \tag{5.7}$$

where the T_0, P_0 and ρ_0 are the temperature, pressure and density of the gas before the supersonic expansion. The terminal Mach number is related to the mean free path at the nozzle as:

$$M_T = 1.17\left(\frac{d}{\lambda_0}\right)^{0.4} \tag{5.8}$$

According to the equipartition theorem [1], monoatomic gases have $\gamma = \frac{5}{3}$, while diatomic gases have $\gamma = \frac{7}{5}$ and the smaller γ is, the lower the achievable final temperature. For this reason, a carrier gas is used: as monoatomic species cool faster and lower than diatomics or polyatomics. In our experiments, a small percentage of the species of interest is seeded in a noble gas. During the expansion, the seeded molecules acquire the flow and the temperature of the carrier gas.

Now, in order to see why there is a terminal Mach number, we need to see this expansion from the perspective of the gas. Once the gas goes through the nozzle orifice, the probability of collisions decreases as the beam diverges. Dimer formation requires a three-body collision (a third partner is required take the extra energy according to energy and momentum conservation laws) and thus only occurs close to the nozzle. After that, there is a region where the two-body collisions are most probable and where the molecular complexes formed are relaxed or destroyed. Further down the expansion, the cooling continues slowly as the probability of any collision is small. Also, as the temperature is lowered, thermal collisions do not have enough energy to destroy any clusters formed. This way, even complexes that are held by very weak interactions are kinetically stable. This collision-free zone (or "zone-of-silence") occurs about $30-40$ orifice diameters after the nozzle head and there the terminal temperature is reached.

Reaching this collision-free zone where the conditions remain practically unchanged for the molecules (unless they hit a cavity wall) gives the terminal Mach number. For our experiments, this is around 20 mm from the nozzle head, and is also where the absorption of the microwaves from the sample occurs. There is also the possibility of complexes of more than two partners to be formed, but that likelihood decreases with the number of partners.

Another effect that we have to take into consideration is the complexes formed by the carrier gas, either with the species in question or between its own atoms, as their formation releases energy that heats up the sample. The larger the carrier gas, the more strongly it binds and therefore the higher the terminal temperature obtainable. For this reason, a neon-expansion would be producing spectra mainly of the lowest states, while more excited states would be accessible using an argon-expansion.

While for recording molecular spectra, the above considerations are of relatively low importance, for complexes it is crucial to have the right kinetics as to "trap" the desired complex in the collision-free zone, with enough collisions to form the complex but not too many as to destroy it. The conditions influencing these kinetics are the nozzle orifice diameter, the pressure inside the cavity, the backing pressure of the sample before the nozzle and the composition of the sample. Only the last two of these are easily modified between experiments. Regarding the backing pressure, it has been repeatedly been found in the group that values between 1-2 bar give optimum results for most complexes. Once a transition was detected, the backing pressure used was optimised by observing the S/N ratio of the signal. The composition of the sample will be examined in detail for each experiment individually later.

5.2.2 The pulsed nozzle

Due to limitations of the pumping speed, in order to maintain the high vacuum and the conditions for the supersonic expansion, the introduction of the gas into the cavity is done using a pulsed nozzle. This is illustrated in figure 5.1 [2]. The nozzle itself consists of a spring inside an armature leading to a poppet that can seal the aperture. The aperture is the hole in the chamber

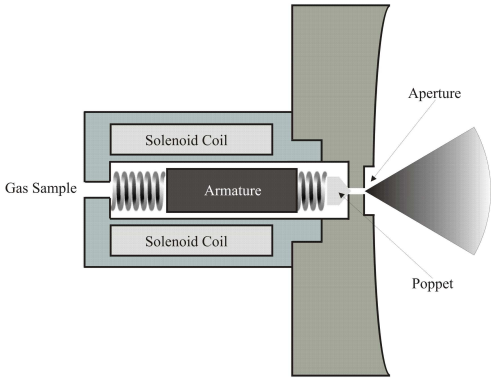

Figure 5.1: The pulsed nozzle [2]

wall through which the gas is introduced. Around the base of the nozzle there is a solenoid coil, that at the application of an electric current pulls the armature back, thus opening the aperture. The current (that triggers the pulse) is regulated by a valve pulser and the pulses are typically at 500 μs with gaps of 100 ms between them.

5.2.3 The gas sample

A pre-made mixture of the desired concentration is made and stored in a cylinder from which the experiment is run. The concentrations of the species in question are usually about $1-5$ % of the gas prepared. Moreover, there is the storing limitation which practically meant that at the best case the sample had to be prepared daily.

If the sample's standard state was liquid, then a bubbler was used: the carrier gas was literally led through a line at the base of a closed metal container wherein the sample was placed. The composition of the emerging gas was controlled by the adjusting the temperature of the sample as to alter its vapour pressure, according to the Antoine equation:

$$T = \frac{B}{A - \log P} \tag{5.9}$$

where A and B are substance-specific parameters, T is the temperature and P is the vapour pressure. To achieve that, the container of the sample is placed in a thermoelectric Peltier-effect cooler, which allowed accurate and stable access to many temperatures. All the gas lines were

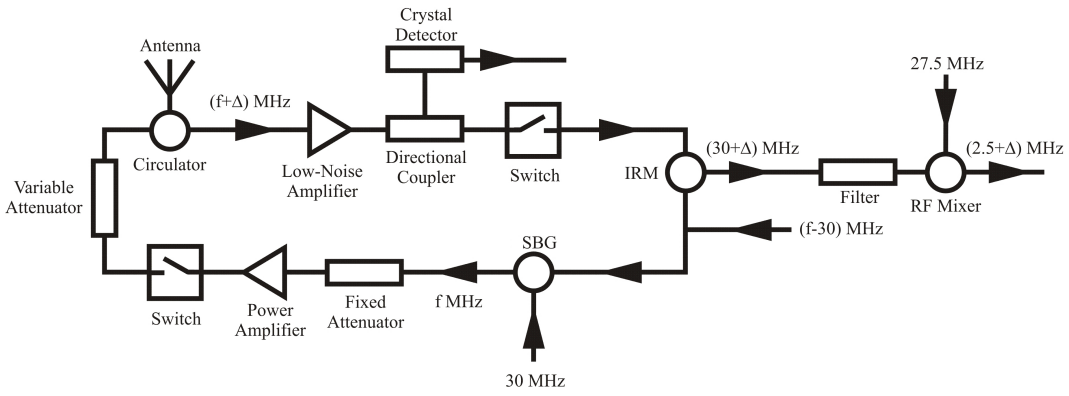

Figure 5.2: The microwave circuit [2]

checked for leaks. All containers, mixing cylinders and gas line connectors are made of stainless steel, while the gas lines were constructed from PTFE. At no stage was a pressure higher than 5 bar used, as this would exceed the safe limits of the setup.

5.3 The Microwave Components

The monochromatic microwave radiation used for the experiments is generated by low noise Wiltron (6747A-20 or 6769B depending on the spectrometer used) swept-frequency synthesiser, with power output set to 15 dBm, which equals 32 mW. If the experiment aims to use radiation of frequency f, then a $f - 30$ MHz locked-phase frequency radiation was produced initially.

This is then split into two (using a power splitter). For both parts an isolator is used to to prevent back-reflection of the radiation. One part is mixed with a 30 MHz frequency to give the desired frequency, produced by a single band frequency generator (SBG), and is first attenuated and then amplified. Then, the first (of two) microwave switches is used to break the continuous radiation to 1 or 2 μs pulses. This radiation is then attenuated, using a variable attenuator which allows optimisation of the power without needing to significantly alter the setup, and is introduced to the experimental chamber via a three-port circulator and the antenna.

A three-port circulator is a three-arm-device where microwaves entering arm one exit on arm two, microwaves entering arm two exit on arm three and similarly microwaves entering arm thee exit only on arm one. In our experiment, arm two is the excitation radiation, which is

coupled into the cavity (arm three), and then the signal from the cavity exits from arm three and is coupled to the arm one which is leading to the detector.

The antenna is practically a coaxial cable, whose central conductor has been exposed at the one end, and is bend to a right angle with respect to the cable. For any radiation of wavelength λ, the optimum length of the antenna is $\frac{\lambda}{2}$. In our experiments two different antennas were used, one of length of 3 cm for frequencies between 8-18 GHz and one of 1.25 cm for frequencies between $4-8$ GHz. The distance x of the antenna to the end of the cavity is also important as the phase of the radiation coming towards the antenna and that reflected back to the antenna from the end of the cavity have to interact constructively. Moreover, in order to minimise reflections and get the most efficient setup, the impedance of the antenna has to match the impedance of the cavity. This depends both on the distance between the antenna and the cavity wall and in the length of the exposed part of the antenna. For the length dependence, ideally the length of the antenna would correspond to half the wavelength of the radiation, which in the case of 10 GHz is 1.5 cm. The distance of the antenna from the mirror is much harder to optimise in advance. In practice, the antenna may be moved further in or out of the cavity, while vacuum is maintained as the entrance of the antenna is sealed by an o-ring.

After a delay to allow for the excitation radiation to decay, the same antenna is used to collect the emitted radiation, which is now $f+\Delta$, and Δ ranges from -1 to 1 MHz. This is normally a weak signal, so after going through the circulator, it is amplified. A directional coupler then splits the power into two unequal parts, one of which (about 10%) is sent to the computer via a crystal detector for cavity tuning[2], while the other part continues to the second microwave switch.

The second microwave switch, is used to protect the detecting part of the circuit from being exposed to the intense radiation used to excite the molecules, and so only allows radiation through after the excitation pulse finishes. This part of the signal is now mixed with the second part of the initial $f-30$ MHz at the image reflection mixer (IRM), so the initial frequency (along

[2]This part of the signal is used for finding the resonant frequency, but is ignored when the signal of the emission of the sample is detected.

with any initial noise) is subtracted[3]. This produces a radiation of $30+\Delta$, which is filtered by a 30 MHz Bandpass Filter. This filter only allows frequencies within a narrow range of 30 MHz to pass, and thus aids noise reduction. This is then mixed with a 27.5 MHz frequency signal to give a final $2.5+\Delta$ MHz signal. Isolators are also used in various places to reduce radiation back-reflections that would lead to phase interactions.

This is then sent to a PC and digitised using a analogue-to-digital (A/D) card. The reason that an $2.5+\Delta$ MHz, rather than a Δ MHz is send to the PC is both to reduce the noise that dominates at low frequencies (and are proportional to $\frac{1}{f}$) and to know the sign of signal (Δ). The A/D can convert directly the microwave power to digital information, and the signal is then managed by the FTMS program. This output is what is used for the detection of the spectra, and the zero seen in the scan corresponds to the 2.5 MHz signal. A diagram of the microwave circuit is given in figure 5.2 [2].

5.4 The Fabry-Perot Cavity

5.4.1 The cavity and modes

The chamber where the species interacts with the radiation in ("the cavity") is a metallic enclosure of hollow space that can store electromagnetic radiation, for a range of wavelengths which fit the boundary conditions. This chamber is sealed in order to maintain vacuum. In our case, it is a tunable Fabry-Perot cavity [63] made up by two near-confocal curved aluminum mirrors, one of which carries the antenna in the centre, while the other is movable and carries the pulsed nozzle. The movable mirror is controlled by a stepper motor.

While there is a clear requirement for the experiment to be carried out in high vacuum (so only the spectrum of the species of interest is recorded and scattering of the sample introduced with molecules already in the cavity is minimised), using a Fabry-Perot cavity offers a number of extra advantages: The radiation is reflected back and forwards between the two mirrors, and

[3]Moreover, from the two possible image combinations, only one is enhanced-the one in phase with the original excitation. Therefore, the other, which is just noise, is dumped leading to better S/N.

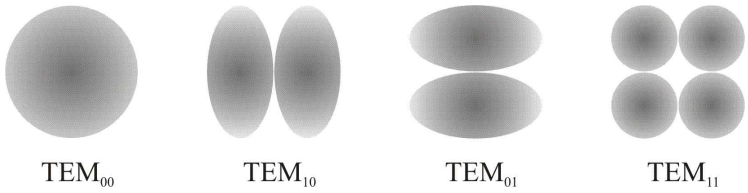

Figure 5.3: The four lowest TEM_{mnq} modes [2]

for a resonant frequency, the constructive interference amplifies the intensity. This way the cavity also acts as a band filter. Furthermore, due to the curvature of the mirrors, although the radiation will tend to diffuse as it propagates from the antenna, here it will remain focused in the middle, where also the supersonic expansion is more directional as well.

If a frequency is resonant in the cavity, the radiation will form a static wave called a mode. There are different transverse modes that may be constructed in the cavity, each of which can be characterised by the number of nodes is each direction. The number of nodes in the radial axis (the cavity axis) is noted as q, while the nodes on the plane perpendicular to that axis as m,n. The total Transverse Electromagnetic mode is written TEM_{mnq}. For a frequency to be resonant, it must form a TEM_{mnq} which satisfies:

$$\nu = \frac{c}{2d}\left(q + \frac{1}{\pi}(m+n+1)\arccos\left(1-\frac{d}{R}\right)\right) \tag{5.10}$$

where c is the speed of light, d is the inter-mirror distance and R the radius of curvature of each mirror. From the different TEM_{mnq} modes, the TEM_{00q} has the greatest power along the cavity axis, i.e. along the direction of the supersonic beam, and therefore this is selected for the experiments. The four lowest TEM_{mnq} modes are shown in figure 5.3 [2].

At exactly confocal arrangement ($d = R$) of the mirrors, nodes with the same value of $(q + \frac{m+n}{2})$ have the same resonant frequency and thus cannot be distinguished. For this reason the mirrors are held to close, but not exact confocal arrangement. In order to select the TEM_{00q}, pads of microwave absorbing foam are used. These are mounted on rotating plates in the corners of the cavity and may be moved in front of the mirrors and back progressively, while the cavity is under vacuum, from outside. By slowly introducing the pads, the intensity of different modes is reduced, but the higher the $m+n$ of the mode, the faster the reduction occurs as its high

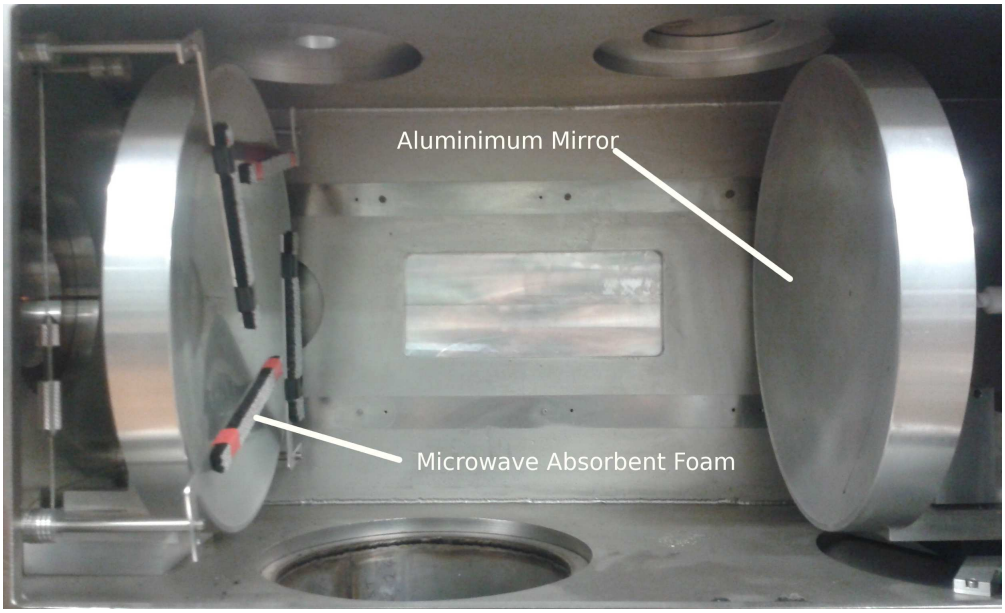

Figure 5.4: The cavity chamber

amplitude points move further from the cavity axis. Thus, the TEM_{00q} may be found by simply seeing which mode's intensity is reduced the slowest upon introducing the foams. The mirror curvature focuses the radiation closer to the centre of the cavity, which is also where most of the sample is located. One useful concept is that of the "beam waist": this is the boundary where the radiation field intensity equals to e^{-1} of its value on its axis of progression. The area where the beam waist is the narrowest is where the radiation is more intense. This typically lies along the centre of the cavity, which is also where the majority of the molecules released via the supersonic expansion are.

5.4.2 The pumping system

The chamber is kept under high vacuum by a pump combination system, consisting of a rotary and a diffusion pump. The diffusion pump has a pumping speed (volume of flow rate) of 2000 dm^3s^{-1}, while a rotary pump of 10 dm^3s^{-1}. The diffusion pump is placed right beneath the cavity and leads to an exhaust connected to the rotary pump. The combination of these two pumps gives a final pressure in the cavity of approximately $4-7\times10^{-5}$ mbar during operation, and even lower when no sample is introduced to the cavity. At these low pressures, a ion gauge is used to monitor the pressure.

The diffusion pump works by evaporating silicon oil which mixes with the gas sample, and then condenses by contact with the cooled walls of the pump. In order to avoid accidental exposure of the hot oil to high pressure (above 10^{-2} mbar), pressure gauges are linked to switches that automatically turn off the heating element if high pressure is detected. The specific diffusion pump used in our experiments is a 25 cm Edwards Diffestak 250/2000M model.

The role of the rotary pump is to both provide a low-pressure environment for the diffusion pump to work and as an exhaust. The rotary pump is a mechanical pump and therefore easy and safe to use. The rotary pump used is Leybold Trivac D40B model. The pressure detection in the cavity is done at the entrance of the rotary pump by Pirani gauges, which measure the thermal conductivity of a gas by tracking the resistance of a heated filament.

5.4.3 The energy storage

The energy coupled into the cavity decays with time, and the time required for a cavity ring down is approximately 300 ns to 1μs (when no attenuation is used). This is significantly faster than the free induction decay (FID) of the radiation given by the species as they relax after excitation, which is typically of the order of 50 μs. That difference is the window that allows us to collect the FID free of cavity ring down radiation. The energy of a specific frequency (ν) stored in the cavity at any one time may be quantified by the quality factor, Q:

$$Q = 2\pi\nu\frac{E_S}{E_L} = \frac{\nu}{\Delta\nu} \tag{5.11}$$

where E_S is the energy stored in the cavity and E_L is the energy lost per unit time. An alternative way of calculating Q is as the ratio of the frequency over the width of the frequency range to which the stored energy drops to half-maximum of its peak value (Full Width Half Maximum, FWHM), $\Delta\nu$. $\Delta\nu$ may be adjusted by moving the absorbent pads. The main pathways leading to energy loss are via:

The mirrors: This might be either due to imperfect reflection, which would cause a phase difference between the forward and reflected radiation, or due to diffraction from the

edges of the mirror if the wave is too large. The latter increases as the radiation wavelength become larger in lower frequencies, and when the sum $(n+m+q)$ of the TEM_{mnq} increases. Furthermore, the mirrors may themselves absorb part of the radiation.

The antenna: In every reflection, some of the radiation is coupled out of the cavity via the antenna. This unfortunately cannot be helped, as the antenna acts symmetrically.

A good, typical, Q value for the experiments run for this work is approximately 10^4. With an input power of the order of 100 milliwatts it is be possible to induce transitions from species with dipole moments as weak as 0.03 Debye.

5.4.4 The Helmholtz coils

In the case of open-shell molecules, the magnetic moment of the unpaired electron interacts with Earth's magnetic field, resulting in a splitting of the energy levels due to the Zeeman effect [1, 36]. These splittings are, at least in first instance, undesirable as they both complicate the spectra and cause the intensity of each transition to be split at different components. Also, if they are not resolved, they decrease the experimental accuracy by producing broader lines.

In order to counteract the Earth's magnetic field, a set of three mutually perpendicular pairs of square Helmholtz coils, which form a cage around the chamber have been arranged. The current passing through these coils is calibrated as to create a nearly uniform field-free environment for the experiment. Once a transition is detected, its Zeeman structure may contain useful information as well as help us assign it. For this reason, these coils can be switched off as well.

5.5 The Signal

5.5.1 Line shapes

The observed transitions are not infinitely sharp, but instead have a finite width, i.e. they span a range of frequencies. This range arises either from perturbation in the energy levels between

which the transition occurs, or due to the experimental conditions. The width of the transitions limits the precision of the experiment, but at the same time can be used to differentiate a true signal from noise. The factors that influence the line width are [15]:

Natural Line Width: This is due to the Heisenberg uncertainty principle, which requires that the product of the uncertainty of the lifetime of a state (Δt) times the uncertainty of its energy (ΔE) cannot be zero:

$$\Delta t \cdot \Delta E \geq \hbar \tag{5.12}$$

Since the Δt is the inverse of the Einstein coefficient for spontaneous emission, equation 5.12 can be solved for the uncertainty in terms of frequency:

$$\Delta \nu = \frac{\Delta E}{h} \approx \frac{1}{2\pi \Delta t}; \quad \Delta t = \frac{1}{A} = \frac{3\varepsilon_0 hc^3}{16\pi^3 \nu^3 |\mu_{ul}|^2} \tag{5.13}$$

$$\Delta \nu \approx \frac{8\pi^2 \nu^3 |\mu_{ul}|^2}{3\varepsilon_0 hc^3} \approx 1.66 \times 10^{20} \nu^3 |\mu_{ul}|^2 \tag{5.14}$$

For microwave transitions, $\Delta\nu$ is of the order of 10^{-9} Hz. However, in coherent experiments, this must be multiplied by the number of coherent emitters, which can be 10^{12} per gas pulse. This gives a limit of about 1 kHz to the possible precision of this kind of experiment.

Pressure Broadening: Collisions between the molecules can be inelastic or elastic. In the case of elastic collisions, the rotating molecule emerges with the same energy, but due to this short interaction, its wavefunction may have changed phase. Although the emitted radiation in this case is as strong as if no collision had occurred, the phase change introduces slightly different frequencies. In the case of an inelastic collision, a radiation-less transition may occur which would limit the lifetime of the excited state. Also, even if molecules do not collide, intermolecular forces might lead to perturbations of the states. These effects lead to a greater line width and increase with pressure. However, in the experiments examined here, the spectroscopy occurs in an almost collision-free zone and therefore this effect is also negligible.

Doppler Broadening: Depending on whether the species is moving towards or away from the microwave radiation, this creates an opposite Doppler effect on the emitted radiation. The Doppler shift is $\pm\nu\,(v/c)$, where ν is the resonant frequency, v is the speed of the species and c is the speed of light. This results in two oppositely shifted frequencies being detected instead of one, with the true transition frequency being in their geometrical mean. Also, as there is a speed distribution with respect to the antenna in both directions, this increases the line width. The frequency observed (f) is:

$$f = \frac{\nu}{1+\frac{v}{c}} \tag{5.15}$$

For a gas at thermal equilibrium, the Doppler broadening $\Delta\nu$ (full width at half maximum) is:

$$\Delta\nu = 7.15\times10^{-7}\nu\sqrt{\frac{T}{M}} \tag{5.16}$$

where T is the temperature and M is the relative molecular mass of the species. The Doppler broadening is the main effect contributing to line width in our experiments and usually results in a spread of 4-10 kHz. However, having the antenna positioned coaxially to the nozzle leads to symmetric Doppler doublets. This way, the geometrical mean can usually be calculated at better precision than the line width.

Instrumental Effects: These are due to the use of the experimental apparatus. One such effect is the collision with the cavity walls, which would also contribute to the line width in low enough pressures that the mean free path of the species is greater than the length of the cavity. Moreover, the microwave synthesizer has an inherent systematic instability. Yet, both of these effects are not expected to contribute significantly[4] in our experiments.

Residual Structure: Various other weak interactions can exist and thus perturb the energy levels, thus resulting in slightly shifted transition frequencies. Examples of these might be tunnelling motions between conformational minima, or large amplitude motions. Moreover, very small hyperfine splittings might not be resolvable thus different lines may

[4]For example, the Wiltron 6769B microwave synthesiser used in one of the experiments has a stability accuracy of 0.0025 Hz, and therefore is beyond the experimental accuracy.

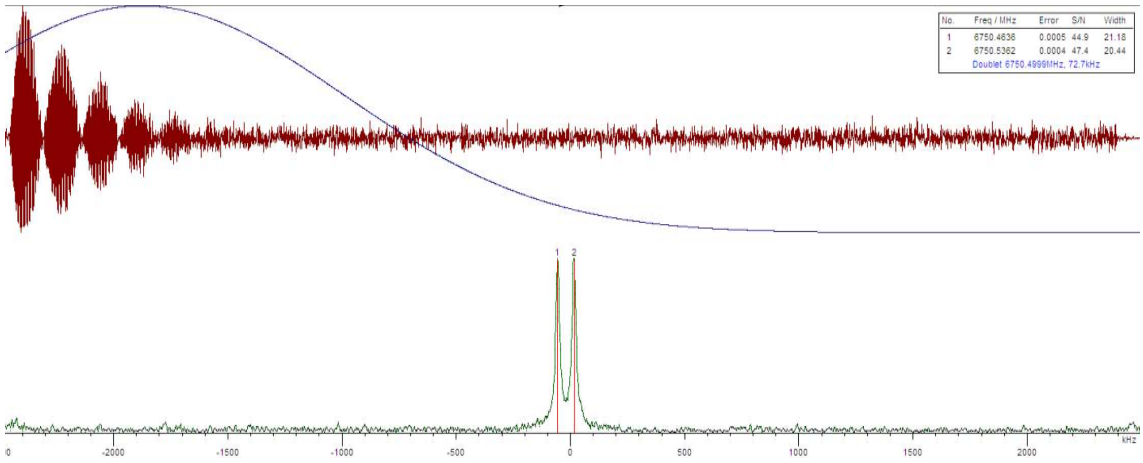

Figure 5.5: An example FID in the time and frequency domain

merge to give a broader one. Finally, any kind of Zeeman splitting for open-shell complexes will depend on the homogeneity of the field and a slightly inhomogeneous (or very small) field could lead to broader lines.

5.5.2 Free Induction Decay

As has been mentioned in already, the signal actually recorded from the microwave circuit is the decaying radiation from the emission of the species, called the free induction decay (FID). A characteristic FID signal is shown in figure 5.5, both as recorded and after it has been Fourier transformed. There, the Doppler broadening might be seen by the circular patterns of the signal.

This signal is then transformed from the time domain to the frequency domain via a Fourier transformation. This represents the time-signal as linear combination of sine and cosine waves. Thus, if the time-domain function is assumed to be $g(t)$ and the frequency domain function is written as $f(\nu)$, then the two may be related as:

$$f(\nu) = \int_{-\infty}^{\infty} g(t)\, e^{-i2\pi t\nu}\, dt \tag{5.17}$$

This is performed by the FTMS program [62], using a Fast Fourier Transform algorithm developed by Tukey and Cooley [65].

5.6 Running the Experiment

Now that all the individual parts of the experiment have been explained, it is time to put them all together and explore any final considerations about the running of the experiment.

5.6.1 Tuning the cavity

As it was mentioned briefly earlier, the cavity tuning is achieved by using the FTMS program and the crystal detector, where approximately 10% of the signal ends. To find the cavity modes a swept frequency is generated from the synthesizer, ranging $\pm$200 MHz from the target frequency. Any frequencies that are not resonant in the cavity are simply reflected back via the antenna, while the resonant frequencies form standing waves. Through the crystal detector, the power output is monitored and sharp dips are noted when the resonant conditions are met. This process is referred to as "tuning the cavity".

When a larger scan (of many sequential frequencies) is performed, the first step is a manual tuning at the initial frequency. Then the maximum depth of the dip against the background "minimum" is taken and then the motor moves the mirrors stepwise every time the measurement for one frequency is completed until a fixed percentage of that depth (usually around 70%) is exceeded in the new frequency.

5.6.2 Timing sequence

Each data collection is controlled by the FTMS program, through a multifunctional card (Amplicon PCI-30). Two digital bits are sent simultaneously, one to the valve pulser to release the gas and the other to the first microwave switch to let through the radiation into the cavity. The radiation is actually released about 750 μs after the gas pulse, to allow for the nozzle to open (about 500 μs) and for the sample to reach the collision-free zone.

The first microwave switch remains open for 1-2 μs, and immediately after it closes, the second one opens as to allow the FID of the sample to reach the detector. This second switch

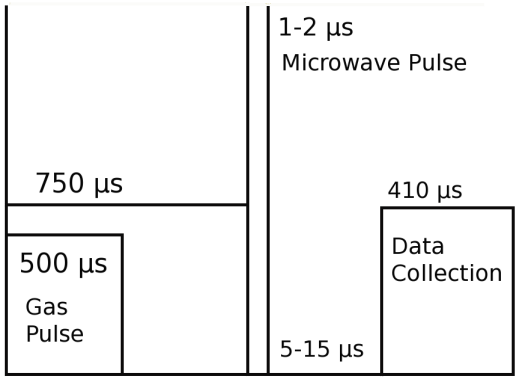

Figure 5.6: The timing sequence of running the experiment (schematic)

remains closed for 5-15 μs, to allow for a complete cavity ring-down, and after that the signal is digitised. During 409.6 μs[5], a total number of 4096 points are collected and transferred to the computer. The timing in the microwave components is coordinated by a series of hardware boxes, and is illustrated in figure 5.6.

Due to the pumping speed, at most 20 gas pulses can be released into the cavity per second, which means a minimum interval of 50 ms between scans. During that time, background scans (exactly the same as the normal scans but with no sample in the cavity) are performed. These scans are then subtracted from the normal scans. This way any systematic noise is subtracted from the signal. Ten background scans are performed between each foreground scan.

[5]This is longer than the emission duration so there is no danger of loss of data.

Chapter 6

The Rotational Spectrum of Tertiary-Butyl Acetate

"*You kind of alluded to it in your introduction. I mean, for the last 300 or so years, the exact sciences have been dominated by what is really a good idea, which is the idea that one can describe the natural world using mathematical equations.*"

- Stephen Wolfram

6.1 Introduction

In this chapter, the work done recording and analysing the rotational spectrum of tertiary-butyl acetate (TBAc) is presented. Tert-butyl acetate is an intriguing molecule to study as it has various possible conformations, arising from different orientation of the t-butyl group with respect to the ester group, and from different orientations of the four methyl groups it contains. Moreover, each one of these methyl groups, as well as the whole t-butyl group may also exhibit large amplitude motion, such as internal rotation in the molecule. For this reason, each conformer's energy levels would be split in either *A* and *E* tunnelling states due to the methyl internal rotor, as explained in chapter 2.

Moreover, both the t-butyl cation and the acetate anions are stable radicals, so potentially the $C_5H_9O_2$-CH_3 bond could elongate and/or weaken which would allow even greater internal rotation and would lower the barrier height compared to what would be expected it the molecule was rigid. All these effects are interesting to investigate as we take the first step away from the rigid rotor picture, and at the same time they provide a rich spectrum which itself is challenging to interpret.

There are many aspects to this work, which are presented in the following order: Initially, the *ab initio* studies performed as part of the investigation are presented. This enabled us to get a first approximation on the equilibrium structure of the molecule and its rotational constants. Using them as a guide, the high-resolution microwave spectrum of the tert-butyl acetate molecule was recorded experimentally. At the same time, by analysing the recorded transitions, we were able to obtain information on the rotational constants of each state and therefore predict the frequencies of yet unseen transitions.

This led to an iterative process where increasingly weaker transitions were recorded and assigned, while obtaining a more and more precise information on the internal rotation states. The final assignment obtained for each state, as well as a simultaneous assignment for all states, is presented in the section after the experimental details.

Finally, a discussion of the assignment is presented. It has been possible to determine the barrier height and the expectation value of the angle between the methyl group internal axis and the molecule's principle axis. These are also then compared with the corresponding values in similar molecules.

6.2 The Experimental Investigation

All experiments were carried out using Fourier transform microwave spectrometers with a supersonic pulsed nozzle. Details of this experiment were provided in chapter 5 so here we only concentrate on how this setup was optimised for recording the spectra of this specific molecule.

TBAc is a liquid at room temperature so in order to introduce the sample to the cavity a bubbler was used. The carrier gas chosen was helium and this was bubbled through TBAc with backing pressure of 1 atm. The container of TBAc was cooled down to approximately 3° C. Helium was chosen for carrier gas as it is not very effective in cooling rotational states. This produced a rich spectrum as many rotational levels were still populated at the time the molecules interacted with the microwave radiation.

An initial scan was performed at the full frequency range between 5.5 and 16.5 GHz, with 500 shots. Following that, various regions were then rescanned with up to 5000 shots in order to improve the signal to noise (S/N) ratio of the weaker transitions. The frequency steps taken were approximately of 0.5 MHz and adjacent spectra were merged to further improve the S/N.

In total, more than 700 transitions with the appropriate Doppler splitting were recorded, the complete list of which is given in the CD attached to this thesis. For most of the transitions the S/N was less than 10, even at 5000 shots, yet there were notable exceptions with S/N greater than 350 at 500 shots. These were used as an initial guide to assign the spectrum.

6.3 *Ab Initio* Calculation

As was mentioned in section 6.1, there are various conformations that the molecule may be found in. Through the use of *ab initio* calculations we are able to find which ones are the most stable. Moreover, part of the output of these calculations were the rotational constants for the various conformers, which could then be compared with the most intense of the observed transitions. Furthermore, the dipole moment expectation value for the ground state in each of the three principle axes is given. Starting with chemical intuition, four different conformers were chosen as candidates to be the most stable. These are shown in figure 6.1.

These were then set as the starting points for energy optimisation calculations. The computational program Gaussian 03 [66] was used for this task and the method initially used was Restricted Hartree-Fock as a self-consistent field method combined with MP2 theory for elec-

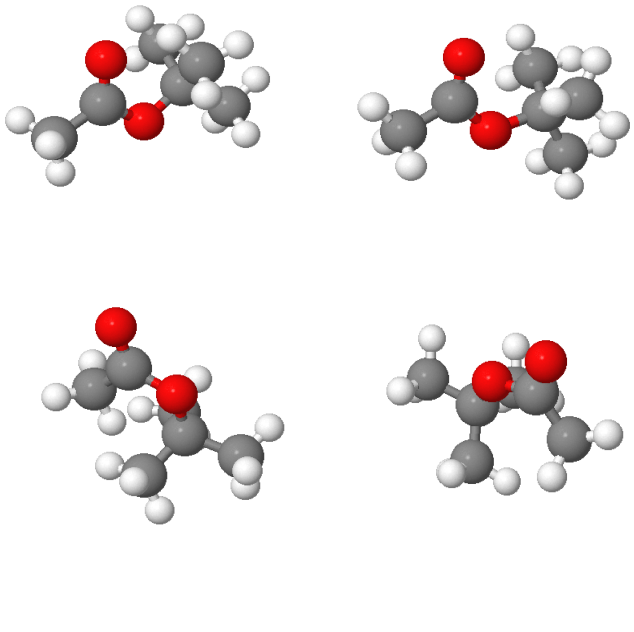

Figure 6.1: The four initial guess geometries used in the energy optimisation *ab initio* calculations

tron correlation[1]. The basis set used has only been introduced briefly so far in chapter 4, and it was a Pople basis set.

In Pople basis sets, Gaussian Type Orbitals (GTOs) are fitted to the, more physically accurate, Slater Type Orbitals (STOs). The basis sets are named as

$$k-nlmG$$

where all k,n,l and m are integers. The numbers in the name of the basis set designate the number of Primitive GTOs (PGTOs) used to represent a STO. This is a split valence basis and, moving from left to right, we move from the core to outer orbitals: k is number of PGTOs used to describe the core orbitals. If only nl are shown, then a single split valence is used, and if all nml is shown then a doubly spin valence is used. G is simply indicating the use of GTOs.

In our calculation we used $6-311G(d,p)$ basis. This means that 6 PGTOs were contracted

[1] A subtle but important point is that the electron density from the MP2 method was used for the dipole moment calculation.

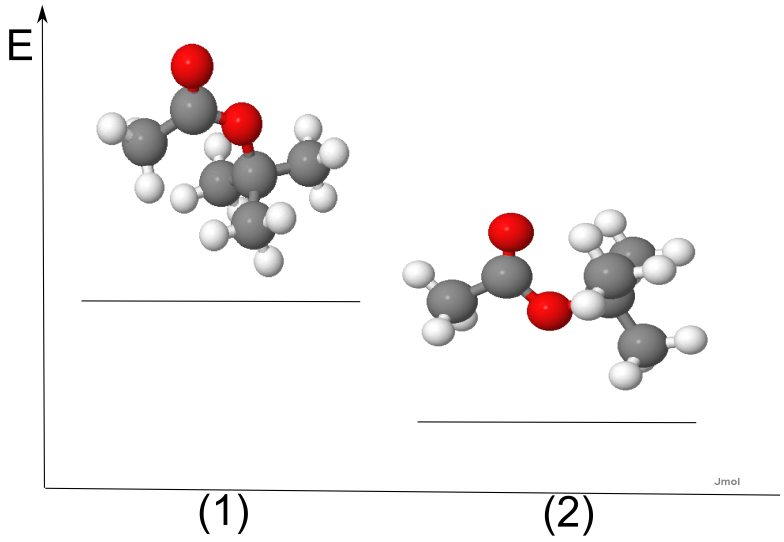

Figure 6.2: The two lowest energy conformers of TBAc.

to represent the core orbitals, and the valence shells are represented by three functions formed by the contraction of 3, 1 and 1 PGTO respectively. Each construction gives rise to a single function, a Contracted Gaussian Type Orbital (CGTO), and therefore, in our basis sets, three different CGTOs were used to describe the valence orbitals. Moreover, the letters in the parenthesis after the name indicate that polarisation functions were also added to the basis, in this case a p- and a d-type orbital analogues[2].

Through the energy optimisation calculation, the four structures shown in figure 6.1, converged to the two shown in figure 6.2. The rotational constants and dipole moments along the principle axes of these are given in table 6.1. From table 6.1, we can see that both of these conformers are very close to a prolate symmetric top. Therefore, to a first approximation, the a-type transitions are expected to be located at frequency $(B+C)J$, where J is the rotational quantum number of the final state.

The result that conformer (2) is the lowest in energy is in agreement with chemical intuition as the steric factors are minimised. Their energy difference is 0.01833 Hartrees which significantly more than room temperature (approximately 0.000943 Hartrees), so only this is expected

[2]In general, one could use a $(k-nlm+G)$ or $(k-nlm{+}{+}G)$ basis. The $(+)$ signs indicates the use of diffuse functions (s- and p-orbitals) as well. One $+$ signifies that diffuse functions were added to the heavy atoms, while $(++)$ indicates that diffuse functions were also added to the hydrogen atoms. However this was not deemed necessary as we were not looking for intermolecular forces but rather the monomer structure.

Table 6.1: *Ab initio* results for the energy, rotational constants and dipole moments of the two lowest energy conformers of TBAc

Conformer	1	2
HF Energy /Hartrees	-384.0227912	-384.0433603
MP2 Energy /Hartrees	-385.3143977	-385.3327311
A / MHz	3179.6	3299.7
B / MHz	1434.6	1451.7
C / MHz	1279.2	1310.4
μ_a /Debye	2.76	0.75
μ_b /Debye	3.18	1.44
μ_c /Debye	0.24	0.00

to be populated in our experiments. Also, since this conformer has no permanent dipole moment along its c principle axis, any $c-$type transition would be forbidden and thus negligibly weak.

6.4 Spectral Assignment and Analysis

Initially, the $(B+C)$ rotational constant sum from the *ab initio* calculations was used to make a rough prediction of the expected spectrum. At this stage we ignored any internal rotation or b-type transitions, and only concentrated on the strongest ones, to simplify the assignment. By examining the transitions close to the predicted values, we were able to assign a basic a-type spectrum. From there on there was an iterative procedure of assignment/prediction, which yielded converged values for rotational constants and centrifugal distortion constants, down to quartic terms.

The Hamiltonian used for assigning the spectrum was Watson's S-reduced Hamiltonian including up to the sextic terms centrifugal distortion. This is given if one substitutes equa-

tions 2.41, 2.43 and 2.44 into equation 2.45:

$$\begin{aligned}\hat{H}_{rot-s} &= A\hat{J}_A^2 + \frac{1}{2}(B+C)\left(\hat{J}^2 - \hat{J}_A^2\right) + \frac{1}{4}(B-C)\left(\hat{J}_+^2 - \hat{J}_-^2\right) - D_J\hat{J}^4 \\ &\quad -D_{JK}\hat{J}^2\hat{J}_A^2 - D_K\hat{J}_A^4 - d_1\hat{J}^2\left(\hat{J}_+^2 + \hat{J}_-^2\right) - d_2\left(\hat{J}_+^4 + \hat{J}_-^4\right) \\ &\quad +H_J\hat{J}^6 + H_{JK}\hat{J}^4\hat{J}_A^2 + H_{KJ}\hat{J}^2\hat{J}_A^4 + H_K\hat{J}_A^6 \\ &\quad +h_1\hat{J}^4\left(\hat{J}_+^2 + \hat{J}_-^2\right) + h_2\hat{J}^2\left(\hat{J}_+^4 + \hat{J}_-^4\right) + h_3\left(\hat{J}_+^6 + \hat{J}_-^6\right) \end{aligned} \quad (6.1)$$

The programs used for the least squares fitting of the Hamiltonian parameters and for predicting the spectra (and the relative transition intensities) were Picketts' SPFIT and SPCAT respectively [22, 23]. Although in practice the lines were determined with an accuracy close to 1 kHz, a conventional 5 kHz experimental uncertainty was assumed. At the end more than 60 lines, including both *a*-type and *b*-type transitions, were assigned at this point.

The next stage was to consider the effects of internal rotation. From the literature [25], it was known that the rotation of the tert-butyl group would have a high barrier (indicatively, in ethyl pivalate the analogous barrier was measured [67] to be 1302 cm^{-1}), and given the molecular mass of the methyl groups, tunnelling of whole CH_3- group was considered unlikely.

Instead, we concentrated at what was the most likely rotation to occur, i.e. of the hydrogen atoms in the acetate methyl group. According to the theory presented in chapter 2, the effect of internal rotation is to lower the rotational constant of the molecule, through the Coriolis contribution. We noted that there was a similar pattern to the one we had assigned a few MHz lower in energy, and therefore we could say that the spectrum we had been working on belonged to the *A* state, while the one lower in energy to the *E* state. Next, the *E* state spectrum was assigned independently, again down to sextic centrifugal distortion constants.

One big difference between the two states is that the *E* state, in contrast to the *A* state, has a non-zero angular momentum around the internal rotor. Following the theory outlined in chapter 2, we can express the total Hamiltonian as a sum of the contributions from the frame ($\hat{H}_{frame}$),

the internal rotor (torsional Hamiltonian: $\hat{H}_{tor}$) and the Coriolis interactions ($\hat{H}_{Cor}$):

$$\hat{H}_{rot,int} = \hat{H}_{frame} + \hat{H}_{tor} + \hat{H}_{Cor} \tag{6.2}$$

As was outlined in the same chapter, accounting for the effect of $\hat{H}_{Cor}$ through perturbation theory yields the first order correction:

$$\langle 0|\hat{H}_{Cor}|0\rangle = \underbrace{-2A_f\lambda_a\langle 0|\hat{l}|0\rangle}_{D_a}\hat{J}_a - \underbrace{2B_f\lambda_b\langle 0|\hat{l}|0\rangle}_{D_b}\hat{J}_b - \underbrace{2C_f\lambda_c\langle 0|\hat{l}|0\rangle}_{D_c}\hat{J}_c \tag{6.3}$$

where $\hat{l}$ is the internal rotor angular momentum, λ_i is the directional cosine between the i principle axis of the molecule and the internal rotor's unique axis and $|0\rangle$ is the tunnelling ground state. The parameters here noted as D_a, D_b and D_c may also be fitted to experimental data, although in our case D_c is zero by symmetry. The second order perturbation theory correction is given by equation 2.61, and its effect may be absorbed into the rotation constants.

At third order perturbation theory, the correction around the a axis is a correction to the D_a constant due to higher order effects:

$$W_A^3 = -\left[\underbrace{\left(D_a^a - \frac{D_a^b + D_a^c}{2}\right)}_{D_a^K}\hat{J}_a^2 + \underbrace{\left(\frac{D_a^b + D_a^c}{2}\right)}_{D_a^J}\hat{J}^2 + \underbrace{\left(\frac{D_a^b - D_a^c}{4}\right)}_{D_a^1}\left(\hat{J}_+^2 + \hat{J}_-^2\right)\right]\hat{J}_a \tag{6.4}$$

and analogous expressions hold for the b and c axis, with constants (D_b^K, D_b^J) and (D_c^K, D_c^J) respectively. Therefore these terms may also be used in the fit.

These extra terms allowed more degrees of freedom in the fitting of the E with respect to the A state, which led to more lines being fitted. At this final stage, we managed to assign 180 lines for the E state and 138 lines for the A state. The error for the E state fit was 3.18 kHz and for the A state 2.49 kHz, respectively. In table 6.2 the molecular constants for each state are given, with the uncertainty quoted as one standard deviation with respect to the last decimal place, in parenthesis. The H_{JK}, H_J and H_K parameters for the A state are put into square brackets since they have not been satisfactorily determined. Two features stand out instantly from table 6.2:

Table 6.2: Experimental constants for each of the two states, fitted individually

	A State	*E* State
A /MHz	3308.38267(52)	3293.87829(40)
B /MHz	1442.68871(18)	1441.430087(152)
C /MHz	1304.06472(18)	1304.092928(149)
D_{JK} /kHz	0.7530(56)	0.4340(55)
D_J /kHz	0.0916(33)	0.08750(260)
D_K /kHz	0.434(56)	0.784(35)
d_1 /kHz	-0.007684(92)	0.006486(77)
d_2 /kHz	0.007140(26)	0.008863(32)
H_J /Hz	[-0.0332(172)]	-0.0691(125)
H_{JK} /Hz	[0.0061(192)]	0.107(179)
H_{KJ} /Hz	-0.907(244)	-1.286(270)
H_K /Hz	[-2.46(226)]	-6.07(135)
D_a /MHz		498.40726(43)
D_b /MHz		153.84427(118)
D_a^K /MHz		-0.1053917(308)
D_a^J /MHz		-0.0159829(41)
D_b^K /MHz		-0.14642(50)
D_b^J /kHz		-2.8585(74)

The first is the similarity of the C rotational constant between the two states, which indicates that even with internal rotation the molecule maintains its axis of symmetry on the A/B plane. This means that the expectation value of the angular momentum of the internal rotor around this axis is zero (averages out over the two directions), which simplifies the analytical expressions of the centrifugal distortion terms, and sets some of them automatically to zero.

The second is the difference between the remaining centrifugal distortion terms between the two states. Since most of the effects are included in constants present exclusively for the E state and the rotational constants, any remaining effects would be of third order or beyond (in perturbation theory terms). However, this is not what was observed, and it is believed that many of these terms are practically fitting parameters rather than representing their exact physical equivalent.

To improve this situation, a third fitting was made, this time including both states at the same time. This was possible by assigning the A as the ground and the E as the first excited vibrational state. This is valid as a hindered internal rotation is formally a vibration. Now,

Table 6.3: Global fit experimental parameters

	Common Terms	*A* State	*E* State
A /MHz		3308.3806(11)	3293.8983(11)
B /MHz		1442.68815(28)	1441.43012(29)
C /MHz		1304.06433(29)	1304.09096(28)
D_{JK} /kHz	0.405(43)		
D_J /kHz	0.0913(68)		
D_K /kHz	2.05(13)		
d_1 /kHz	-0.00773(84)		
d_2 /kHz	0.00789(37)		
H_J /Hz	[0.018(51)]		
H_{JK} /Hz	-1.67(27)		
H_{KJ} /Hz	-16.0(26)		
H_K /Hz	152.1(91)		
D_a/MHz			498.4075(12)
D_b /MHz			-153.8510(32)
D_A^K /MHz			-0.10545(10)
D_A^J /MHz			-0.016068(31)
D_B^K /MHz			0.1903(49)
D_B^J /kHz			0.00439(15)

all the centrifugal distortion constants were forced to be the same for the two states, while the rotational constants were fitted for each state individually. The terms corresponding to the perturbation due to the Coriolis terms were fitted to the *E* state only. This time, only 156 lines were fitted before the accuracy of the fit was reduced. However, this final fit is expected to have the greatest physical significance and is given in table 6.3. Now the above constants may be used to characterise both states of the molecules and all (but H_J) are well-determined. The final error of this fit was 0.0182 MHz. The fitted lines are also given in the CD attached to this thesis.

6.5 Internal Rotation Analysis

Once we had these constants, we were able to describe the molecule in both states. Then, we could take a more analytical approach to investigate the internal rotation by including the $\hat{H}_{tor}$ effects.

As the *C* rotational constant is virtually the same in both states, the difference between the

two numbers may be attributed to second order corrections due to the Coriolis perturbation. Thus, we can logically assume that the unique axis of the methyl group lies on the plane created by the *AB* principle axis of the molecule and there is virtually no contribution of the internal rotation angular momentum around the *c*-axis ($\lambda_c = 0$). This simplifies the expressions for the directional cosines, which are used in equation 6.3:

$$\lambda_A \rightarrow \sin\tau \qquad \lambda_B \rightarrow \cos\tau$$

where τ is the torsional angle. Therefore, from equation 6.3:

$$\frac{D_a}{D_b} = \frac{2A_f\lambda_A\langle 0|\hat{l}|0\rangle}{2B_f\lambda_B\langle 0|\hat{l}|0\rangle} = \frac{A_f}{B_f}\tan\tau \tag{6.5}$$

Also:

$$\lambda_a\langle 0|\hat{l}|0\rangle = \frac{D_a}{2A_f} \quad \lambda_b\langle 0|\hat{l}|0\rangle = \frac{D_b}{2B_f} \tag{6.6}$$

So, if the frame rotational constants are known, it is possible to calculate the torsional angle and the expectation value of the torsional angular momentum. Taking into account only the second order perturbation theory correction to the rotational constants, the *A* rotational constant of either (*A* or *E*) state equals:

$$A = A_f - 4A_f^2\lambda_A^2\sum_{n\neq 0}\frac{\langle 0|\hat{l}|n\rangle\langle n|\hat{l}|0\rangle}{E_n - E_0} \tag{6.7}$$

If we approximate that the molecule is rigid, the rigid molecule rotational constants would be given by A_{av} and B_{av}:

$$A_{av} = \frac{A_{Astate} + 2A_{Estate}}{3} \quad B_{av} = \frac{B_{Astate} + 2B_{Estate}}{3} \tag{6.8}$$

A_{av} and B_{av} differ from A_f and B_f by the contribution of the internal rotor (methyl group). This is easier to show, if instead of the rotational constants, we consider the corresponding moments

of inertia. Thus, around the a-axis:

$$I_{A,f} = I_{A,av} - I_{tor}\lambda_a \tag{6.9}$$

where $I_{A,f}$ is the frame moment of inertia around the a-axis, $I_{A,av}$ is the corresponding averaged rotational constant and I_{tor} is the rotational constant of the methyl group.

The obvious problem in using equation 6.7, is that we do not know the matrix elements $\langle 0|\hat{l}|n\rangle$ or the energy difference between the ground and excited states. However, if we had a value for b_{eff} and V we could calculate the required eigenfunctions and eigenvectors by diagonalising the torsional Hamiltonian:

$$\hat{H}_{tors} = b_{eff}\hat{l}^2 + \hat{V}(\tau) \tag{6.10}$$

where $\hat{V}(\tau)$ is the torsional potential, and the $|n\rangle$ states can be taken as the eigenstates of the torsional Hamiltonian. The potential function may be taken to have, to a first approximation, a V_3 shape:

$$\hat{V}(\tau) \approx \frac{1}{2}V_3\,(1-\cos 3\tau) \tag{6.11}$$

Since the A and E states do not mix, we can evaluate the terms of the torsional Hamiltonian for each state individually, by constructing and diagonalising the corresponding Hamiltonian matrices. Moreover, we can use the projection of the internal angular momentum operator ($\hat{l}$) onto the internal rotor unique axis (m) to construct the eigenstates for the Hamiltonian: For the A state, m is zero or multiples of three, while the rest of the m values correspond to an E state. Therefore, we can write the A state matrix elements for our basis functions $|i\rangle$ as:

$$|i\rangle = |m = i*3\rangle + |m = -(i*3)\rangle \tag{6.12}$$

where i here may only take positive values or zero. For the E state, the basis set may be written as:

$$|i\rangle = |m = i*3+1\rangle \tag{6.13}$$

And now i can take both positive and negative values. The Hamiltonian matrix elements in both cases are:

$$\langle i|\hat{H}_{tors}|i\rangle = b_{eff}m^2 + \frac{V_3}{2} \tag{6.14}$$

$$\langle i|\hat{H}_{tors}|i\pm 1\rangle = -\frac{V_3}{4} \tag{6.15}$$

While the value of b_{eff} is not known, this is related to the rotational constant of the methyl group, for which we can take the literature value [25] $b_0 = 153,460$ MHz, by:

$$b_{eff} = b_0 + A_f\lambda_A^2 + B_f\lambda_B^2 \tag{6.16}$$

So we have four rotational constants (A and B for the A and E state) plus fitted values of D_a and D_c, and we need to find the frame rotational constants (A_f and B_f), as well as the angle τ and the barrier height to internal rotation V_3. The way to solve this problem is by a many step iterative procedure, starting with the assumption that $b_{eff} \approx b_0$. Thus, if we start with the initial value $b_{eff} = b_0$, then $A_f = A_{av}$ and $B_f = B_{av}$, which allows one to calculate a first guess of τ and $\langle 0|\hat{l}|0\rangle$. Next, we use the values of τ and $\langle 0|\hat{l}|0\rangle$ to calculate a new value for b_{eff}. Through this iteration we obtained a better value of b_{eff}.

By also assuming an initial value of V_3, we were able construct and diagolise the torsional Hamiltonian, and the eigenstates and eigenvalues calculated were used to calculate $\langle 0|\hat{l}|0\rangle$ and the rotational constants of the A and E states (using also A_f) via equation 6.7. The V_3 value was then iteratively refined until all results were consistent. The torsional Hamiltonian was set up and diagonalised using Microsoft Excel. The basis set used for E state were $-38 \leq m \leq 37$, avoiding any m value that was a multiple of three, and for the A state, $0 \leq |m| \leq 39$ in steps of $|m| = 3$. The final values obtained are given in the table 6.4.

Finally, we saw the limits of the accuracy of our results by trying to reproduce the experimentally fitted D_a^K, D_a^J, D_b^K and D_b^J values from the third order perturbation theory corrections using the calculated torsional Hamiltonian eigenvectors. However this time the agreement was not good, and one explanation could be that our description of the potential as a simple V_3

Table 6.4: The frame rotational constants, V_3 barrier to rotation and torsional angle for TBAc

A_f /MHz	3346.18
B_f /MHz	1446.41
V_3/ cm^{-1}	110.690
τ /Degrees	35

function (i.e. ignoring the higher terms, such as V_6) is insufficient.

6.6 Conclusion

We have successfully recorded and analysed the spectrum for the ground (A) and the first excited (E) rotational state of TBAc. The full frequency range from 5.5 GHz to 16.5 GHz was scanned which yielded a large number of transitions.

The spectrum was analysed both in terms of rotational and centrifugal distortion constants and in terms of the quantum effects these represent. In the former approach, the constants for both states were fitted individually and at the same time with very low error. The fitting accounted for all the strongest lines in the spectrum.

Through the latter approach, the expectation value of the torsional angle and the barrier of the methyl group rotation were determined, by assuming a V_3 potential. It is interesting to compare our value (110.690 cm^{-1}) with the value determined for acetic acid [68] (168 cm^{-1}), for methyl acetate [69] (99.6 cm^{-1}) and for ethyl acetate [70] (101.6 cm^{-1}). It seems that the bonding in acetic acid is very strong, creating a very high barrier to internal rotation. After that the barrier to rotation seems to drop sharply in methyl acetate and then, as expected, to slowly rise with increasing steric hindrance. Therefore our value seems to agree with the general trend. It would be interesting to conduct an analogous experiment to isopropyl acetate [71] to determine the trend more precisely.

Finally, now we can assess the accuracy of the *ab initio* calculations used against the averaged values of the rotational constants. For the A rotational constant the difference is only

0.982 MHz, while for the $(B-C)$ value, the difference is 3.47 MHz. The errors may be attributed to basis set incompleteness and errors in the MP2 method, but clearly the results can be used to predict and assign the spectrum satisfactorily. Upon completing this project, we discovered that researchers in the Prof. Stahl group from the University of Aachen, Germany, had also been working on the same topic and we are currently preparing a common manuscript for publication.

Chapter 7

Intermolecular Forces and Potentials

"*The reality we can put into words is never reality itself.*"

- Werner Heisenberg

7.1 Introduction

The importance of intermolecular forces in nature would be hard to overestimate. The existence of any state of matter other than plasma and ideal gas happens due to interactions amongst atoms and molecules, which are here collectively referred to as intermolecular forces. Over the years, there have been very different approaches to describing these forces, owing to the fact that their effect is significant from an atomic scale (causing the potential between two atoms as they approach each other) to polymers and macromolecules (for example influencing their viscosity). Since here we are more interested in the former order of magnitude than the latter, the approach taken in this work is more analytical. The aim of our study of intermolecular forces is to be able to construct a potential function that can represent the Potential Energy Surface (PES) of the system studied.

Intermolecular forces are traditionally distinguished between short and long range forces [72]. The former can be represented as a negative exponential function of the distance while the latter as a negative inverse power of the distance. The easiest way to define

mathematically the intermolecular potential between molecules A and B is to write the energy of the system $W(A,B)$ as:

$$W(A,B) = W_A + W_B + U_{AB} \tag{7.1}$$

where W_i is the energy of the i-th molecule when in isolation and U_{AB} is their pair potential. For a three member system this becomes:

$$W(A,B,C) = W_A + W_B + W_C + U_{AB} + U_{AC} + U_{BC} + \underbrace{U_{ABC}}_{\text{Three-body correction}} \tag{7.2}$$

Forces are said to be pairwise additive if the three-body, or higher order, corrections can be ignored for the level of precision desired. Then the energy of a system of more than two bodies can be calculated as the sum of the two-body interactions. Also it should be noted that in the following discussion the internal coordinates of the species will be considered constant, as will their properties, although strictly speaking this is not correct. Moreover, to keep with the formulation used in the rest of this work, the spherical tensor representation of the intermolecular forces theory is mainly used.

7.2 Electrostatic Interactions Between Molecules

One way to consider the electrostatic interaction between molecules is to imagine the interaction as that of molecule A responding to the field created by molecule B, and vice versa.

7.2.1 Molecules in electric fields

If we consider a molecule A in an external potential, $V(\mathbf{r})$, then we can express that potential as a Taylor series between the origin of that potential and its distance from A [72, 3]:

$$V(\mathbf{r}) = V(0) + r_\alpha V_\alpha(0) + \frac{1}{2} r_\alpha r_\beta V_{\alpha,\beta}(0) + \ldots \tag{7.3}$$

where $V(0)$ is the potential at its origin, r_i is the distance between the origin of the potential and molecule A along axis i and

$$V_{\alpha,\beta,\ldots} = \left(\frac{\partial}{\partial r_\alpha}\frac{\partial}{\partial r_\beta}\ldots\right)V(0) \tag{7.4}$$

The Hamiltonian for a molecule in a field can be written in analogy to classical mechanics:

$$\widehat{H}_{es} = \sum_a e_a \widehat{V}(r_\alpha) \tag{7.5}$$

where the sum is taken over all nuclei and electrons of the molecule A and e_a is the charge of the corresponding particle interacting with the potential. Recognizing $\sum_a e_a$ as the charge (zeroth moment), $\sum_a e_a r_a$ is the dipole moment (first moment) and so on, this can be written as:

$$\widehat{H}_{es} = qV(0) + \widehat{\mu}_\alpha V_\alpha + \frac{1}{3}\widehat{\Theta}_{\alpha\beta}V_{\alpha\beta} + \ldots + \frac{1}{2n-1}\widehat{\xi}^n_{\alpha\beta\ldots\nu}V_{\alpha\beta\ldots\nu} \tag{7.6}$$

where $V_\alpha = r_a V_\alpha(0)$ and $\widehat{\xi}^n$ is the 2^n-pole moment:

$$\widehat{\xi}^n_{\alpha\beta\ldots\nu} = \frac{-1^\nu}{n!}\sum_a e_a r_a^{2n+1}\left(\frac{\partial}{\partial r_\alpha}\frac{\partial}{\partial r_\beta}\cdots\frac{\partial}{\partial r_\nu}\right)\frac{1}{r_a} \tag{7.7}$$

The Einstein summation convention is used: if an index is repeated it implies a summation over all its possible values. For example, if i could take only the values $1,2,3$:

$$c_i x_i = c_1 x_1 + c_2 x_2 + c_3 x_3 \tag{7.8}$$

From formula 7.7 it is obvious that the multipole moments are symmetric with respect to permutations of the indices. It is also important to note that moments, of higher order than the dipole moment, are usually constructed to be traceless.

The l-pole multipole moment of a molecule might also be represented in spherical polar coordinates. To do this, we use the spherical harmonics ($\mathscr{Y}^l_m$) and regular spherical harmonics

($\mathscr{R}_{lm}$), which were introduced in chapter 3:

$$\widehat{Q}_{l,m} = \sum_a e_a \mathscr{R}_{lm}(\mathbf{a}) = \sum_a e_a r_a^n \mathscr{Y}_m^l \tag{7.9}$$

where l is the rank and m the projection of that moment onto individual axes, e_a is the charge of the species and $\mathbf{a}$ is its position vector. Therefore, $l = 0$, $m = 0$, is the monopole (charge), $l = 1$, $m = \pm 1, 0$ is the dipole, etc. Expressing equation 7.6 in terms of spherical tensors gives:

$$\widehat{H}_{es} = \sum_{l,m} (-1)^m \widehat{Q}_{l,-m} V_{l,m} \tag{7.10}$$

where

$$V_{l,m} = [(2l-1)!!]^{-1} \mathscr{R}_{l,m}(\nabla) V|_0 \tag{7.11}$$

where $\mathscr{R}_{l,m}(\nabla) V|_0$ is a regular spherical harmonic whose argument is the vector gradient operator evaluated at the field at $r = 0$, multiplied by a normalisation function. Also, $(2l-1)!! = (2l-1)(2l-3)...5 \times 3 \times 1$.

Next, we introduce the concept of an interaction tensor, initially again in Cartesian coordinates:

$$T_{\alpha\beta\ldots\nu} = \frac{1}{4\pi\varepsilon_0} \nabla_\alpha \nabla_\beta \ldots \nabla_\nu \frac{1}{R} \tag{7.12}$$

where R is the distance between the molecules[1]. Using interaction tensors, the field created by the other molecule may be expanded in terms of its moments. For example, the interaction of molecule A created by the charge in molecule B[2] is

$$V^A = \frac{q^A}{4\pi\varepsilon_0 R} = q^A T \tag{7.13}$$

Similar terms may be written for higher order interactions. The rank of the resulting tensor in this case is zero ($\Gamma_q^0 \otimes \Gamma_T^0$, in group theory terms). From spherical tensor operator theory, only the dot product of tensors of the same rank exists, therefore the rank of the product of the

[1] Here it can be seen that the $T_{1,2,\ldots,z}$ has an R^{-z-1} dependence.

[2] Just to clarify that superscripts denote which molecule the term "belongs" to.

interaction tensor with the multipole moment of one species must be the same as the rank of the other multipole it interacts with. Therefore, the term in equation 7.13 can interact with the 0-rank multipole moment in molecule B, i.e. q^B. This enables us to write the interaction intuitively as the interactions of the multipole moments of the two molecules, with the appropriate interaction tensor as to give a non-zero scalar product. In Cartesian tensors that may be written as:

$$\widehat{H}_{es} = q^A T_0 q^B + q^A T_\alpha \mu^B_\alpha + \frac{1}{3} q^A T_{\alpha\beta} \Theta^B_{\alpha\beta} + \dots \tag{7.14}$$

In spherical tensor formulation the analogous expression is:

$$\widehat{H}_{es} = \sum_{l_1,l_2,k_1,k_2} \widehat{Q}^A_{l_1,k_1} T^{l_1,l_2}_{k_1,k_2} \widehat{Q}^B_{l_2,k_2} \tag{7.15}$$

where T_i is the appropriate interaction tensor and $\widehat{Q}^j_{l_i,k_i}$ is the appropriate multipole moment spherical tensor for molecule j.

One important point is that any interaction may only be evaluated in one axis system at a given time. Therefore these expressions refer to a common interaction axis system, i.e. the space fixed axis system. However, it is much more convenient to evaluate the multipole moments of the molecules in their own axis system rather than in the space-fixed axis system. One of the great advantages of the spherical tensor formulation is that the rotation between the two can be simply achieved by a Wigner rotation matrix. This transforms the above equation to [72]:

$$\widehat{H}_{es} = \frac{1}{4\pi\varepsilon_0} \sum_{l_1,l_2,k_1,k_2} \sqrt{\frac{(2l_1+2l_2+1)!}{(2l_1)!(2l_2)!}} \widehat{Q}^A_{l_1,k_1} \widehat{Q}^B_{l_2,k_2} S^{k_1,k_2}_{l_1,l_2} R^{-l_1-l_2-1} \tag{7.16}$$

where all the appropriate molecule orientation transformations between the axis systems are grouped [73, 74] in $S^{k_1,k_2}_{l_1,l_2}$:

$$S^{k_1,k_2}_{l_1,l_2} = i^{l_1-l_2-j} \sum_{m_1,m_2,m} D^{l_1}_{m_1,k_1}(\Omega_1)^* D^{l_2}_{m_2,k_2}(\Omega_2)^* D^{j}_{m,0}(\Omega_{12})^* \begin{pmatrix} l_1 & l_2 & j \\ m_1 & m_2 & m \end{pmatrix} \tag{7.17}$$

where l_1, l_2 are the multipole ranks of the tensors of the interacting species 1 and 2, k_1 and k_2

their projection on the monomer axis system and j is the vector sum of l_1 and l_2. Ω_1, Ω_2 and Ω_{12} are the Euler angles for species 1 and 2, and the vector joining their centres in the space-fixed axis system. If the axis system is not space-fixed, but complex-fixed, m in the last equation has to be zero [75], so $m_1 = -m_2$.

Note should be taken that the above expression is only valid for point charge representation of the molecules, and therefore it fails (does not converge) if the charge distributions are not far enough apart.

Although it is arguably more physical to place the charge densities at atoms or molecular centres, in theory the above expression forms a complete representation of space and the multipole moments can be distributed at will, as to make convergence faster (or even possible at all) for small distances.

7.3 Long Range Forces

As mentioned in the introduction to this chapter, long-range forces vary as a negative inverse power of the distance between interacting partners. The treatment given here is based on the expressions derived in the previous section for representing the intermolecular potential as a multipole moment expansion. Although this approach does allow for a quantum mechanical treatment, the main limitation is that the overlap between the species is ignored.

There are three kinds of long range intermolecular forces: permanent electrostatic, induction and dispersion. Using the expression for the electrostatic Hamiltonian, and assuming that the charge density centres are far enough apart, the interaction between molecules in the long range regime can be treated by perturbation theory. The reference Hamiltonian ($\widehat{H}^0$) is taken as sum of the Hamiltonians for the individual, separated molecules and the perturbation Hamiltonian

($\widehat{H}'$) as the electrostatic Hamiltonian:

$$\widehat{H}_{total} = \widehat{H}^0 + \widehat{H}' \tag{7.18}$$

$$\widehat{H}^0 = \widehat{H}^A + \widehat{H}^B \tag{7.19}$$

$$\widehat{H}' = \widehat{H}_{es} \tag{7.20}$$

The first order perturbation theory correction to the energy is simply:

$$\langle 0_A 0_B | \widehat{H}_{es} | 0_A 0_B \rangle = \langle 0_A | \widehat{H}_{es} | 0_A \rangle \langle 0_B | \widehat{H}_{es} | 0_B \rangle \tag{7.21}$$

where $|0_A 0_B\rangle$ indicates that the ground state eigenfunction of molecule A and B is operated on. An approximation used in the right hand side of the equation above is that as the overlap between the wavefunctions of the two molecules is negligible, we can take the total wavefunction as the product of the functions of each molecule. Then $\langle 0_A | \widehat{Q}^A_{l_1,k_1} | 0_A \rangle$ is the expectation value of that specific moment operator. Thus, the first order correction can be calculated by the expectation values of that moment of the molecules in their ground state. This clearly represents the permanent electrostatic interaction between the molecules.

For the second order correction, the following matrix elements need to be evaluated, where at least one of m_A or m_B needs to be non-zero:

$$W^2 = \sum_{m_A, m_B}{}' - \frac{\langle 0_A 0_B | \widehat{H}_{es} | m_A m_B \rangle \langle m_A m_B | \widehat{H}_{es} | 0_A 0_B \rangle}{\Delta E_{m_A - 0_A} + \Delta E_{m_B - 0_B}} \tag{7.22}$$

where $|m_B\rangle$ indicates the m-th excited state of molecule B, and $\Delta E_{m_B - 0_B}$ is the difference in energy of that state to the ground state, and the prime in the summation indicates that it does not include the level $m_a = m_b = 0$. If only one molecule is excited (so either $m_A = 0$ or $m_B = 0$ in equation 7.22), then this is classified as induction. Physically, this occurs when the ground state moment of one species causing a mixing of ground and excited states of the other. Therefore,

the perturbation due to molecule B inducing an electrostatic interaction with A is:

$$W^2_{ind} = \sum_{m_A \neq 0} -\frac{\langle 0_A 0_B | \widehat{H}_{es} | m_A 0_B \rangle \langle m_A 0_B | \widehat{H}_{es} | 0_A 0_B \rangle}{\Delta E_{m_A - 0_A}} \tag{7.23}$$

On the other hand, if both molecules are excited ($m_A \neq 0, m_B \neq 0$), then it is dispersion. There is no classical analogue to dispersion, which is caused by instantaneous fluctuations of the electron clouds becoming correlated, thus lowering the energy. Both induction and dispersion are attractive forces. The perturbation due to dispersion is given by:

$$W^2_{disp} = \sum_{m_A, m_B \neq 0} -\frac{\langle 0_A 0_B | \widehat{H}_{es} | m_A m_B \rangle \langle m_A m_B | \widehat{H}_{es} | 0_A 0_B \rangle}{\Delta E_{m_A - 0_A} + \Delta E_{m_B - 0_B}} \tag{7.24}$$

As the electrostatic Hamiltonian now appears twice, the interaction tensors now appear twice leading to higher order distance dependencies. For uncharged species, the leading dispersion term has an R^{-6} dependence (and corresponding to first order interaction tensors). It is common practice to group terms according to their radial dependence with a single fitting parameter. In that case, if the angle-dependence of the multipole moments and the interaction tensors is neglected, the leading dispersion term becomes:

$$U^6_{disp} = -\frac{C_6}{R^6} \tag{7.25}$$

However, equation 7.25 is clearly only correct for a spherical species-spherical species interaction. That angle dependence becomes more complex the higher the inverse power as different terms are grouped together[3]. It is important to note that the induction and, less so, the dispersion energies are not additive.

[3]For example dipole-hexadecapole and quadrupole-octapole both have an R^{-12} dependence but different angular dependencies.

7.4 Short Range Forces

At short range, the overlap of the wavefunctions of the interacting species becomes significant and regarding the molecules as point-charges (an assumption that the multipole expansion is based on) fails. Conceptually there is a problem as the distance separating the molecules becomes shorter, as we can no longer represent each atom as a centre with multipole moments. Also mathematically, the negative power dependence on the distance of the multipole moment terms leads to unphysical values, which is called the "short-range catastrophe" [3, 72].

Moreover, the eigenstates that were used so far to treat the long range forces via perturbation theory become problematic: in order to be able to describe the system AB as a set of states $|a\rangle|b\rangle$, it is implied that the $\langle a|b\rangle$ spatial overlap integral for the same electron is close to, or exactly zero. Otherwise, in order to obtain the one-electron wavefunction, the antisymmetrised product of the two spacial functions would need to be taken, in accordance with the Pauli Exclusion Principle. The closer the two species get, the more the orbitals of one become contaminated by the other, and the less valid the approach of treating the interaction as a perturbation to the original orbitals is.

Finally, at short range, the possibility of the electrons being found at the same place[4] for the two species introduces a new interaction, the exchange-repulsion, which is dominant. For these reasons, a different approach needs to be taken. Except in cases of bond-formation, the overall interaction becomes repulsive.

The exchange-repulsion is actually representing two opposing effects: exchange allows electrons from one species to be attracted to the nucleus of the other significantly, while repulsion (which dominates) is due to Coulomb repulsion between same charges. There is also the effect of penetration to core shells which supplements the exchange effect. Penetration actually exists also as a correction to long range expansion, but as it decreases exponentially with distance it is only significant at close range.

[4]This only applies in cases of same-spin electrons, as the overlap integral for coupled-spin electrons disappears due to the orthogonality of the spin functions and therefore there is no exchange-repulsion.

Different perturbative treatments have slightly different definitions of the exchange perturbation term [76], but to a good approximation it depends on the square of the overlap between the orbitals of the molecules. As the electronic wavefunctions decay exponentially with distance, in general the short range effects can be represented collectively as:

$$U_{exch-rep} = Ce^{-\alpha(R-\rho)} \tag{7.26}$$

where α describes the slope (steepness) of the function and is found to vary little between systems. ρ describes the separation at which the interaction reaches the pre-exponential factor and is strongly dependent on the orientation of the system, i.e. it has an angular dependence. The angular dependence can be expressed as a series of appropriate functions. In theory, α and even C might also have an angular dependence, but might make it difficult to distinguish between them. It should be noted that all of these parameters are a way to represent the interaction in a simple way, and as they are correlated, they have no unique value.

Finally, another possible interaction is a charge transfer between the species, leading to an ionic-like contribution to the energy. This has been shown to be small even if present, and it originates from a short-range induction term where one species has excited its electron to another species' orbital.

7.5 Intermolecular Potentials

In general, we can distinguish two kinds of potential functions: first principle potentials derived from theoretical analysis, including all potentials fitted exclusively to *ab initio* calculations, and empirical potentials, which are fitted as to reproduce experimental data using a suitable function. Also, combinations of these two categories are often met in literature. The main "problem" of empirical potentials is that the parameters do not necessarily have a physical underlying meaning and might not be uniquely defined: They could instead be just one of a set of similar mathematical structures capable of fitting the data. First principle potentials may not be more accurate, but generally are more explicit in their limitations and approximations.

Moreover, the strictly theoretical potentials can cover all spectral regions, which is useful for future research, and can highlight fortuitous degeneracies or resonance effects, and lead to a better physical insight of the interaction [77]. The following analysis is not aimed at being exhaustive but rather to act as a basis to explain the work presented in the following chapters. For this reason, the main focus is placed on first principle potentials.

7.5.1 Complete set expansions

One approach is to note that a linear combination of a complete set of functions, with the appropriate variable-dependence, should be able to fit any function of the space it spans. Therefore, a slightly crude method is to fit an *ab initio* calculated potential to a complete set of functions.

Furthermore, the space the potential needs to be represented in may be separated into subspaces. Then, the potential can be represented as a product of the appropriate functions of subspaces, e.g. a complete set of angular and radial functions:

$$V_{tot}(R,\theta) = \sum_{\lambda} V_{\lambda,radial}(R) V_{\lambda,angular}(\theta) \tag{7.27}$$

where R is the intermolecular distance and θ is a collective index for all the angles. The approach of representing the potential by a weighted complete set of functions of the space it spans is called Linear Expansions in the Anisotropy of the Potential (LEAPOT) [78]. The $V_{\lambda,radial}$ are also called radial strength functions [79]. The angular functions can be products of Wigner D-matrices, one for each species, which is a further separation of subspaces.

One advantage of this approach is that any kind of function may be represented, given a long enough linear combination. Moreover, the symmetry of the species involved can be taken into account: In the case of a system of closed-shell linear molecules, the angular dependence for each molecule may be represented by spherical harmonics[5] [81, 82], while for closed-shell linear molecule-atom systems the complete angular dependence can be represented by a linear

[5] Actually, since the rotation of the whole system in isotropic space does not have any effect on the energy, only the dihedral angle is important and this expression simplifies to a pair of Legendre polynomials multiplied by a cosine function [80].

combination of Legendre polynomials [83]. However, in the case of an open-shell species, additional degrees of freedom for the orientation of the open-shell orbital need to be included [84].

Further simplification can occur if the species involved have some symmetry, e.g. in the case of a homonuclear diatomic, the potential must be indistinguishable if the two nuclei are interchanged by rotation. This means that any function differentiating between the two geometries cannot contribute, thus only even rank Legendre polynomials may be used.

The radial functions can also be any complete set of functions, e.g. Gaussians, polynomials [85], cubic splines [86] etc.

7.5.2 Born-Mayer and Buckingham potentials

If a potential that resembles the physical reality is desired, then expressions for short and long range forces can be used. Born and Mayer suggested that the repulsion between atoms can be represented roughly as an exponential function of their distance, as it depends on the overlap of their wavefunctions [3, 76, 72]:

$$U_{BM} = Ae^{-BR} \tag{7.28}$$

where R is the intermolecular distance, usually taken between the centres of mass of the molecules. The Born-Mayer potential practically includes the exchange-repulsion and penetration effects[6], although a common criticism has been that due to its simplicity this expression gives too stiff a potential.

Buckingham extended the Born-Mayer expression to include long-range attractive forces, starting with the leading dispersion term $-\frac{C_6}{R^{-6}}$. Later on, with Corner, they also included an $-\frac{C_8}{R^{-8}}$ term. In theory, this can be extended to include as many terms for the long range terms as appropriate, giving rise to the Modified Buckingham (MB) potential. However, this expression was derived for atom-atom potentials. For non-centrosymmetric molecules where different orientations contribute unequally to the interaction, odd power terms should also be included, as well as the angular dependence of all terms.

[6] But only in the short-range regime.

The induction terms are usually neglected, even for polar systems, due to their relatively small contribution. Furthermore, part of what is actually induction can be practically accommodated in the "dispersion" fitted coefficients.

In the case of interactions between non-spherical species, the angular dependence must also be included in the exponent. This can again be done as an expansion of a complete set of appropriate functions. Moreover, the radial dependence of the exponent in the Born-Mayer potential might be expanded to higher order terms, either as a positive or negative power of R [87]. The negative power expansion is thought to be more physically accurate as at very long distance it disappears naturally. In some models, a radial dependence is also included in the pre-exponential factor.

7.5.3 Damping functions

As $R \to 0$, the expressions for the long range forces (R^{-n}) go to minus infinity. To avoid this short-range catastrophe, damping functions are used to suppress the singularity. These functions are multiplied by the multipole moment expressions so the latter at short distances go to either a constant or zero.

The most commonly used expression for this purpose was proposed by Tang and Toennies [88] for atom-atom potentials:

$$f_n(R) = 1 - e^{-bR} \sum_{k=0}^{n} \frac{(bR)^k}{k!} \tag{7.29}$$

where n is the inverse power of the long-range expression to be damped and b is the Born-Mayer factor. As these functions were originally proposed for atom-atom potentials they are not valid for damping induction terms. One of the most attractive features of this expression is that, if the b parameter is set to be the same as in the Born-Mayer potential, there are no additional fitting parameters.

Usually the angular dependencies of the damping functions are ignored when applied to

multi-atom systems, so this was explored in the present work. What was discovered was that setting b to the completely symmetric exponential term and then relaxing when convergence is very near (i.e. getting the optimum fit when b was fixed to the Born-Mayer term and then lifting this limitation) is a good approximation and allowed for a quick convergence. On the other hand, if an angular dependence was included in the short range exponential term, and this was also included in the damping functions, correlation between the long and short range forces caused convergence problems. The possibility of including only the same kind of angular dependence in the damping functions to the C_n term being damped was explored, however this gave the same result. It should also be noted [7] that since the Tang and Toennies expression is empirical, there is no strict requirement for the exponent in the damping functions to be the same as for the short-range force.

Including the Tang and Toennies damping functions, the potential might be represented as:

$$U(R,\theta) = A(\theta)e^{-\alpha(\theta)(R-\rho(\theta))} + U_{ind} + \sum_{n=3} f_{2n}(R)\frac{C_{2n}(\theta)}{R^{-2n}} \tag{7.30}$$

where θ and R are collective indices for the angular and the radial dependence respectively, both of which might be expanded as a series. R might also be expressed with respect to a reference geometry[7].

Correspondingly to LEAPOT, this kind of potential where the anisotropy of the Born-Mayer and multipole factors is explored is also called Linear Expansion in the Anisotropy of Parameters (LEAPAR). As it is closer to the physical reality and also any LEAPAR exponential term may be expanded as a series of LEAPOT terms, LEAPAR models potentially use fewer parameters which may have physical meaning. The physical meaning of the parameters is of multiple importance: it can be used to assess whether the expansions are convergent and whether the values of the parameters are reasonable or if some important effect is missed.

[7] For example as $\frac{R-R_m}{R_m}$ [78, 89].

7.5.4 Atom-atom potentials

Here the same principles are applied as for the molecule-molecule potential, but the interaction centres are the atoms. This approach helps with the problem of poor convergence of the multipole expansion met in van der Waals complexes, where the intermolecular distance is no longer large with respect to the charge distribution of the separate molecules [90], so the multipole approach is not really valid.

Usually a Born-Mayer and a long-range part are fitted for each atom-atom pair. The main problem of this approach is that the number of parameters can go up rapidly with the more interacting centres [57] and these might be strongly coupled, which could lead to unphysical values and fitting problems.

Values obtained by fitting similar systems can be used, best as first guesses, as to give the parameters their appropriate relative size. Also, to avoid too many fitting parameters, terms that contribute little (and can to an extent be included in other terms), for example induction, are often neglected.

One method used in this work to avoid correlation between the short-range repulsion and long-range damping functions is to keep the damping functions' exponential value fixed at the values obtained from the previous fitting cycle. Otherwise, small changes in exponential function can cause major changes in the value of the long-range coefficients. Also, it was noted that the damping functions on atom-atom potentials are more isotropic (possibly more dominated by the leading term) than those of intermolecular multipoles [57]. This meant neglecting the angular dependence of the damping functions was more justified.

At close distances a redistribution of electron charge might occur, which can be dealt with by adding another centre, e.g. at mid-bond. This was also explored in the present research but no significant improvement in fitting the potential was gained by this approach.

7.5.5 Scaling the potential

A full potential of a two-species complex would have to span from the very highly repulsive region of short range interaction to the asymptotic-to-zero interaction at long range. If a function is fitted to an *ab initio* PES, a least squares fit will tend to fit the greater deviations better and average over the smaller ones. The measure of the quality of the fit used is firstly the Root Mean Square Deviation (RMSD):

$$RMSD = \sqrt{\sum_{i=1}^{N_d} \left(\frac{\frac{[y_{calc}(i) - y_{obs}(i)]^2}{u(i)^2}}{N_d} \right)} \tag{7.31}$$

where $y_{obs}(i)$ is the i-th point to be fitted, $y_{calc}(i)$ is the value the fit would predict the i-th point to have, N_d is the number of points and $u(i)$ is the statistical weight. When fitting an *ab initio* potential, where all points are determined at equal precision by the calculation, setting $u(i) = 1$ seems logical.

Unfortunately this would mean that rather than fitting the well-region accurately and having a large error at the close range, instead it will try to fit the short-range repulsion equally well to the minimum. This can mean that a very large number of functions is required and may lead to correlation problems between the parameters.

In the case of van der Waals complexes, assuming a strong enough interaction, only the minimum region of the potential is important, as long as the very long and very short range parts are fitted to a number of the right magnitude. For this reason, the approach of scaling the potential is sometimes taken. This modifies the potential so that, up to a threshold V_0, the potential remains unchanged, and over that, the potential tends towards a pre-set value [91].

Chapter 8

The Electronic States of the NO-O_2 Complex

"*Computers are useless. They can only give you answers.*"

- Pablo Picasso

8.1 Introduction

As was noted in the introductory chapter 1, one of the key motivations behind this work was to understand what the interaction between the constituent molecules ("monomers") of a van der Waals complex when these are open-shell species. Chemical intuition would predict that when two radicals meet a covalent bond is formed, and indeed this is usually the case.

However, there is a handful of diatomic and triatomic open shell species (such as NO, NO_2 and O_2 [11]) which do not follow this rule and instead form weakly-bonded molecular complexes. At the same time, radicals that exhibit such behaviour are abundant and important in atmospheric chemistry and biological systems, which makes these cases hard to ignore. To

make matters even more intriguing, these species do react on occasion, for example:

$$2NO + O_2 \rightarrow 2NO_2 \tag{8.1}$$

$$2NO_2 \rightarrow N_2O_4 \tag{8.2}$$

Yet, even then, the type of bonding the products of these reactions are held by is not always a typical chemical bond. One example of this is the N_2O_3 molecule, formed in the following reaction:

$$NO + NO_2 \rightarrow N_2O_3 \tag{8.3}$$

which is held together by a bond in-between a covalent bond and van der Waals bond [92].

This chapter falls under the "theoretical investigations" part of this thesis. Here we isolate and target the question of bonding of such complexes using high level *ab initio* calculations. The system that we chose to study these effects is the van der Waals complex formed between the open shell molecules of nitric oxide and oxygen (NO-O_2). This is particularly interesting as in our investigations we have to take into account both the effects of symmetry and of spin coupling between the two molecules, as will be shown later. Moreover, one of the PESs links to the ground state of the nitrate radical NO_3 [93]. Furthermore, the NO-O_2 van der Waals complex has recently been argued [94] to be an intermediate in reaction 8.1. The variety of contributing factors and possible outcomes makes this a fascinating system to study.

In the following section, the complex in question and its constituent molecules are presented. Then, the *ab initio* calculations performed are presented and these are discussed briefly. Finally, a discussion is given as to how our results may be incorporated into the theory of intermolecular forces and our conclusions are presented.

8.2 The NO-O_2 Complex

As mentioned in the previous section, in this chapter we investigate the various electronic states of the NO-O_2 complex. In order to understand how these are formed we fist look at the monomer

species, NO and O_2 and then at the complex itself.

8.2.1 The NO molecule

The electronic configuration of NO is:

$$1\sigma^2 2\sigma^2 3\sigma^2 1\pi^4 2\pi^1$$

To characterise the ground state of NO, we can use its term symbol, ${}^{2\Sigma+1}\Lambda_\Omega$, where Σ, Λ and Ω are the projections of the electron spin angular momentum $\mathbf{S}_{NO}$, the orbital angular momentum $\mathbf{L}_{NO}$, and the total angular momenta $\mathbf{J}_{NO}$ along the internuclear axis which are related by:

$$\mathbf{S}_{NO} + \mathbf{L}_{NO} + \mathbf{N}_{NO} \rightarrow \mathbf{J}_{NO} \tag{8.4}$$

$$\Sigma + \Lambda = \Omega \tag{8.5}$$

where $\mathbf{N}_{NO}$ is the rotational angular momentum of NO. If there is more than one possible term symbol, as in the case of NO where Ω may be either $\frac{1}{2}$ or $\frac{3}{2}$, a guide to which term indicates the state with the lowest energy is provided by Hund's rules [36], which were proposed by considering the effects of electron-electron repulsion. These are:

1. The rule of maximum multiplicity: The state whose term symbol has the maximum multiplicity will be lower in energy.

2. The rule of maximum angular momentum: The state with the greater orbital angular momentum quantum number will be lower in energy.

3. If the valence shell is less than half-full, then a minimum total angular momentum is lower in energy, and the opposite is true for a more than half-full valence shell.

These rules were originally drawn for atoms, however, within the limits of Molecular Orbital (MO) theory, they have been successfully applied to molecules. The single unpaired electron in the antibonding π orbital gives NO a ground state term symbol ${}^2\Pi$. Furthermore, according

to Hund's third rule the lowest energy state has term symbol $^2\Pi_{1/2}$ and the first excited state $^2\Pi_{3/2}$. The energy difference between these two states corresponds to the spin-orbit coupling constant[1] $\zeta = 123\ \mathrm{cm}^{-1}$ [2, 62].

As the nitrogen nucleus has spin angular momentum of $I_N = 1$, there are in total four sources of angular momentum in this molecule: the electron spin, the orbital, the nuclear spin and the rotational angular momentum. However, for our purposes of distinguishing PESs of the complex we will only use the electron spin angular momentum.

8.2.2 The O_2 molecule

The electron configuration of the oxygen molecule is [95, 36]:

$$1\sigma_g^2 1\sigma_u^2 2\sigma_g^2 1\pi_u^4 1\pi_g^2$$

The term symbol of O_2 may be calculated by the direct product of the irreducible representations of the orbitals of the unpaired electrons:

$$\Pi \otimes \Pi = \left[\Sigma^-\right] \oplus \Delta \oplus \Sigma^+$$

while the symmetry with respect to inversion is given by the direct product:

$$g \otimes g = g \tag{8.6}$$

According to the Pauli principle, the electronic part of the wavefunction should be antisymmetric with respect to the exchange of a pair of electrons. Therefore, the symmetric spatial (orbital) wavefunctions need to be combined with antisymmetric spin eigenstates. Therefore, according to Hund's rules, the term symbol for the ground state of O_2 is $^3\Sigma_g^-$. Yet, the first excited state, $^1\Delta$ is only 7,918 cm^{-1} higher in energy and the second excited state, $^1\Sigma_g^+$ is only 13,195

[1] The non-standard ζ symbol is used for the spin-orbit coupling constant to distinguish it from the A rotational constant.

cm^{-1} higher [17]. As the oxygen nucleus does not have any angular momentum ($I_O = 0$) and there is no orbital angular momentum in the ground state, there are only two sources of angular momentum for O_2: the electron spin ($\mathbf{S}_{O_2}$) and the molecular rotation.

8.2.3 The states of the complex

Even when the NO and O_2 molecules are in their ground electronic states, there are four possible electronic states that the complex may be formed in, with corresponding PESs. Assuming that the complex is planar, we may use symmetry as well as spin multiplicity to distinguish them.

In terms of spin multiplicity, we define the total electron spin angular momentum, $\mathbf{S}$ of the complex as:

$$\mathbf{S}_{NO} + \mathbf{S}_{O_2} \rightarrow \mathbf{S}$$

Thus, the complex may be formed with $S = \frac{1}{2}$ (a doublet spin state) or $S = \frac{3}{2}$ (a quartet spin state). While Hund's first rule would predict that the $S = \frac{3}{2}$ state is lower in energy, on the grounds of electron-electron repulsion, there is another approach, based on the Heitler-London theory [95] which would make the opposite prediction: namely that the minimum multiplicity should be lowest in energy.

Heitler-London theory is the basis of Valence-Bond (VB) theory [36, 96] treatment of the bonding in the hydrogen molecule (H_2). While a detailed discussion of that treatment is beyond the scope of this thesis, the key point for us is that covalent bonding occurs due to exchange interaction between the two hydrogen atoms which is only possible when the spin magnetic quantum numbers of the two species are of opposite sign[2].

Therefore, we are faced with a dilemma, as Hund's rule, based on electron-electron repulsion and MO theory would predict maximum multiplicity as the most stable while Heitler-London theory based on exchange interaction and VB theory would predict the minimum multiplicity but also a covalent bond which is not observed. At the same time, since both NO and O_2

[2]In the original theory concerning two hydrogen atoms, as well as in subsequent discussions, the phrasing [97] usually speaks of "spin pairing", however this becomes problematic when three electrons are considered. For clarity in the text we will refer to this case as the spins of the electrons being "coupled".

are radical species, chemical intuition would also expect a chemical bond. Finally, both Hund's rules and Heitler-London theory are stressed outside their original domain by being applied to this case: Hund's rules were originally stated for atoms, not molecules and one might expect even less so for molecular complexes, while Heitler-London theory was derived for H_2, which has no core electrons and thus minimum electron-electron repulsion.

As mentioned earlier, we will use high level *ab initio* methods to examine this complex, which (as described in chapter 4) are based on MO theory. Our hypothesis however is that, while the dominant intermolecular interaction in NO-O_2 is similar to other van der Waals complexes, as described in chapter 7, there is also a "pseudo-covalent" contribution stemming from the exchange interaction which is only possible if the spins are "coupled", in a mechanism similar to what is described by Heitler-London theory. If such a "pseudo-covalent" contribution is present, then the ordering of the energy levels should follow the Heitler-London argument i.e.:

$$E_{S=\frac{1}{2}} < E_{S=\frac{3}{2}} \tag{8.7}$$

This assumes an exchange interaction between the molecules, which lowers the energy via nuclear-electron attraction and shielding of the nuclear-nuclear repulsion, and would shift the electron density in the intermolecular region.

The reason we call this interaction "pseudo-covalent" is because the logic behind it is analogous to the Heitler-London theory for the covalent bond formation between two atoms, but in our case the role of the atomic orbitals is played by molecular orbitals. Also, the final bond is between two molecules that retain their identity rather than two atomic centres. This is clearly different from a traditional covalent bond in that the shape of the molecular orbitals of NO and O_2 will determine the overlap between the molecules, rather than the atomic orbitals. Moreover, it is described as a "contribution" rather than a "bond", as the overall potential remains that of a van der Waals complex.

If on the other hand no such contribution is found, then the main argument should be on the grounds of electron-electron repulsion and the energy ordering of the states of different

multiplicity would be as predicted by Hund's first rule. The reasoning behind that argument is that electrons sharing the same spin wavefunctions would not coincide in space due to the Pauli Exclusion Principle. This effect of creating a Fermi hole [36, 96] in the electron distribution leads to lower electron-electron repulsion.

In terms of symmetry, for a planar complex, the π orbitals of the monomers may be either perpendicular to, or lie along the plane of the complex. A π orbital along the plane of the complex is symmetric with respect to reflection on that plane, thus can be assigned A' symmetry, while if it is perpendicular, and thus antisymmetric with respect to reflection on the plane, the orbital has A'' symmetry.

O_2 will have an unpaired electron in each of its π orbitals, i.e. both in A' and A'' orbitals, thus its symmetry is always:

$$A' \otimes A'' \rightarrow A''$$

NO will have its unpaired electron either in a A' orbital on the plane (thus giving an overall A'' state), or in an A'' orbital perpendicular to the plane (thus giving an overall A' state). Thus, the four states that the complex may be formed in are:

1. $^2A''$: the orbital of the unpaired electron of NO lies in the complex plane, and has a spin coupled to the spin of O_2. If a pseudo-covalent contribution occurs, this would be the most promising for favourable interaction as orbitals with unpaired electron spins from NO and O_2 meet on the plane of the complex.

2. $^4A''$: the orbital of the unpaired electron of the NO is on the plane of the complex, but now its spin magnetic number is of the same sign as the spin of O_2. Under the Heitler-London argument this state would have the highest energy.

3. $^2A'$: the spin magnetic quantum numbers of NO and O_2 are of the opposite sign, but the unpaired electron of the NO is on the orbital perpendicular to the plane of the complex. Therefore, if a pseudo-covalent contribution occurs, the overlap between the molecular orbitals would be lower than for the $^2A''$ state and therefore weaker.

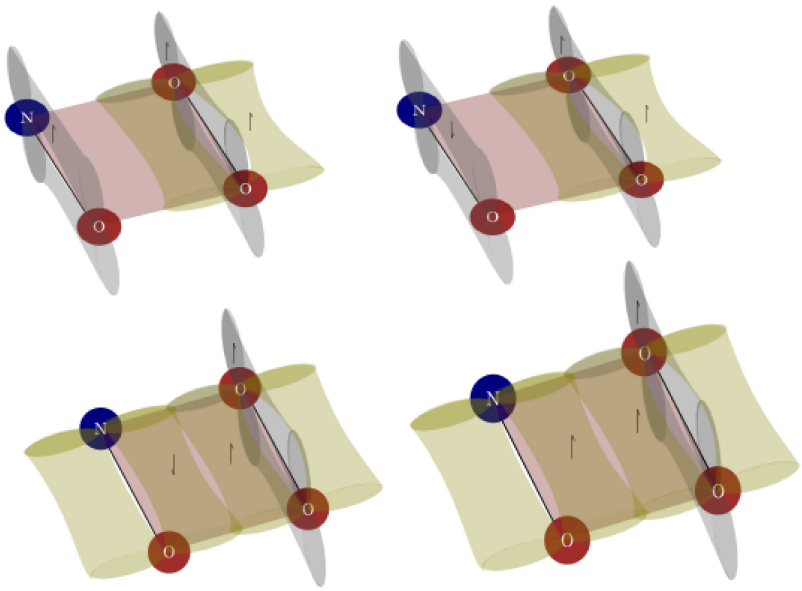

Figure 8.1: The four electronic states of the complex, clockwise from the top left: Quartet A', Doublet A', Quartet A'' and Doublet A''.

4. $^4A'$: here the orbital containing NO's unpaired electron is perpendicular to the plane, but now all the spin magnetic quantum numbers are of the same sign. Thus, no pseudo-covalent interaction can take place, but also the electron repulsion is weaker than in case 2, as the orbitals are parallel instead facing each other.

The four states are also illustrated in figure 8.1, where the plane of the complex is drawn as a red plane. The orbitals on the plane are coloured green and the ones perpendicular gray: This complex has previously been studied in the group by Starkey [2] who performed RSPT2 calculations on a limited configuration space (for both planar and non-planar geometries of the complex) and myself during my Part II project [84], when I modelled and extended the PESs of Starkey, aiming to perform quantum dynamics on them. Yet, there were various issues with the previous PESs, both in the geometry specifications for when the complex was not planar and in terms of unnatural values of the supermolecular binding energy. For this reason we decided to perform a more extensive study of higher level calculations to understand the interactions better and also formulate a suggestion for what *ab initio* methods to use when studying similar systems.

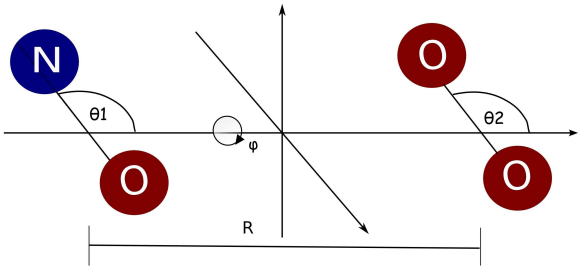

Figure 8.2: The coordinate system used for the NO-O_2 calculations

8.3 The *Ab Initio* Calculations

In order to investigate the ordering of the different energy states, we have performed high level *ab initio* calculations to obtain the PES of all different states.

In the figure 8.2, the axis system used for calculating the PES is presented. θ_1 is the angle between the line between the centre of mass of NO and O_2 with the NO axis of symmetry, θ_2 is the corresponding angle for O_2, and ϕ is the dihedral angle between the principal axes of the two molecules, where $\phi = 0^\circ$ corresponds to a planar complex. R is the distance between the centres of mass of the two molecules.

Yet, the symmetry distinction into A' and A'' states is only valid for planar geometries. Therefore, in order to have an unambiguous characterisation of the different PESs, we have restricted ϕ to zero. The θ_1 angle was varied every 30° degrees between 0-180°, while θ_2 angle was varied every 30° degrees between 0-150° degrees, as the rest of the points are related to one of the calculated geometries by symmetry. R was varied from 2.9 to 4.9 Å in steps of 0.1 Å.

In choosing the *ab initio* methods to be used, the first question was whether a single reference method (such as MPn) would be suitable, or if it were necessary to use a multireference method. The doublet complex spin state may be formed by either a combination of the ground state of NO ($S_{NO} = \frac{1}{2}$) with the ground state of O_2 ($S_{O_2} = 1$), or by a combination of the ground state of NO with the first excited state of O_2 ($S_{O_2} = 0$). Thus, a multireference method is required to take both Slater determinants into account. The quartet state on the other hand may only be formed by the ground states of NO and O_2, so a single reference method seems appropriate.

Although the aim of this project was to explore what happens when two radical species meet, we also wanted our exploration to be of practical use for other parts of this project, namely for the complex between nitrogen dioxide and oxygen (NO_2-O_2), which is presented later, in chapter 11. For this reason, the electron correlation methods chosen are all based on multireference applications of perturbation theory[3], i.e. RSPT2, NEVPT2 and CIPT2. MRCI methods were not used as their size inconsistency may lead to significant errors when used for very weakly bound van der Waals complexes. Moreover, as RCCSD(T) is a reliable method for systems that may be described by a single Slater determinant, this is also used to perform calculations for the quartet spin states PESs, in order to use them for comparison with the PESs from the multireference perturbation theory methods. Ideally, we would like to correct for the Basis Set Superposition Error (BSSE) using the counterpoise procedure, as explained previously in chapter 4. However, as will be explained when discussing the CIPT2 surfaces, this was not possible, and instead we could only approximate the binding energy by subtracting the energy of the complex at the intermolecular distance of $R = 150$ Å. However, it should be noted that the question of whether the counterpoise procedure is appropriate for multireference methods remains an open one. Furthermore, if one takes the difference between the PESs, as the counterpoise correction is identical for all states, it would cancel.

In the following sections the PESs calculated by different methods are discussed in turn and finally a comparison between them is made. All calculations were made using the MOLPRO2010 [98] package and the PESs are also given in the CD attached to this thesis. The basis set used for all calculations was aug-cc-pVTZ, unless otherwise stated.

8.3.1 The RSPT2 PESs

The first method to be used is the RSPT2 method. As it was noted in chapter 4, this has been perhaps the most widely implemented method for van der Waals complexes. This is because it is one of the oldest and also computationally least expensive ways to perform multirefer-

[3] For a description of these methods please see chapter 4.

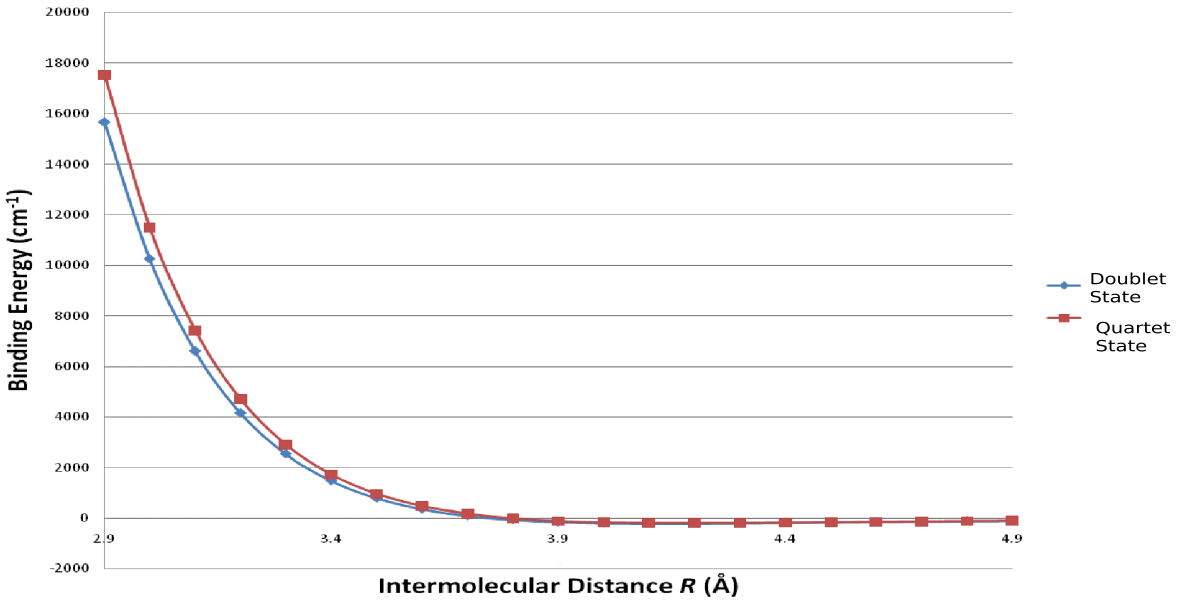

Figure 8.3: RSPT2 PEC for the linear NO-OO geometry

ence electron correlation corrections. Moreover, this method has been used previously in the group [2, 84], so it was a natural starting point.

The first observation to be made is that the ordering of the PESs depends on the orientation chosen. It seems that, depending on the geometry of the complex, different effects are dominating the interaction. For the majority of the geometries calculated however, the splitting between the surfaces of the two multiplicities for the A'' state is greater than for the A' state, which can be rationalised in terms of increased overlap between the NO and O_2 valence π orbitals.

The easiest way to discuss these observations and what they imply for the interaction between NO and O_2 is by examining some key geometries. The first orientation to be examined is where $\theta_1 = \theta_2 = 0°$, which corresponds to the linear geometry NO-OO. At this geometry, there are no separate A' and A'' states, so there are only two surfaces, due to the two multiplicities. One important feature is that there is no potential well as the monomers approach each other. In the long range, all the potential energy curves (PECs) coincide. At close distances however, there is a separation between the four PECs into two groups depending on their multiplicity, the doublet states being lower in energy. The PECs for this geometry are given in figure 8.3. Before any further analysis, it should be noted that an interesting point was noted from this method: The Size Consistency Error (SCE) depended on the multiplicity of the states, and states of the

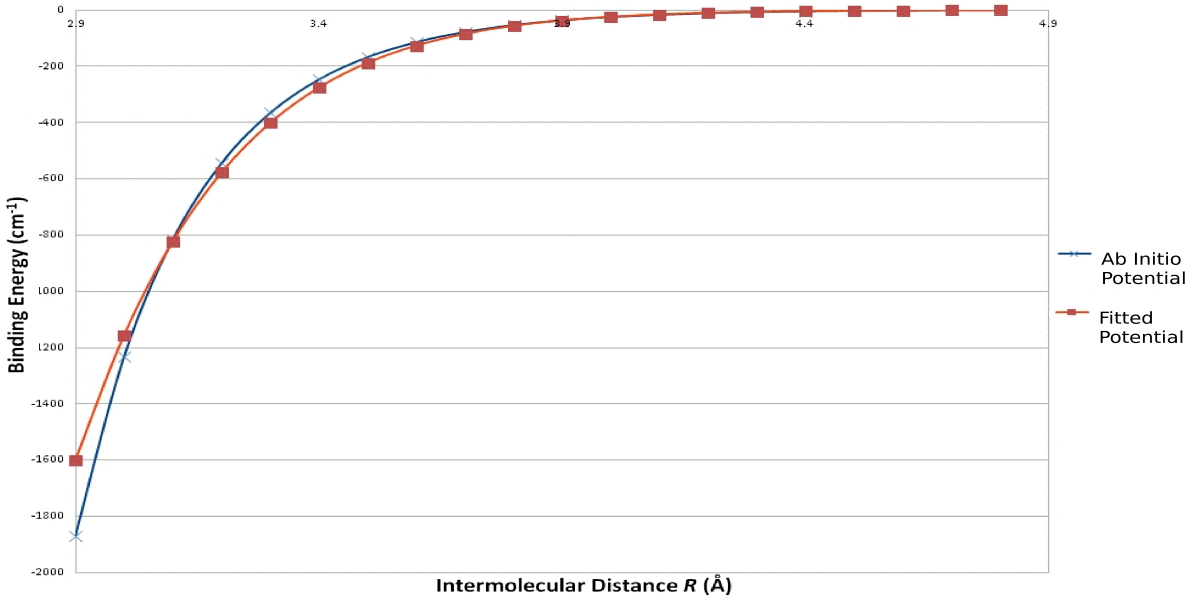

Figure 8.4: *Ab initio* (RSPT2) and fitted difference potentials between the doublet and quartet states for the linear NO-OO geometry

same symmetry but different multiplicity had an energy difference of approximately 21.5 cm^{-1} at $R = 150$ Å. Therefore, one has to subtract the energy of the molecules at large separation in a specific state in order to cancel the SCE difference, as we have done in figure 8.3, otherwise different multiplicity states tend asymptotically to different values at large R.

What is interesting is to take the difference between the singlet and the quartet states. If we plot the energy difference between the two spin states against the intermolecular distance, the shape of the graph is exponential and, if we subtract the SCE, it can be fitted with the simple expression:

$$\Delta V_{doublet-quartet} = \exp\left[a + bR + \frac{c}{R}\right] \tag{8.8}$$

with values $a = 29.58, b = -5.42, c = -18.81$. An inverse polynomial of distance was chosen as this will naturally disappear in long distances rather than result in spurious minima. The *ab initio* and fitted PECs are shown in figure 8.4. The RMSD of the fit was 14.4 cm^{-1}, but this was mostly in the values up the repulsive wall, where the difference between the PECs was more than 1500 cm^{-1}. Our interpretation of this graph and potential energy contribution is that the difference between the two spin states originates from a pseudo-covalent contribution to the doublet state binding energy, which is only possible when the spins of the unpaired electrons

are coupled. The fact that this interaction is roughly exponential, mirroring a Born-Mayer expression [7] but with the opposite effect, is to be expected as the origin of the interaction is also the exchange-repulsion.

The next important geometries to discuss are those when one of the monomers is positioned perpendicular to the intermolecular axis while the other lies at an angle up to but not including 90°. Now, all four PECs are separated, and their energy ordering is:

$$E\,^2A'' < E\,^2A' < E\,^4A' < E\,^4A''$$

Once more, the doublet spin states are lower in energy than the quartet ones. The ordering in terms of the different symmetries may be explained with the argument presented in the introduction of this chapter, i.e. depending on the overlap. The A'' state has greater overlap between the O_2 π orbital and the π orbital of the unpaired electron of NO, and therefore the splitting of different spin states is greater. Another interesting examination is to take the spin-averaged potential for the different symmetries:

$$V_{\text{av}} = \frac{V_{\text{Doublet}} + 2V_{\text{Quartet}}}{3} \tag{8.9}$$

where the weighting is according to the spin degeneracy of each state. When even one molecule does not lie along the intermolecular axis, then the difference between the two states varies exponentially, and in a similar magnitude to the difference between the two spin states. One interesting thing to note is that the SCE cancels when the difference of the average potentials for each symmetry is taken in this way.

For the geometry $\theta_1 = 30°$ and $\theta_2 = 90°$, the spin-averaged potential was fitted using the function of equation 8.8 with $a = 46.97, b = -7.98, c = -57.01$ and RMSD=0.77 cm^{-1} (although the largest energy difference fitted this time was only 68.38 cm^{-1}). The *ab initio* and fitted difference between the average potentials for this geometry is shown in graph 8.5. The fact that the spin-averaged potential may be modelled using a second Born-Mayer-type contribution is interesting. It represents the difference in the overlap of the two symmetries: even

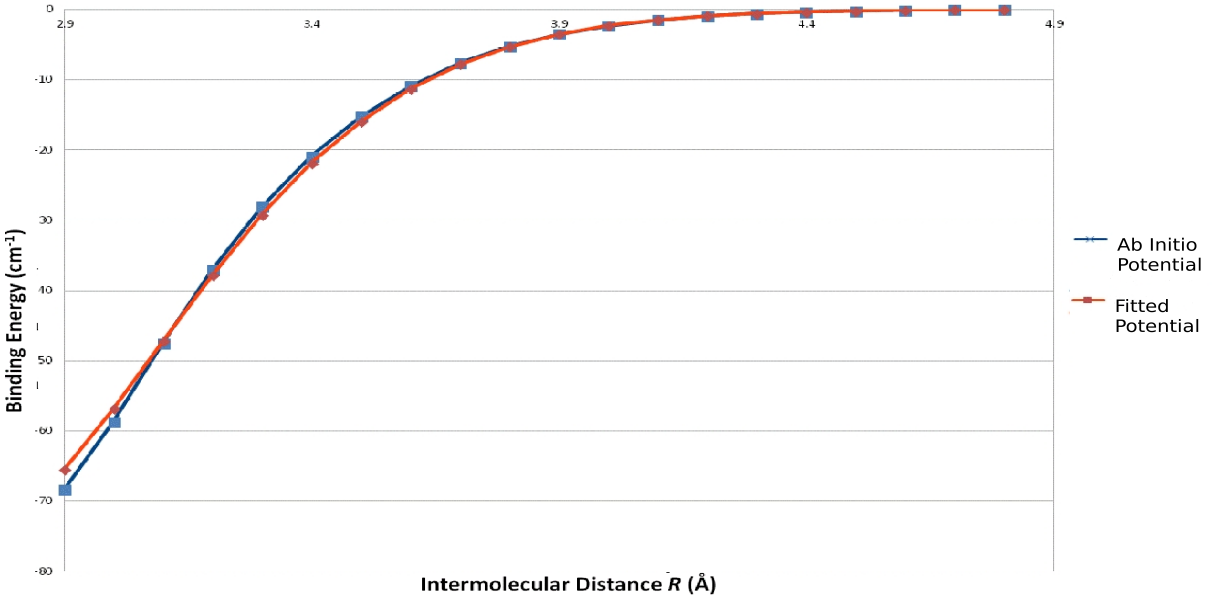

Figure 8.5: Difference between the spin-averaged RSPT2 potentials for the geometry $\theta_1 = 30^\circ, \theta_2 = 90^\circ$

if the effects of spin pairing are averaged out, there is an additional overlap in the A'' symmetry state with respect to A' symmetry. As the difference between two exponentials is itself an exponential, this may be fitted to a similar function.

Thus, one could model the PESs by taking into account three parts so far: The potential function similar to what one would expect for a pair of closed shell molecules, plus a Born-Mayer potential to represent the effects of spin coupling, plus another Born-Mayer term to represent different symmetries. After Herzberg, it should be noted that when we refer to "spin coupling" this is used as an indication of the states, which themselves are separated due to exchange interaction [97]. The actual spin-spin effect is very small in comparison and will be presented in chapter 9.

Another intriguing feature of these PESs is that, while on the whole the doublet states are lower in energy than the quartet ones, this is reversed in very specific geometries and distances and for the A'' state only. More specifically, it happens only for distances up to $R = 3.9$ Å if O_2 (but not NO) lies along the intermolecular axis, and for the angles $\theta_2 = 30^\circ, 120^\circ, 150^\circ$ and for the geometry ($\theta_1 = 150^\circ$, $\theta_2 = 30^\circ$).

Before moving on however, there are two more important cases to consider. The first one

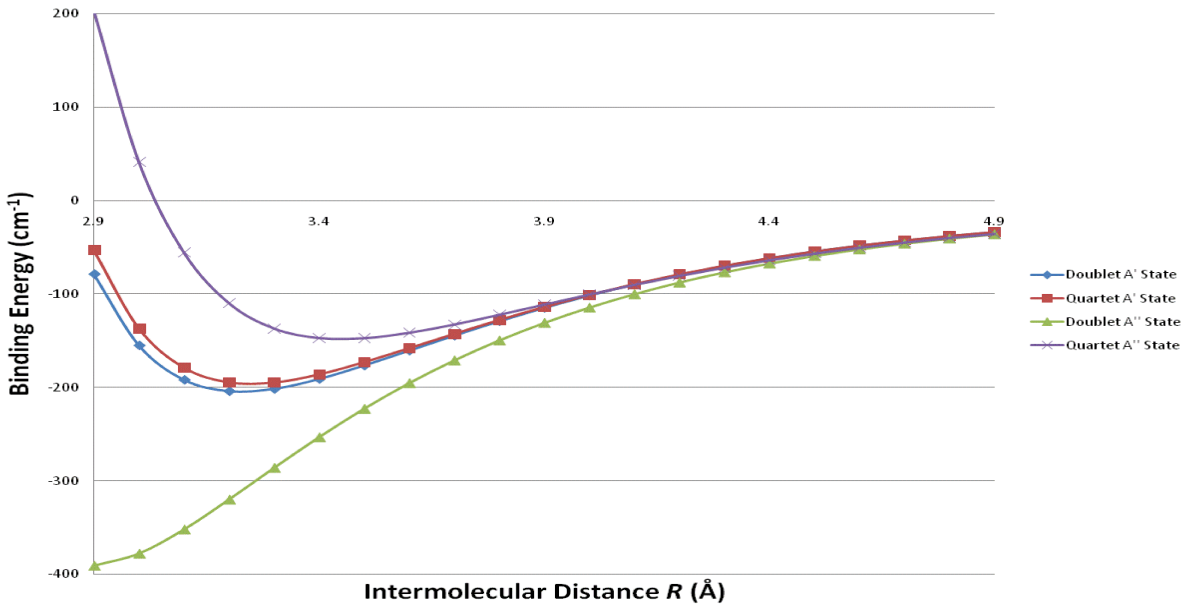

Figure 8.6: RSPT2 PECs for the parallel arrangement of the NO and O_2 ($\theta_1 = \theta_2 = 90°$)

occurs when the molecules are parallel to each other. The PECs for this case are given in figure 8.6. There is a number of points to consider in this graph. The first one is to observe that in this geometry the effect of spin coupling is greater than the difference between the averages for each symmetry: the difference between the two multiplicities in the A'' state reaches 615.7 cm^{-1}, while between the two averages barely 67.2 cm^{-1}.

Moreover, the interaction for the $^4A''$ state becomes repulsive much earlier than for the $^4A'$ state, which emphasises the importance of valence electrons. Perhaps the most surprising finding however is that the $^2A''$ state seems to go on directly to form NO_3 without any barrier. The main point of this graph is the clear ordering of the energy states: the doublet states are lower than the quartet ones, demonstrating the pseudo-covalent contribution to the interaction, and the splitting of the two A'' states is larger than of the A' states due to the increased overlap of the valence orbitals of NO and O_2.

The second extreme case is when $\theta_1 = 180°$ and $\theta_2 = 60°/90°$. In these cases the energy difference between the two spin states starts at approximately 28 Hartrees for the A'' state and 16 Hartrees for the A' state and decreases with distance. This is also the area where most of the convergence problems were met. At all these geometries, the quartet states have values typical of the PES (differing less than 0.1 Hartree between all different geometries) and it was

the doublet state energies that are significantly lower.

A clue to this unnatural behaviour comes from the calculated dipole moments: while for all geometries, apart from when $\theta_1 = 180^\circ$ and $\theta_2 = 60^\circ/90^\circ$, no dipole moment was over 1 Debye, in the geometry of $\theta_1 = 180^\circ, \theta_2 = 60^\circ$, $R = 3$ Å, the dipole moment $|\mu_z| = 10.383$ Debye. A possible explanation is a charge transfer, which would also explain the large dipole moment and the abnormal binding energy. Yet, the energy increases with distance, which is clearly an artefact and shows that the RSPT2 method is not suitable for these geometries.

Finally, it is interesting to note the lowest energy geometry: If we ignore the cases where the large dipole moment indicates a possible charge transfer, the global energy minimum occurs at values $\theta_1 = \theta_2 = 90^\circ$ and at $R = 2.9$ Å, which is the smallest distance calculated for the $^2A''$ state. This is reasonable as according to RSPT2 this state would lead to a formation of NO_3.

8.3.2 The NEVPT2 PESs

The next method examined is NEVPT2. As explained in chapter 4, the two key advantages of this method when compared to other multireference perturbation methods are its size consistency and its virtual absence of any intruder states. Thanks to the former there is no difference between the energies of the different states at $R = 150$ Å, unlike for RSPT2.

In general, different states are separated according to multiplicity and geometry along the same lines as the RSPT2 PES, although for NEVPT2 the energy differences tend to be smaller at close distances. Nevertheless, as the zeroth order Hamiltonian is different for the two methods, the complex energy is not directly quantitatively comparable. One key geometry to compare the NEVPT2 and RSPT2 PESs is when $\theta_1 = \theta_2 = 90^\circ$. The graph for this geometry is given in figure 8.7.

As can be seen from the graph, the ordering of the PECs is the same as for RSPT2. One difference is that the energy of the lowest state ($^2A''$) starts to increase at close distances. For all surfaces, the repulsive wall seems to be much steeper with this method. Moreover, the binding energy of all PECs goes to zero at large distances as expected. Still, the PECs do not look as

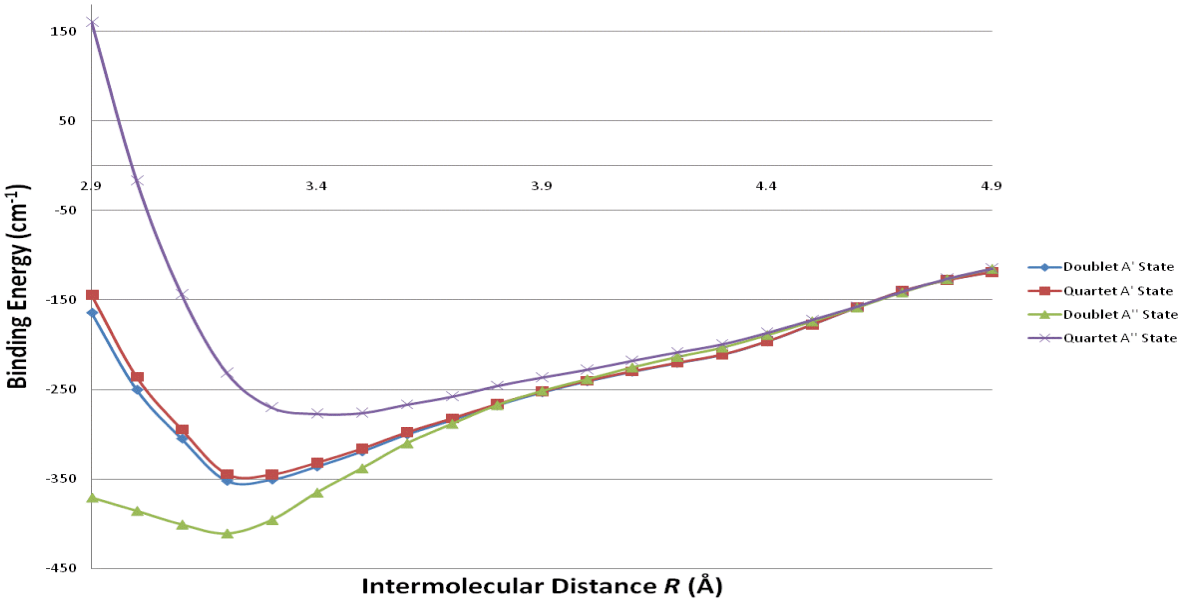

Figure 8.7: NEVPT2 PECs for the parallel arrangement of the NO and O_2 ($\theta_1 = \theta_2 = 90°$)

smooth as they did for the RSPT2 method, and we will revisit this point later.

Another difference is that, with NEVPT2, this geometry does not lead to NO_3 formation for the $^2A''$ state, but actually forms a shallow minimum at 3.2 Å. This geometry is also the global minimum for this method.

The other important geometry to compare is when $\theta_1 = 180°$ and $\theta_2 = 60°/90°$. Here the same very large dipole moments are found again, which encourages us to believe that it may be a charge transfer effect taking place. Moreover, the anomalous behaviour of RSPT2 where the binding energy was increasing with distance is not met. Instead what is found is that the energy of the complex is very high: 2.8-2.9 Hartrees higher than for the other geometries. This is in contrast to RSPT2, that predicted the energy in these geometries to be significantly lower than for the other geometries for the doublet spin states. Also, the quartet state seems to form again a van der Waals minimum at close distances, while the doublet state energy keeps decreasing as the molecules come closer.

The high dipole moments along with the high energy of the complex at this geometry are intriguing. In [7] and [99], Stone *et al.* have argued that the contribution of charge transfer in van der Waals complexes is very small and an exaggerated part of induction. However, this comes from the assumption that the charge transfer should be originating from one molecule's

electrons being excited to the virtual orbitals of the other molecule. However, in our case the "receiving" orbitals are not virtual but unfilled orbitals in the ground state configuration, as the species are open shell. This is believed to only happen for $\theta_1 = 180^\circ$ rather than for $\theta_1 = 0^\circ$, as the unpaired electron in mainly localised on the nitrogen rather than oxygen atom. Because of the difference in ionisation energies (9.26 eV for NO versus 12.08 eV for O_2 [100]) and electron affinities (0.02 eV for NO versus 0.44 eV for O_2 [100, 101]) between the two molecules, this interaction only occurs in the ON-OO linear geometry, i.e. giving an (ON^+)-(O_2^-) ionic contribution.

Finally, we return to the cases where the energy difference between the states of same symmetry and different multiplicity is favourable for the quartet rather than the doublet state. This again remains the exception rather than the norm. However, there is a greater number of points that this occurs in NEVPT2 calculations compared to RSPT2. To begin with the A'' symmetry, although there is a greater number of geometries where this is met (86 versus 21 points) the angular geometries where this is met are the same, just the effect extends to larger distances, up to $R = 4.9$ Å. The maximum difference of this effect here was 748.42 cm^{-1}, which is significantly larger than the 500.39 cm^{-1} for RSPT2. For the A' state, there were no points where this effect was observed in RSPT2, but there are 21 points where this occurs in NEVPT2, which correspond to the geometry $\theta_1 = 90^\circ, \theta_2 = 30^\circ$.

8.3.3 The CIPT2 PESs

The next method to be examined is CIPT2. As this method treats the active space via CI, it is expected to be the most accurate in terms of interactions between the different states, but also the one with the worst SCE. Interestingly however, the energy difference between the two states of different multiplicity at the $\theta_1 = \theta_2 = 0^\circ$ linear geometry is asymptotically tending to 6.91 cm^{-1}, which is smaller than the corresponding number for RSPT2. Therefore, it seems the SCE in this method is less dependent on multiplicity.

In terms of the global minimum and the minimum of the pseudo-covalent bond, both are

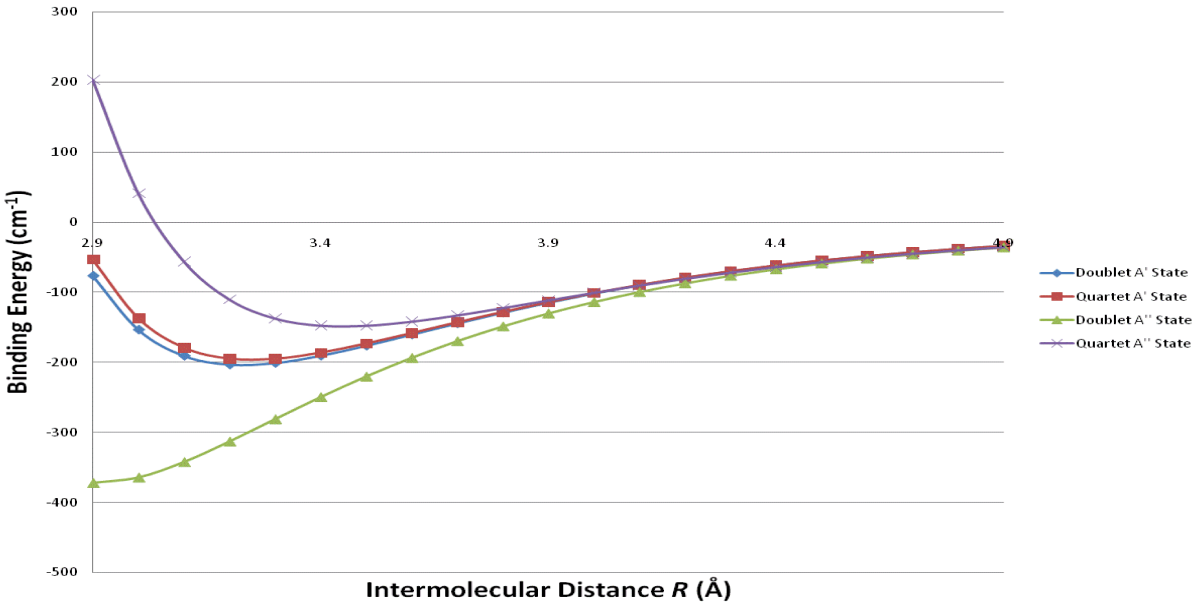

Figure 8.8: CIPT2 PECs for the parallel arrangement of the NO and O_2 ($\theta_1 = \theta_2 = 90°$)

in line with the RSPT2 and NEVPT2, all predicting the same angular geometries. However, for CIPT2, the lowest point in the PESs is at the same distance as RSPT2, $R = 2.9$ Å, which indicates that the interaction is dominated by the spin-coupling effects. One would expect this to lead to NO_3 formation, although without counterpoise correction we cannot be certain. Unlike RSPT2, all PECs converged to the same value in the long range, and unlike NEVPT2 all PECs were smooth curves. The CIPT2 results for the parallel geometry are given in figure 8.8.

In the geometries $\theta_1 = 180°, \theta_2 = 60°, 90°$, we met severe convergence problems, as was the case with all the previous methods. However, there were no unnaturally large exchange contributions, as were noticed for the RSPT2 results, although the calculated energies for the complex were approximately 2.8 Hartrees higher than for the rest of the geometries. The shape of the PEC is similar to the NEVPT2 case, with the quartet state forming a van der Waals minimum while the doublet states' energy continues to drop as the intermolecular distance decreases, again leading to NO_3 formation.

Here we should note why no counterpoise correction was performed: the NO monomer has one single valence electron, and to the CI program (which is used to treat the CIPT2 active space orbitals), this is equivalent to NO being an one-electron species. Thus, no two-electron

excitation is possible and no CI calculations may be performed with[4] NO, and therefore no counterpoise correction was possible. Thus, as was mentioned in the introduction, the binding energies were approximated by subtracting the difference from a calculation of the same state with $R = 150$ Å, which also corrected (uniformly) for the size consistency error.

Finally, like RSPT2, in the CIPT2 calculations there were no points that the quartet state was lower in energy than the doublet state for the A' geometry. For the A'' states again it happens only in the limited number of geometries specified before. The dependence of this effect on the intermolecular distance is intermediate to the RSPT2 and NEVPT2 surfaces, as it now extends to $R = 4.3$ Å. At most, the quartet state is lower than the doublet by 592.32 cm^{-1}, which is between the values predicted by the RSPT2 and NEVPT2 surfaces.

8.3.4 The Coupled-Cluster PESs

Finally, we examine the results from the coupled cluster calculations. As this is a single reference method, it is only possibly appropriate for the quartet states. At the geometry $\theta_1 = \theta_2 = 0°$ there is no difference between the two symmetries. The PECs for all methods in this geometry are shown in the figure 8.9:

As it can be seen from the graph, the shape of the PECs is roughly the same for all methods. It is interesting that the RSPT2 and CIPT2 methods give practically the same energy, which is lower than the RCCSD(T) result, while NEVPT2 gives a largest binding energy than all and is furthest from the RCCSD(T) result. This ordering is representative of most geometries.

For the rest of the analysis, the energy difference between the two quartet states is used. One surprising finding was that this was virtually the same (with a maximum difference of 8.23 cm^{-1}, but typically with a deviation of less than 1 cm^{-1}) between the CIPT2 and RSPT2 methods. It is believed that this was a result of the large active space used in these calculations. For this reason, we will not discuss CIPT2 separately in this section, but any conclusions on RSPT2 may be inferred for CIPT2 as well.

[4]The interested reader may find more information on [102], where a similar situation, this time for the lithium atom, is explored.

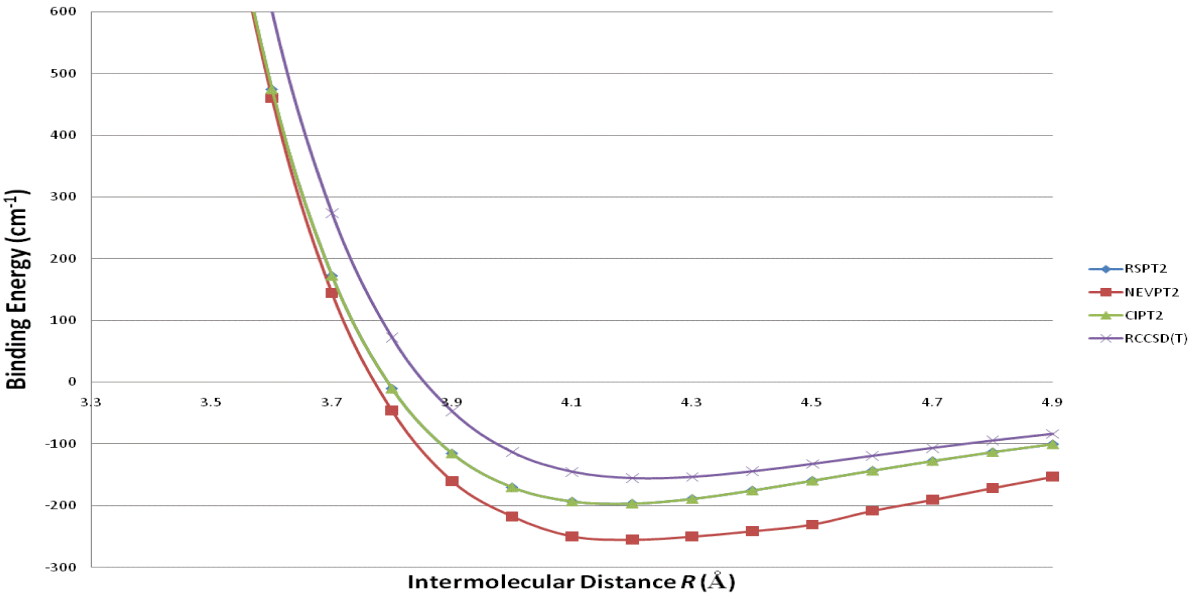

Figure 8.9: PEC of the quartet state as calculated by different methods for the NO-OO linear geometry

Typically NEVPT2 seemed to give the largest difference between the two quartet states, while RCCSD(T) the lowest, although in some cases RCCSD(T) became the lowest. Yet, as RSPT2/CIPT2 and NEVPT2 operated on multireference wavefunctions, while RCCSD(T) operated on a RHF wavefunction, as well as each having a different Hamiltonian, these results are not directly comparable. What is comparable is the shape of the PECs at different geometries. In most cases, all methods give an exponential difference between the two symmetries (except when the complex is linear), as demonstrated in figure 8.10 for the $\theta_1 = 120°, \theta_2 = 30°$ geometry. This graph is the typical for most geometries. Also, all PECs converge as expected at the long range. This is also true for the critical $\theta_1 = 90°, \theta_2 = 90°$ geometry, as it may be seen from figure 8.11.

Still, two issues were noticed. The first one concerned the NEVPT2 method, whose variation with distance sometimes did not give a smooth curve which was the case for the rest of the methods[5]. This is particularly obvious in the case of the geometry where $\theta_1 = 30°$ and $\theta_2 = 90°$, which is shown in figure 8.12. This is also one of the few cases that the RCCSD(T) curve overtakes the RSPT2/CIPT2 curve at short range.

[5]It should be stated clearly that this only occurs when the difference between the two quartet states are considered. The complex energy PECs are a smooth function of distance.

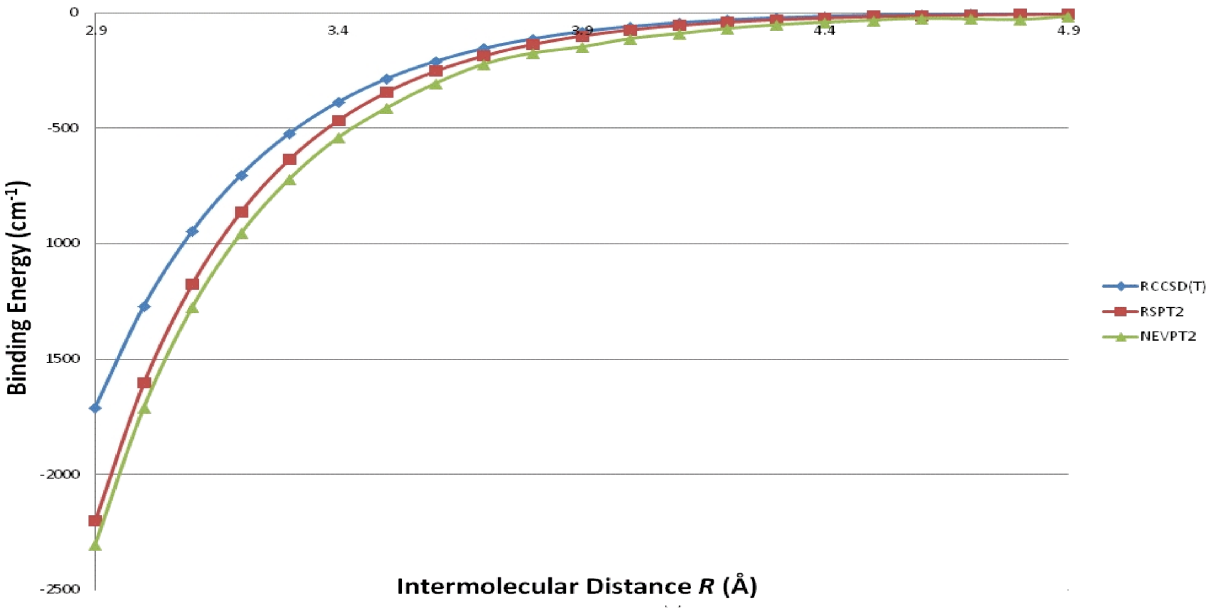

Figure 8.10: Difference PEC between the A' and A'' symmetry quartet spin states for $\theta_1 = 120°, \theta_2 = 30°$

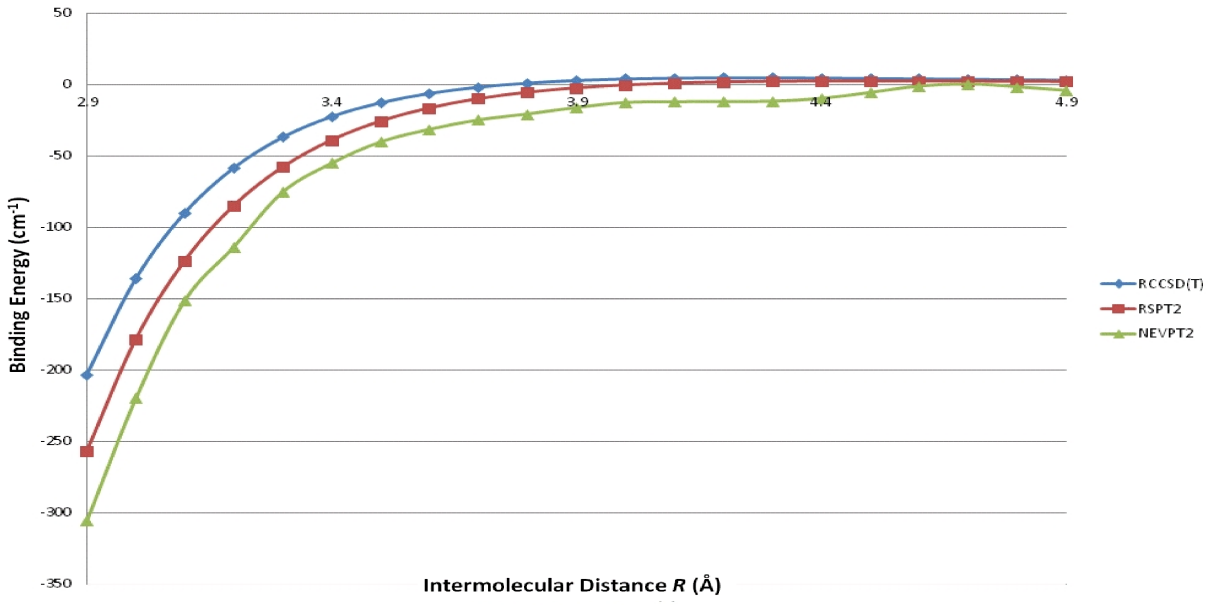

Figure 8.11: Difference PEC between the A' and A'' symmetry quartet spin states in parallel arrangement of the NO and O_2 ($\theta_1 = \theta_2 = 90°$)

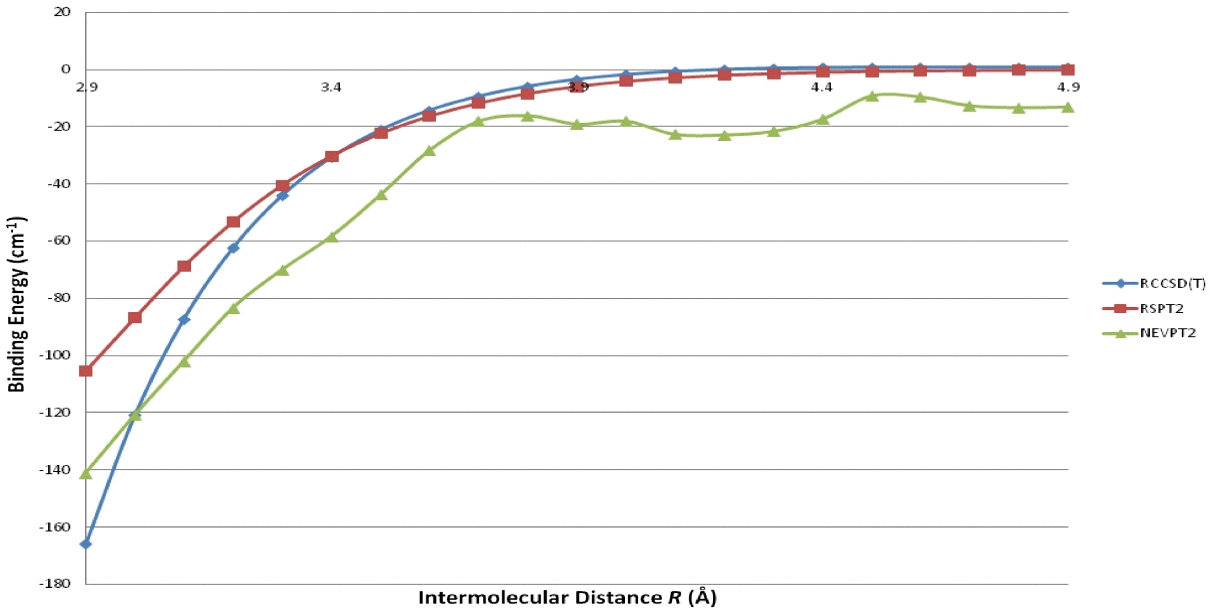

Figure 8.12: Difference PEC between the A' and A'' symmetry quartet spin states for $\theta_1 = 30°, \theta_2 = 90°$

The second issue found was that at specific geometries, namely ($\theta_1 = 0°, \theta_2 = 30°$), ($\theta_1 = 90°, \theta_2 = 30°$) and ($\theta_1 = 90°, \theta_2 = 60°$), the multireference perturbation methods and the RCCSD(T) method predict a different trend altogether for the energy. For the last two of these cases, the RSPT2/CIPT2 curves are similar to the rest of the geometries, while the variation of the RCCSD(T) curve is of the opposite sign, as is portrayed by the ($\theta_1 = 90°, \theta_2 = 60°$) PECs in figure 8.13. It seems that the NEVPT2 curve is sampling both trends, giving overall a non-smooth line. This unclear trend may be related to the result that for this geometry NEVPT2 predicted the energy of the $^2A'$ to be higher to the $^4A'$ state, which does not relate with the rest of the observations made.

The difference between the RSPT2/CIPT2 and the RCCSD(T) PECs may be better explained by the ($\theta_1 = 0°, \theta_2 = 30°$) geometry, shown in figure 8.14. Here it is clear that in the long range the RSPT2/CIPT2 and RCCSD(T) curves coincide, while the NEVPT2 curve is not-smooth. By the appearance of this graph, it is possible that this is a case of curve crossing. In that case, only the MR methods would be able to continue on the lowest energy curve as seen, while the RCCSD(T) method will keep on the initial curve.

To assess this hypothesis we used the T1 diagnostic that may be calculated using coupled

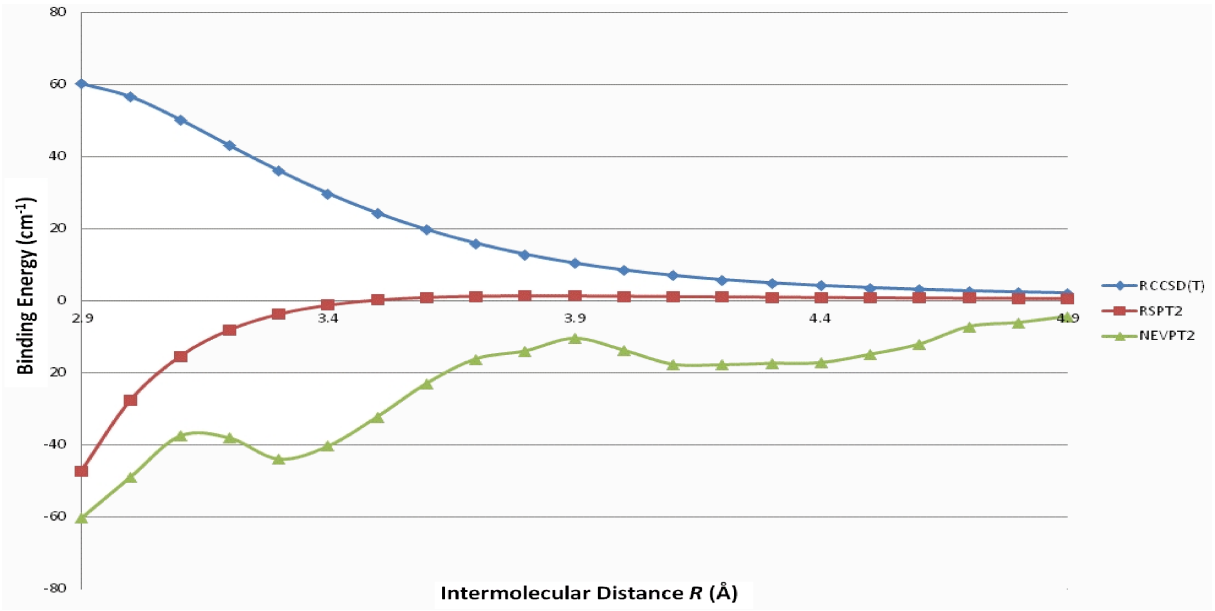

Figure 8.13: Difference PEC between the A' and A'' symmetry quartet spin states for $\theta_1 = 90°, \theta_2 = 60°$, where RCCSD(T) and MR methods predict an opposite energy trend with respect to distance

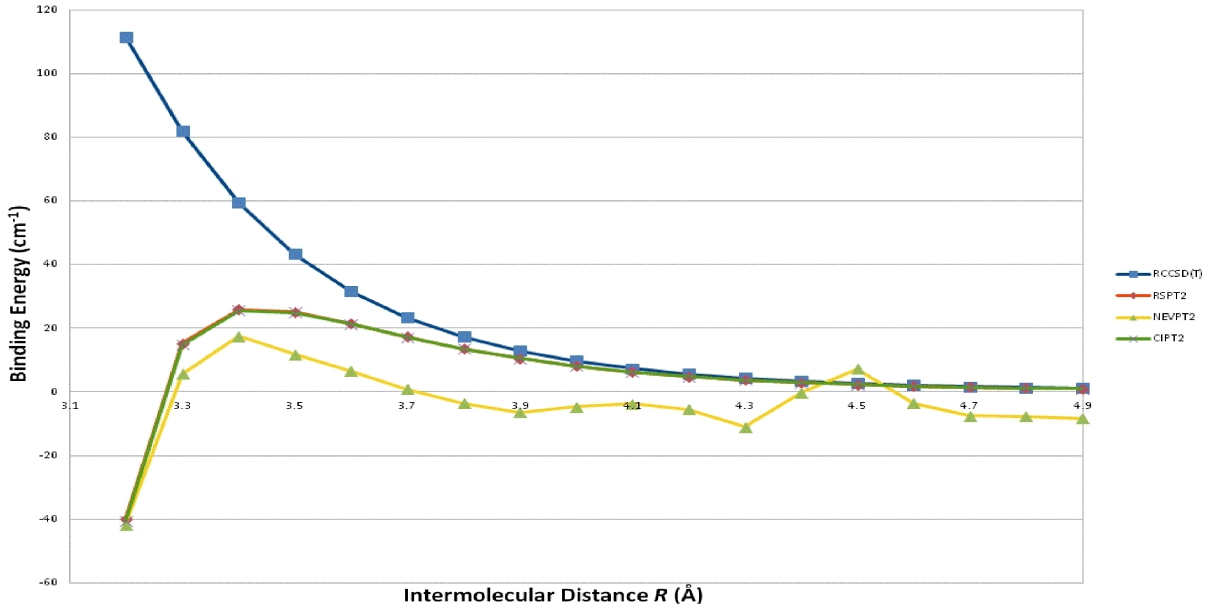

Figure 8.14: Difference PEC between the A' and A'' symmetry quartet spin states for $\theta_1 = 0°, \theta_2 = 30°$, where RCCSD(T) and MR methods differentiate at small distances

cluster methods. A value below 0.02 it usually taken to indicate a valid single reference case. For the quartet states of NO-O_2, the typical value is between 0.014-0.015, which is reassuring. For the $\theta_1 = 0^\circ, \theta_2 = 30^\circ$ geometry, the T1 value increases as the intermolecular distance decreases, reaching the value T1$= 0.039$ at $R = 3.1$ Å. Therefore, it is possible that the difference between the RSPT2/CIPT2 and RCCSD(T) PECs for ($\theta_1 = 0^\circ, \theta_2 = 30^\circ$) above can be explained as the wavefunction gradually obtains a multireference character. It is also interesting to note that the points calculated for all distances at the $\theta_1 = 180^\circ$ and $\theta_2 = 60^\circ$ geometry also had T1 > 0.02. This is the distance that charge transfer is possibly occurring.

Finally, the PEC of RCCSD(T) for the ($\theta_1 = 180^\circ, \theta_2 = 60^\circ, R = 2.9$ Å) geometry had many convergence problems for the aug-cc-pVTZ basis set. It was found however that this could be overcome by increasing the basis set to aug-cc-pVQZ. This gave a smooth line, but the T1 diagnostic (although lowered) still remained in the multireference range. It is interesting to note that the energies of the complex again were calculated approximately 2 Hartrees higher than in the rest of the geometries. Thus the RCCSD(T) method is not suitable for the interactions found at this angular geometry.

8.4 Discussion

In the previous sections we saw how different *ab initio* methods described the potential energy between the NO and the O_2 molecules when these meet in a planar configuration. It is clear that all methods have their limitations and no single approach can provide the whole answer. Nevertheless, by the combination of these methods we can obtain a good picture of the physical reality.

We showed that, in general, it is the Heitler-London rule rather than Hund's first rule that predicts the energy order of the surfaces with respect to their multiplicity. Therefore, the decisive interaction for the energy state ordering is the added exchange between the valence electrons, rather than the electron-electron repulsion for the case of open-shell open-shell species. As was shown earlier, this interaction, referred to as a pseudo-covalent contribution to the po-

tential energy, may be modelled by a second Born-Mayer term. This may be rationalised if we consider that the energy difference between these spin states only occurs when the spins of the molecules interact, which depends on the corresponding orbitals overlapping, and at large separations all spin states should be degenerate.

Previous work [103, 104, 105] has hinted at such an exponential interaction, for the O_2-O_2 complex, which was modelled using the Heisenberg effective Hamiltonian [50, 106]:

$$\hat{H}_{Heisenberg} = J(\omega, R)\mathbf{S}_a \cdot \mathbf{S}_b \tag{8.10}$$

where ω represents the angular coordinates of the system, R the intermolecular distance and S_a, S_b are the spin quantum numbers of the two states. However, Dhont *et al.* [50] showed that this expression cannot be used for more than two states, and since it is an effective Hamiltonian it offers no guiding principle in energy ordering of the states. Traditionally, different orientations of the molecules with respect to each other were included in the ω term of equation 8.10. However, we have shown that different symmetries influence the strength of the pseudo-covalent contribution due to the overlap of the electron orbitals. It was demonstrated earlier that this interaction may also be modelled by an exponential expression.

All three of the multireference perturbative electron correlation methods agreed on the ordering of the states, both in terms of symmetry and spin at the global minimum geometry $\theta_1 = \theta_2 = 90^\circ$. However, NEVPT2 predicted a van der Waals minimum for the $^2A''$ state, while RSPT2 and CIPT2 calculations suggested NO_3 formation with no barrier.

RSPT2 and CIPT2 methods are also known to suffer from SCE. Although CIPT2 is expected to be less size-consistent than RSPT2, when the difference between PESs of the same symmetry but different multiplicity is taken, there seems to be a large degree of SCE cancellation, which is not true for RSPT2. Namely, in the calculations with R=150 Å, the former has a difference of SCE of 21.5 cm^{-1}, while the latter of only 5.9 cm^{-1}. The rest of the methods did not have any difference in the energy of the states at $R = 150$ Å.

Particularly interesting are the geometries where $\theta_2 = 180^\circ$ and $\theta_1 \geq 60^\circ$. In these geome-

tries, a different effect seems to be taking place and a charge transfer between the two molecules may occur. This agrees with the calculated dipole moments as well as with the monomer relative ionisation energies and electron affinities, as well as with the large values of the T1 diagnostic. Although previous research [7, 99, 107] suggests that usually this is a small effect, it was argued how a complex of free radicals is a special case. In this case, RSPT2 unfortunately provided unnatural results. The same calculation was attempted again with RSPT3, and the results were still unnatural, and actually the SCE difference between the different multiplicities seemed to increase. From these we decided that the RSPT3 was also unsuitable, however the large difference between the RSPT2 and RSPT3 results indicates that the active space used may be insufficient and higher energy states could contribute.

Finally, the energy difference between the two quartet spin states was used to compare the multireference perturbation method results to the "gold standard" RCCSD(T) calculations. It was found that the NEVPT2 approach sometimes gave PECs which are not a smooth function of distance and contained false minima. This limited our trust on the results of the NEVPT2 method. Also, it was found that all the perturbative methods usually predicted a larger separation between the quartet states than RCCSD(T).

The concluding suggestion for modelling analogous systems is a combination of the difference between the CIPT2 surfaces superimposed on the RCCSD(T) surface for the single-reference state. CIPT2 seems to provide the most consistent answers (in terms of fewer unnatural results) than RSPT2 and also its SCE depends less on the multiplicity of the state. RSPT2 unfortunately gave unnatural results for some geometries and NEVPT2 showed inconsistent separation between states of the same multiplicity but different symmetry, while CIPT2 suffered from neither of these problems. However, CIPT2 unfortunately had problems in performing the counterpoise correction calculations, but this can be overcome if one uses the difference between different PESs rather than the PESs themselves.

Finally, we have fitted the difference between the PESs of different spin but same symmetry (calculated using the CIPT2 method), for both symmetries, as well as the difference between the two spin-averaged potentials between different symmetries. For all cases, a global fit was

Table 8.1: RMSD in global fits of the NO-O_2 PESs

PES	RMSD/cm^{-1}
Difference of spin states in A' symmetry	1.584
Difference of spin states in A'' symmetry	1.462
Difference between spin-averaged potentials of different symmetries	1.680

performed, which covered all geometries. The function used was an exponential, with an inverse polynomial expansion for the distance variable multiplied by an angular dependent function. For the latter, we chose a linear combination of a product of associated Legendre polynomials ($\mathscr{P}^2_m(\theta)$), one representing the angular variable of each molecule. As only the case of $\phi = 0°$ was examined, no ϕ dependence was included in the potential, and also $m_{NO} = -m_{O_2} = m$. The sum of the ranks of the associated Legendre polynomials was limited to 6. An odd-rank associated Legendre polynomial for O_2 would distinguish between configurations where the two oxygen atoms were interchanged, so only even-rank polynomials were used.

Moreover, a constant C function was added to ensure all points were of the same sign so that the fit could be done using the natural logarithm of the points, making the calculations easier:

$$\begin{aligned}
V &= C+\exp\left[\left(a+bR+\frac{c}{R}\right)\left(1+c_{120}\mathscr{P}^1_0(\theta_{NO})\mathscr{P}^2_0(\theta_{O_2})+c_{121}\mathscr{P}^1_1(\theta_{NO})\mathscr{P}^2_1(\theta_{O_2})\right.\right.\\
&+ c_{140}\mathscr{P}^1_0(\theta_{NO})\mathscr{P}^4_0(\theta_{O_2})+c_{141}\mathscr{P}^1_1(\theta_{NO})\mathscr{P}^4_1(\theta_{O_2})\\
&+ c_{220}\mathscr{P}^2_0(\theta_{NO})\mathscr{P}^2_0(\theta_{O_2})+c_{221}\mathscr{P}^2_1(\theta_{NO})\mathscr{P}^2_1(\theta_{O_2})+c_{222}\mathscr{P}^2_2(\theta_{NO})\mathscr{P}^2_2(\theta_{O_2})\\
&+ c_{240}\mathscr{P}^2_0(\theta_{NO})\mathscr{P}^4_0(\theta_{O_2})+c_{241}\mathscr{P}^2_1(\theta_{NO})\mathscr{P}^4_1(\theta_{O_2})+c_{242}\mathscr{P}^2_2(\theta_{NO})\mathscr{P}^4_2(\theta_{O_2})\\
&+ c_{320}\mathscr{P}^3_0(\theta_{NO})\mathscr{P}^2_0(\theta_{O_2})+c_{321}\mathscr{P}^3_1(\theta_{NO})\mathscr{P}^2_1(\theta_{O_2})+c_{322}\mathscr{P}^3_2(\theta_{NO})\mathscr{P}^2_2(\theta_{O_2})\\
&+ c_{420}\mathscr{P}^4_0(\theta_{NO})\mathscr{P}^2_0(\theta_{O_2})+c_{421}\mathscr{P}^4_1(\theta_{NO})\mathscr{P}^2_1(\theta_{O_2})+c_{422}\mathscr{P}^4_2(\theta_{NO})\mathscr{P}^2_2(\theta_{O_2})\\
&+ c02\mathscr{P}^2_0(\theta_{O_2})+c04\mathscr{P}^4_0(\theta_{O_2})+c10\mathscr{P}^1_0(\theta_{NO})+c20\mathscr{P}^1_0(\theta_{NO})\\
&+ \left.\left. c30\mathscr{P}^3_0(\theta_{NO})+c40\mathscr{P}^1_0(\theta_{NO})\right)\right] \qquad (8.11)
\end{aligned}$$

Therefore, 26 fitting parameters were required for approximately 860 points in every case (at some points the calculation failed). The fit for all surfaces surfaces was performed using MATHEMATICA8 [108] and the RMSD values are given in the table 8.1. and the parameters for the

fits are given along with the code used to perform the fitting in CD attached to this thesis. The RSME values are good considering that the error is mostly localised at areas were the energies fitted were in excess of 3,000 cm^{-1}.

8.5 Conclusion

In this chapter we have examined the van der Waals complex formed by the open-shell molecules NO and O_2. The aim of this chapter was to understand the major contributions in the energy ordering of the PESs, how different *ab initio* methods portray that ordering, how could this be represented functionally and finally to formulate a suggestion for studying such systems.

Three multireference perturbative methods were examined: RSPT2, NEVPT2 and CIPT2. For each one in turn, their strengths and weaknesses were discussed, mainly with respect to the energy ordering they predicted and the splitting of different spin states. Then, with reference to the RCCSD(T) method, the splitting between different symmetries was discussed for the quartet spin states. What was found was that for all the methods, the decisive contribution in energy ordering was the added exchange interaction between the molecules, rather than the electron-electron repulsion. This means that the energy state ordering is better predicted by the Heitler-London rule rather than the Hund's first rule. This was referred to as a "pseudo-covalent" contribution to the potential energy of the monomers, as the orientations of the molecules were not ordered to lead to classic covalent bonding between two atoms, but rather to maximise the overlap between molecular orbitals.

Moreover, at certain geometries, a charge transfer interaction was found, which proved challenging for all the methods. Although charge transfer is usually considered a small contribution, in this case it was explained how open-shell open-shell complexes may be an exception. Furthermore, it was demonstrated that both the difference between different spin states and different symmetries follows an exponential form. Using the function in equation 8.11, all of these interactions were modelled with a limited number of parameters to a good level of precision.

In closing, our suggestion for studying such systems is to take the difference between PESs of the spin states calculated using the CIPT2 method and use this to generate the surfaces from an RCCSD(T) PES. Also one should be careful of the points where the same surface varies significantly between the CIPT2 and RCCSD(T) result. The T1 diagnostic was found to be a reliable in predicting the multireference behaviour in various geometries. Future research may wish to examine how our results compare to surfaces calculated using a full MRCI method, or different basis sets.

Chapter 9

Fine and Hyperfine Interactions

"*It is the harmony of the diverse parts, their symmetry, their happy balance; in a word it is all that introduces order, all that gives unity, that permits us to see clearly and to comprehend at once both the ensemble and the details.*"

- Henri Poincare

9.1 Introduction

In chapter 2, the rigid rotor model was introduced, and it was shown how that gives rise to the rotational spectra of various kinds of molecules. However, the only source of angular momentum considered at that stage was the rotational angular momentum of the molecule. Now, having covered the necessary mathematics in chapter 3, we are equipped to explore the effects of the coupling between the different angular momenta.

The different possible sources of angular momenta, apart from the rotation of the molecule, are:

- The electron spin angular momentum, $\hat{S}$
- The nuclear spin angular momentum, $\hat{I}$

- The electron orbital angular momentum, $\hat{L}$

Of course not all of the above are present in every molecule or complex. For example, in closed electronic shells all electron spins are paired so there is no overall electron spin angular momentum. Therefore, only open-shell species may have a non-zero spin angular momentum. In these cases, the interaction of $\hat{S}$ with rotational and/or orbital angular momentum, gives rise to what is called fine structure. If a nucleus has a non-zero angular momentum, then its interactions with the rest of the angular momenta present gives rise to hyperfine structure. This case will be explored first in this chapter.

Moreover, only in the case of atoms and linear molecules is the nuclear electric field symmetric enough to define an orbital angular momentum. For linear molecules, Hund [11] has distinguished five extreme cases, two of which we will look at in more detail towards the end of this chapter. However, until then, the orbital angular momentum will be ignored.

The discussion in this chapter is specific to the terms that will be of use to us later on, i.e. those that arise in the van der Waals complexes of NO_2 with Ne and/or O_2. Therefore, only the case of a single nucleus with a non-zero angular momentum is considered. Furthermore, many terms are simplified due to the symmetry of the specific molecules studied[1].

Finally, the expressions given in this chapter are only valid for the molecules in their own principle axis system, and the complications that arise when used to evaluate the same matrix elements of a molecule in a different axis system (e.g. a space or complex-fixed) will be examined in a later chapter. The evaluation of the matrix elements of the terms introduced here depend on the coupling scheme used in every case. As this differs for the different complexes considered, this will be done in later chapters for each case individually.

[1]The full expressions may be found in references [109] and [110].

9.2 The Electric Quadrupole Interaction

If a nucleus has angular momentum $I > \frac{1}{2}$, then we can consider its interaction with the electric field created by the electrons in an analogous way to how we treated the electrostatic forces between molecules in chapter 7. That is, we can consider the interactions between the multipole moments of the nucleus with the field created by electrons.

The first term in this expansion would correspond to the interaction of the nuclear total charge (monopole) with the field, which is completely isotropic and thus produces no splittings in a microwave spectrum. Furthermore, by symmetry arguments [16], all odd-rank nuclear moments (e.g. dipole) are necessarily zero, thus the first surviving term with an effect on the spectrum is the quadrupole interaction[2]. In order to have a quadrupole moment, the nucleus needs to have an angular momentum $I \geq 1$. Just as for a molecule, the quadrupole moment of a nucleus transforms as a second rank spherical tensor operator, $T^2_{q_1}(Q)$.

The interaction has to yield a scalar result, which can be obtained by the dot product of the quadrupole tensor with the same rank field component. This corresponds to the electric field gradient $T^2_{q_2}(\nabla E)$:

$$\hat{H}_Q = eT^2(Q) \cdot T^2(\nabla E) \tag{9.1}$$

where e is the electronic charge. The expectation value of $T^2(Q)$ depends on the nuclear angular momentum state of the molecule:

$$\langle I', m'_I | T^2(Q) | I, m_I \rangle$$

However, as the separation between different nuclear states is far larger than that of rotational states, we can ignore all non-diagonal terms with respect to I. $T^{k_2}_{q_2}(\nabla E)$ represents the second derivative of the potential created by the electrons at the nucleus and is a property of the molecule in question, independent of its rotational state. For this reason, we can take the expec-

[2] As the quadrupole itself is often too weak to be resolved, the next surviving term, i.e. the hexadecapole moment, is ignored.

tation values of $T^2_{q_2}(\nabla E)$ as:

$$\langle \eta | T^2(\nabla E) | \eta \rangle$$

where $|\eta\rangle$ are vibrational and electronic states of the molecule. In theory these may be calculated by *ab initio* calculations, however these are subject to many errors as was explained in chapter 4. Instead, for molecules that these have been measured experimentally[3], as is the case for NO_2, it is best to relate these matrix elements to the experimental parameters [109].

In general, there are five independent components to a second rank tensor, but in the case of NO_2 being a planar molecule, there are only three [110]. Due to the symmetry axis of NO_2, this is further reduced to only two independent parameters. These are related to the experimentally-defined parameters as:

$$aa_Q = \frac{2eQ}{2I(2I-1)} \langle T^2_0(\nabla E) \rangle \tag{9.2}$$

$$\frac{1}{2}(bb_Q - cc_Q) = \frac{\sqrt{6}eQ}{2I(2I-1)} \langle T^2_{\pm 2}(\nabla E) \rangle \tag{9.3}$$

where $Q = 2\langle I, I | T^2_0(Q) | I, I \rangle$.

9.3 Magnetic Hyperfine Interactions

Now we move to the case of an open-shell species. In this case, we have to consider the interaction of the spin angular momentum with the other angular momenta. First we consider the interaction between spin ($\hat{S}$) and the nuclear angular momentum ($\hat{I}$): The motion of the unpaired electron creates a magnetic field, which interacts with the magnetic moment of the nucleus. This may be taken at two extreme cases, when the electron and the nucleus are far enough apart as to be validly considered as point multipoles, and when the distance between the two is too small for that assumption to be valid.

In the former case, the interaction may be considered in an analogous way to the multipole

[3] The matrix elements used for this fitting along with expressions on the intensities of the corresponding lines may be found in reference [11].

expansion used in chapter 7. Then, the interaction can be analysed as the interaction of a nuclear multipole with an electron multipole via an interaction tensor. The first term in such an expression would correspond to the Coulomb interaction between the nuclear charge and the electron charge[4]. The next term, which dominates this interaction, is that between the nuclear magnetic dipole with the electron spin dipole. This interaction will be examined first.

In the other case, i.e. when the distance between the electron and the nucleus is too close for them to be considered as two point multipoles, we have the Fermi contact interaction. This is dominated by the interactions between the nucleus and the electrons that can be found at the nucleus, i.e. those in the s-orbitals. This interaction is examined later.

Therefore, the overall magnetic hyperfine Hamiltonian may be expressed as:

$$\hat{H}_{magn} = \hat{H}_{FC} + \hat{H}_{dd} \tag{9.4}$$

where the first term corresponds to the Fermi contact and the second to the dipole-dipole interaction.

9.3.1 The Magnetic Dipole-Dipole Interaction

This is a through-space anisotropic interaction between the dipole moments of an electron and the nucleus. Therefore, in a similar way to the multipole expansion used earlier, we consider both the nucleus and the electron as point multipoles. For this reason, the expressions derived below are only valid when there is a large enough distance between the two.

Following similar arguments as those presented in chapter 7, this interaction may be considered as a scalar product between the second rank vector product of two first rank tensors (one for the nuclear and one for the electron spin) and a second rank interaction tensor:

$$\hat{H}_{dd} = -\sqrt{10} g \mu_B g_N \mu_N T^2(S,I) \cdot T^2(C) \tag{9.5}$$

[4]In our case we take this interaction into account by the *ab initio* calculations.

where g and g_N are the electron spin and nuclear spin g-factors respectively, μ_B and μ_N and the Bohr and nuclear magnetons, and $T^2(C)$ is the interaction tensor for this coupling. The g-factors and the magnetons appear in the equation above as the relationship between the Cartesian dipole and the angular momentum for the electron spin and the nucleus is:

$$\hat{\mu}_S = g\mu_B\hat{S} \qquad \hat{\mu}_I = g_N\mu_N\hat{I}$$

while the factor of $\sqrt{10}$ is the proportionality between Cartesian and spherical tensor coordinates.

According to expression 3.102, the vector sum of the nuclear and electron spin angular momenta is equal to:

$$T^2_p(S,I) = -(-1)^p\sqrt{5}\sum_{p_1,p_2} T^1_{p_1}(S)T^1_{p_2}(I)\begin{pmatrix} 1 & 1 & 2 \\ p_1 & p_2 & -p \end{pmatrix} \tag{9.6}$$

The expectation values of the nuclear and electron spin angular momentum depend on the corresponding quantum numbers in the basis set. Yet, as the energy separation between different spin or nuclear states is very large, we can ignore all but the diagonal contributions. Finally, we need to consider the interaction tensor $T^2_q(C)$. The expectation values of this operator depend on the electronic and nuclear wavefunctions, which are represented by $|\eta\rangle$:

$$\langle T^2_q(C)\rangle = \left\langle \eta \left| \frac{\mathscr{C}^2_q(\theta,\phi)}{R^3} \right| \eta \right\rangle \tag{9.7}$$

where $\mathscr{C}^2_q(\theta,\phi)$ is a second rank Racah harmonic, and the arguments (R,θ,ϕ) are the polar coordinates of the electron with respect to the nucleus. This expectation value is characteristic of the molecule in question, and, where available, it is possible to connect the expectation values of the various components of the operator to experimentally fitted constants. As with the electric quadrupole interaction, there are in theory five independent components to the interaction

tensor, but in the case of NO_2, this again simplifies to only two non-zero components:

$$g\mu_B g_N \mu_N \langle T_0^2(C)\rangle = \frac{1}{2} aa_I = -\frac{1}{2}(bb_I + cc_I) \tag{9.8}$$

$$g\mu_B g_N \mu_N \langle T_2^2(C)\rangle = g\mu_B g_N \mu_N \langle T_{-2}^2(C)\rangle = \frac{1}{\sqrt{24}}(bb_I - cc_I) \tag{9.9}$$

There is a subtlety hidden in the indices used in the above expression: the spin and nuclear angular momenta are usually quantised in space, while in equation 9.7, the projections are taken on the molecular axis. As was noted in chapter 3, all spherical tensor operators must be transformed in the same frame of reference before being evaluated. This can be done using the formulæ 3.75 and 3.76.

9.3.2 The Fermi Contact Interaction

The approximation that the nucleus may be treated as a point charge, which was used in the dipole-dipole case, fails when the electrons come into very close proximity to the nucleus. The dominant effect comes from s-orbital electrons, as they have a non-zero probability of being found at the nucleus. Due to the spherical distribution of the s-orbitals, this is an isotropic effect. The Fermi contact interaction Hamiltonian is:

$$\hat{H}_{FC} = \alpha_F T^1(S) \cdot T^1(I) \tag{9.10}$$

where the α_F is the Fermi contact constant for the molecule in question. α_F depends on the electron distribution at the nucleus, and is characteristic of the molecule in a specific electronic state.

9.4 Electron Spin-Rotation Interaction

This interaction physically represents the interaction of the magnetic moment of the electron with the magnetic field generated by the rotation of the molecule (motion of the charged elec-

trons and nuclei). As both the rotation of the molecule and the nuclear spin are represented by first rank tensors, their vector product gives rise to a zeroth, a first and a second rank tensor:

$$T^1(S) \otimes T^1(N) = T^0(N,S) \oplus T^1(N,S) \oplus T^2(N,S) \tag{9.11}$$

Then, an interaction tensor of the same rank can be matched to each of the terms in the right hand side (as to have the same rank) to give an overall scalar product. Therefore, we may write this interaction as:

$$\hat{H}_{SR} = \sum_{k=0}^{2} \Big(T^k(\varepsilon) \cdot T^k(N,S) \Big) \tag{9.12}$$

where $T^k(\varepsilon)$ is the interaction tensor for the spin-rotation Hamiltonian and $T^k(N,S)$ is the product tensor of rank k from the coupling of the rotation and spin angular momenta:

$$T^k_p(N,S) = -(-1)^p \sqrt{5} \sum_{p_1,p_2} T^1_{p_1}(N) T^1_{p_2}(S) \begin{pmatrix} 1 & 1 & k \\ p_1 & p_2 & -p \end{pmatrix} \tag{9.13}$$

The $T^k(\varepsilon)$ expectation values depend on the molecule's electronic wavefunction, which is also usually implicit:

$$\langle \eta | T^k(\varepsilon) | \eta \rangle$$

Again, these may be related to the experimentally-determined [111] constants. In the case of NO_2, due to symmetry only the following components survive:

$$\langle T^0_0(\varepsilon) \rangle = -\frac{1}{3}(\varepsilon_{aa} + \varepsilon_{bb} + \varepsilon_{cc}) \tag{9.14}$$

$$\langle T^2_0(\varepsilon) \rangle = \frac{1}{6}(2\varepsilon_{aa} - \varepsilon_{bb} - \varepsilon_{cc}) \tag{9.15}$$

$$\langle T^2_{\pm 2}(\varepsilon) \rangle = \frac{1}{2}(\varepsilon_{bb} - \varepsilon_{cc}) \tag{9.16}$$

The above are defined in the molecule-fixed axis system. Yet, there is a problem that the rotation of the molecule cannot be defined in the molecular frame, for reasons explained in chapter 3. Although at this stage we are not concerned with evaluating the matrix elements for the operators introduced, it is worth noting that for this reason there is a necessary difference be-

tween the frame that the rotation angular momentum, and the interaction tensor needs to be transformed. This necessarily leads to including a D-matrix, in order to transform the rotational angular momentum to the space-fixed frame. Since the D-matrix will depend on the Euler angles between the two frames, which are the same angles that the rotational angular momentum operates on, this will result in equation 9.12 being non-Hermitian. In order to resolve this, the usual procedure is to symmetrise the operator as:

$$\hat{H}_{SR} = \sum_{k=0,2} \Big(T^k(\varepsilon) T^k(N,S) + T^k(N,S) T^k(\varepsilon) \Big) \tag{9.17}$$

9.5 Electron Spin-Electron Spin

In the case that there is more than one unpaired electron, as is the case for the ground state oxygen molecule, their interaction gives rise to additional fine structure. Here, we consider the case of two electron spins (S_1, S_2). Once again, we can view this interaction as the interaction between two point multipoles, one on each electron. Similarly to the nuclear-electron spin angular momenta interaction, the dominant term when the two electrons are well separated is a magnetic dipole-dipole interaction:

$$\hat{H}_{SS} = \sqrt{6} g^2 \mu_B^2 T^2(C) \cdot T^2(S_1, S_2) \tag{9.18}$$

where g is the electron g-factor and μ_B the Bohr magneton. However, since the two spins are interacting, we may couple their angular momenta as:

$$S_1 + S_2 \rightarrow S \tag{9.19}$$

and now we can express the interaction in terms of the total spin angular momentum, S. Thus, in the coupled representation, the magnetic electron spin-electron spin interaction becomes:

$$\hat{H}_{SS} = \frac{2}{3} \lambda_{SS} T_0^2(S) \tag{9.20}$$

where λ_{SS} is the experimentally-defined spin-spin constant (again measured in the molecule-fixed frame) and S is the total spin angular momentum.

9.6 Orbital Angular Momentum: Hund's Cases

The one possible source of angular momentum that was mentioned in the introduction of this chapter, but so far ignored in this chapter, is that due to the orbital motion of the electrons.

In linear molecules the electric field is symmetric around the internuclear axis (which is different from non-linear molecules) and thus creates a directional field that interacts with the orbital angular momenta. If the interaction between the electric field of the nuclei and the orbital angular momentum is strong, then the projection of the orbital angular momentum L along the internuclear axis (Λ) may be a good quantum number.

Furthermore, the spin angular momentum (S) interacts with the magnetic field created by the orbital motion of the electrons (spin-orbit coupling). If both the spin-orbit coupling and the interaction between the orbital angular momentum and the electric field around the internuclear axis is strong, then not only Λ, but also the projection of S along the internuclear axis, Σ can be good quantum numbers. It is worth noting that if S couples to the internuclear axis, it does so via L and not directly.

Hund [16] defined five limiting cases for the possible order of coupling of L, S and R (the rotational angular momentum of the molecule). From these, we will only examine the two first ones, as these are the most common and of greater use to us.

Hund's Case (a): In Hund's case (a) the strongest interactions are between L and the electric field around the internuclear axis and with S. Therefore, as L is strongly coupled to the molecule, Λ is a good quantum number. Due to the strength of the S coupling to L, Σ is also a good quantum number. Thus, in this case, we can define the intermediate quantum

number G, and the coupling scheme would be:

$$L+S \rightarrow G \tag{9.21}$$

$$G+R \rightarrow J \tag{9.22}$$

where J is the total angular momentum in absence of any nuclear spin. Moreover, the projection of J along the internuclear axis (Ω) is a good quantum number:

$$\Omega = \Lambda + \Sigma \tag{9.23}$$

Hund's Case (b): In Hund's case (b), L is still strongly coupled to the internuclear axis, but now the spin-orbit interaction is too weak to couple S to the nuclear motion. Therefore, the coupling scheme now becomes:

$$L+R \rightarrow G \tag{9.24}$$

$$G+S \rightarrow J \tag{9.25}$$

Therefore, Λ remains a good quantum number, but Σ and Ω do not. This is the case for the oxygen molecule, where $\Lambda = 0$. Interestingly, it is possible for molecules to transits from case (a) to case (b) in higher rotational levels, as the increased rotation of the nuclei to be too fast and may uncouple S from the molecular axis.

Chapter 10

The Rotational Spectrum and Quantum Dynamics of the Ne-NO_2 Complex

"*I knew I had to succeed, as I was running out of things to fail.*"

- Thomas Edison

10.1 Introduction

In the introduction chapter, the motivation behind this thesis was explained: we wanted to investigate the grey area where the lines between van der Waals complexes and chemical species become blurry. We concentrated on two parameters: the degree of internal rotation (which are low-lying vibrational motions for the complex or hindered rotations for the constituent monomers) and the nature of the bonding between radical species. Moreover, we separated these two parameters to examine each one individually. The interactions taking place in a van der Waals complex between two radical species were examined theoretically in detail and were modelled using the NO-O_2 complex in chapter 8. Using this system it was possible to investigate both the effect of different spin states as well as of different symmetries.

In this chapter we concentrate on the effects of large amplitude motion within a van der

Waals complex. To do this, we have chosen one very weakly bound system, where it is questionable whether the semi-rigid model will be sufficient: the complex between an atom of neon and nitrogen dioxide (Ne-NO_2). As neon has a low polarisability, the bonding in Ne-NO_2 is expected to be very weak and thus the dynamical effects should be significant. Moreover, the unpaired electron of NO_2, gives rise to a rich fine and hyperfine structure which is sensitive to the intermolecular potential and thus may be used to probe the internal states of the complex in great detail.

Furthermore, the Ne-NO_2 complex falls into a series of Rg-NO_2 complexes that have been investigated by the group over the years, namely Ar-NO_2 [112, 113], Xe-NO_2 [114] and Kr-NO_2 [115], using the semi-rigid approach. This past experience in the group gave us confidence that we are able to understand the spectrum of such complexes. Yet, when the past Part II student, Lee Dyer [116], recorded a number of transitions of the Ne-NO_2 complex, he discovered that it was not possible to finish their analysis using the semi-rigid model. Therefore, it was deemed necessary to perform the complete quantum dynamics for this complex, which, as will be seen later, also offered new insight into the fitted constants of the previously investigated complexes.

10.2 The Ne-NO_2 Complex

Before presenting our approach and results, we will briefly discuss the NO_2 molecule as well as some key findings of previous research for the Rg-NO_2 complexes.

10.2.1 NO_2 molecule

In contrast to our approach to when examining the NO-O_2 van der Waals complex in chapter 8, here we are interested in predicting and assigning the rotational spectrum of the Ne-NO_2 complex including its fine and hyperfine structure, rather than simply investigating the energy order-

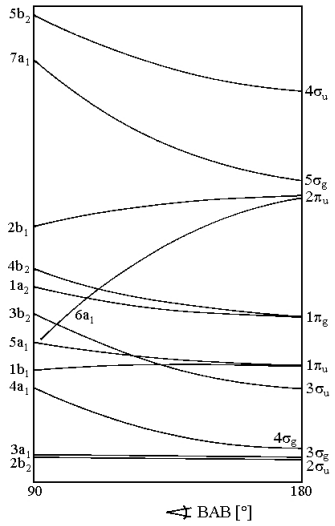

Figure 10.1: Walsh Diagram for AB_2 molecules [117]

ing of the states. For this reason we will use the full molecular Hamiltonian of the monomers. Since neon is a rare gas atom with no internal structure, we only need to consider NO_2.

The shape of the NO_2 molecule can be correctly predicted to be bent (C_{2v} point group symmetry) by the Walsh diagrams for AB_2 molecules [1], shown in figure 10.1 [117], with an electron configuration [118]:

$$1b_2^2, 1a_1^2, 2a_1^2, 3a_1^2, 2b_2^2, 4a_1^2, 3b_1^2, 5a_1^2, 1b_1^2, 4b_2^2, 1a_2^2, 6a_1^1$$

Thus, the term symbol of the ground state[1] is $^2A_1$. The angle of NO_2 is unusually wide (134.4° degrees) for the uncharged molecule, and changes dramatically with the occupancy of the valence orbital: NO_2^+ is linear with an electron configuration of:

$$1\sigma_u^2, 1\sigma_g^2, 2\sigma_g^2, 3\sigma_g^2, 2\sigma_u^2, 4\sigma_g^2, 3\sigma_u^2, 1\pi_u^4, 1\pi_g^4$$

while NO_2^- has an angle[2] of 114° degrees [120] with the electron configuration:

$$1b_2^2, 1a_1^2, 2a_1^2, 3a_1^2, 2b_2^2, 4a_1^2, 3b_1^2, 5a_1^2, 1b_1^2, 4b_2^2, 1a_2^2, 6a_1^2$$

[1]The first excited electronic state is doublet B_2, which is 1.289 eV higher than the ground state, and only mixes with the ground state in high vibrational levels, so for our purposes it may be ignored [119].

[2]The bond length on the other hand only varies from 1.1934 Å in the uncharged molecule by 0.05 Å at most in the ions.

Table 10.1: NO_2 rotational constants

Parameter	Value /MHz
A	23 9905.41 (63)
B	13 002.262 (123)
C	12 304.888 (66)

This demonstrates that NO_2 lies in the sensitive balance between linear and bent geometry. Because of this sensitive balance, it has proved challenging for *ab initio* calculations to correctly predict the geometry of the ground state. It is generally accepted that a multireference method, such as CASPT2 or MRCI [121] is required to achieve this, although in ref. [119] it was argued that RCCSD(T) is also able to provide the correct answer using a single configuration approach[3].

Experimentally, the question of the equilibrium geometry was settled by Bird [122, 123] in 1956. The NO_2 rotational constants were later determined with higher precision by Cabana et al. [124] and are given in table 10.1, where the numbers in the parenthesis give the uncertainty as one standard deviation with respect to the last decimal place quoted. Since Ray's asymmetry parameter[4] equals -0.99387 for NO_2 and the value for a prolate symmetric top is -1, to a good approximation, NO_2 can be thought of as a near-prolate symmetric top.

10.2.1.1 Fine and hyperfine structure

Due to the presence of both an unpaired electron and a nuclear spin angular momentum, NO_2 has a rich fine and hyperfine structure. Details about each interaction were given in chapter 9.

The unpaired electron's spin interacts with the magnetic field created by the rotation of the molecule, which gives rise to its spin-rotation interaction. This causes the largest splittings in the NO_2 spectra. Moreover, the nitrogen nucleus has a spin angular momentum $I_N = 1$. This interacts with the field created by the rest of the nuclei and the surrounding electrons, giving rise

[3] Although in all the PES that were calculated, the monomer geometry was fixed to its equilibrium value, it is questionable whether a method that cannot predict the correct geometry for the monomer ground state could describe the interaction accurately.

[4] See chapter 2

Table 10.2: Experimentally measured fine and hyperfine constants for the NO_2 molecule

Parameter	Value / MHz	Parameter	Value / MHz
ε_{aa}	5401.76 (7)	aa_Q	0.45(6)
ε_{bb}	7.65 (2)	bb_Q	-1.7(8)
ε_{cc}	-95.24(2)	cc_Q	1.26(5)
aa_I	-22.16 (7)	a_F	147.23(3)
bb_I	39.85 (11)	cc_I	-17.69(8)

to the electric quadrupole interaction. The interaction between the nuclear angular momentum and the field created by the motion of the unpaired electron gives rise to the magnetic hyperfine interactions, namely the dipole-dipole and the Fermi contact interactions. The Fermi contact interaction is the strongest of the fine and hyperfine interactions in NO_2.

Therefore the Hamiltonian for the NO_2 molecule may be written as:

$$\hat{H}_{NO_2} = \hat{h}_{rot} + \hat{h}_{SR} + \hat{h}_{DD} + \hat{h}_Q + \hat{h}_{FC} \tag{10.1}$$

where $\hat{h}_{rot}$ is the rotational, $\hat{h}_{SR}$ the spin-rotation, $\hat{h}_{DD}$ the dipole-dipole, $\hat{h}_Q$ the electric quadrupole and $\hat{h}_{FC}$ the Fermi contact operators[5]. All the fine and hyperfine molecular constants used in this work are given in table 10.2 [125], following the notation used in chapter 9.

10.2.1.2 Nuclear spin statistics

According to the Pauli principle, the overall wavefunction of fermions (i.e. particles with half-integer spin) must be antisymmetric with respect to the interchange of two indistinguishable particles, whilst in the case of bosons (integer spin) it must be symmetric. The total wavefunction may be written as a product of the electronic (including the electron spin), the translational, the vibrational, the rotational and the nuclear spin wavefunctions:

$$|\psi_{total}\rangle = |\psi_{el}\rangle|\psi_{tranl}\rangle|\psi_{vibr}\rangle|\psi_{rot}\rangle|\psi_{ns}\rangle \tag{10.2}$$

[5] Analytic expressions for these terms may also be found in references [111] and [123].

The vibrational wavefunction can be taken as the solution to the Schrödinger equation for a harmonic oscillator, i.e. proportional to a Hermite polynomial, $\mathscr{H}_v$:

$$\psi_{vibr} = N_v \mathscr{H}_v(y) \exp[y^2/2] \tag{10.3}$$

$$y = \frac{x}{a} \quad ; \quad a = \left(\frac{\hbar}{mk}\right)^{\frac{1}{4}} \tag{10.4}$$

where v is the vibrational quantum number, x is the displacement from a reference position and a is a scaling factor, which in the case of the harmonic oscillator depends on the force constant of the parabolic potential (k) and the mass (m) of the object. N_v is a normalisation constant. The formula for generating Hermite polynomials is:

$$\mathscr{H}_v(x) = (-1)^v e^{x^2} \frac{d^v}{dx^v} e^{-x^2} \tag{10.5}$$

Therefore, for odd v, $|\psi_{vibr}\rangle$ is antisymmetric with respect to the vibrational coordinate changing sign, while for even v (including the ground state) it is symmetric. In our case, all molecules are in their ground states ($v = 0$), so $|\psi_{vibr}\rangle$ is symmetric. The translational wavefunction does not depend on any internal coordinates, and therefore is symmetric to the interchange of any identical particles.

As the oxygen nuclei have $I_O = 0$, they are bosons, and the total wavefunction of equation 10.2 should be symmetric with respect to their permutation. A 180° degree rotation of NO_2 around its b-axis is a symmetry operation and also corresponds to permuting two oxygen nuclei. If the b-axis of the molecule is used as the quantisation axis, then taking the total wavefunction as a linear combination of Wigner D-matrices[6], the dependence of the wavefunction on that rotation angle, χ, is:

$$exp[-\imath \chi K]$$

To obey the Pauli principle, it is required that the wavefunction has the same value and sign when χ changes by π, and therefore only even values of K may be taken.

[6] See chapter 3.

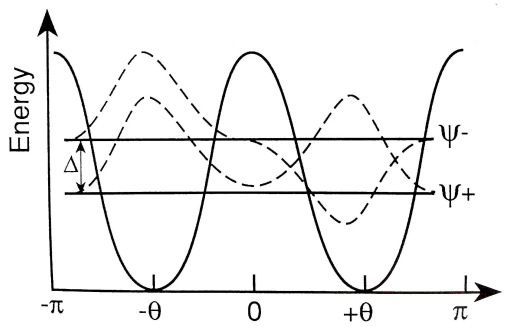

Figure 10.2: The two tunnelling states due to the rotation of NO_2 around its *a*-axis [126]

10.2.2 Tunnelling states of NO_2

The nuclear spin statistics effect explained in the previous section has a very interesting consequence when NO_2 forms a van der Waals complex with a rare gas atom, as was discovered by previous members of the group through the semi-rigid approach analysis. Due to the high symmetry of the atom, the rotation of the NO_2 molecule around its *a*-axis is also a symmetry operation for the van der Waals complex. However, this motion is now an internal rotation between two minima, and is quenched by the presence of the rare gas atom (i.e. has a potential energy barrier).

If we suppose that the barrier for the rotation around the *a*-axis is low enough that the nitrogen nucleus can tunnel through, this introduces a new kind of vibration which can be represented by its own (librational) wavefunction, $|\psi_{tunn}\rangle$. At the limit of high barriers, these librational wavefunctions are separate and degenerate. For NO_2, if we assumed no tunnelling then we could assign a $|\phi_1\rangle$ and $|\phi_2\rangle$ wavefunction each corresponding to the nitrogen nucleus being on one side of the oxygen nuclei line of the NO_2 molecular plane. However, if the energy barrier is low enough, the nitrogen nucleus can tunnel through and therefore these libration wavefunctions mix to give a symmetric and an antisymmetric combination:

$$|\psi_{tunn,\pm}\rangle = \frac{1}{\sqrt{2}}\left(|\phi_1\rangle \pm |\phi_2\rangle\right) \tag{10.6}$$

with an energy separation between them, Δ. The tunnelling motion may also be regarded as a vibration of the NO_2 molecule, i.e. $v_3 = 1$. According to equation 10.5, the symmetric tunnelling

$|\psi_{tunn,+}\rangle$ ($v_3 = 0$) state is symmetric with respect to permutation of the two oxygen atoms, and therefore only when combined with a symmetric (K even) state can the Pauli exclusion principle be satisfied. Correspondingly, the higher tunnelling state ($v_3 = 1$), may only be combined with antisymmetric rotational wavefunctions, i.e. $K = 1$.

Therefore, in the $|\psi_{tunn,+}\rangle$ librational state, only even K are possible. This way, both the librational and the rotational wavefunctions are symmetric, and for the antisymmetric $|\psi_{tunn,-}\rangle$ state on the other hand, only odd K values are allowed. Thus, a transition between even and odd K values involves a rotation around the a-axis. Due to the large A rotational constant of NO_2, these lines appear at much higher frequency than we can access with the equipment described in chapter 5. Therefore, practically for the Ne-NO_2 complex only transitions between even K values are detectable in our experiments.

10.2.3 Previous work on the Ne-NO_2 complex

The investigation of the Ne-NO_2 complex was started by a Part II student of the B. J. Howard group, Lee Dyer [116]. For his project, he used *ab initio* calculations to estimate the minimum geometry of the complex and performed extensive searches using FTMS with the apparatus described in chapter 5. Using these estimates, and with the programs SPFIT and SPCAT [22, 23], Dyer was able to detect the a-type $K = 0$ transitions for $N = 1 \leftarrow 0, 2 \leftarrow 1$ and $N = 3 \leftarrow 2$, by approximating the complex as a semi-rigid asymmetric top. Also, by taking the A rotational constant from *ab initio* calculations as a first estimate, he recorded additional transitions that are believed to correspond to the $|K| = 2$ transitions of the complex.

For the fine and hyperfine constants, he scaled the constants of the other Rg-NO_2 complexes previously recorded and analysed by the Howard group [112, 113, 114, 115] to the mass of Ne. With this effective approach, Dyer was able to record and assign 24 transitions for $K = 0$. However, despite long efforts it was not possible to assign any transitions for either set of $|K| = 2$ for $N = 3 \leftarrow 2$ transitions. It is believed that the reason the $|K| = 2$ transitions could not be assigned lies with the large amplitude motion of NO_2 and Ne in this weakly bound complex.

For this reason we believe that, in order to understand and assign the spectrum, we need to perform the full quantum dynamics, thus explicitly including the rotation of NO_2.

In our approach the first stage was to obtain the counterpoise-corrected PES using high level *ab initio* methods. This was then fitted to an appropriate function that could be included into an effective Hamiltonian. Next we solved the Schrödinger equation for the Ne-NO_2 complex using this effective Hamiltonian and from the calculated eigenvectors we obtained the calculated values for the rotational transitions of the complex. Although these calculated values come from a different approach to the semi-rigid model used previously in the group, they should still reproduce the observed pattern, i.e. only have transitions between even K values in our experimental range. In order to make the calculations more manageable, at this stage we neglected the electron spin and nuclear angular momentum contributions.

Finally, taking the eigenfunctions and eigenvalues calculated by the quantum dynamics, we predicted the expectation values of the fine and hyperfine operators. This yielded both a predicted spectrum, as well as the energy levels and the fine and hyperfine constants of the complex, which were then used to assign any remaining transitions. At the same time, an extensive experimental investigation was carried out which both confirmed Dyer's observations and also revealed previously unrecorded transitions. Using the theoretical and experimental results, a new assignment of the rotational spectrum of the Ne-NO_2 van der Waals complex was made.

10.2.4 The states of the complex and the coupling scheme

As neon is a rare gas atom with no chemically relevant internal structure or angular momenta, the state of this complex is solely determined by NO_2, which was presented earlier. Therefore, the ground state term symbol of the complex is $^2A_1$, and there are three sources of angular momenta to consider: the unpaired electron's spin (**S**), the nitrogen nuclear angular momentum (**I**), the NO_2 rotation ($\mathbf{n}_{NO_2}$), and the total rotational angular momentum (**N**).

As Lin [111] points out, there are different possible coupling schemes that may be adopted.

The one we chose is given below:

$$\mathbf{I}+\mathbf{S}\rightarrow\mathbf{G} \tag{10.7}$$

$$\mathbf{N}+\mathbf{G}\rightarrow\mathbf{F} \tag{10.8}$$

The reason for this coupling scheme is simply that of all the interactions, the Fermi contact, which couples the electron spin and nuclear angular momentum together, is the strongest one.

The total Hamiltonian of the complex may be written as:

$$\hat{H}_{Ne-NO_2}=\hat{T}+\hat{V}+\hat{h}_{compl,rot}+\hat{h}_{NO_2} \tag{10.9}$$

where the first term represents the kinetic energy of the complex, the second the potential energy between the monomers, the third the end-over-end rotation of the complex and the fourth the Hamiltonian for the NO_2 molecule. The latter contribution may be expanded as:

$$\hat{h}_{NO_2}=\hat{h}_{rot,NO_2}+\hat{h}_{FC}+\hat{h}_{DD}+\hat{h}_{Q}+\hat{h}_{SR} \tag{10.10}$$

where the first term represents the rotation of NO_2, the second term the Fermi contact interaction, the third term the electron spin and nuclear spin dipole-dipole interaction, the fourth term the nuclear electric quadrupole interaction, and the fifth term the electron spin interaction with the electric field created by the rotation of the molecule[7].

The basis set that we will use to solve the Schrödinger equation using the Hamiltonian of equation 10.9 is:

$$|I,S,N,K,G,F,m_F\rangle|n_{NO_2},\mu,K\rangle \tag{10.11}$$

where I is the nuclear angular momentum of nitrogen, S is the spin angular momentum, N is the complex end-over-end rotation angular momentum with K being its projection onto the complex intermolecular axis and m_F is the space-fixed projection of the composite angular momentum F. n_{NO_2} is the rotational angular momentum of NO_2, with projections μ onto its b-axis, and K

[7]The last four terms are presented analytically in chapter 9.

on the intermolecular axis of the complex.

As excitations of the nuclear angular momentum or changes of the spin state of NO_2 require high energy transitions that are outside the scale of our experimental setup, we only consider the cases where $I = 1, S = \frac{1}{2}$, thus $G = \frac{3}{2}, \frac{1}{2}$. Also it is worth noting that the projection of the total rotation angular momentum (**N**) on the complex (intermolecular) axis (K) is the same as the projection of the NO_2 rotational angular momentum on the same axis.

10.3 The *Ab Initio* Calculations

The first step in our approach is to calculate the PES of the complex. Before us, Dyer performed a number of *ab initio* calculations at single points as well as calculated part of the PES for this complex. For the single points calculations the UHF with MP4(SDQ) level of theory was used with aug-cc-pVXZ basis sets, where $X = D, T, Q$. He then extrapolated to the CBS limit with the formulæ presented in chapter 4, using both aug-cc-pV(D/T)Z and aug-cc-pV(T/Q)Z points and showed that the deviation between the extrapolated binding energies was less than 5 cm^{-1}. This was taken as an indication that the extrapolation formula can provide good results with the aug-cc-pV(D/T)Z basis set. However, when Dyer tried to compute the PES of the complex using the same method, he found a "nonsensical geometry" minimum which had an "unrealistically high binding energy (of ca. 125 cm^{-1})" [116], and therefore he abandoned the PES calculation.

Given that, according to ref. [119], multireference or at least RCCSD(T) methods should be used in order to correctly calculate the minimum geometry of the NO_2 molecule, the reason for the problems Dyer encountered may be due to that the MP4(SDQ) level of theory cannot explain the monomer, let alone the PES. Thus, in our approach we used RHF with RCCSD(T) method to calculate the full counterpoise-corrected PES with aug-cc-pVDZ and aug-cc-pVTZ basis sets. The coordinate system used in our calculation is given in figure 10.3. R is the distance between the neon atom and the NO_2 centre of mass, θ is the angle between the NO_2 b-axis (which is the C_2 symmetry axis of the molecule) and the intermolecular axis, and χ is the angle of rotation around the NO_2 axis. Initially, θ was varied between 0° and 180° degrees

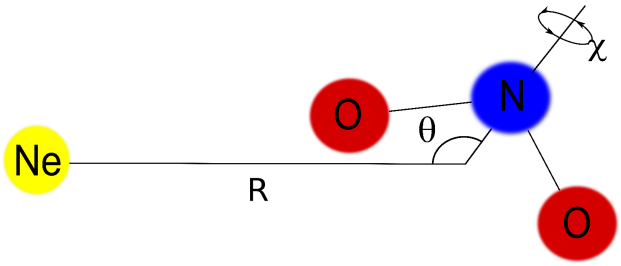

Figure 10.3: The coordinate system used for *ab initio* calculations of the Ne-NO_2 complex

Table 10.3: The geometry and binding energy of the lowest point of the RCCSD(T) PES for Ne-NO_2

Binding Energy/ cm^{-1}	-78.5915
θ/ degrees	120
χ/ degrees	90
R/ Å	3.1

in steps of 20°, χ between 0° and 90° in steps of 30° and R took the values 2.9, 3.0, 3.1, 3.2, 3.3, 3.4, 3.5, 3.6, 3.7, 3.8, 4.2, 4.6 and 5 Å. Moreover, in the geometries ($\chi = 90°, \theta = 80°/100°/120°/140°/160°$), R also took the values 2.7 and 2.8 Å. In total 492 geometries were included in the counterpoise corrected PES. Unlike the PES of Dyer, the RHF-RCCSD(T) PES did not have any "nonsensical" values, and the strongest binding energy was found in the geometry given in table 10.3 and depicted in figure 10.4.

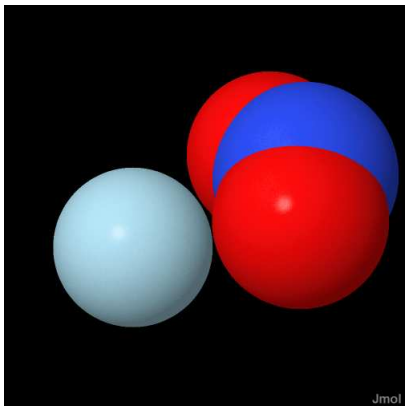

Figure 10.4: The minimum energy geometry of the Ne-NO_2 complex according to the RCCSD(T) calculations

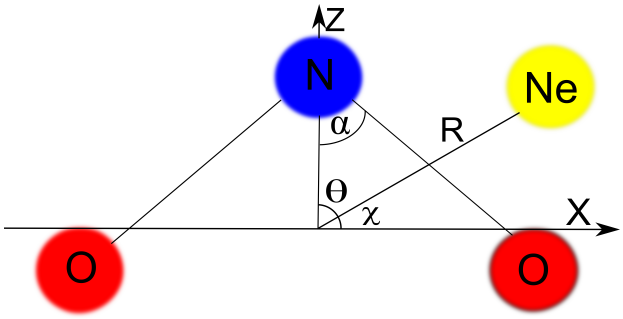

Figure 10.5: Axis system used to transform the centre-of-mass coordinates to atom-atom coordinates

10.4 Fitting Of The PES

The next step was to represent the calculated potential using an appropriate function. Three different approaches were explored before achieving a satisfactory fit, however due to space limitations we only concentrate on the most successful one which was finally used: the atom-atom fit. Details of other approaches may be found in Appendix D. From our efforts to try to fit the potential using a LEAPOT[8] or a centre-of-mass model, it became clear to us that if we wanted a physically meaningful fit, we needed a model capable of closely representing the anisotropy around each nucleus, as neon's small size enabled it to sample the potential around NO_2 in detail. For this reason, we decided to use an atom-atom potential.

To do this, initially the centre-of-mass coordinates that were used for the *ab initio* calculations had to be transformed into an atom-atom distance. Using the axis system shown in figure 10.5, the coordinates of Ne with respect to the centre of mass of NO_2 are:

$$Z_{Ne} = R\cos(\theta) \tag{10.12}$$

$$X_{Ne} = R\sin(\theta)\cos(\chi) \tag{10.13}$$

$$Y_{Ne} = R\sin(\theta)\sin(\chi) \tag{10.14}$$

while the (X,Y,Z) coordinates for the nitrogen atom are $(0,0,Z_N)$ and for the first oxygen atom $(X_{O1},0,Z_{O1})$ and for the second oxygen atom $(X_{O2},0,Z_{O2})$, where $X_{O1} = -X_{O2}$ and $Z_{O1} = Z_{O2}$.

[8]LEAPOT is the acronym of *Linear Expansion in the Anisotropy of the Potential*, as described in chapter 7.

The NO_2 parameters with respect to the centre of mass are:

$$Z_N = 0.326 \quad \text{Å} \tag{10.15}$$

$$X_{O1} = 0.775 \quad \text{Å} \tag{10.16}$$

$$Z_{O1} = 0.136 \quad \text{Å} \tag{10.17}$$

Thus, the distances between the Ne and each of the atoms may be calculated as a function of the original coordinate R and the sines and cosines of the angles θ and χ. For example, the distance between nitrogen and Ne may be taken as:

$$R_N = \sqrt{X_{Ne}^2 + Y_{Ne}^2 + (Z_{Ne} - Z_N)^2} \tag{10.18}$$

and R_{O1} and R_{O2} are similarly defined as the distances to the two oxygen atoms, and X_{O1-Ne}, X_{O2-Ne}, etc., as the distance between pairs of atoms on individual axes. For example:

$$Z_{N-Ne} = Z_{Ne} - Z_N \tag{10.19}$$

Moreover, in order to have a faster converging series, we rotated the oxygen coordinates by $\pi \pm \alpha$. The rationale behind this was that a potential expansion in the new rotated axis (i.e. on the N-O bond) would mirror better the symmetry around each oxygen atom, thus giving a faster

converging series. This introduced a second atom-atom axis system for the two oxygen atoms:

$$\begin{aligned}
X'_{O1-Ne} &= X_{O1-Ne}\cos(\pi-\alpha) - Z_{O1-Ne}\sin(\pi-\alpha) && (10.20)\\
&= (R\sin(\theta)\cos(\chi) - X_{O1})\cos(\pi-\alpha) \\
&- (R\cos(\theta) - Z_{O1})\sin(\pi-\alpha) && (10.21)\\
Z'_{O1-Ne} &= X_{O1-Ne}\sin(\pi-\alpha) + Z_{O1-Ne}\cos(\pi-\alpha) && (10.22)\\
&= (R\sin(\theta)\cos(\chi) - X_{O1})\sin(\pi-\alpha) \\
&+ (R\cos(\theta) - Z_{O1})\cos(\pi-\alpha) && (10.23)\\
X'_{O2-Ne} &= X_{O2-Ne}\cos(\pi+\alpha) - Z_{O2-Ne}\sin(\pi+\alpha) && (10.24)\\
&= (R\sin(\theta)\cos(\chi) + X_{O1})\cos(\pi+\alpha) \\
&- (R\cos(\theta) - Z_{O1})\sin(\pi+\alpha) && (10.25)\\
Z'_{O2-Ne} &= X_{O2-Ne}\sin(\pi+\alpha) + Z_{O2-Ne}\cos(\pi+\alpha) && (10.26)\\
&= (R\sin(\theta)\cos(\chi) + X_{O1})\sin(\pi+\alpha) \\
&+ (R\cos(\theta) - Z_{O1})\cos(\pi+\alpha) && (10.27)
\end{aligned}$$

Thus, the potential now was separated into three parts as three pair-wise atom-atom interactions:

$$V_{Ne-NO2} = V_{N-Ne} + V_{O1-Ne} + V_{O2-Ne} \qquad (10.28)$$

where to be physically meaningful V_{O1-Ne} and V_{O2-Ne} are restricted to have the same parameters, and only differ on whose oxygen atom's coordinates each depends on. In using this model, we assumed that any three body effects were negligible. Now, the potential between each pair of atoms may be fitted to a Modified Buckingham potential with the Tang and Toennies damping functions, as given by equation 7.30. To a first approximation, the individual atom-atom potentials could be modelled without any angular parameters, however this would be ignoring the shift in electron density during the formation of the covalent bonds in NO_2. To include the angular dependence, a complete set of functions of the corresponding variables was chosen: the Wigner D-matrices. However, as there are only two angles that the potential depends on

(θ and χ), these D-matrices were reduced to spherical harmonics using equation 3.56 and then to a product of an associated Legendre polynomial with a cosine function, according to equation 3.23. Thus, for the nitrogen atom, the potential function between itself and the neon atom was modelled as:

$$\begin{aligned} V_{N-Ne} &= A_N \exp\left[-b_N\left(R_N - R_0\right) + g_N\left(R_N - R_0\right)^2 + \sum_{\ell=0,2} d_{N,\ell,m}\mathscr{P}_m^{\ell}\left(\cos\theta_N\right)\cos\left(m\chi_N\right)\right] \\ &- \frac{\left(1 - e^{-b_N R_N}\sum_{k=0}^{6}\frac{\left(b_N R_N\right)^k}{k!}\right)}{R_N^6}\left(\sum_{\ell=0,2} c_{6N,\ell,m}\mathscr{P}_m^{\ell}\left(\cos\theta_N\right)\cos\left(m\chi_N\right)\right) \\ &- \frac{\left(1 - e^{-b_N R_N}\sum_{k=0}^{8}\frac{\left(b_N R_N\right)^k}{k!}\right)}{R_N^8} c_{8N,0,0} \end{aligned} \tag{10.29}$$

Similarly, the oxygen-neon atom-atom potentials were modelled for each oxygen-neon pair using the function:

$$\begin{aligned} V_{O_i-Ne} &= A_O \exp\left[-b_O\left(R_{O_i} - R_0\right) + g_O\left(R_{O_i} - R_0\right)^2 + \sum_{\ell=0,2} d_{O,\ell,m}\mathscr{P}_m^{\ell}\left(\cos\theta_{O_i}\right)\cos\left(m\chi_{O_i}\right)\right] \\ &- \frac{\left(1 - e^{-b_O R_{O_i}}\sum_{k=0}^{6}\frac{\left(b_O R_{O_i}\right)^k}{k!}\right)}{R_{O_i}^6}\left(\sum_{\ell=0,2} c_{6O,\ell,m}\mathscr{P}_m^{\ell}\left(\cos\theta_{O_i}\right)\cos\left(m\chi_{O_i}\right)\right) \\ &- \frac{\left(1 - e^{-b_O R_{O_i}}\sum_{k=0}^{8}\frac{\left(b_O R_{O_i}\right)^k}{k!}\right)}{R_{O_i}^8} c_{8O,0,0} \end{aligned} \tag{10.30}$$

where $i = 1, 2$ indicates which oxygen atom this potential refers to. One difference between the potential functions of equation 10.29 and equation 10.30 is that, in the former only even (including zero) values are allowed for m, while in the latter, both odd and even values were allowed. The reason for this is that around the nitrogen atoms, the bonds have the same symmetry as NO_2: rotation of θ_N by 180° simply interchanges the two N-O bonds, so the potential should be symmetric with respect to this operation. Around the oxygen atom though, the situation is different as rotation of θ_{O_i} by 180° moves between where there is an N-O bond to where there is none. Thus, zero, odd and even positive integer values were allowed for each m up to the corresponding ℓ. For all cases R_0 was chosen as 3.3 Å.

While $\theta_N, \chi_N, \theta_{O_i}, \chi_{O_i}$ are used in equations 10.29 and 10.30, what may be more conveniently calculated from the coordinates are the values of $\cos(\theta_N)$, $\cos(\theta_N)\sin(\chi_N)$ and $\cos(\theta_N)\cos(\chi_N)$ by the ratios:

$$\cos(\theta_N) = \frac{Z_{N-Ne}}{R_N} \tag{10.31}$$

$$\sin(\theta_N)\cos(\chi_N) = \frac{X_{N-Ne}}{R_N} \tag{10.32}$$

$$\sin(\theta_N)\sin(\chi_N) = \frac{Y_{N-Ne}}{R_N} \tag{10.33}$$

and the corresponding expressions apply for the oxygen angles. For this reason, the expressions of equations 10.29 and 10.30 were rearranged in terms of the sines and cosines of the corresponding angles, using the tables from [27] and [29].

Furthermore, a weighted fitting was used where the weights used were set using equation:

$$w_j = \left(\frac{40}{120 + V_j}\right)^2 \tag{10.34}$$

where w_j is the weight of point j, and V_j is the *ab initio* calculated point. This simple expression ensures that the weight of the points decreases as they move away from the minimum of the potential.

The fitting of the potential of equations 10.28, 10.29 and 10.30 was performed using the Levenberg-Marquardt method [127] and a combination of the programs MATHEMATICA8 [108] and Microsoft Excel [128]. The RMSD of the final fit was 1.7 cm^{-1}, and this error was met mainly in areas remote from the energy minimum. In total 24 parameters were used, which are given along with the coded potential expression in the MATHEMATICA8 files in the CD attached to this thesis. Although more terms could have been added to this potential, this fitting was found satisfactory and it seemed that more terms made the expressions unphysical. For example, an anisotropic (R^{-8}) term was added, and although this lowered the RMSD to 0.7 cm^{-1}, the coefficients of the expansions did not appear to be part of a convergent series and the terms did not have the expected relative magnitude. Thus, to our experience it proved critical to have a physical significance behind the different fitting parameters, as this enabled

us to decide whether the fitted coefficients were meaningful and if all major contributions had been included.

In general, the potential was found to be highly anisotropic: while the radial variable (R) changes the energy dramatically, a similar effect is caused by even small deviations in the angle χ. However, the second angle (θ) does not cause nearly such a strong effect. The reason behind this is a combination of factors: the large angle of NO_2 leads to a very small anisotropy around the θ angle. Neon is small enough that can fit between the two oxygen atoms, as is demonstrated in figure 10.4, but the effect of χ which brings the long bonds and oxygen atoms towards neon is much larger, and similar in amplitude to the distance changing.

10.5 The Rotational Quantum Dynamics

Once we had fitted the potential, the next step was to perform the quantum dynamics using an effective Hamiltonian. In reality this was done in two ways: at a single R value and including all the degrees of freedom of the potential. However, due to space limitations, we will only concentrate on the latter, more complete approach.

At first stage, we will neglect the effect of the unpaired electron spin and nuclear angular momentum, in order to reduce the size of the basis set used. Therefore, the Hamiltonian used for the dynamics is:

$$\hat{H}_{Ne-NO_2,Dyn} = \hat{T} + \hat{h}_{rot,compl} + \hat{h}_{rot,NO_2} + \hat{V}_{Ne-NO_2} \tag{10.35}$$

where the first term is the kinetic energy operator for the molecular complex, the second term corresponds to the complex's end-over-end rotation, the third the NO_2 rotation and the last the intermolecular potential. The basis set used for the dynamics was:

$$|\Psi_{Ne-NO_2,Dyn}\rangle = |N,K,v\rangle|n_{NO_2},K,\mu\rangle \tag{10.36}$$

where N is the total rotational angular momentum of the complex, K its projection on the

Axis of equation 2.27	Principle axis of NO_2
x	c
y	a
z	b

Table 10.4: The correspondence between the NO_2 principal axis and the dynamics monomer axis system

internuclear axis, n_{NO_2} is the rotational angular momentum of the NO_2 molecule, with K being its projection on the internuclear axis, μ being its projection on the NO_2 b-axis, and v is the vibrational state of the complex.

In the following sections, each of the terms of the Hamiltonian of equation 10.35 will be examined in turn. Following this, the program written to perform the quantum dynamics calculation will be presented and discussed. In each of the following sections, only the relevant part of the basis set will be discussed, and therefore the terms are diagonal to any quantum numbers not shown. All results in the following subsections are quoted in cm^{-1}.

10.5.1 The NO_2 Rotation

NO_2 is an asymmetric top and its rotational Hamiltonian was given in equation 2.27. The corresponding matrix elements are given in equations 2.29 and 2.30. The correspondence between the axis (xyz) used in these equations and the principle axis of NO_2 was given in table 10.4. The k_{NO_2} quantum number is the projection of the NO_2 rotational angular momentum on the intermolecular axis, and μ its projection on the NO_2 b-axis (corresponding to "K" in equations 2.29 and 2.30).

10.5.2 The complex rotation

We can describe the complex rotation as the rotation of a pseudo-diatomic, with Ne and NO_2 each being a dimensionless "atom". Then, the rotation of the complex is difference between the

total rotational angular momentum (**N**), from the rotation of the NO_2 molecule ($\mathbf{n}_{NO_2}$):

$$\begin{aligned} \hat{h}_{rot,compl} &= \hat{B}_{compl}\left(\hat{N}-\hat{n}_{NO_2}\right)^2 && (10.37)\\ &= \hat{B}_{compl}\left(\hat{N}^2+\hat{n}_{NO_2}^2-\left[2\hat{N}_z\hat{n}_{NO_2,z}\right.\right. \\ &+ \left.\left.\hat{N}^+\hat{n}_{NO_2,-}+\hat{N}^-\hat{n}_{NO_2,+}\right]\right) && (10.38)\end{aligned}$$

where $N^{\pm}$ are the "anomalous" lowering and raising operators for the complex, while $n_{NO_2,\pm}$ are the normal raising and lowering operators. The complex rotational constant contains a $\frac{1}{R}$ operator that depends on the expectation value of the vibrational level, and its expectation value for each vibrational state is:

$$\langle \hat{B}_{compl} \rangle = \left\langle v' \left| \frac{\hbar}{4\pi c \mu R^2} \right| v \right\rangle \delta_{v'v} \tag{10.39}$$

where c is the speed of light, μ is the reduced mass of the complex, R is the intermolecular distance and $\delta_{v'v}$ is the Kronecker delta function. To model the vibrational energy levels we used harmonic oscillator functions:

$$|v\rangle = N_v \mathscr{H}_v(y)\, e^{-\frac{(y)^2}{2}}; \quad a = \left(\frac{\hbar}{\mu k}\right)^{\frac{1}{4}}; \quad y = \frac{x}{a} \tag{10.40}$$

where $x = R - R_0$ is the displacement from a reference position $R_0 = 3.3$ Å, and $\mathscr{H}_v(y)$ is a Hermite polynomial whose definition was given in equations 10.3, 10.4 and 10.5.

The rationale behind this choice is that if the complex geometry is fairly localised in the radial direction, then the convergence should be faster if localised functions that represent deviation from the equilibrium distance were used. Furthermore, as will be seen in the next section, this choice also simplifies the treatment of the kinetic energy operator matrix elements. k in a harmonic oscillator is the potential force constant. This was set at $k = 560$ cm^{-1}, by fitting a parabola at using the points with $R = 3.0, 3.1, 3.2$ Å, at the minimum energy angular geometry. This gave a value of classical amplitude $a = 0.256$ Å, indicating that the complex is quite floppy, as expected. Using these results, we evaluated the expression of equation 10.39 using

Gauss-Hermite quadrature [129].

Within each vibrational state, the diagonal matrix elements with respect to N, K and n_{NO_2} are:

$$\langle N, K, n_{NO_2} | \hat{h}_{rot,compl} | N, K, n_{NO_2} \rangle = \langle \hat{B}_{compl} \rangle \left[N(N+1) + n_{NO_2}(n_{NO_2}+1) - 2K^2 \right] \quad (10.41)$$

while the off-diagonal Coriolis forces contributions are:

$$\begin{aligned} \langle N, K \pm 1, n_{NO_2} | \hat{h}_{rot,compl} | N, K, n_{NO_2} \rangle &= -\langle \hat{B}_{compl} \rangle \sqrt{(N(N+1) - K(K \pm 1))} \\ &\times \sqrt{(n_{NO_2}(n_{NO_2}+1) - K(K \pm 1))} \end{aligned} \quad (10.42)$$

10.5.3 The kinetic energy

The next contribution to be examined is the kinetic energy operator:

$$\hat{T} = -\frac{\hbar^2}{2\mu} \frac{\partial^2}{\partial R^2} \quad (10.43)$$

The way we handled this was to add and subtract Hooke's law: $\frac{1}{2}kR^2$. Thus, the kinetic energy operator plus Hooke's law was equivalent to the harmonic oscillator Hamiltonian. Since the vibrational wavefunctions employed were eigenfunctions of the harmonic oscillator, the matrix elements of that part were simply the diagonal harmonic oscillator eigenvalues:

$$\left\langle v' \left| \hat{T} + \frac{1}{2}kx^2 \right| v \right\rangle = \left(v + \frac{1}{2} \right) \hbar \sqrt{\frac{k}{\mu}} \delta_{v'v} \quad (10.44)$$

where μ is the reduced mass of the complex, k the force constant as described in the previous section and $\delta_{v'v}$ the Kronecker delta function. The remaining part:

$$\left\langle v' \left| -\frac{1}{2}kx^2 \right| v \right\rangle \quad (10.45)$$

can give non-zero matrix elements only if $v' = v$, and was calculated using Gauss-Hermite quadrature.

10.5.4 The potential energy

The final term that we need to consider is the intermolecular potential. The effect of the potential is to mix different n_{NO_2} and K states together. The NO_2 molecule was approximated as a rigid symmetric top, and therefore its wavefunctions could be represented using Wigner D-matrices. Furthermore, the potential depended on the vibrational wavefunctions which were modelled using harmonic oscillators eigenfunctions. It should be noted that for the evaluation of the potential matrix elements, the coordinates used were the Euler angles (θ, χ) of NO_2 with respect to the axis complex axis system, and the intermolecular coordinate, R, which were used in the *ab initio* calculations. Given that the potential does not mix different vibrational states, we set $v' = v$. Setting $y = \left(\frac{x}{a}\right)$ for clarity, the expression to be evaluated is:

$$\begin{aligned}\left\langle v' \left| \left\langle n'_{NO_2} K' \mu' \left| \hat{V}_{Ne-NO_2} \right| n_{NO_2} K \mu \right\rangle \right| v \right\rangle &= \iiint V_{Ne-NO_2}(\theta,\chi,y)\mathscr{H}_v(y)\mathscr{H}_v^*(y) \\ &\times d^{n'_{NO_2}}_{K',\mu'}(\theta) d^{n_{NO_2}}_{-K,-\mu}(\theta) \exp[-\imath(K'-K)\chi] \exp[-y^2] \\ &\times \frac{\sqrt{\left(2n'_{NO_2}+1\right)\left(2n'_{NO_2}+1\right)}}{2^v v! 8a\sqrt{\pi^5}} \\ &\times \sin(\theta) d\chi d\theta dR \end{aligned} \tag{10.46}$$

The integral in equation 10.46, was then evaluated by Gauss-Legendre quadrature for the θ variable, Gauss-Chebyshev quadrature for the χ variable, and Gauss-Hermite quadrature for the R variable.

10.5.5 The program written

To perform the dynamics a program was written using the MATHEMATICA8 package. This worked in two stages to optimise performance and avoid repeated calculations: Initially the user

chose the maximum number of N, K, n_{NO_2}, v to be used in later calculations. Then, the program compiles and stores a look-up table for the matrix elements of the operators:

$$\left\langle v' \left| \left\langle n'_{NO2}, K', \mu' \left| \hat{V}_{Ne-NO_2} - \frac{1}{2}k(x)^2 \right| n_{NO2}, K, \mu \right\rangle \right| v \right\rangle$$

and

$$\langle v' | \hat{B}_{compl} | v \rangle$$

using the expressions shown in the previous sections. In the second stage, a MATHEMATICA8 function is defined that computes the Hamiltonian matrix and diagonalises it, to return the corresponding eigenstates and eigenvalues. This way the user may repeat rapidly (under ten minutes usually) the calculation on any set of N, K, n_{NO_2}, v values up to what was originally selected, without having to re-do the quadrature calculation.

Four versions of this program were written in total, to perform the dynamics for a single R value or globally, and including or neglecting the off-diagonal Coriolis contributions described in equation 10.42. To compute the reduced d-matrices and Hermite polynomials internal MATHEMATICA8 functions were used. For the integral evaluation, 12 point Gauss-Hermite, 30 point Gauss-Chebyshev and 64 point Gauss-Legendre quadrature points were used and the corresponding subroutine was written from scratch. The abscissas and points were taken from [129]. The code was also modified so that it could be executed in parallel whenever possible, to improve performance. The code of these programs is given in the CD attached to this thesis.

10.5.6 Discussion of the quantum dynamical results

Using the program described above, we were able to predict the rotational transitions of Ne-NO_2, and to compare our predictions to experimental data. There is one subtlety in the notation of the K quantum number: in the dynamics, K is the projection of the $\mathbf{n}_{NO_2}$ angular momentum along the internuclear axis. This is slightly different to the K that would nominally be assigned to the dynamic's eigenvectors if they were analysed as an asymmetric top, i.e. the semi-rigid

notation of K. We note this "semi-rigid K" as K_r, and we can now use it to define the eigenstates computed by the dynamics. The difference lies in that the potential and the Coriolis interactions mix in different K values in the same K_r: For example, if $N = 2$, what is nominally named $K_r = 0$, actually will have a small part of $K = \pm 1, \pm 2$ mixed in by the Coriolis interactions and the potential. Moreover, the upper $|K_r| = 2$ level will be noted as $K_r = 2^+$, while the lower as $K_r = 2^-$.

One result obtained at this stage is that, in agreement with the measurements of Dyer and all previously recorded Rg-NO_2 complexes [112, 113, 114, 115], the $|K_r| = 1$ lines are found to be much higher in energy than the $K_r = 0$ levels, and therefore outside our experimental range. At the same time, the $|K_r| = 2$ levels are lower in energy than the $|K_r| = 1$ levels, and close to the $K_r = 0$ ones. This was somewhat expected as the small size of neon and the small binding energy of the complex do not significantly quench the rotation around the NO_2 a-axis, and thus the tunnelling splitting is high. Therefore, the K_r values that the complex can take are even (including zero) for the ground tunnelling state as described in section 10.2.2.

The program written can perform the dynamics using the Hamiltonian matrix elements for any chosen set of (N, K, n_{NO_2}, v) values, and the main limitations were practical. There were three main limiting factors: As the expression given in section 10.5.5 had to be calculated and stored for all basis set states, if the table holding that information was stored in the HDD rather than in the RAM this slowed down the calculations at least ten-fold. The second limitation is the size of the actual Hamiltonian matrix which needs to be diagonalised. While the former limitation only concerns the maximum possible numbers K, n_{NO_2}, v, the latter also scales with N. Finally, the number of quadrature points needed for the accurate calculation of the potential matrix elements increases with n_{NO_2} and v. Although this latest point is not a limitation on storage space required but on the time each calculations takes, it can scale rapidly.

To find a suitable basis set size to achieve useful estimates of the energy levels, eigenstates and transition frequencies, first we tested the convergence with respect to n_{NO_2}, using the single-R version of the program. The results are given in table 10.5. As it can be seen from table 10.5, by taking the maximum value of n_{NO_2} to be 19, the energy levels have converged a to better

Table 10.5: Single-*R* quantum dynamics eigenvectors for the Ne-NO_2 complex

	Energy Level/cm^{-1}			
	$N=0,K_r=0$	$N=1,K_r=0$	$N=2,K_r=0$	$N=2,K_r=2^-$
$n_{NO_2,max}=8$	-55.4789	-55.2719	-54.8584	-53.4643
$n_{NO_2,max}=10$	-55.8899	-55.6872	-55.2830	-53.9487
$n_{NO_2,max}=12$	-55.9514	-55.7500	-55.3486	-54.0231
$n_{NO_2,max}=14$	-55.9560	-55.7549	-55.3539	-54.0292
$n_{NO_2,max}=16$	-55.9562	-55.7551	-55.3541	-54.0295
$n_{NO_2,max}=18$	-55.9563	-55.7551	-55.3541	-54.0295
$n_{NO_2,max}=19$	-55.9563	-55.7551	-55.3541	-54.0295
	$N=2,K_r=2^+$	$N=3,K_r=0$	$N=3,K_r=2^-$	$N=3,K_r=2^+$
$n_{NO_2,max}=8$	-53.4637	-54.2397	-52.8436	-52.8404
$n_{NO_2,max}=10$	-53.9476	-54.6791	-53.3422	-53.3369
$n_{NO_2,max}=12$	-54.0218	-54.7494	-53.4211	-53.4149
$n_{NO_2,max}=14$	-54.0280	-54.7554	-53.4279	-53.4217
$n_{NO_2,max}=16$	-54.0282	-54.7557	-53.4282	-53.4220
$n_{NO_2,max}=18$	-54.0283	-54.7557	-53.4283	-53.4221
$n_{NO_2,max}=19$	-54.0283	-54.7558	-53.4283	-53.4221

than 0.001 cm^{-1}. The convergence of the energy levels may be taken as an indication of the convergence of the corresponding eigenstates, which will be useful for the next section, where these are used to calculate the expectation values of the fine and hyperfine operators. However, at the current stage we are more interested to the convergence of the transition frequencies, which is illustrated in table 10.6. As it may be seen from table 10.6, the convergence in terms of the transitions is even better, and already from using maximum n_{NO_2} number 16, the subsequent change in energy is under 1 MHz. Having established that using up to $n_{NO_2}=19$ gives us a good angular convergence, we used $n_{NO_2}=19$ to examine the convergence in terms of the number of vibrational functions (v) used. In table 10.7, the corresponding transition frequencies are given, now calculated with the program including the kinetic energy operator.

In table 10.7, there are no numbers with $v=7$ for the $N=3$ levels as computing these were beyond the capabilities of our machines. Unfortunately the convergence of the transitions including the vibrational coordinates was only to tens of MHz, while the corresponding convergence of the energy levels was at the 0.1 cm^{-1} level. One thing to note is that the energy of the ground state systematically decreases (in accordance to the variation principle), while

Table 10.6: Rotational transition frequencies calculated by single-R dynamics for the Ne-NO_2 complex

	Transition Frequency/ MHz		
	$N = 1 \leftarrow 0, K_r = 0$	$N = 2 \leftarrow 1, K_r = 0$	$N = 3 \leftarrow 2, K_r = 0$
$n_{NO_2,max} = 8$	6,206.59	12,395.63	18,549.98
$n_{NO_2,max} = 10$	6,075.56	12,119.92	18,102.53
$n_{NO_2,max} = 12$	6,036.05	12,035.59	17,962.65
$n_{NO_2,max} = 14$	6,029.90	12,022.31	17,940.18
$n_{NO_2,max} = 16$	6,029.61	12,021.64	17,938.98
$n_{NO_2,max} = 18$	6,029.61	12,021.65	17,938.99
$n_{NO_2,max} = 19$	6,029.60	12,021.63	17,938.96
	$N = 3 \leftarrow 2, K_r = 2^-$	$N = 3 \leftarrow 2, K_r = 2^+$	
$n_{NO_2,max} = 8$	18,609.51	18,684.66	
$n_{NO_2,max} = 10$	18,181.72	18,309.99	
$n_{NO_2,max} = 12$	18,047.99	18,194.40	
$n_{NO_2,max} = 14$	18,026.19	18,175.37	
$n_{NO_2,max} = 16$	18,024.91	18,174.20	
$n_{NO_2,max} = 18$	18,024.93	18,174.21	
$n_{NO_2,max} = 19$	18,024.90	18,174.19	

Table 10.7: Rotational transition frequencies calculated with many vibrational levels for the Ne-NO_2 complex

	Transition Frequency/ MHz		
	$N = 1 \leftarrow 0, K_r = 0$	$N = 2 \leftarrow 1, K_r = 0$	$N = 3 \leftarrow 2, K_r = 0$
$v_{max} = 0$	6,016.83	11,991.68	17,900.58
$v_{max} = 1$	5,839.95	11,646.92	17,384.94
$v_{max} = 2$	5,771.00	11,503.02	17,169.09
$v_{max} = 3$	5,723.03	11,410.08	17,031.18
$v_{max} = 4$	5,684.06	11,332.14	16,914.26
$v_{max} = 5$	5,660.07	11,287.17	16,839.32
$v_{max} = 6$	5,642.09	11,254.19	16,794.35
$v_{max} = 7$	5,633.09	11,233.21	-
	$N = 3 \leftarrow 2, K_r = 2^-$	$N = 3 \leftarrow 2, K_r = 2^+$	
$v_{max} = 0$	17,999.51	18,143.41	
$v_{max} = 1$	17,450.89	17,582.80	
$v_{max} = 2$	17,220.05	17,345.97	
$v_{max} = 3$	17,070.16	17,199.07	
$v_{max} = 4$	16,944.24	17,067.16	
$v_{max} = 5$	16,866.30	16,986.21	
$v_{max} = 6$	16,812.34	16,932.25	

Table 10.8: The experimentally measured $K_r = 0$ rotational transitions of Ne-NO_2

Transition	Frequency/MHz
$N = 1 \leftarrow 0, K_r = 0$	5,899.15
$N = 2 \leftarrow 1, K_r = 0$	11,761.98
$N = 3 \leftarrow 2, K_r = 0$	17,544.09

the average distance between the NO_2 and Ne seems to increase, thus decreasing the transition frequency.

Our best estimate for the Zero Point Energy (ZPE) comes as the difference of the energy of the $N = 0, K = 0$ state with maximum $v = 7$ and $n_{NO_2} = 19$ which is -42.79 cm^{-1} from the potential minimum, which is -79.67 cm^{-1}. Therefore, the ZPE of Ne-NO_2 complex according to our calculations is 36.88 cm^{-1}. Similarly, as the average of the two $N = 1, K_r = 1^{\pm}$ levels would (for an asymmetric top), coincide with the $N = 1, K_r = 0$ transition, we can calculate the tunnelling frequency. This turns out to be 4.521 cm^{-1}, or approximately 135.54 GHz.

If one averages over the fine and hyperfine splittings, the assigned transitions from Dyer are given in table 10.8. These are approximately 258*N MHz higher than our predictions using maximum $n_{NO_2} = 19$ and up to $v = 6$ vibrational states. Physically, this means that our prediction foresees a looser binding than what actually happens, which probably is because the fitted potential is slightly less attractive than in reality. This could simply be due to our weighting of the potential well region slightly skewing the parameters.

However, the real advantage of performing the full quantum dynamics is the prediction of where the $|K_r| = 2$ transitions lie. According to the rigid asymmetric rotor picture, the interaction between $\Delta K = 2$ states should separate the $K_r = 0$ and $K_r = 2$ transitions by the same amount, thus resulting in having the same separation between $K_r = 0$ to $K_r = 2^-$ with $K_r = 2^-$ to $K_r = 2^+$. Any deviation from this picture should be small and modelled by the D_{NK} constant. However, if we take the average of the fine and hyperfine structure, the transitions that Dyer recorded and are expected to correspond to $|K_r| = 2$, these are given in table 10.9. As it may be seen from table 10.9 the pattern is not symmetric, and therefore it is not surprising that fitting these values was very difficult for Dyer. The corresponding separation in the quantum

Table 10.9: The experimentally measured $|K_r| = 2$ rotational transitions of Ne-NO_2

Transition	Frequency/MHz	Separation from $N = 3 \leftarrow 2$, other K_r/ MHz
$N = 3 \leftarrow 2, K_r = 2^-$	17,627.04	82.95
$N = 3 \leftarrow 2, K_r = 2^+$	17,765.03	137.99

Table 10.10: Fitting of experimentally measured and predicted (dynamics) transitions of Ne-NO_2 complex with semi-rigid model constants

Parameter Fitted	Value (Error) Dynamics /MHz	Value (Error) Experimental [116]/ MHz
$A-(B+C)/2$	$10,336.393(70)$	$10,044.69^c$
$B+C$	$5,643.705(600)$	$5,901.5028(46)$
$B-C$	$642.348(296)$	$710.584(132)^d$
D_N	$0.14969(297)$	0.0691^c
D_{NK}	$4.2744(97)$	2.55^c

dynamics' results is 17.99 and 119.91 MHz, which is 46.07 MHz and 43.86 MHz smaller than the experimental values. Therefore, we see that the effect of the dynamics is to make the K level splitting asymmetric. Our results seem to overestimate the dynamical effects (by approximately 45 MHz), yet this effect is almost symmetric to the two splittings and thus, the dynamics effects are modelled well.

In order to test the compatibility of the two approaches (semi-rigid and dynamical) we fitted the experimentally predicted energy levels using the program SPFIT. The error in the fit was 0.44 MHz and the parameters obtained are given in table 10.10 along with the values obtained by Dyer in his fit of the $K_r = 0$ transitions. The error quoted in the parenthesis is one standard deviation with respect to the last significant figure of the value[9].

The values marked with a "*c*" on Dyer's data were not obtained by the fit, but rather were fixed to a value reasonable if one considers the trend amongst the Rg-NO_2 complexes and scales the parameters by the mass of neon [112, 113, 114, 115]. However this is an inherently semi-rigid approach. The values marked "*d*" on Dyer's data are only determined by second order

[9]We were hesitant to also include h_N at this stage, given the number of variables to constants fitted. However, it was noticed that in order to fit the complete spectrum semi-empirically (including the fine and hyperfine structure, as will be described later) this was needed. Thus, the agreement between the dynamics and the experimental results may be even better than presented here.

Table 10.11: Centrifugal distortion constants for the Ar-NO_2 and Kr-NO_2 complexes

Parameter Fitted	Ar-NO_2	Kr-NO_2
D_N/kHz	19.909(5)	7.8825(37)
D_{NK} /kHz	349.40 (8)	129.161(40)

effects, as only $K_r = 0$ transitions were fitted.

If one ignores the difference between the $(B+C)$ values which just shifts the origin of the transitions, the most interesting feature is the centrifugal distortion constants. Namely, in our data it is obvious that D_{NK} is much larger than in Dyer's fit, and it becomes clear that it is a fitting parameter able to mimic the effects of the dynamics in the Coriolis forces. These forces, along with the potential, mix different K values thus introducing an angular-Coriolis effect. D_N on the other hand remains a "normal" centrifugal distortion constant, demonstrating that the most important Coriolis contribution comes from the angular part of the potential.

It is also interesting to compare our results from the fit to similar species [10], namely Ar-NO_2 and Kr-NO_2. The corresponding data [113, 114] are given in the table 10.11. As it can be seen from table 10.11, in all the complexes the values of D_{NK} are somewhat anomalous (and not in line with the corresponding values of D_N), even though this has not been pointed out in previous studies. As the Rg becomes smaller, this effect increases, as expected. Moreover, the well-depth of Ar-NO_2 (approx. [113] 120 cm^{-1}) is deeper than what we calculated for Ne-NO_2 (79.67 cm^{-1}), again as expected. The only unexpected result when comparing to other complexes was that our tunnelling frequency (approx. 135 GHz) is less than the corresponding one for Ar-NO_2 (approx. 180 GHz), although the latter was only estimated by a semi-empirical potential. What is possibly happening is that Ne is small enough to fit between the two oxygen atoms and quench the motion around the a-axis of NO_2 more effectively than Ar. It is noted that in the limit of free NO_2 rotation this frequency would correspond to the A rotational constant of NO_2, i.e. approx. 240 GHz.

[10] In all cases, the transitions of the van der Waals complex of NO_2 with the major isotope of the rare gas are quoted. For Xe-NO_2, the D_N and D_{NK} values were estimated using the Ar-NO_2 values, and therefore are not quoted.

10.6 The Fine and Hyperfine Structure

Once the pure rotational part of the problem had been solved, the next step was to predict and analyse the fine and hyperfine pattern of these transitions. Our approach to achieve this was to calculate the expectation values of the corresponding operators for each N, K_r energy level using the results of the rotational dynamics, then solve the fine and hyperfine interaction Schrödinger equation to compute the energy levels. Next we can take the appropriate differences to calculate the transition frequencies. The fine and hyperfine interactions in NO_2 were presented in chapter 9.

In order to use the experimentally determined constants of NO_2 (which are quantified in the NO_2 molecular frame and are given in table 10.2) in predicting the fine and hyperfine splittings of the Ne-NO_2 complex, we need a transformation between the molecular and the complex frame. What is more, as the nuclear and electron spin angular momenta refer to their laboratory-frame definitions, **I** and **S** are quantised in the space fixed frame. Therefore, a total of two transformations of the operators are needed: from the NO_2 molecular frame (the projections of the various spherical tensor operators in this frame are noted as q), to the Ne-NO_2 frame (the projections of the spherical tensor operators in this frame are noted as c) and then to the space-fixed frame (the projections in this frame are noted by p). Following the work of Sears [109], Brown, Bowater [110] and Howard [33], this is done using spherical tensor operator algebra.

To facilitate the transformation between different frames we derived the following useful formula for transforming an operator $T_c^n(X)$, operating only on the angular momentum[11] **X** from a body-fixed frame (whose projection is noted as c) to a space fixed one (with projection p). Normally, this includes use of a Wigner D-matrix and a summation over all possible p values, as shown in equation 3.75, which can be computationally expensive. However, using equations 3.27, 3.28, 3.37, 3.39 and 3.75, we were able to derive the following equality using a reduced rotation matrix, as defined by equation 3.92. All the quantum numbers but N may have

[11] It is important to note that **X** cannot be the rotational angular momentum operator of the body. In our case $\mathbf{X} = \mathbf{G}, \mathbf{I}$ or $\mathbf{S}$.

either integer or half-integer values. The coupling scheme used for the derivation is $\mathbf{N}+\mathbf{X}\rightarrow\mathbf{F}$:

$$\begin{aligned}\left\langle F,m_F,X',N',K'\left|T_c^n(X)\right|F,m_F,X,N,K\right\rangle &= (-1)^{N+F+X'-3X-c}\begin{Bmatrix} N' & X' & F \\ X & N & n\end{Bmatrix} \\ &\times \left\langle N',K'\left|\left|\mathscr{D}^{k*}_{\cdot,-c}\right|\right|N,K\right\rangle \\ &\times \left\langle X'||T^n(X)||X\right\rangle \end{aligned} \tag{10.47}$$

This expression is notably similar to equation 3.105, the only difference being the phase factor. This occurs as strictly speaking the rotational matrices are not spherical tensor operators. Using the formula of equation 10.47 along with the expressions presented in chapter 3, the expressions for the expectation values of the different fine and hyperfine operators were calculated and will be given in the following sections. It should be noted that $F'=F$ in all cases.

10.6.1 The Electric Quadrupole Term

The first term to be examined is the electric quadrupole interaction. The Hamiltonian for this interaction was given in equation 9.1, and the formula to evaluate this interaction when both the nitrogen nuclear angular momentum and the unpaired electron's spin are quantised in space is:

$$\begin{aligned}\left\langle F,m_F,G',N',K'\left|\left\langle n'_{NO_2},K',\mu'\left|eT^2(Q)\cdot T^2(\nabla E)\right|n_{NO_2},K,\mu\right\rangle\right|F,m_F,G,N,K\right\rangle &= \\ \sqrt{(2G'+1)(2G+1)(2N'+1)(2N+1)(2n'_{NO_2}+1)(2n_{NO_2}+1)}& \\ \times\sum_{q,c}^{2}\begin{pmatrix} n'_{NO_2} & 2 & n_{NO_2} \\ -\mu' & q & \mu\end{pmatrix}\begin{pmatrix} n'_{NO_2} & 2 & n_{NO_2} \\ -K' & c & K\end{pmatrix}\begin{pmatrix} N' & 2 & N \\ -K' & c & K\end{pmatrix}\begin{Bmatrix} N' & G' & F \\ G & N & 2\end{Bmatrix}& \\ \times\begin{Bmatrix} I' & G' & S' \\ G & I & 2\end{Bmatrix}(-1)^{N-3G+G'+N'+F-\mu'+I+S}e\langle T_q^2(\nabla E)\rangle\langle I\left|\left|T^2(Q)\right|\right|I\rangle&\end{aligned} \tag{10.48}$$

where in the summation $c=\pm2,\pm1,0$ and $q=\pm2,0$. The $\left(e\langle T_q^2(\nabla E)\rangle\langle I\left|\left|T^2(Q)\right|\right|I\rangle\right)$ values are now related to the values measured experimentally for the NO_2 molecules, by equations 9.2 and 9.3.

10.6.2 The Dipole-Dipole Term

The second term we will examine is the interaction of the nuclear angular momentum with the field created by the electron spin, the so-called dipole-dipole interaction. The Hamiltonian for this interaction is given by equation 9.5 and the matrix elements in our representation can be calculated with the formula:

$$\begin{aligned}\left\langle F,m_F,G',N',K'\left|\left\langle n'_{NO_2},K',\mu'\left|-\sqrt{10}g\mu_B g_N\mu_N T^2(S,I)\cdot T^2(C)\right|n_{NO_2},K,\mu\right\rangle\right|F,m_F,G,N,K\right\rangle &= \\ -\sqrt{50(2G'+1)(2G+1)(2N'+1)(2N+1)(2n'_{NO_2}+1)(2n_{NO_2}+1)} & \\ \times\sum_{q,c}^{2}\begin{pmatrix} N' & 2 & N \\ -K' & c & K\end{pmatrix}\begin{pmatrix} n'_{NO_2} & 2 & n_{NO_2} \\ -\mu' & q & \mu\end{pmatrix}\begin{pmatrix} n'_{NO_2} & 2 & n_{NO_2} \\ -K' & c & K\end{pmatrix} & \\ \times(-1)^{N-2G+'+N'+F-\mu'}\begin{Bmatrix} N' & G' & F \\ G & N & 2\end{Bmatrix}\begin{Bmatrix} I & I & 1 \\ S & S & 1 \\ G' & G & 2\end{Bmatrix} & \\ \times g\mu_B g_N\mu_N\langle T^2_q(C)\rangle\sqrt{I(I+1)(2I+1)S(S+1)(2S+1)} & \end{aligned} \tag{10.49}$$

where the same range applies for c,q as for the electric quadrupole term in the previous subsection. Equation 10.49 is naturally similar to equation 10.48, the main difference being, apart from the different proportionality constant, the presence of a 9-j symbol, as both **I** and **S** are involved, which also changes the phase factor slightly. The reduced matrix elements for the spin and nuclear angular momenta were evaluated using equation 3.88, and the $\left(g\mu_B g_N\mu_N\langle T^2_q(C)\rangle\right)$ may be related to the experimentally determined values using equations 9.8 and 9.9.

10.6.3 The Spin-Rotation Term

The next term that we will examine is the interaction between the electron spin and the field created by the rotation of the complex, the so-called spin-rotation interaction, whose Hamiltonian was given in equation 9.17. Unlike the previously examined terms, this has the added complication explained in sections 3.5.2 and 9.4, arising from the fact that the argument of one

of the interaction operators (the rotation of the complex, $T^1(N)$) is the same as that of the rotation matrices, namely the Euler angles of NO_2. For this reason, as described in section 3.5.2 these two do not commute and a resolution of the identity was used, which led to the following final expression being a bit more complicated than the rest:

$$\begin{aligned}
&\left\langle F,m_F,G',N',K' \left| \left\langle n'_{NO_2},K',\mu' \left| \textstyle\sum_{k=0,2} \frac{1}{2} \left(T^k(\varepsilon)T^k(N,S) + T^k(N,S)T^k(\varepsilon) \right) \right| n_{NO_2},K,\mu \right\rangle \right| F,m_F,G,N,K \right\rangle = \frac{1}{2} \textstyle\sum_{c,q,c_1,c_2} \sum_{k=0,2} \\
&\times \sqrt{S(S+1)(2S+1)(2G'+1)(2G+1)(2N'+1)(2N+1)(2n'_{NO_2}+1)(2n_{NO_2}+1)} \\
&\times \begin{pmatrix} N' & 1 & N \\ -K' & c_2 & K \end{pmatrix} \begin{pmatrix} 1 & 1 & k \\ c_1 & c_2 & c \end{pmatrix} \begin{pmatrix} n'_{NO_2} & k & n_{NO_2} \\ -\mu' & q & \mu \end{pmatrix} \begin{Bmatrix} N' & G' & F \\ G & N & 1 \end{Bmatrix} \begin{Bmatrix} S & G' & I \\ G & S & 1 \end{Bmatrix} \\
&\times \left[(-1)^{K'+n_{NO_2}-K} \sqrt{n_{NO_2}(n_{NO_2}+1)(2n_{NO_2}+1)} \begin{pmatrix} n'_{NO_2} & k & n_{NO_2} \\ -K' & c & K+c_1 \end{pmatrix} \begin{pmatrix} n_{NO_2} & 1 & n_{NO_2} \\ -c_1-K & c_1 & K \end{pmatrix} \right. \\
&\left. + (-1)^{n'_{NO_2}} \sqrt{n'_{NO_2}(n'_{NO_2}+1)(2n'_{NO_2}+1)} \begin{pmatrix} n'_{NO_2} & k & n'_{NO_2} \\ -K' & c_1 & K'+c_1 \end{pmatrix} \begin{pmatrix} n'_{NO_2} & k & n_{NO_2} \\ c_1-K' & c & K \end{pmatrix} \right] \\
&\times (-1)^{N'-K'+S+N-2G+F-c-\mu'} \langle T^k_q(\varepsilon) \rangle
\end{aligned} \tag{10.50}$$

where c and q have the same range as before, k can be either 0 or 2, c_1 and c_2 can be ± 1 or zero (as long as $c_1 + c_2 = -c$) and $\langle T^k_q(\varepsilon) \rangle$ is related to the experimentally determined values of the spin-rotation constants of NO_2 by equations 9.14, 9.15 and 9.16.

10.6.4 The Fermi Contact Term

The final term to discuss is the Fermi contact interaction. Since this is an isotropic interaction, there is no change to its expression as we move between the different frames of reference. The Hamiltonian operator for the Fermi contact interaction was given in equation 9.10 and its matrix

elements may be evaluated by using:

$$\langle F, m_F, G, N, K \left| \alpha_F T^1(S) \cdot T^1(I) \right| F, m_F, G, N, K \rangle = \frac{\alpha_F}{2} \sqrt{(G(G+1) - S(S+1) - I(I+1)} \tag{10.51}$$

where α_F is the Fermi contact constant for NO_2, and clearly this is a diagonal-only contribution with respect to all the quantum numbers.

10.6.5 The Programs Written

To compute the expectation values of the fine and hyperfine operators for each N, K_r level, a program was written using the package MATHEMATICA8. This operated on two stages. From the quantum dynamics calculations described in section 10.5, the eigenvectors for each of the N, K_r states had been calculated as a linear combination of NO_2 functions. At the first stage, the program evaluated the expressions 10.48, 10.49, 10.50 and 10.51 for each term in the linear combination of each of the N, K_r states. This program obtained what practically is the "rotated constants" from the monomer to the frame of the complex for each rotational state of each fine and hyperfine contribution (spin-rotation, dipole-dipole etc.). Moreover, as the eigenvectors may be obtained from any of the four versions of the dynamics program (one or many vibrational levels, and with or without off-diagonal Coriolis contributions), this approach enabled us to look in detail at individual effects.

Due to the large energy separation between levels of the same K_r but different N, relative to the fine and hyperfine matrix elements, any off-diagonal elements were neglected. Also, it was verified that, as would be expected from symmetry arguments, there are no surviving contributions between $K_r = 2^-$ and $K_r = 2^+$ states of the same N. Thus, we are only concerned with the matrix elements where $N' = N$ and $K'_r = K_r$.

At the second stage, the program used the values calculated from the first stage, to compile a Hamiltonian matrix of all fine and hyperfine contributions for all the F and G levels for a given N, K_r state. Diagonalising this matrix yielded the fine and hyperfine energy splittings for each

of the N, K_r states. Finally, by combining these energy levels to the rotational energy levels calculated by the dynamics and taking the corresponding differences, we predicted the fine and hyperfine structure of each rotational transition.

10.6.6 Discussion of the fine and hyperfine structure results

As was noted in the previous section, four different sets of eigenvectors could have been used to calculate the "rotated constant", depending on the version of the dynamics program used previously. The Fermi contact interaction is isotropic, so it is not influenced by inclusion or not of different vibrational levels or Coriolis contributions, and thus will be not be discussed here. For the rest of the terms, we may obtain the number before it is multiplied by the 6-j and/or 9-j symbols in equations 10.48, 10.49 and 10.50, and these are quoted in table 10.12. In all cases, $n_{NO_2} = 19$ was used and all possible K levels were included.

As the numbers in table 10.12 are yet to be multiplied by the 6-j or 9-j symbols of expressions 10.48, 10.49 and 10.50 to give the corresponding matrix elements for the different F, G levels for each each N, K_r state, themselves are not easily interpretable. However, given that what they will be multiplied with is the same for a given state irrespective of what eigenvectors were used, one can qualitatively see the effect of vibrational states and Coriolis interactions. The $N = 0, K_r = 0$ state constants are not included in the table as all contributions (but the Fermi contact) are zero due to the triangle condition between the tensor operators and the rotational angular momenta in the corresponding 3-j symbol.

The first thing to note is that even with full Coriolis, in the case of a single vibrational state, both the dipole-dipole and the quadrupole interaction constants are very close to zero, and the strong effect that the inclusion of more vibrational levels has on these values. This is somewhat surprising as the main dynamical effects that mix different n_{NO_2} states are expected to be due to the angular (instead of radial) motion. However, including more vibrational levels allows the Ne to adjust radially its position (move in and out) as NO_2 rotates.

Next, we note the effect of the Coriolis interactions to the constants. According to the

Table 10.12: The "rotated hyperfine constants", as computed using different eigenvectors

	Rotated Fine or Hyperfine Constant/MHz		
	One vibrational level, with full Coriolis		
State	Spin Rotation	Dipole-Dipole	Quadrupole
$N=1, K_r=0$	125.53	0.08	-0.36
$N=2, K_r=0$	-265.96	0.64	0.3
$N=2, K_r=2^-$	324.13	0.01	-0.4
$N=2, K_r=2^+$	309.22	-0.71	-0.31
$N=3, K_r=0$	408.37	-1.95	-0.19
$N=3, K_r=2^-$	-23.51	0.14	0.01
$N=3, K_r=2^+$	38.54	2.19	-0.25
	Four vibrational levels, with full Coriolis		
State	Spin Rotation	Dipole-Dipole	Quadrupole
$N=1, K_r=0$	90.43	1.99	-0.77
$N=2, K_r=0$	-186.74	-0.78	0.66
$N=2, K_r=2^-$	763.43	2.22	-0.85
$N=2, K_r=2^+$	746.79	0.84	-0.67
$N=3, K_r=0$	273.78	-1.48	-0.45
$N=3, K_r=2^-$	-462.59	-0.24	0.04
$N=3, K_r=2^+$	-392.57	3.69	-0.47
	Four vibrational levels, only diagonal Coriolis		
State	Spin Rotation	Dipole-Dipole	Quadrupole
$N=1, K_r=0$	0.00	1.72	-0.73
$N=2, K_r=0$	0.00	-1.88	0.79
$N=2, \lvert K_r\rvert=2$	833.65	1.84	-0.79
$N=3, K_r=0$	0.00	2.14	-0.90
$N=3, \lvert K_r\rvert=2$	-697.25	0.00	0.00

semi-rigid model it is the Coriolis interaction between the $K_r = 0$ and the $K_r = 2^+$ level that pushes them apart and thus separates the two $|K_r|$ levels. This is mirrored here as both $|K_r| = 2$ levels have the same effective fine and hyperfine constants in absence of Coriolis interactions. Also there is no spin-rotation contribution for the $K_r = 0$ level if no Coriolis contributions are included: the contributions average out in both directions of the rotation, but this symmetry is broken when $K_r = 0$ and $|K_r| = 2$ are mixed.

When no off-diagonal Coriolis contributions are included, there are no different K states mixed into the K_r, and thus[12] $K_r = K$. In this case, variation of the numbers for the dipole-dipole and quadrupole contributions is simply mirroring the first 3-j symbol of equations 10.48 and 10.49:

$$\begin{pmatrix} N' & 2 & N \\ -K' & c & K \end{pmatrix}$$

This may be taken as independent of the n_{NO_2} state and assumed constant for each N, K_r level. Also, as now we can assume $K' = K$, we only need to consider the case where $c = 0$. From [29] we find that the dependence of the 3-j symbol on N and K is

$$(-1)^{N-K} \frac{3K^2 - N(N+1)}{N(N+1)}$$

This reproduces exactly the trend in both the dipole-dipole and the quadrupole constants in the case where only diagonal Coriolis interactions are included. This agreement indicates that what is reasonably expected from a semi-rigid model perspective is replicated in these results. It also explains why there are no contributions in this case for the $N = 3, |K_r| = 2$ level. Comparing these results now with the corresponding constants calculated from the eigenvectors with four vibrational states and full Coriolis, we can see how significant these contributions are for Ne-NO_2.

Next we used the numbers in table 10.12 to calculate the fine and hyperfine energy level splittings for each of the N, K_r states. These were then added to the calculated dynamics rotational energy levels, to obtain the energy level diagram for the Ne-NO_2 complex. Finally, we

[12] Although, strictly speaking K_r is a label, while K a quantum number, they both here have the same value.

Table 10.13: Fitted fine and hyperfine constants from dynamics calculations spectrum

Parameter	Value (Error) Dynamics /MHz	Value (Error) Experimental [116]/ MHz
aa_I	0.153 (53)	4.297 (35)
a_F	147.23 (not fitted)	147.44 (128)
ε_{aa}	-113.638(53)	59 (not fitted)
$\varepsilon_{bb}+\varepsilon_{cc}$	38.07 (39)	37.781 (548)
$\varepsilon_{bb}-\varepsilon_{cc}$	50.97 (36)	59.530 (508)
aa_Q	-0.586 (253)	0.233 (41)

took the appropriate differences and used the program SPFIT to fit the predicted spectrum to a semi-rigid model. It was interesting to discover that only once we had included both different vibrational states and the off-diagonal Coriolis interactions, we were able to make the two approaches compatible. However, once this was done, we were able to fit the predicted spectrum[13] with an accuracy of 0.185 MHz. This demonstrates that the two approaches do meet and thus, although fitting the rotational transitions with the semi-rigid approach for such a floppy molecule was somewhat forced (as indicated by the very large D_{NK} value), for the fine and hyperfine structure the dynamics and semi-rigid approaches agree better. The fitted constants are given in table 10.13, next to the values that Dyer obtained by fitting the $K_r = 0$ transitions, while the predicted energy levels and spectrum may be found in appendix D. The Fermi contact interaction constant was set to the value of the NO_2 molecule.

Three things are to be noticed from this table: The first is the great agreement between the spin-rotational constants that contribute to the spectrum of the $K_r = 0$ transitions (i.e. $\varepsilon_{bb} \pm \varepsilon_{cc}$) between the dynamics and fitted values. Next is that, although the quadrupole contribution is the correct order of magnitude, the dipole-dipole contribution is very different between the experimentally fitted data and the dynamics result. However, it is worth mentioning that Dyer also used the off-diagonal contributions of both the dipole-dipole and the quadrupole terms ($bb_Q - cc_Q$ and $bb_I - cc_I$) to obtain his fit to the experimental data (with error of approximately 6 kHz), while in fitting the dynamics predictions these contributions came too close to zero to be determined. Therefore, overall the dynamics gave a very good agreement with the experimental

[13]To be precise this was done in two stages, where the pure rotational transitions were fitted first, and then the fitted constants were used to predict the spectrum including the fine and hyperfine structure. This way the 0.185 MHz error is only due to the fine and hyperfine structure and not due to the rotational levels.

data on the most significant contributions, although for the hyperfine structure the deviation was not as good. Looking at the difference between Dyer's fitted Fermi contact constant (a_F) and the dynamics analytically calculated one, there are two possible explanations: either the assumption that the electron cloud of NO_2 is not permuted by the complexation with Ne is not correct even close to the nitrogen nucleus (thus the difference in a_F), or some of Dyer's fitted constants may also have been fitting parameters to allow such impressive agreement with the fitted data. We suspect that the truth lies in a combination of these explanations.

It should also be noted that using only the predicted spin-rotation constants and the Fermi-contact interaction, the energy ordering of the transitions predicted agreed with the experimental observation (for the fitted $K_r = 0$ transitions) except in three (out of twenty-four) cases. This demonstrates that the dynamics results are reliable enough to provide a first assignment of the spectrum down to fine structure, even though to then obtain a kHz-level fit, the semi-rigid approach is more appropriate.

Yet, the major difference between the sets in table 10.13, is noted on the ε_{aa} constant. While in the dynamics this could be fitted exactly (by fitting virtual transitions to all energy levels rather than only to the allowed ones), in the semi-rigid approach this was restrained to a "reasonable" value, by scaling the values obtained in the Ar-NO_2 and Kr-NO_2 complexes. It is sad to note that Dyer made an unfortunate sign error in his extrapolation, without which, as we will see later, he may have been able to fit the $K_r = |2|$ transitions as well. The correct extrapolated number thus is $\varepsilon_{aa} \approx -59$ MHz. Therefore, the dynamics number came as a factor of two larger than the extrapolated number. The decisive contribution to this number is the degree of rotation that NO_2 performs around its a-axis, and the larger the number, the higher the degree of rotation. As was seen from the dynamics rotational transitions, our fitted potential has a lower barrier with respect to this rotation than what happens in reality, and therefore this number may be seen to represent the upper bound of ε_{aa}.

10.7 Experimental Work

In parallel with the theoretical work detailed in the previous sections, an extensive experimental search was performed for the Ne-NO_2 rotational transitions using FTMS and the apparatus presented in chapter 5.

The sample used contained 0.5% of NO_2 in 99.5% Ne and the experiments were conducted with 1.5 bar backing pressure. All of the lines that Dyer [116] recorded were verified. This was successful for all $K_r = 0$ transitions, which were also assigned by Dyer, but some of the lines reported by Dyer for $|K_r| = 2$ could not be reproduced. Instead, we were able to record two new transitions, which proved critical in identifying a pattern and thus fitting the previously unassigned transitions, as will be explained the next section.

10.8 Assignment Of The Spectrum

Thanks to the dynamics calculations, we were now fairly certain of which set of transitions belonged to each N, K_r level, and also that we could fit the hyperfine structure using a semi-rigid Hamiltonian. It should not be forgotten that before we performed the quantum dynamics, the highly asymmetric splitting between the $K_r = 0$ and $K_r = 2^-$, and the $K_r = 2^-$ and $K_r = 2^+$ sets of transitions made it questionable if what was recorded did correspond to Ne-NO_2 and if this could be fitted in the same way as for the rest of the Rg-NO_2 complexes.

Also thanks to the dynamics, we could identify what were the major contributions for the fine and hyperfine structure. It was clear that the only parameter significantly contributing to the $K_r = |2|$ transitions that was not fitted by the $K_r = 0$ transitions was ε_{aa}, but a good initial value was required to make an initial assignment. We decided to use an initial assignment of the $K_r = |2|$ transitions from the dynamics calculations and fit them along with Dyer's $K_r = 0$ assigned transitions, but with the former having greatly higher errors assigned to them compared to the later. This was actually a series of fits, where ε_{aa} was fixed and gradually varied from the dynamics value towards the value calculated from extrapolating the Ar-NO_2 and Kr-NO_2

Table 10.14: Experimentally fitted data for the Ne-NO_2 complex for $K_r = 0, 2^-, 2^+$ transitions

Parameter	Value (Error) /MHz	Parameter	Value (Error)/ MHz
$A-(B+C)/2$	10044.69 (not fitted)	ε_{aa}	-50.8663(220
$(B+C)$	5,901.933 (69)	$\varepsilon_{bb}+\varepsilon_{cc}$	37.769 (72)
$(B-C)$	685.841(14)	$\varepsilon_{bb}-\varepsilon_{cc}$	57.516 (76)
D_N	1.779(4) $\times 10^{-1}$	aa_Q	2.413 (387) $\times 10^{-1}$
D_{NK}	4.3008(41)	$(bb_Q - cc_Q)$	8.160 (6240) $\times 10^{-1}$
h_N	4.407(185) $\times 10^{-3}$	aa_I	4.305(22)
a_F	147.223(193)	$(bb_I - cc_I)$	-38.668(364)
Daa_I	-2.046(56) $\times 10^{-2}$	$D(\varepsilon_{bb}+\varepsilon_{cc})$	6.513 (63) $\times 10^{-1}$

numbers.

This way a pattern emerged, as the energy ordering of transitions proved to be essentially unaffected by the absolute value of ε_{aa}, and, even more impressively, all but one splittings between transitions were approximately constant. Furthermore, the pattern was shared between the two $K_r = 2^{\pm}$ sets of transitions. Thanks to the two newly recorded lines, we could now match the pattern to the observed lines. All but one (the weakest according to tables in ref. [11]) $\Delta F = \Delta N = 1$ lines were assigned for both sets (five for each set). The assigned spectrum may be found in appendix D, and the fitted numbers are given in table 10.14. The error in this fit unfortunately is 0.025 MHz, which is significantly higher than Dyer's, but that is also due to the fact that the last set of transitions were recorded very close to the end of the range of our spectrometer (at 17.8 GHz and our setup fails completely at 18 GHz) with great difficulty and worse than the usual precision.

It is worth noting that this pattern was also reproduced in the predicted fine and hyperfine spectrum from the dynamics calculations. In fact, the energy ordering of the assigned spectrum was correctly predicted by the dynamics, and this may be seen in appendix D.

A few things may be noticed in table 10.14. The first one is that we also had to include the off-diagonal contributions to the dipole-dipole and quadrupole interaction, but also centrifugal distortion terms for the diagonal dipole dipole (Daa_I) and the dominant spin-rotation term for the $K_r = 0$ transitions (D$(\varepsilon_{bb}+\varepsilon_{cc})$) in order to fit all the transitions. Yet, this was also done for both Ar-NO_2 [112, 113] and Kr-NO_2 [115], so it is reasonable to include these for the -even

Table 10.15: Ar-NO_2 and Kr-NO_2 ε_{aa} values [112, 113, 115]

Parameter	Ar-NO_2	Kr-NO_2
ε_{aa} /MHz	-48.037(8)	-43.171(3)

floppier- Ne-NO_2.

The next thing to note is that the deviation of the Fermi contact constant from the NO_2 molecular value is in the opposite direction to Dyer's data (both given in table 10.13) and smaller. This indicates that it probably is a fitting parameter and should not be taken as an indication of permutation of the electron cloud.

One may also notice the large value $(bb_Q - cc_Q)$ and mainly $(bb_I - cc_I)$. However, these are practically the same value that Dyer fitted. With respect to ε_{aa} , which proved to be the decisive term for the $|K_r| = 2$ transitions, it follows the trend of the values obtained for Ar-NO_2 and Kr-NO_2 (given in table 10.15), even though one may have expected a larger number based on the relative masses of the Rg atom. It is more surprising that the dynamics results were out by a factor of two, although unfortunately this was also the case for the dipole-dipole and quadrupole constants.

10.9 Conclusions

In this chapter we examined the weakly-bound van der Waals complex Ne-NO_2, by both theoretical and experimental methods. With respect to the theoretical analysis, we obtained the PES of the complex using the RCCSD(T) method and extrapolated to the CBS limit. In that we overcame the problems Dyer had in calculating the PES of the complex.

Next, a program was written (with several versions) to perform the rigid rotor quantum dynamics for this system in MATHEMATICA8. This was able to reproduce the shape of the experimentally measured spectrum, although the calculation had to be truncated due to the large size of the basis set. Fitting the calculated energy levels via a semi-rigid approach, we found that

the agreement was not as good as would be expected, possibly indicating that for very floppy complexes the semi-rigid approach has some limitations. Moreover, we found it necessary to accept an unphysically large value of D_{NK} in order to even have a fit with 0.44 MHz error. Re-examining the previously recorded Rg-NO_2 spectra, we found that the large value of D_{NK} is not uncommon and correlates with the importance of dynamical effects.

Next we used the eigenvectors calculated for each N, K_r level to calculate the energy level splitting due to the fine and hyperfine interactions. In order to achieve this we expressed these interactions for the complex in terms of the experimentally determined fine and hyperfine constants for NO_2 using spherical tensor operator algebra. We also derived the useful expression given in equation 10.47. A program was written to perform this calculation, and in combination with the different versions of the rotational dynamics program, we qualitatively highlighted the importance of including many vibrational levels and the off-diagonal Coriolis interactions. Once all these effects were included, the fine and hyperfine structure could be fitted to a semi-rigid Hamiltonian with a relatively low error, showing that the two approaches are compatible at this level. Although the calculated constants for the dipole-dipole and quadrupole interactions were not in agreement with the previously fitted values, the major contributions for the $K_r = 0$ transitions (spin-rotation) were in very good agreement, which allowed the program to predict the energy order of almost all of the previously assigned transitions, correctly.

However, for the $K_r = |2|$ levels, the major contribution (ε_{aa}) was a factor of two different from its finally assigned value. Yet, using this value, the pattern of the transitions was still predicted correctly through the semi-rigid approach. Nevertheless, although the dynamics were successful in the prediction of the pure rotational spectrum, for the fine and hyperfine structure the results are best seen qualitatively and a semi-rigid approach is better suited. This is actually a hopeful result as the fine and hyperfine programs were very demanding computationally, and thus it is convenient that a semi-rigid Hamiltonian may provide an at-least as good an analysis.

Experimentally, long searches were performed up to the limits of our setup. These allowed us to verify all the previously recorded transitions as well as record two new ones. With these two transitions and the predictions from the dynamics calculations, we were able to identify a

pattern and thus finally assign the ten strongest transitions for the $K_r = 2^{\pm}$ sets.

Chapter 11

The study of the NO_2-O_2 van der Waals complex

"*An expert is someone who knows some of the worst mistakes, which can be made, in a very narrow field.*"

- Niels Bohr

11.1 Introduction

This chapter presents our work to predict and record the rotational spectrum of the van der Waals complex formed between a molecule of nitrogen dioxide (NO_2) and of oxygen (O_2). As the motivation behind this thesis was to investigate van der Waals complexes between pairs of open shell molecules, this system seemed like an ideal candidate: as will be explained in more detail below, there are only two possible states that the species may be formed in, both of the same symmetry but differing in their multiplicity.

The study of this complex was first undertaken by a previous D.Phil. candidate in the group, Antony Starkey [2]. Starkey computed a section of the PES of the complex, to determine the minimum energy geometry. That geometry was then used to obtain the molecular complex's

rotational constants and to transform the fine and hyperfine constants of NO_2 and O_2 to the complex's principle axis frame. Then an effective Hamiltonian was used to solve the Schrödinger equation and calculate the energy levels assuming that geometry. Experimentally, Starkey used a mixture of NO with O_2 gases which was expected to produce the spectra of both NO-O_2 and NO_2-O_2. Although a number of transitions were recorded, no definite assignment was made for either complex.

Following Starkey, we used the same *ab initio* method[1] to calculate the full configuration space PES of the complex. This yielded a different minimum energy structure to the one that Starkey had predicted. Then, a previous Part II student of the group, Markus Frise [130], used our new results in the same approach as Starkey. However, the major part of Frise's work was the extensive experimental investigation close to the region that the rotational spectrum of the complex would lie if it were an asymmetric top with the predicted geometry. Frise used a gas sample of the same composition as Starkey's and six weak transitions believed to belong to this complex were recorded. Yet, again, no definite assignment could be made.

The approach used in this work is drastically different. Learning from previous experience, it was not assumed that the complex's structure could be approximated to any semi-rigid geometry. Instead, the full quantum dynamics were performed on *ab initio* PESs, which allowed us to include in our predictions the large amplitude motion of the monomers. On the experimental side, a different mixture was used, where the NO_2 in our sample was provided directly from a NO_2 gas cylinder rather than from oxidation of NO, which was hoped to limit the presence of by-products.

11.2 The NO_2-O_2 complex

Before diving into the computational details of how we approached this project, it is important to know what kind of interactions need to be considered. For this reason, in this section we will first present monomers and then the states that the complex may be formed in when these come

[1] The method used was RSPT2, the details of these calculations will be provided later in this chapter.

together. As the NO_2 monomer was presented in detail in chapter 10, here we only provide some additional information on the O_2 monomer.

11.2.1 O_2 molecule

The electron configuration and term symbols for the ground state of O_2 was derived in chapter 8, where it was shown to be $^3\Sigma_g^-$. Here we compliment that information by considering the fine and hyperfine interactions. The interaction between the unpaired electrons gives rise to the spin-spin interaction. There is also a spin-rotation interaction between the total spin and the rotation of the molecule, which is analogous to the corresponding term in the NO_2 Hamiltonian. Therefore, the total Hamiltonian for O_2 is given by:

$$\widehat{H}_{O_2} = \hat{h}_{rot} + \hat{h}_{SR} + \hat{h}_{SS} \tag{11.1}$$

where the first term corresponds to the rotational, the second to the spin-rotational and the last to the spin-spin Hamiltonians. However, due to the lack of any orbital angular momentum in its ground state, the coupling of the spin to the internuclear axis is very weak, and thus O_2 is a Hund's case (b) molecule.

As the oxygen nucleus is a boson, we need to consider the nuclear spin statistics. The translational and vibrational wavefunctions are symmetric for the same arguments as for NO_2, presented in chapter 10. The symmetry of the rotational wavefunction varies as:

$$(-1)^N$$

where N is the rotational quantum number. As the combination of the rotational and electronic (antisymmetric) wavefunctions need to be symmetric, only odd N values are possible for O_2. The molecular constants [53, 97] used in this work are given in table 11.1. where B is the rotational constant, λ the spin-spin interaction constant and γ the spin-rotation interaction constant.

Table 11.1: O_2 molecular constants

Parameter	Value/MHz
B	43 099.795
λ	59 501.471
γ	252.5872

11.2.2 The states of the complex and the coupling scheme

As there are several sources of angular momenta in this complex (namely the nuclear angular momentum of the nitrogen, the spins of the unpaired electrons and the rotational angular momenta of the monomers and of the complex), there are many possible coupling schemes that could be used. Our choice was based on the following reasons: The stronger interactions in this complex are the spin-spin interaction in the oxygen molecule and the Fermi contact interaction in nitrogen dioxide. Moreover, the oxygen spin is only weakly coupled to its intermolecular axis. Furthermore, as it was seen in chapter 8, it is convenient to have the total spin to distinguish between different *ab initio* PESs. Therefore, we chose to couple oxygen's unpaired electron spins together, then with the NO_2 electron spin, and finally with the NO_2 nuclear angular momentum. Thus the coupling scheme is:

$$\mathbf{S_{O_2,1}} + \mathbf{S_{O_2,2}} \rightarrow \mathbf{S_{O_2}} \tag{11.2}$$

$$\mathbf{S_{NO_2}} + \mathbf{S_{O_2}} \rightarrow \mathbf{S} \tag{11.3}$$

$$\mathbf{I} + \mathbf{S} \rightarrow \mathbf{G} \tag{11.4}$$

$$\mathbf{N} + \mathbf{G} \rightarrow \mathbf{F} \tag{11.5}$$

where $\mathbf{S_{O_2,1}}, \mathbf{S_{O_2,2}}$ are the spin angular momenta of the unpaired electrons in O_2, $\mathbf{S_{NO_2}}$ is the spin of the NO_2 unpaired electron, $\mathbf{I}$ is the nuclear angular momentum of the nitrogen nucleus and $\mathbf{N}$ is the total rotational angular momentum of the complex. We will use $\mathbf{n_{O_2}}$ for the rotation of O_2 and $\mathbf{n_{NO_2}}$ for the rotation of NO_2. The projection of $\mathbf{n_{O_2}}, \mathbf{n_{NO_2}}$ and $\mathbf{N}$ onto the complex axis will be noted as k_{O_2}, k_{NO_2} and K respectively, while the projection of $\mathbf{n_{NO_2}}$ onto the NO_2

b-axis will be noted as μ. It follows that:

$$K = k_{O_2} + k_{NO_2} \tag{11.6}$$

The nuclear, electron spin and total angular momenta are quantised in the space-fixed axis frame, and their respective projections are m_I, m_S and m_F. Therefore, the total basis set to be used in these calculations is:

$$|\Psi_{NO_2-O_2}\rangle = |\eta, S_{NO_2}, S_{O_2}, I, S, G, J, K, F, m_F\rangle |n_{O_2}, k_{O_2}\rangle |n_{NO_2}, k_{NO_2}, \mu\rangle \tag{11.7}$$

where η represents any other quantum numbers here neglected. As was shown in chapter 9, the O_2 spin-spin interaction may be expressed in terms of $\mathbf{S}_{O_2}$, and therefore $\mathbf{S}_{O_2,1}, \mathbf{S}_{O_2,2}$ were absorbed into η. The vector addition of the total O_2 spin ($\mathbf{S}_{O_2}$) with the NO_2 spin gives rise to an overall quartet state ($S = \frac{3}{2}$), and a doublet state ($S = \frac{1}{2}$). Following the arguments presented in chapter 8 for the NO-O_2 complex, it is expected that the doublet state will be lower in energy, due to the pseudo-covalent contribution in the potential energy.

11.2.3 Tunnelling of NO_2 in the complex

In chapter 10, we saw that for Rg-NO_2 complexes, the rotation of the NO_2 around its a-axis is equivalent to a symmetry operation that interchanges the two oxygen atoms (which are bosons) and thus the complex wavefunction has to be symmetric with respect to this interchange. If the potential energy barrier to that motion is low enough that the NO_2 nitrogen nucleus may tunnel through it, then this leads to only certain combinations of tunnelling states with the rotational functions being permitted. More specifically, the symmetric tunnelling states can only be combined with the symmetric rotational states of the complex (i.e. with K even, including zero), while the antisymmetric tunnelling states may only be combined with the antisymmetric rotational states of the complex (i.e. with K odd). This model agrees with the experimental results for all detected Rg-NO_2 complexes, and also with our predictions from the dynamics for Ne-NO_2, which were presented in chapter 10.

However, this model becomes more complicated and unclear when O_2 is substituted in the place of Ne. There are two major factors that now come into play: The first is the strength of the interaction and the energy barrier to the NO_2 nitrogen tunnelling. If NO_2-CO was considered, then by the same arguments as before, the symmetry operation would include both the rotation of NO_2 around its *a*-axis and a corresponding rotation of CO, for the overall motion to be a symmetry operation of the complex. This is expected to increase the energy barrier to this symmetry operation and thus decrease the tunnelling frequency and bring the $K = 0$ and $K = 1$ levels closer in energy. If this is the case, similar pattern to the Rg-NO_2 complexes would be expected.

There is also the second possibility, that the larger energy barrier, along with the pseudo-diatomic contribution and the larger non-covalent forces (dispersion and induction), would quench completely the tunnelling motion. In this case, no nuclear spin statistical effects need to be considered, and all K levels would appear in the spectrum as for any other asymmetric top.

Finally, as we are interested in O_2, rather than CO, there is a third case: while interchange of the oxygen atoms between the two monomers is unfeasible under our experimental conditions, there is the possibility of the tunnelling of the O_2 oxygen atoms. All previous arguments would still apply, but due to the antisymmetric electronic wavefunction of the oxygen molecule, the pattern would be reversed: i.e. the odd K levels would now be combined with the symmetric tunnelling wavefunction and the antisymmetric oxygen electronic wavefunction to give an overall symmetric wavefunction with respect to the interchange of bosons. The other combination would be the even K (symmetric) rotational wavefunction with the oxygen electronic wavefunction (antisymmetric) and the antisymmetric tunnelling state. Therefore, if this case corresponds to the physical reality, then the observed spectrum would have the opposite pattern to what has been observed for the Rg-NO_2 complexes: only the odd K levels should appear in our experimental range.

The simple answer to which of these cases corresponds to reality is that we cannot predict it in advance! Moreover, in the semi-rigid approach, only the second case would be valid, while the first and third cases could be accommodated by artificially removing any non-observed

levels. Yet, as the quantum dynamics calculations performed for Ne-NO_2 in chapter 10 were able to not only predict the pattern observed but also its deviations from the semi-rigid theory, it is believed that a similar approach can provide the answer.

11.2.4 Research approach

The approach used to study this complex was to perform the complete quantum dynamics on an *ab initio* calculated PES. This is expected to yield the complex's rotational energy levels. The steps to achieve this are:

1. The PES for complex in both multiplicities has to be calculated.
2. A functional form has to be fitted to the calculated PESs which can then be used in an effective Hamiltonian.
3. The Schrödinger equation for the complex has to be solved using this effective Hamiltonian.
4. The energy levels and eigenvectors calculated may now be used for assignment and predictions of the microwave spectrum of the NO_2-O_2 complex.
5. At the same time with the theoretical investigation described above, an extensive experimental investigation must be carried out.

Each of these steps will now be examined in turn in the following sections.

11.3 The *Ab Initio* Calculations

11.3.1 The choice of the RSPT2 method

The first question in deciding what *ab initio* methods to use to calculate the PESs, concerned the choice of HF methods. As the different states are distinguished by their spin multiplicity, it

was thought crucial to avoid any spin-contamination. For this reason all reference states were constructed using the ROHF method.

The next choice concerned the electron correlation method. A single-configuration method, such an MPn or a Coupled Cluster method, is in general easier to perform (as one does not need to choose an active space) and less prone to errors. Yet, as it was noted in chapter 10, the only single-reference method that correctly predicted the equilibrium geometry of NO_2 is RCCSD(T) [119].

Similarly to the case of the NO-O_2 spin states discussed in chapter 8, while the quartet state of the complex may only be formed between the ground states of $S_{NO_2} = \frac{1}{2}$ and $S_{O_2} = 1$ (i.e. from the vector addition of a triplet and a doublet spin state), the doublet state of the complex may only be formed from the vector addition of the $S_{NO_2} = \frac{1}{2}$ with either a $S_{O_2} = 1$ (ground state) or a $S_{O_2} = 0$ (low-lying excited state). Thus, as the interaction between the ground and the low-lying excited states of O_2 is important to take into account, a multireference method is required in the PES calculation for the doublet spin state of the complex.

There are two main approaches when considering a multireference method: either an MRCI approach, or an approach based on perturbation theory. At the point of setting up the original calculations it was hoped[2] that the dynamics could be performed directly on the calculated PESs and in that case the size consistency error of the MRCI and CIPT2 methods could potentially generate a serious error in calculating the binding energy.

As the NEVPT2 method was only available from 2010, while we started the calculation on 2008, the only remaining options were CASPT2 and CASPT3. We decided on the CASPT2 method for the following reasons: On the practical side, the computational effort increased substantially by including the third order corrections. Moreover, as was explained in chapter 7, induction and dispersion can be modelled as second order perturbation theory (PT2) corrections to the energy, and thus, a PT2 method should be able to account for -at least- the major part of the interaction.

[2]Later it was discovered that more calculations were required as will be explained shortly.

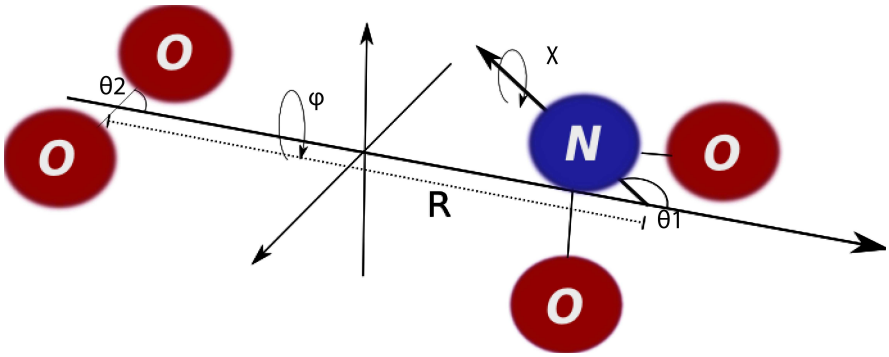

Figure 11.1: The coordinate system used for the NO_2-O_2 calculations

Furthermore, by resemblance to MPn methods, it has been noted [38] that the MP2 method tends to overestimate the interaction, while MP3 tends to underestimate it, but usually the former is closer to the correct answer [34]. Since for the single reference case, CASPT2 and CASPT3 are reduced to MP2 and MP3, it was suspected that an analogous relationship might hold. What is more, Werner *et al.* [53], have argued that the third order corrections are rarely significant. Finally, our choice was supported by the previous research of Starkey [2], who also used CASPT2 methods and obtained reasonable PESs.

As the active orbitals are expected to vary depending on the orientation and distance between the monomers, a CAS approach was preferred to an RAS one. Thankfully, the system studied was small enough that it was possible for all the $2p$ electrons of all the atoms to be included into the active space, while the $1s$ and $2s$ shells of all atoms were kept closed for all configurations. This method is expected to be accurate enough to identify all the major contributions, while fast enough for the surfaces to be calculated in a reasonable time.

11.3.2 The coordinate system

For the calculations, a centre of mass system was used between the molecules. The main reason for this choice was that it facilitated the use of symmetry to reduce the configuration space that we needed to cover. The angles used are demonstrated in figure 11.1. θ_1 is the angle between the b-axis of NO_2 and the intermolecular axis of the complex, θ_2 is the angle between the O_2 internuclear axis and the intermolecular axis, R is the distance between the centres of mass of

the molecules, χ is the angle of rotation around the NO_2 *b*-axis and ϕ is the dihedral angle between the two molecules. Although Starkey [2] used the same *ab initio* method, he used a different coordinate system and calculated only a part of the PES. For this reason, the PES for each state was calculated from scratch and the PESs calculated by Starkey were only used for reference and comparison.

There are four symmetry operations for the complex:

$$\chi \rightarrow \chi + \pi \tag{11.8}$$

$$\theta_2 \rightarrow \theta_2 + \pi \tag{11.9}$$

$$\theta_1 \rightarrow \pi - \theta_1; \quad \phi \rightarrow \phi + \pi \tag{11.10}$$

$$\chi \rightarrow 2\pi - \chi; \quad \phi + \pi \rightarrow \phi \tag{11.11}$$

These operations reduce the number of points to be calculated. Moreover, further reductions of the number of points was achieved for geometries with higher symmetry[3]. The grid chosen for the PES was to vary θ_1 and θ_2 in steps of 20° with range $0-180°$ and $0-80°$ respectively. χ and ϕ were varied in steps of 30° with ranges $0-150°$ and $0-180°$ respectively, while R was varied between 2.9 to 3.9 Å in steps of 0.1 Å. The final five-dimensional PES for each state of the complex contained 26,950 geometries, although not all points were successfully calculated. The convergence threshold used was 1.0×10^{-8} Hartrees, so that the results converged to better than 1 cm^{-1}.

11.3.3 The RSPT2 surfaces

The initial plan was to calculate the counterpoise-corrected PES for each complex state using the Dunning aug-cc-pVDZ and aug-cc-pVTZ basis sets, and then extrapolate to the CBS limit using the procedure described in chapter 4. This meant four PESs being calculated for every basis set (one for each complex spin state and two for the counterpoise correction).

[3]For example, if $\theta_2 = 0°$, then only one ϕ value needed to be calculated.

Table 11.2: The geometry and binding energy for the lowest energy points calculated using AVDZ basis set and RSPT2 method for each of the spin states

	Doublet	Quartet
Binding Energy/ cm^{-1}	-308.633	-217.220
R/ Å	3.2	3.4
θ_1/degrees	160	120
θ_2/degrees	60	60
χ/degrees	90	90
ϕ/degrees	120	90

The aug-cc-pVDZ PESs were calculated using the program MOLPRO 2006.2 [98]. In line with the arguments presented in chapter 8, the doublet state was consistently lower in energy than the quartet, and therefore we observed a pseudo-covalent contribution in the potential energy of this van der Waals complex as well. Moreover, in contrast to the NO-O_2 PESs, at no geometry did RSPT2 give any unnaturally large binding or complex energy and the dipole moments were less than 1 Debye in all geometries. These are strong indications that the problems met with RSPT2 in chapter 8 are not present in these calculations and this is a suitable method to study this complex.

The counterpoise-corrected binding energies and geometries for the lowest energy points calculated of the two states are given in table 11.2. The results seem to be consistent with the discussion of the NO-O_2 complex in chapter 8: the energy ordering follows the Heitler-London [95] theory as the minimum multiplicity has the strongest binding energy. The attractive pseudo-covalent interaction allows the monomers in the doublet spin state to get closer, thus the minimum of the doublet surface occurs at smaller R. In contrast to NO-O_2 though, there is no PES that does not meet a repulsive wall in our PESs using the RSPT2 method. This is significant as it would seem to agree with the explanation that the strongly binding NO-O_2 PES leads to bond formation and NO_3, while there is no analogous NO_4 species. Thus, NO_2-O_2 is predicted to be a "pure" van der Waals complex at all geometries and no evidence of charge transfer was found. Furthermore, the method used here, RSPT2, gave the strongest effect for NO-O_2 of all the methods investigated, so it is unlikely that we would be underestimating these effects.

The doublet spin state minimum geometry, which is also the global minimum, is shown in

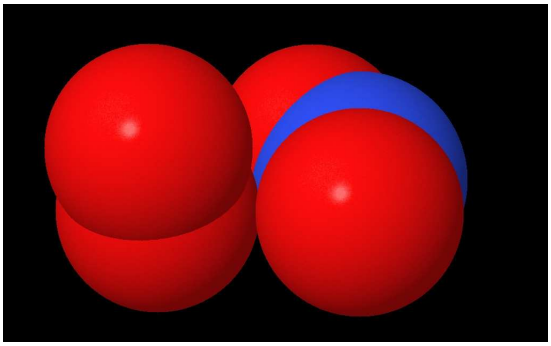

Figure 11.2: The energy minimum geometry for the doublet spin state of the NO_2-O_2 complex

figure 11.2. As it may be seen, this is a very close packed arrangement of the molecules, very different to the parallel geometry preferred for NO-O_2. This is possibly as the unpaired electron in NO_2 is in an A_1 symmetry orbital, which allows good overlap with the π orbitals of O_2 over a greater range of angles. Therefore the molecules come closer to also increase the attractive dispersion interaction between them.

In figure 11.3, the PECs of both states are plotted against the intermolecular separation at the angular geometry of the doublet state minimum. As can be seen from the graph, the separation between the states increases as the molecules come closer, which mirrors the increasing overlap between the electron clouds, while at the long range limit their splitting decreases. This interaction is analogous to the pseudo-covalent contribution to the potential energy met in NO-O_2, described in chapter 8. To demonstrate this, the energy difference between the two states in the geometry of the doublet state lowest energy point was modelled by a Born-Mayer-type of potential:

$$\Delta V_{quartet-doublet} = \exp\left[a + bR + \frac{c}{R}\right] \tag{11.12}$$

with parameters: $a = -20.1133, b = 3.9028, c = 36.4879$, and the RMSD of the fit was 1.298 cm^{-1}, while the range of the fitted data was 90.4 cm^{-1}. The fittings were performed using MATHEMATICA8 [108].

Once we obtained the aug-cc-pVDZ PES, the next step was to start working on the aug-cc-pVTZ ones. However, as each aug-cc-pVTZ point required approximately ten times more CPU time to the corresponding aug-cc-pVDZ point, a program was written to scan the aug-cc-pVDZ PES of the doublet state and print to comma delimited files (*.csv*) the coordinates of the points

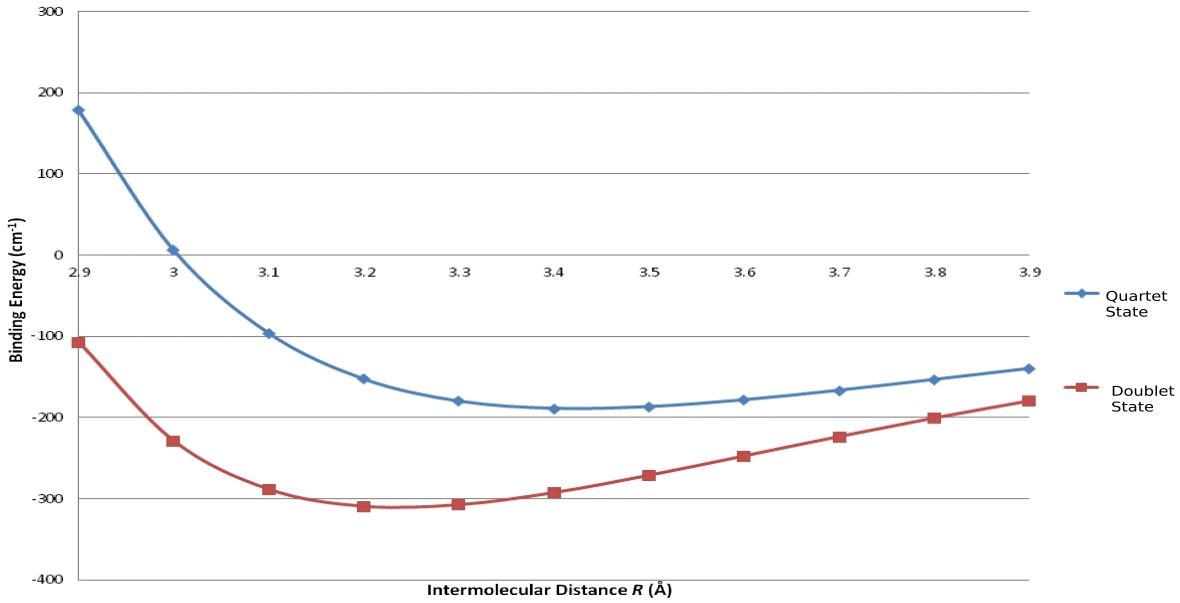

Figure 11.3: The PECs of both spin states at the angular geometry of the global minimum: $\theta_1 = 160^\circ, \theta_2 = 60^\circ, \chi = 90^\circ, \phi = 120^\circ$

with energy within some preset limits. This program was written in Visual Basic and was run through MS Office Excel [128].

Using this program, the aug-cc-pVTZ PES was gradually calculated starting from the lowest energies. The rationale behind this approach is that the complex wavefunction is more sensitive to the shape of the potential close to the energy minimum, which has to be represented accurately. The geometries higher in energy on the other hand are decreasingly influential, so the difference in the value between the aug-cc-pVDZ and the aug-cc-pVTZ basis sets values (and therefore between the aug-cc-pVDZ and extrapolated CBS value) is less important. Since the doublet spin state PES is consistently lower in energy compared to the quartet state, we used this to select the most important points.

Each of these geometries were then calculated for both the molecular complex's doublet and quartet spin states, and for the surfaces needed to perform the counterpoise correction. This way a total of 6,758 points were calculated for each of the four PESs (two spin states and two for the counterpoise correction). These PESs covered all geometries with negative binding energy and positive binding energy up to 200 cm^{-1} for the doublet state. The aug-cc-pVTZ were performed using the MOLPRO2010 [98] program. In performing these calculations, the help and resources

Table 11.3: The size consistency error for the doublet spin state using the AVDZ and AVTZ basis sets

	aug-cc-pVDZ	aug-cc-pVTZ
SCE /cm^{-1}	-23.3	-24.6

of the NSCCS are gratefully acknowledged [131].

Moreover, the size consistency error (SCE) was calculated for both basis sets and is given in table 11.3. These values are in agreement with reference [132], where it was argued that the SCE increases with basis set size and that CASPT2 is only slightly size inconsistent. Unfortunately however, two significant problems arose from the calculations described above: The first one concerned the counterpoise correction, and the second the convergence of the RHF calculations.

As was noted in chapter 4, the question of how to perform counterpoise correction in multireference cases remains open. While increasing the basis set size had a stabilizing effect on the complex and the monomers, this was greater for the monomers than for the complex, including the counterpoise surfaces. This resulted in, when the counterpoise-corrected energies were extrapolated to the CBS limit, only a few points still having a negative interaction energy. This effect was partially attributed to the overcompensation that the counterpoise procedure has been accused off: It is reasonable that the "ordinary" overcompensation is amplified if a multireference calculation is performed.

To investigate this further, we calculated the complex energy, the monomer energies and the counterpoise corrections for a small selection of points in aug-cc-pVDZ, aug-cc-pVTZ, aug-cc-pVQZ and aug-cc-pV5Z basis sets. What was found was that the extrapolation expression of Starkey was very good in all cases and the shape of the extrapolation curve follows the calculated points. What is interesting though, which also demonstrates the problem found, is that if one uses the extrapolation formula for the monomer energies and the complex energy and then takes the difference between the extrapolated values, the binding energy calculated is 6035.22 cm^{-1}. This is quite different to the value of -951.9 cm^{-1} that is obtained if the counterpoise corrected value is calculated in every basis set and then this is extrapolated. In both

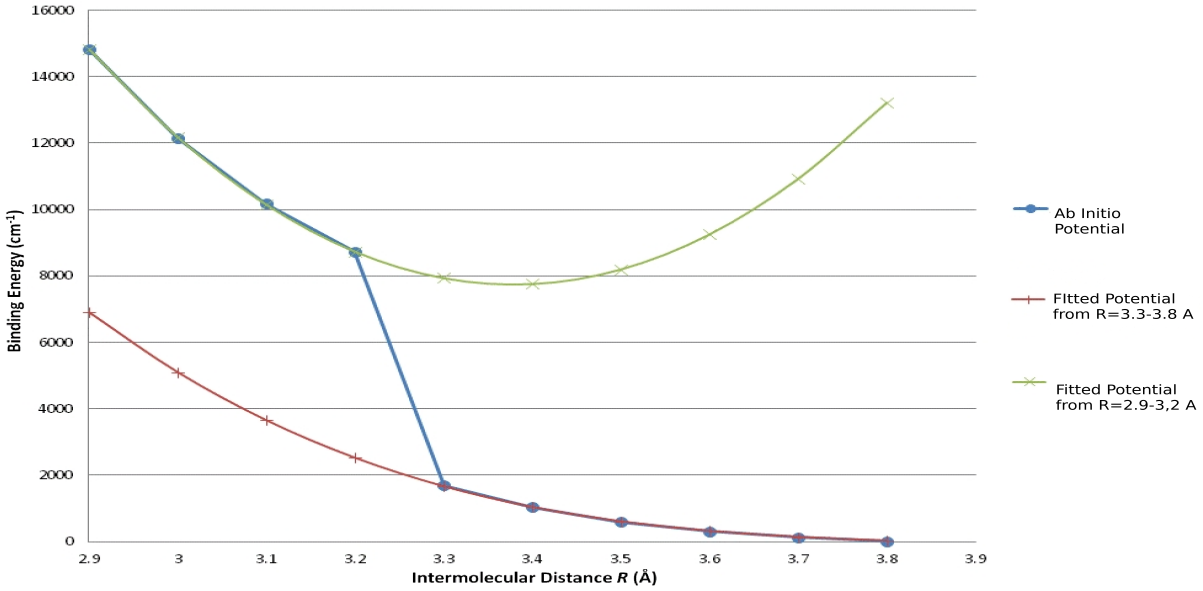

Figure 11.4: Fitted and *ab initio* PEC for the doublet spin state at the angular geometry $\theta_1 = \theta_2 = 60^\circ, \chi = \phi = 0^\circ$

cases the extrapolation was made using aug-cc-pVDZ and aug-cc-pVTZ basis sets. This effect is believed to again originate from the multireference nature of our calculation, but is different to the overcompensation of the counterpoise procedure mentioned above. Instead, in this case the convergence of the monomer energies is much faster than of the complex, and therefore when extrapolated, the deviation in the rate of convergence may cause a significant error. One possible solution is to note that, as pointed out in chapter 8, any counterpoise correction is common to both states of the complex. Therefore, if one is to take the difference between these states, this issue is avoided.

The second problem arose from the ROHF part of the calculations, which are single-reference and were used before the RSPT2 calculations were performed. To demonstrate the effect, the potential energy curve of the counterpoise-corrected doublet complex state at the geometry $\theta_1 = \theta_2 = 60^\circ$ and $\chi = \phi = 0^\circ$ is given in figure 11.4. As can be seen from the graph, there is a pronounced sudden change in energy between $R = 3.2$ Å and $R = 3.3$ Å. By simply fitting a (fourth order) polynomial of distance to the points from $R = 3.3$ Å to 3.8 Å and taking the difference of that function to the *ab initio* methods in the distances $R = 2.9$ Å to 3.2 Å, we find that there the jump is approximately in the region of 6,000-8,000 cm^{-1}. This is an intruder state problem, which is a known problem for the RSPT2 method [133, 134]. In

this particular case, the intruder state is coming from the first excited state of the O_2, which is nearly-degenerate to the ground state.

Removing by eye these "excited oxygen state" points adds an extra uncertainty to the PESs. Interestingly, these points were found in both the doublet and the quartet surfaces. Yet, if at a single geometry only one state was incorrectly calculated, then taking the energy difference between the two spin states would give an abnormally large number, which can be easily detected. If both states were incorrectly calculated, then it was hoped that a cancellation of errors would occur for the major part of the interaction. Thus, again the difference between the doublet and quartet states was thought to be more reliable than the individual PESs.

11.3.4 The RCCSD(T) surfaces

The problems described at the end of the previous section cast a suspicion on whether the final RSPT2 PESs would be accurate and robust enough to use.

For that reason, an expensive and time consuming new approach was taken: As was mentioned earlier, the quartet state of the complex can be adequately described by a single reference method, as it is uniquely formed by the combination of the doublet state of NO_2 with the triplet state of O_2. Moreover, at least a RCCSD(T) method is required for the NO_2. Thus, the approach taken was to calculate the PES of the quartet state of the complex using RCCSD(T). Then, the difference between the states could be taken from the RSPT2 approach and that could be added to the RCCSD(T) PES to generate the doublet spin state PES. This would allow for a large cancellation of errors. Moreover, according to Bartolomei *et al.* [51, 52], this approach at least sometimes provides a better answer than the similar procedure of taking the difference between MRCI calculations and adding this to a Coupled Cluster PES.

The PES of the quartet complex state was calculated using the ROHF and RCCSD(T) methods and the aug-cc-pVDZ basis set. The same coordinate system was used, with the same steps and ranges for the angular coordinates. However, a different range was selected for R, which took the values 2.9, 3.1, 3.2, 3.3, 3.4, 3.6, 3.8, 4.2, 4.6 and 5 Å. A dense radial grid was used in

Table 11.4: The binding energy and geometry of lowest energy point calculated with RCCSD(T) method and the AVDZ basis set

RCCSD(T) Quartet State Minimum	
Binding Energy/ cm^{-1}	-159.747
R/ Å	3.3
θ_1/degrees	120
θ_2/degrees	80
χ/degrees	90
ϕ/degrees	90

the region of the minima of the complex, while we felt that we also need to expand the coverage to represent regions governed only by long-range interactions[4]. The Gaussian09 [135] computational program was used to perform these calculations and the convergence criterion was set to "Tight".

However, the RCCSD(T) method is computationally expensive, and a single point aug-cc-pVTZ calculation required approximately 10 times more than a RCCSD(T) aug-cc-pVDZ calculation, and double that of an RSPT2 aug-cc-pVTZ calculation. For this reason, it was not feasible with our computer resources to calculate the PES using a aug-cc-pVTZ basis set as well. For these calculations, the help and resources of the Oxford Supercomputer Centre are gratefully acknowledged [136]. All PESs (RSPT2 and RCCSD(T)) are given in the CD attached to this thesis.

The coordinates of the lowest energy point calculated of the counterpoise-corrected RCCSD(T) aug-cc-pVDZ PES is given in table 11.4. The first thing to note is that the geometry is very similar to the minimum calculated by the RSPT2 method for the quartet state. As RCCSD(T) is considered a robust method this may be seen to indicate that the RSPT2 method is a suitable choice for the quartet spin state, at least in predicting the equilibrium geometry. The small difference in the intermolecular distance may be attributed to contributions that in perturbation theory terms would correspond to higher than second order corrections in the dispersion and induction interactions, which are left out in the RSPT2 case but are taken into

[4]This decision was influenced by our experience with the Ne-NO_2 complex that was described in chapter 10. It may be interesting to the reader to know that we started the RSPT2 calculations on NO_2-O_2 before investigating the Ne-NO_2 complex.

account in RCCSD(T). Moreover, the fact that a very similar geometry was predicted by both methods increases our confidence that these may be combined.

Finally, we must notice that the minimum predicted by RCCSD(T) is much shallower, by approximately 57.5 cm^{-1} which is slightly more that 25% of the binding energy predicted by RSPT2. This could be due to the overestimation of the interaction that RSPT2/MP2 methods have been noted[5], and could contribute to the reasons why it has been so difficult to detect this complex experimentally.

11.4 Fitting the PESs

Having calculated the PESs, the next step in our approach is to represent them by a suitable function that may be included in an effective Hamiltonian. The approach taken here is the Linear Expansion in the Anisotropy of the POTential (LEAPOT [78]), where the potential function is constructed by a linear combination of a product of radial and angular functions[6]:

$$V_{tot}(R,\theta) = \sum_i V_{i,radial}(R) V_{i,angular}(\omega) \tag{11.13}$$

where ω is here a collective index for all the angles, and R is the intermolecular distance. In the first stage, we will concentrate on the angular part of the potential.

11.4.1 The mathematical form

In order for the function to be able to represent the potential, it needs to have the same degrees of freedom. The approach here is to represent the angular part of the potential by a linear combination of a product of two complete sets of functions, one for each monomer.

[5] Similarly, for NO-O_2 we noticed that the splitting between different states was greater in the RSPT2 in comparison to the RCCSD(T) calculations in chapter 8.

[6] See chapter 7.

The intermolecular potential may be expressed in terms of the coordinates of the molecules. Since here we are interested for the angular part only, these coordinates correspond to the Euler angles of the molecules with respect to the axis system of the complex. For NO_2 these are (ϕ_1, θ_1, χ), while O_2 (being linear) can be characterised using only two angles, therefore its Euler angles are $(\phi_2, \theta_2, 0)$. The quantum numbers m_{NO_2}, l_{NO_2} and λ are associated with the NO_2 Euler angles, and m_{O_2} and l_{O_2} with the O_2 ones. Wigner D-matrices form a complete set of functions that span the Euler angles, and therefore the angular potential may be written as a linear combination of a product of D-matrices, one for each molecule:

$$V_{angular} = \sum_{l_{O_2}, l_{NO_2}, m_{O_2}, m_{NO_2}, \lambda} C^{l_{O_2}, l_{NO_2}}_{m_{O_2}, m_{NO_2}, \lambda} \underbrace{\mathscr{D}^{l_{O_2}}_{m_{O_2},0}(\phi_2, \theta_2, 0) \mathscr{D}^{l_{NO_2}}_{m_{NO_2},\lambda}(\phi_1, \theta_1, \chi)}_{(-1)^{m_{O_2}} \sqrt{\frac{4\pi}{2l_{O_2}+1}} \mathscr{Y}^{l_{O_2}}_{-m_{O_2}}(\omega_{O_2}) \mathscr{D}^{l_{NO_2}}_{m_{NO_2},\lambda}(\omega_{NO_2})} \tag{11.14}$$

where we used equations 3.57 and 3.58 to substitute the D-matrix for the O_2 for a spherical harmonic. We also used the shorthand ω_k to denote the Euler angles of molecule k.

As the potential depends only on the relative angle between the molecules ($\phi = \phi_1 - \phi_2$), it follows that:

$$m = -m_{O_2} = m_{NO_2} \tag{11.15}$$

For clarity, we will use the index i for the summation over all combinations of $l_{O_2}, l_{NO_2}, m_{O_2}, m_{NO_2}$ and λ. We can now substitute the expressions 3.8, 3.9 and 3.49 in equation 11.14:

$$V_{angular} = \sum_i C^i \sqrt{\frac{2}{2l_{O_2}+1}} \Theta_{l_{O_2},m}(\theta_2) \underbrace{\exp[\imath m(\phi_1 - \phi_2)]}_{\exp[\imath m \phi]} d^{l_{NO_2}}_{m,\lambda}(\theta_1) \exp[-\imath \lambda \chi] \tag{11.16}$$

Using equations 3.14 and 3.51, we can relate the Theta functions ($\Theta_{l,m}(\theta)$) and reduced D-matrices to their value when the sign of m is reversed. Therefore, we can add the corresponding functions and limit the range of m to $m \geq 0$. Applying this and using equation 3.13 to express the $\Theta_{l_{O_2} m}(\theta_2)$ function as an associated Legendre polynomial, the expression for the potential

becomes:

$$V_{angular} = \sum_j C_j \sqrt{\frac{(l_{O_2}-m)!}{(l_{O_2}+m)!}} d^{l_{NO_2}}_{m,\lambda}(\theta_1)\mathscr{P}^{l_{O_2}}_m(\theta_2) \times \left(\underbrace{\exp[\imath m\phi]\exp[-\imath\lambda\chi]+\exp[-\imath m\phi]\exp[\imath\lambda\chi]}_{=\cos(m\phi-\lambda\chi)} \right) \quad (11.17)$$

In deriving equation 11.17 we used the fact that, by symmetry, λ can only be even or zero. This follows from the fact that, as will be seen in the next section, λ links the projections of the NO_2 rotational angular momentum on its own axis (μ). As the quantisation axis chosen on the NO_2 molecule is the *b*-axis, due to nuclear spin statistics [111], μ (and thus λ) can only be even.

In equation 11.17, the summation over j now includes all non-negative integer values for m, as long it is smaller than both l_{O_2} and l_{NO_2}, and all even integer of λ which are less than or equal to l_{NO_2}. In the case that $m = 0$, only positive values of λ are included. The factorial terms were absorbed into the parameters, so the fitted coefficients (W_j) are related to the C_j coefficients by:

$$W_j = \sqrt{\frac{(l_{O_2}-m)!}{(l_{O_2}+m)!}} C_j \quad (11.18)$$

Finally, if l_{O_2} was odd, then the potential would change if the two oxygen nuclei in O_2 were interchanged. As this is unphysical, l_{O_2} was restricted to even values.

11.4.2 The program written

To fit the function of equation 11.17 to the calculated PESs, a double precision program was written using FORTRAN90. The input to this program was a comma delimited file including a potential energy surface cut at a single distance. Only one PES was fitted at each time. The user specified the distance of this surface and the maximum values for l_{O_2}, l_{NO_2}, m and $|\lambda|$. These were limited to 9, 8, 3 and 6 respectively, as to always be less than the number of θ_2, θ_1, χ and ϕ values calculated at the PES. Moreover, the option was given for the user to specify only a maximum value for $(l_{O_2} + l_{NO_2})$ and the program created a set of all possible combinations for

l_{O_2}, l_{NO_2}, m and λ.

Using that input, a linear non-weighted least squares fit was performed to determine the coefficients of the potential expansion and the RMSD. In order to achieve this, all the functions in the expansion were evaluated for all the points that were successfully calculated in the PES via the following recurrence relations [32, 129, 137, 138]:

$$\mathscr{P}_m^m(\cos\theta) = \frac{2m+1}{2m+2}\sin(\theta)\mathscr{P}_{m-1}^{m-1}(\cos\theta) \tag{11.19}$$

$$\begin{aligned}\mathscr{P}_m^l(\cos\theta) &= \frac{2l-1}{\left[l^2-m^2\right]^{1/2}}\cos(\theta)\mathscr{P}_m^{l-1}(\cos\theta) \\ &- \left[(l-1)^2-m^2\right]^{1/2}\mathscr{P}_m^{l-2}(\cos\theta)\end{aligned} \tag{11.20}$$

$$d_{l,0}^l(\theta) = -\frac{1}{2}\sqrt{\frac{2l(2l-1)}{l^2}}\sin(\theta)d_{l-1,0}^{l-1}(\theta) \tag{11.21}$$

$$d_{l-1,\lambda}^l(\theta) = -\frac{2(l\cos(\theta)-\lambda)}{\sqrt{2l}\sin(\theta)}d_{l,\lambda}^l(\theta) \tag{11.22}$$

$$\begin{aligned}d_{m,\lambda}^l(\theta) &= \frac{2(\lambda-(m+1)\cos(\theta))}{\sin(\theta)\sqrt{(l+m+1)(l-m)}}d_{m+1,\lambda}^l(\theta) \\ &- \frac{(l-m-1)(l+m+2)}{\sqrt{(l+m+1)(l-m)}}d_{m+2,\lambda}^l(\theta)\end{aligned} \tag{11.23}$$

$$d_{l,\lambda}^l(\theta) = -\sqrt{\frac{l-\lambda+1}{l+\lambda}}\frac{l\cos(\theta)-\lambda}{\tan(\theta)(l\cos(\theta)-\lambda+1)}d_{l,\lambda-1}^l(\theta) \tag{11.24}$$

and using the fact that $d_{0,0}^0(\theta) = \mathscr{P}_0^0(\cos\theta) = 1$ as a starting point. These were derived bearing in mind the symmetry of the potential function, e.g. that λ is only even or zero. The double precision matrix inversion subroutines were taken from the computational packages LAPACK [139] and BLAS [140, 141, 142, 143, 144, 145, 146, 147].

The program's output came in the form of three comma delimited files. The first one, "results.csv", contained the coefficients for the potential function. The second one, "index.csv", contained a table of the monomer basis functions used in the fit, in the same order that the coefficients were printed. This enabled the user to assess how significant each function was to the fit and truncate the series appropriately. Also, the coefficients calculated were used to predict the potential at the input geometries, and this was printed in the file "vj2.csv". Finally, the program calculated the RMSD of the fit.

Unfortunately, the RMSD of the linear fit for the RSPT2 surfaces at close distances (including the distances of the energy minima for all PESs) was tens of cm^{-1}, even when all possible functions were used. This was simply not useful for predictions for microwave spectroscopy of species trapped in a potential energy well. The main reason suspected for this was that the potential at some geometries is very repulsive, which pulled the fit. As we were more interested in the bottom of the well, the option was given to the user to scale the fit. The scaling function used in the program was:

$$V_{scaled} = V_0 \tanh\left(\frac{V_{or} - V_{min}}{V_0}\right) \tag{11.25}$$

where V_{or} is the original calculated potential and V_{scaled} is the scaled potential. V_{min} was the lowest value in the original potential, which is automatically found by the program, and V_0 is a scaling parameter set by the user. At small $\frac{V_{or}-V_{min}}{V_0}$ values, the potential remains unchanged, while as the V_{or} tends to the V_0 value, the potential smoothly goes to V_0. For the scaling to take place the potential is lifted so that its lowest value corresponded to 1 cm^{-1}. However, now there were a lot of points with the value V_0 at physically important distances (R =3-3.4 Å), which acquired a large statistical weight. Moreover, fitting many angular coordinates to the same value required a large number of angular functions. Thus, although the RMSD was lowered it was still not good enough. The next improvement implemented in the program was to give the option of a non-linear weighted least squares fit. This allowed the user to specify weights/ uncertainties on points based on their energy. This was designed to be used in combination with the scaling. The points were broken down to four groups, the first one being the unchanged potential, and rest were separated gradually until the scaled final upper value.

For this, the Levenberg-Marquant [127] method was used and the linear least squares coefficients were given as initial values. The user was probed at the end of every successful iteration whether to continue and another similar checkpoint was added every ten iterations. The lowest RMSD coefficients only were kept. The potential re-calculated by the non-linear weighted least squares method is also printed by the program in the file “check3.csv”.

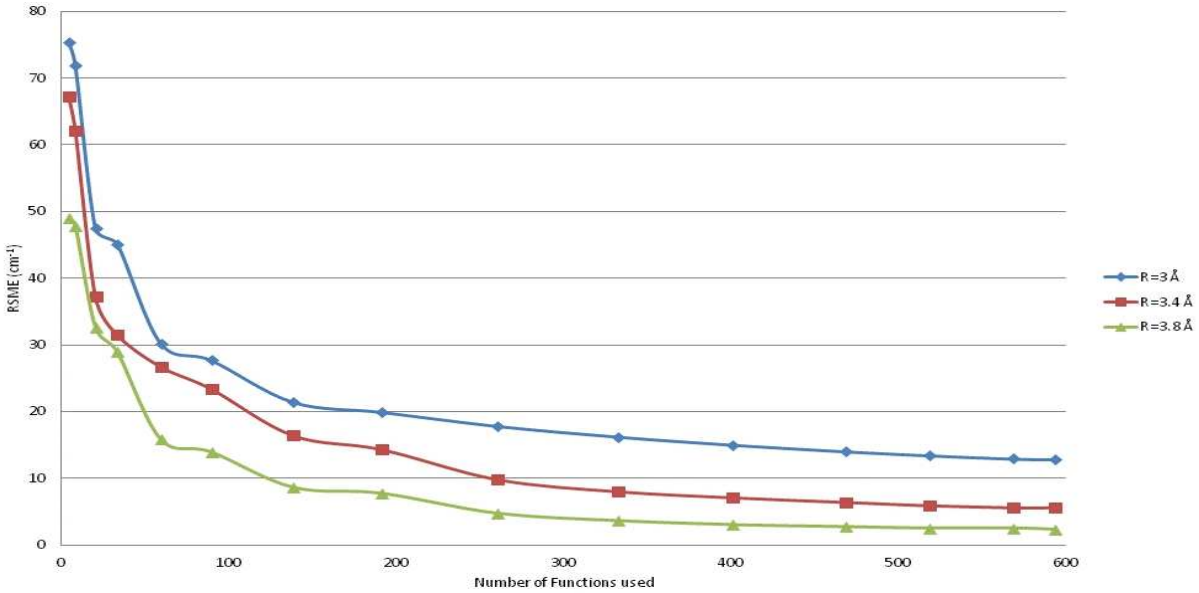

Figure 11.5: The RMSD of the fit versus the number of functions used at $R = 3, 3.4$ and 3.8 Å.

11.4.3 PES fitting discussion

The fitting program allowed a lot of flexibility in the choice of both the formulation of the potential expansion as well as the method for the fitting. The user was informed at launching the program of the number of parameters that would be fitted, the number of points to be used in the fit and at the end, the RMSD of the linear non-weighted least squares fit. The program also printed the minimum and maximum values of the potential to help with the selection of scaling parameters.

Initially we will concentrate on the fitting of the RSPT2 surfaces, as these proved more challenging, and then we will move to the RCCSD(T) surface. Moreover, as the doublet state is physically the most important one (as it is the ground state), we will use it to demonstrate the performance of the fitting program.

In figure 11.5, the RMSD of the linear non-weighted least squares fit is plotted as the number of functions is increased. The number of functions rises as we increase the maximum ($l_{NO_2} + l_{O_2}$) value by one, thus giving the 16 points plotted for all distances. In every case the maximum possible number of m and λ values were used in the fit. The values for the diagram are given in the table 11.5, RMSD is quoted in cm^{-1}.

Table 11.5: Linear Non-Weighted Fitting of the RSPT2 Doublet Spin State Potential

$l_{NO_2}+l_{O_2}$	No. of functions	RMSD at $R=3.0$ Å	RMSD at $R=3.4$ Å	RMSD at $R=3.8$ Å
2	5	75.4	67.3	49.0
3	9	71.9	62.11	47.8
4	21	47.5	37.2	32.6
5	34	45.1	31.5	28.9
6	60	30.2	26.7	15.8
7	90	27.7	23.4	13.9
8	139	21.4	16.4	8.6
9	192	19.9	14.3	7.7
10	261	17.8	9.8	4.7
11	333	16.2	8.0	3.6
12	401	15.0	7.1	3.0
13	469	14.0	6.4	2.7
14	519	13.4	5.9	2.5
15	569	12.9	5.6	2.5
16	594	12.8	5.6	2.3

For the fittings presented in this graph, the potential was scaled with a maximum value of 500 cm^{-1} relative to the lowest point. As it can be seen this trends asymptotically to a number even over 10 cm^{-1} for part of the chemically important region. Sadly, this is simply not precise enough for FTMS predictions. The asymptotic shape of the curve indicates that a very large number of functions is required for convergence. Another interesting feature is that there is a sharp drop every two $(l_{NO_2}+l_{O_2})$ values until $(l_{NO_2}+l_{O_2})=6$. This is because λ is restricted to be even, and for this reason, only even values of $(l_{NO_2}+l_{O_2})$ increase the possible values of λ. This trend stops after $(l_{NO_2}+l_{O_2})=6$ as this is the maximum possible λ value for the PESs computed. Finally, one may notice that as the R value increases, the RMSD of the fit decreases. This is logical as the potential becomes less anisotropic at larger separation of the molecules, and thus easier to fit.

For the remaining diagrams, a cut of the RSPT2 surface of the doublet spin state is used, at $R=3.2$ Å, calculated using the aug-cc-pVDZ basis set and scaled with a maximum value of 500 cm^{-1}. Figure 11.6 demonstrates visually the increasing quality of the fit as more functions are used. The horizontal axis is simply an index of the number of the points as these are arranged in order of increasing energy, and it is clear that the functions are following the shape of the potential.

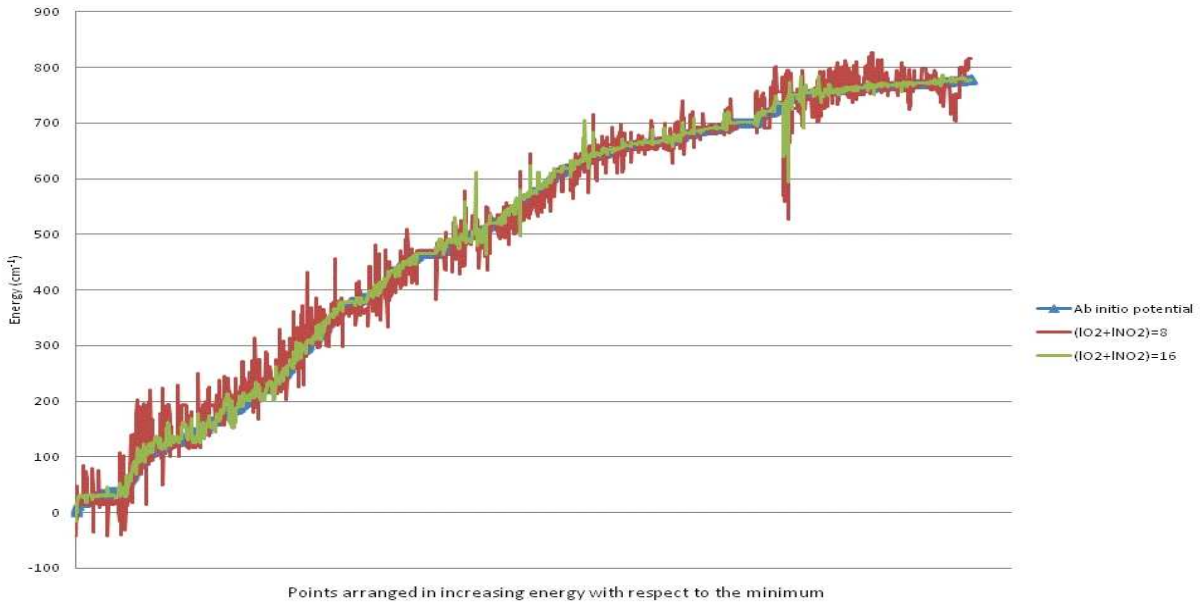

Figure 11.6: *Ab initio* and linearly fitted potentials for $R = 3.3$ Å for the doublet spin state with different number of functions

In figure 11.7 the difference between the weighted and non-weighted approach may be seen. The points are arranged again in order of increasing energy. It is clear that the linear non-weighted least square method provides an equally good fit for all the points, while the weighted non-linear fit has large errors at high energies but is fits the lower energy points much better. Yet, as may be seen in this graph, the lowest points are still not very well fitted. This occurs as there is a greater number of points with binding energy 60-100 cm^{-1} from the minimum, than in the lower regions of the potential. As these points are so close to the minimum, neither the scaling nor the weighting may significantly distinguish them from it, and they acquire a large statistical weight. For this reason, very severe scaling and weighting, as well as the maximum number of functions was required to obtain an acceptable RMSD value of below 3 cm^{-1} which represented the minimum region accurately.

Moving now to the RCCSD(T) PES fitting, table 11.6 represents the change of RMSD over different distances as more functions were included. Again, the scaling was used to even out any points with energy over 500 cm^{-1} from the minimum and equal weighting was used for all points. What can be clearly seen is that the RMSD is generally lower than it was for the RSPT2 surface. By observing the PESs, this is believed to be as the RCCSD(T) PES is much smoother than the RSPT2 ones and therefore was easier to fit with periodic functions. Again,

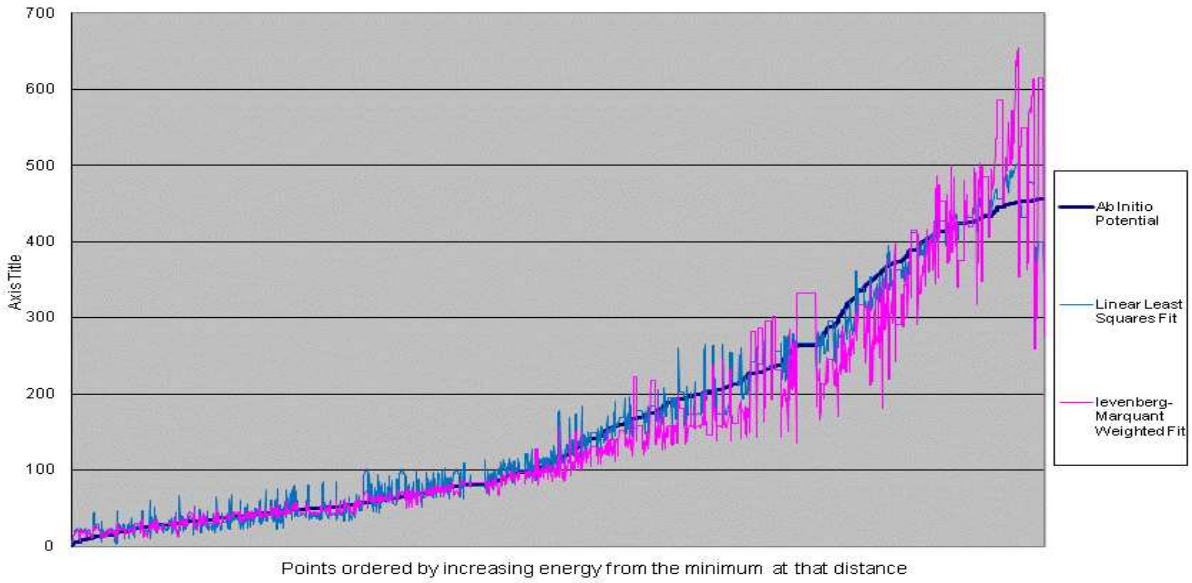

Figure 11.7: *Ab initio*, linearly fitted, and weighed fitted potentials for $R = 3.5$ Å for the doublet spin state with $l_{NO_2} + l_{O_2} = 8$

Table 11.6: Linear Non-Weighted Fitting of the RCCSD(T) Potential

$l_{NO_2} + l_{O_2}$	No. of functions	$R = 3.2$ Å RMSD	$R = 3.4$ Å RMSD	$R = 3.6$ Å RMSD
2	5	105.1	98.5	78.4
3	9	97.0	85.5	64.7
4	21	50.8	51.6	46.27
5	34	42.0	42.6	41.45
6	60	28.4	30.4	21.9
7	90	21.8	25.4	17.2
8	139	15.5	14.4	11.6
9	192	11.3	10.0	8.8
10	261	7.3	6.5	5.4
11	333	5.1	4.6	4.8
12	401	4.1	3.0	3.0
13	469	3.6	2.3	2.2
14	519	3.4	1.8	1.7
15	569	3.3	1.6	1.6
16	594	3.2	1.5	1.6

the fit RMSD decreases with the increasing number of functions used and also with larger intermolecular distances.

11.5 The Dynamics Program

The program written and presented in the previous section is able to give the best possible fitting for the potential function chosen. Now, that fitted function can be used to solve the angular part of the Schrödinger equation. The computer program described in this section was designed to achieve this. Apart from getting a first estimate of the eigenvalues to predict the spectrum, this may be able to answer the question of what is the effect of the nuclear spin statistics on this complex.

Also, assuming that the complex's wavefunction would be fairly localized to its equilibrium distance, using the eigenvectors calculated for the angular part of the Hamiltonian could give a good indication of the frequency region that the microwave spectrum would lie, which will aid our experimental investigation.

11.5.1 The angular Hamiltonian

The strongest mixing of the two spin states comes from the spin-spin interaction of O_2. As the separation between the states in the geometries close to the energy minimum is of the order of 100 cm^{-1}, and the spin-spin constant in oxygen is approximately 1.9 cm^{-1}, the two states are not strongly mixed. Therefore, the effect of the quartet state on the doublet state may be taken by perturbation theory at a later stage. For this reason, we can solve the Schrödinger equation for one spin state at the time. Thus, the Hamiltonian of the molecular complex may be written as:

$$\hat{H}_{total}(\omega,R) = \hat{T}_{complex}(R) + \hat{h}_{rot,compl}(\omega,R) + \hat{h}_{NO_2}(\omega) + \hat{h}_{O_2}(\omega) + \hat{U}_{d/q}(\omega,R) \qquad (11.26)$$

where the first term is the kinetic energy operator of the complex, the second the end-over-end rotation of the complex, the third is the Hamiltonian of the NO_2 molecule, the fourth is the Hamiltonian of the O_2 molecule, the fifth is the potential energy operator for the spin state investigated. ω is used to indicate that the term depends on the angular coordinates, while R indicates a radial dependence. We separate the Hamiltonian of equation 11.26 to an angular and a radial part. The angular Hamiltonian is:

$$\hat{H}_{angular} = \hat{h}_{rot,compl}(\omega;R) + \hat{h}_{NO_2}(\omega) + \hat{h}_{O_2}(\omega) + \hat{U}_d(\omega;R) + \hat{U}_q(\omega;R) \tag{11.27}$$

where now there are only terms that depend parametrically on the intermolecular distance. The next approximation made was to ignore the fine and hyperfine components. This was decided as it led to the basis set size being reduced by a factor of six, and hence reduce the computational cost. Moreover, the fine and hyperfine terms are not critical in order to understand and predict the basic rotational energy pattern of this complex, and hence the effects of dynamics, and thus may be taken into account latter. Therefore, the Hamiltonian used to perform the dynamics is:

$$\hat{H}_{dynamics} = \hat{h}_{rot,compl}(\omega;R) + \hat{h}_{NO_2,rot}(\omega) + \hat{h}_{O_2,rot}(\omega) + \hat{U}_d(\omega;R) \tag{11.28}$$

and the basis set is:

$$|\Psi_{NO_2-O_2,angular}\rangle = |\eta,N,K\rangle|n_{O_2},k_{O_2}\rangle|n_{NO_2},k_{NO_2},\mu\rangle \tag{11.29}$$

where the motion of the monomers is quantised in the complex (rotating) axis system. In the following sections, each of the terms in the Hamiltonian, and their evaluation will now be examined in turn. For clarity, only the quantum numbers that are relevant to the evaluation of the contribution of each term are included, and the expressions are diagonal to any quantum numbers ignored.

11.5.2 The O_2 and NO_2 rotation terms

For both of the monomers, as the fine and hyperfine structures are here ignored, the only surviving contributions are from their rotational Hamiltonians. For oxygen, which is a linear top, the rotational energy operator was given in equation 2.16, while its matrix elements can be evaluated using equation 2.17. The NO_2 rotational Hamiltonian and its matrix elements were given in chapter 10 and exactly the same apply here.

11.5.3 The complex rotation term

The next term to consider corresponds to the end-over-end rotation of the complex. Similar to what was discussed in chapter 2, the motion of the NO_2 and O_2 fragments may be regarded as internal rotations. Then, the rotation of the complex may be expressed as the rotation of a pseudo-diatomic, where each of the monomers is one of the dimensionless "atoms", separated by distance R from the other.

In the absence of any nuclear or spin angular momentum, we can express the operator for the pseudo-diatomic rotational energy, in a manner similar to what was used in equation 2.56, as:

$$\begin{aligned}
\hat{h}_{rot,compl} &= B_{pd}\left(\hat{N}-\hat{n}_{NO_2}-\hat{n}_{O_2}\right)^2 \\
&= B_{pd}\left[\hat{N}^2+\hat{n}_{NO_2}^2+\hat{n}_{O_2}^2-2\hat{N}_z\left(\hat{n}_{O_2,z}+\hat{n}_{NO_2,z}\right)+2\hat{n}_{O_2,z}\hat{n}_{NO_2,z}\right. \\
&+ \hat{N}^+\hat{n}_{NO_2,-}+\hat{N}^-\hat{n}_{NO_2,+}+\hat{N}^+\hat{n}_{O_2,-}+\hat{N}^-\hat{n}_{O_2,+}+\hat{n}_{NO_2,+}\hat{n}_{O_2,-} \\
&+ \left.\hat{n}_{NO_2,-}\hat{n}_{O_2,+}\right] \qquad (11.30)
\end{aligned}$$

where B_{pd} is the pseudo-diatomic rotational constant, $\hat{N}_z, \hat{n}_{NO_2,z}$ and $\hat{n}_{O_2,z}$ are the rotational angular momentum of the complex, the NO_2 and the O_2, onto the intermolecular axis respectively. $\hat{n}_{NO_2,\pm}$ and $\hat{n}_{O_2,\pm}$ are the raising and lowering operators for the NO_2 and O_2 molecules respectively, following the "normal definition" given in equation 2.24. $\hat{N}^+$ and $\hat{N}^-$ are the raising and lowering operators defined for the anomalous commutation relationships, given in

equation 3.68.

The diagonal matrix elements of the operator 11.30 are given by:

$$\begin{aligned}\langle N,K,n_{NO_2},k_{NO_2},n_{O_2},k_{O_2}|\hat{h}_{rot,compl}|N,K,n_{NO_2},k_{NO_2},n_{O_2},k_{O_2}\rangle = \\ = B_{pd}\left[N(N+1)+n_{NO_2}(n_{NO_2}+1)\right. \\ \left.+n_{O_2}(n_{O_2}+1)+2\left(k_{NO_2}k_{O_2}-K^2\right)\right]\end{aligned} \tag{11.31}$$

In addition to these, there are off-diagonal Coriolis forces matrix elements. These may be diagonal in K:

$$\begin{aligned}\langle N,K,n_{NO_2},k_{NO_2}\pm 1,n_{O_2},k_{O_2}\mp 1|\hat{h}_{rot,compl}|N,K,n_{NO_2},k_{NO_2},n_{O_2},k_{O_2}\rangle = \\ = B_{pd}\sqrt{(n_{NO_2}(n_{NO_2}+1)-k_{NO_2}(k_{NO_2}\pm 1))(n_{O2}(n_{O_2}+1)-k_{O_2}(k_{O_2}\mp 1))}\end{aligned} \tag{11.32}$$

or off-diagonal in K:

$$\begin{aligned}\langle N,K\pm 1,n_{NO_2},k_{NO_2}\pm 1,n_{O_2},k_{O_2}|\hat{h}_{rot,compl}|N,K,n_{NO_2},k_{NO_2},n_{O_2},k_{O_2}\rangle = \\ = B_{pd}\sqrt{(N(N+1)-K(K\pm 1))(n_{NO_2}(n_{NO_2}+1)-k_{NO_2}(k_{NO_2}\pm 1)}\end{aligned} \tag{11.33}$$

$$\begin{aligned}\langle N,K\pm 1,n_{NO_2},k_{NO_2},n_{O_2},k_{O_2}\pm 1|\hat{h}_{rot,compl}|N,K,n_{NO_2},k_{NO_2},n_{O_2},k_{O_2}\rangle = \\ = B_{pd}\sqrt{(N(N+1)-K(K\pm 1))(n_{O_2}(n_{O_2}+1)-k_{O2}(k_{O_2}\pm 1))}\end{aligned} \tag{11.34}$$

11.5.4 The potential energy term

The final term that we need to consider represents the intermolecular potential energy. This is modelled using the fitting program described earlier, and it has the same functional form for both the doublet and the quartet states. The intermolecular potential only mixes different monomer states and is independent of N, therefore the only part of the basis set that it acts on is:

$$|n_{NO_2},\mu,k_{NO_2}\rangle|n_{O_2},k_{O_2}\rangle$$

Conveniently, we can express these basis functions in terms of Wigner D-matrices using equations 3.59 and 3.60. The integration then to calculate the potential matrix elements can be done using equation 3.63. Therefore the potential matrix elements are:

$$
\begin{aligned}
&\langle n'_{NO_2},\mu',k'_{NO_2}|\langle n'_{O_2},k'_{O_2}|\sum_j C^j\Big(\mathscr{D}^{l_{O_2}}_{-m,0}(\phi_2,\theta_2,0)\mathscr{D}^{l_{NO_2}}_{m,\lambda}(\omega_2)\\
&+\mathscr{D}^{l_{O_2}}_{m,0}(\omega_2)\mathscr{D}^{l_{NO_2}}_{-m,-\lambda}(\phi_1,\theta_1,\chi)\Big)_j|n_{NO_2},\mu,k_{NO_2}\rangle|n_{O_2},k_{O_2}\rangle =\\
&=\sum_j C^j\frac{\sqrt{(2n'_{NO_2}+1)(2n_{NO_2}+1)(2n'_{O_2}+1)(2n_{O_2}+1)}}{(8\pi^2)^2}(-1)^{K-\mu}\\
&\times\Bigg(\int\mathscr{D}^{n'_{NO_2}}_{k'_{NO_2},\mu'}(\omega_1)\mathscr{D}^{l_{NO_2}}_{m,\lambda}(\omega_1)\mathscr{D}^{n_{NO_2}}_{-k_{NO_2},-\mu}(\omega_1)d\Omega\int\mathscr{D}^{n'_{O_2}}_{k'_{O_2},0}(\omega_2)\mathscr{D}^{l_{O_2}}_{-m,0}(\omega_2)\mathscr{D}^{n_{O_2}}_{-k_{O_2},0}(\omega_2)d\Omega\\
&+\int\mathscr{D}^{n'_{NO_2}}_{k'_{NO_2},\mu'}(\omega_1)\mathscr{D}^{l_{NO_2}}_{-m,-\lambda}(\omega_1)\mathscr{D}^{n_{NO_2}}_{-k_{NO_2},-\mu}(\omega_1)d\Omega\int\mathscr{D}^{n'_{O_2}}_{k'_{O_2},0}(\omega_2)\mathscr{D}^{l_{O_2}}_{m,0}(\omega_2)\mathscr{D}^{n_{O_2}}_{-k_{O_2},0}(\omega_2)d\Omega\Bigg)\\
&=\sum_j C^j\sqrt{(2n'_{NO_2}+1)(2n_{NO_2}+1)(2n'_{O_2}+1)(2n_{O_2}+1)}(-1)^{K-\mu}\\
&\times\Bigg(\begin{pmatrix}n'_{NO_2}&l_{NO_2}&n_{NO_2}\\-k'_{NO_2}&m&k_{NO_2}\end{pmatrix}\begin{pmatrix}n'_{NO_2}&l_{NO_2}&n_{NO_2}\\-\mu'&\lambda&\mu\end{pmatrix}\begin{pmatrix}n'_{O_2}&l_{O_2}&n_{O_2}\\-k'_{O_2}&-m&k_{O_2}\end{pmatrix}\\
&\times\begin{pmatrix}n'_{O_2}&l_{O_2}&n_{O_2}\\0&0&0\end{pmatrix}+\begin{pmatrix}n'_{NO_2}&l_{NO_2}&n_{NO_2}\\-k'_{NO_2}&-m&k_{NO_2}\end{pmatrix}\begin{pmatrix}n'_{NO_2}&l_{NO_2}&n_{NO_2}\\-\mu'&-\lambda&\mu\end{pmatrix}\\
&\times\begin{pmatrix}n'_{O_2}&l_{O_2}&n_{O_2}\\-k'_{O_2}&m&k_{O_2}\end{pmatrix}\begin{pmatrix}n'_{O_2}&l_{O_2}&n_{O_2}\\0&0&0\end{pmatrix}\Bigg)
\end{aligned}
\tag{11.35}
$$

where (ω_1) and (ω_2) are the Euler angles for NO_2 and O_2 respectively with respect to the axis system of the complex, and the integration is over all angles. In the above formula we used the fact that:

$$k_{NO_2}+k_{O_2}=K \tag{11.36}$$

To evaluate the 3-j symbols, we used the programs provided by Zare [27].

11.5.5 The angular dynamics program

To solve the angular Schrödinger equation for the complex, another FORTRAN90 double precision program was written. This computed the Hamiltonian matrix using the expressions given in the previous sections. The calculations were performed for one N at the time, as N is a good quantum number for the Hamiltonian given in equation 11.28.

At launching the program, the user chooses the rotational angular momentum of the complex (N), and of the monomers (n_{NO_2} and n_{O_2}). Moreover, the user may select to limit the maximum K and $(n_{NO_2} + n_{O_2})$ values in order to truncate the size of the basis set. Then the user is asked to provide the choices used in the fitting program. The results of the fitting can be used directly from the dynamics program if the two are placed in the same folder. Also, the intermolecular distance R has to be specified, which is used to compute the pseudo-diatomic rotational constant.

The program then performs the calculation taking into account all possible basis sets within the specifications given. The diagonalisation subroutines were taken from LAPACK and BLAS and the eigenvalues are printed in energy order in the output file "levels.csv", and the eigenstates are printed in the same order in the file "states.csv". The FORTRAN codes for the fitting and the angular dynamics programs may be found in the CD attached to this thesis.

11.5.6 Angular dynamics results and discussion

Using the programs described, we were able to fit and perform the dynamics on the RSPT2 and RCCSD(T) PESs, as well as at the combined PES taken as:

$$E_{RCCSD(T)+\Delta RSPT2} = E_{RCCSD(T)} - \left(E_{RSPT2,Quartet} - E_{RSPT2,Doublet}\right) \tag{11.37}$$

Following the notation used in chapter 10 when discussing the Ne-NO_2 complex, the quantum number K is equal to $k_{NO_2} + k_{O_2}$, while K_r corresponds to the state of the molecular complex that would be assigned from a semi-rigid approach. Thus, the state $(N = 1, K_r = 0)$ would be primarily composed from $(N = 1, K = 0)$, but will have a small degree of $(N = 1, K = \pm 1)$

Table 11.7: The lowest energy level calculated by performing the angular dynamics on different PESs and intermolecular distances

PES	Distance/Å	RMSD/ cm^{-1}	Complex Ground State Energy/ cm^{-1}
RCCSD(T)	3.2	0.94	107.4558
RCCSD(T)	3.3	0.81	88.43918
RSPT2- Quartet	3.2	2.06	103.7697
RSPT2- Quartet	3.3	2.01	96.7180
RSPT2- Doublet	3.2	2.70	118.9498
RSPT2- Doublet	3.3	2.48	107.0748
RCCSD(T)+Δ RSPT2	3.2	2.70	118.9497
RCCSD(T)+Δ RSPT2	3.3	1.56	95.9222

states mixed in due to the Coriolis interaction. $K_r = 1^{\pm}, 2^{\pm}$ will be used to signify the upper and lower $K_r = |1|$ and $K_r = |2|$ doublets if the energy levels and the spectrum were assigned as an asymmetric top.

In table 11.7, the results of the dynamics and the fitting are given for the region of the minimum, $R = 3.2 - 3.3$ Å. As the potential was shifted with respect to its minimum, the eigenvalues for the complex ground state ($N = 0, K_r = 0$) also correspond to the zero-point energy (ZPE). For these calculations, the fitting was performed with $(l_{O_2} + l_{NO_2}) = 16$ and potential was scaled to even out for values above 500 cm^{-1} from the minimum. The RMSD in the table 11.7 refers to the fitting. For the dynamics, $(n_{O_2} + n_{NO_2}) = 16$ was used, which was the largest possible calculation if one wants to include all N and K values up to 3 in our machine[7]. This resulted in 2,912 basis functions being used for the dynamics for the ground state ($N = K_r = 0$), 8,704 for the first excited state ($N = 1$), 14,384 for the second excited state ($N = 2$) and 19,874 for the third ($N = 3$) excited state calculation of the complex. As may be seen from table 11.7, the combined PES (RCCSD(T)+Δ RSPT2) is fitted equally well, if not better, to the RSPT2 PES of the doublet state, while the RCCSD(T) one is clearly providing the best fit. The ZPE is similar from all surfaces, but it can be seen that it changes rapidly with distance.

If we assume that each angle (θ_1, θ_2, ϕ and χ) is a possible degree of freedom for vibrations, this would mean that on average each one has approximately a ZPE of 22-30 cm^{-1}. As the

[7]The computer used has 8 GB of RAM plus another 4GB of swap memory.

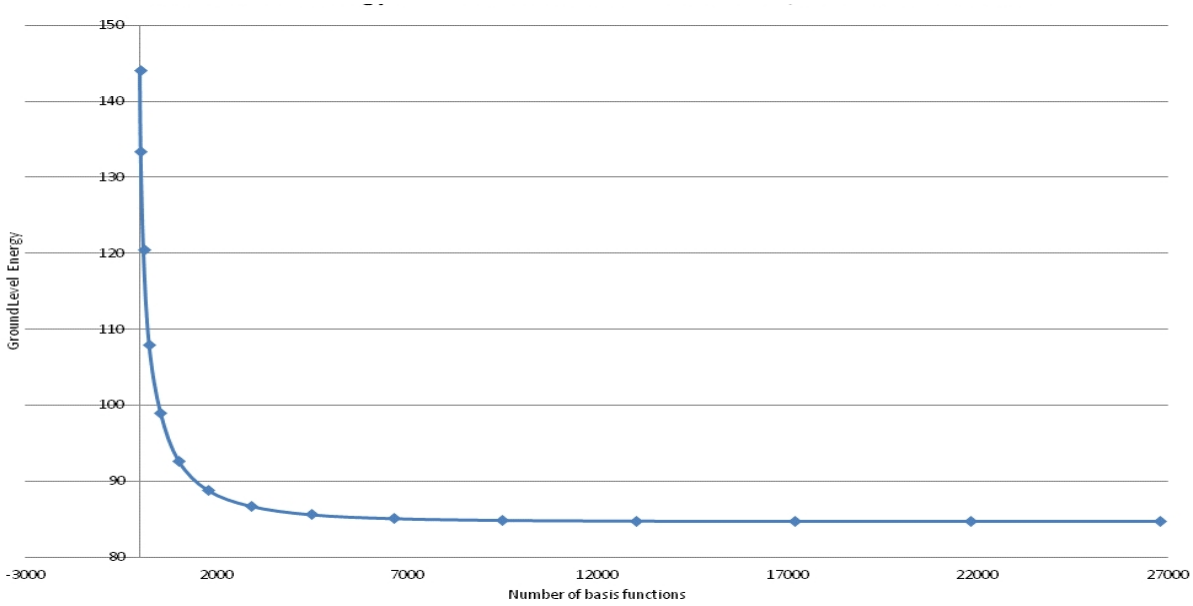

Figure 11.8: Convergence of the $N = 0, K_r = 0$ ground state energy for $R = 3.3$ Å

minimum of the combined surface has $R = 3.3$ Å, this distance was used for further analysis. The energy of the ground state of the complex versus the number of basis functions used in the calculation is shown in figure 11.8. As may be seen from figure 11.8, a very large number of functions (more than 9,500) are required for the convergence of the ground state energy to below 1 cm^{-1}. To our view this is related to the way that the potential is modelled and to the high RMSD values of the fit: rotation of the monomers (in a given R) may change significantly the distance between the atoms. For example, if the two monomers are arranged in parallel with the N atom perpendicular to the oxygen plane, then the separation between the oxygen molecules is approximately the intermolecular distance. If on the other hand the four oxygen atoms are arranged in a line, then the distance of the two inner oxygen atoms is approximately 1.8 Å shorter. This effect leads to a large range of binding energies for each R, which in turn creates an anisotropic potential that requires highly oscillating functions in order to be fitted. Then, for the effect of these functions to be included in the potential, a large basis set is required.

We can now look at the predicted energy levels, using the RCCSD(T)+Δ RSPT2 PES. Again we set $(n_{O_2} + n_{NO_2})$=16. This was the largest possible calculation when including all N, K values up to 3, which is necessary in order to have $|K_r| = 2$ transitions. For all calculations, all possible K values were included. As can be seen from figure 11.8, the calculated energy levels are not

Table 11.8: The NO_2-O_2 rotational transitions for $R = 3.3$ Å from fixed-distance dynamics

	$N = 1 \leftarrow 0$	$N = 2 \leftarrow 1$	$N = 3 \leftarrow 2$
$K_r = 0$	4,524.9837	9,047.6121	13,565.5437
$K_r = 1^-$		8,833.7490	13,249.6401
$K_r = 1^+$		9,274.1605	13,909.9117
$K_r = 2^-$			13,601.8267
$K_r = 2^+$			13,611.7712

expected to be more converged than a couple of cm^{-1}, but the transitions between them should fare better. The calculated transitions are given in table 11.8, all numbers are quoted in MHz.

The first thing to note is that both the $|K_r| = 1$ and $|K_r| = 2$ are predicted to be in range, so both sets should be seen experimentally. However, these splittings between the $|K_r| = 1$ and $|K_r| = 2$ levels show a deviation from what would be expected if the molecular complex was treated as an asymmetric top. What is happening is that the NO_2 rotation around its a-axis is taking place and the pattern is similar to the Rg-NO_2 spectra. Yet, two effects have significantly lowered the tunnelling frequency: the stronger interaction with O_2, and also the fact that an O_2 rotation (which itself is quenched by the presence of the NO_2) is required to complete the symmetry operation. Thus, the tunnelling frequency has been sufficiently lowered, that the $|K_r| = 1$ transitions are now in range. By taking the average difference between the $K_r = 0$ from the $|K_r| = 1$ and $|K_r| = 2$ states, we were able to calculate the tunnelling frequency to be 8,719.31 MHz. This is significantly lower than the value obtained for Ne-NO_2. Moreover, this shows that the possible tunnelling between the oxygen molecule's atoms is not correlated to the tunnelling of NO_2, otherwise the $|K_r| = 1$ states would be lower in energy than the $K_r = 0$ states, which is not observed. One reasonable explanation for this, is that the oxygen molecule plus the nitrogen nucleus has a much higher mass to tunnel, compared to the nitrogen nucleus alone.

Finally, we were able to fit these values in a semi-rigid approach using the program SPFIT [22, 23]. The values fitted correspond to virtual transitions from the ground state to all levels, thus containing 13 virtual lines. The results are given in table 11.9, and the RMSD of the fit is 0.041 MHz, which is far better than the expected precision of the numbers (all values

Table 11.9: Semi-rigid Parameters for NO_2-O_2

$A - \frac{B+C}{2}$/MHz	14,640.646(56)
$\frac{B+C}{2}$/MHz	2,262.472(24)
$\frac{B-C}{4}$ /MHz	55.044(5)
D_N/kHz	-5.80(218)
D_{NK} /MHz	-1.098(6)

were given an uncertainty of 0.1 MHz). This means that this complex, in contrast to Ne-NO_2 described in chapter 10, may be fitted using a semi-rigid approach. This is reasonable given the stronger interaction between the monomers. However, like Ne-NO_2, both of the included centrifugal distortion constants are abnormally large, especially if one realises that since this is a fixed-R calculation, there is no real centrifugal distortion! What is happening is that D_N and, mainly, D_{NK} have suitable dependencies to accommodate the dynamical effects of the angular Coriolis forces. An abnormally large value of D_{NK} is again found to be an indicator of significant dynamical effects, as also concluded in chapter 10.

Unfortunately, due to the very large size of basis set required to converge the energy levels, it was not possible to include any vibrational levels as well. Moreover, another problem of the PESs prevented us from treating the radial motion adiabatically: due to the RSPT2 predicting a far greater interaction than RCCSD(T), the difference between the two spin states PESs in RSPT2 was sometimes incompatibly large in relation to the RCCSD(T) binding energies. As was predicted in chapter 8, the difference between the two spin states increases at closer distances, so this created an unphysical PES for RCCSD(T)+Δ RSPT2 at close range. For these reasons, having obtained both an estimate of where the transitions should be and what the expected pattern is, we continued the investigation of the NO_2-O_2 complex experimentally.

11.6 Experimental Investigation

Prolonged experimental searches were performed over the course of this investigation in various frequency regions from 7 to 18 GHz, using initially a mixture of NO and O_2 gas and Ar as

a carrier gas, then Ne as a carrier gas and finally a mixture of NO_2 and O_2 gases in a Ne supersonic expansion with 1 bar backing pressure. Although the lines that Frise recorded were not reproduced, experiments using the latter mixture yielded a total of more than 170 weak transitions (most of them required between 5000 and 7500 shots) of the appropriate Doppler splitting that appeared to be part of a rich hyperfine structure.

These appeared to correspond to the spectrum of a species with rotational constants approximately in the right values for NO_2-O_2, as well as the right pattern. However, upon a closer examination of the fine and hyperfine structure observed, it is now believed that these correspond to another species, possibly an NO_2 or NO polymer. All recorded lines are given in the CD attached to this thesis.

11.7 Conclusion and Suggestions for Future Work

A large amount of theoretical work was performed in our investigation of the NO_2-O_2 van der Waals complex. The PESs of the complex were computed using both RSPT2 and RCCSD(T) methods in order to combine the strengths of these methods and achieve a large cancellation of errors. The RSPT2 PESs were computed for the low-energy geometries using both aug-cc-pVDZ and aug-cc-pVTZ basis sets which allowed extrapolation to the CBS limit. All the PESs are given in the CD attached to this thesis. From these we obtained the approximated minimum energy geometry of the complex. The PESs were in agreement to the arguments presented in chapter 8 with respect to the energy ordering of the spin states and a pseudo-covalent contribution to the potential energy was again found.

A program was written to fit an appropriate angular function to single-distance cuts of the PESs. This program offers the user a lot of flexibility to how this function is constructed and the options of performing a linear, scaled and weighted least squares fitting. A second program was written to perform the angular quantum dynamics for the complex. From this we obtained estimates of the zero point energies of the angular motion of the monomers. Moreover, we were able to settle the question of the effect of the nuclear spin statistics in this complex, predict

the pattern of the spectrum and also provide a first estimate of the tunnelling frequency for the rotation of NO_2 around its *a*-axis. The calculated fixed-*R* dynamics transition frequencies were also successfully fitted using a semi-rigid approach, indicating that this approach is suitable for this complex. In agreement to the conclusions of chapter 10, it was found that the centrifugal distortion constants may be used as fitting parameters to accommodate the effects of dynamics in the spectrum.

However, even after extensive search and although a large number of weak transitions were recorded, it was not possible to find sets of transitions that could be unambiguously assigned to this complex. This is not too surprising as its binding energy is small and the oxygen molecule is very weakly polarisable. Therefore only a small amount of the complex would be formed and any transitions would be very weak.

Yet, last year we were happy to learn that the spectrum of this complex has been recorded by the Lehmann group at the University of Virginia, using helium droplet spectroscopy. According to the results presented in the 67^{th} Ohio State University International Symposium on Molecular Spectroscopy [148], these researchers observed both odd and even *K* transitions, which is in agreement with our analysis.

Chapter 12

Conclusion

"*The actual process of arriving at one correct solution required some five years time, and proceeded by a series of halting steps which may now be described with deceptive economy*"

- G. Bird *et al.* [123]

Although four different systems have been investigated in total in this work, they all fell under the basic question introduced in chapter 1: how can one model the interactions in an open-shell open-shell van der Waals complex? There are two questions that arise from this first one: how can one model a van der Waals complex and how can one model the radical-radical interactions in such a complex? The first of these questions is challenging due to the degree of large amplitude motion that the constituent molecules demonstrate. Two main approaches have been used to-date: the semi-rigid approach and the quantum dynamics approach. The semi-rigid approach approximates the van der Waals complex as a semi-rigid top molecule with internal rotation, and then one can fit the constants of an effective Hamiltonian to reproduce the spectrum. This approach has been used extensively by spectroscopists as the constants fitted have a direct relation to the spectrum's appearance. In this approach the motion of the "frame" is separated from that of the "internal rotor", although the two are linked by Coriolis interactions.

In chapter 6 we used the theory of internal rotation in semi-rigid molecules to analyse the rotational spectrum of t-butyl acetate (TBAc). A large number of lines were recorded experimentally using high resolution pulsed-nozzle Fourier-transformed microwave spectroscopy (FTMS). One limitation of the semi-rigid approach that was already apparent was that it cannot intrinsically account for the symmetry properties of the internal rotor. In the well-established case of a methyl group rotation, this was done in a practical way by including the A and E states as non-mixing vibrational levels. Although this is correct, the reason for not having any transitions between them was implemented by setting the corresponding dipole moments as zero, i.e. in an *ad hoc* manner. Moreover, in order to determine more information about the system, such as the barrier to rotation and the expectation value of the torsional angle, we had to perform what practically were dynamical calculations using second order perturbation theory on an approximate V_3 potential. This demonstrates the fact that even for a strongly-bound molecule whose rotational spectrum may be fitted well by a semi-rigid effective Hamiltonian, if one wants to understand the details of the internal rotation it is necessary to investigate the dynamical effects and the mixing of excited internal rotor states, even if using a semi-empirical expression for the potential.

Yet, TBAc is a strongly-bound molecule rather than a weakly-bound molecular complex, so the other end of this continuum was explored in chapter 10, when investigating the van der Waals complex between an atom of neon and a molecule of nitrogen dioxide (Ne-NO_2). The very weak binding energy of this complex (≈ 79 cm^{-1}) indicated that the quenching of the rotation of NO_2 was going to be very weak. Indeed, the dynamical effects were so strong, that the original researcher (Dyer [116]) could not even fit the rotational transitions using a semi-rigid Hamiltonian. This was also in contrast to the rest of the Rg-NO_2 complexes investigated by the group, all of which were successfully (although not easily) fitted using a semi-rigid approach. We performed high level *ab initio* calculations to obtain the PES of the complex and fitted this PES to an appropriate function that could be used in a dynamics Hamiltonian. Fitting the PES was itself challenging, and it became evident that only an atom-atom potential that was able to represent the anisotropy of the interaction around each atomic centre accurately. This is both because of the small size of neon, which enabled it to sample the space around the NO_2 in

detail, as well as due to the different motions of NO_2: the large angle of the O-N-O bond meant that any motion around the *b*-axis caused great shifts in energy, while the motion around the *a*-axis was almost a free-rotation. Using our atom-atom potential we represented the PES in a physically meaningful way (i.e. based on the theory explained in chapter 7), and the coefficients of the function themselves reflected this (i.e. were part of convergent series).

To perform the dynamics at various levels of approximation (with or without Coriolis, including or neglecting the radial motion) different programs were written using MATHEMATICA8. The results obtained from these programs were not only able to reproduce from first principles the effects of the nuclear spin statistics that have been observed now in all the Rg-NO_2 complexes, but also predict the shape of the spectrum including the uneven splitting between between the $K_r = 0$ and $|K_r| = 2$ transitions that cannot easily be explained using semi-rigid theory. It was found, however, that a very large number of functions were required for convergence and the basis set used for these dynamical calculations had to be truncated, even in such a small and weakly-bound system. The results of our quantum dynamics calculations were then fitted to a semi-rigid Hamiltonian to test the compatibility between the two approaches. Interestingly, the fitting was not as good as one would perhaps expect, with an RMSD of approximately 0.44 MHz. One insight was that, in order to fit the predicted transitions, the D_{NK} value was very large (4.3 MHz), and not in line with the value of D_N (0.14 MHz), which itself was normal. Re-examining the other Rg-NO_2 complexes previously analysed by the group, we found that indeed the value of D_{NK} is often abnormally large (especially in the Ar-NO_2 complex [113]) and correlates well with the importance of dynamics in van der Waals complexes, and thus may be used as an indicator. Therefore, one may use the semi-rigid approach to investigate such complexes, but should be wary of the centrifugal distortion constants and their abnormally large values. Moreover, we determined the tunnelling frequency, zero point energy and minimum geometry of the complex from the dynamical calculations.

Studying the Ne-NO_2 complex, we had already started crossing the boundary to the second question: that of radical nature in the context of van der Waals complexes. As NO_2 has an unpaired electron, as well as a nuclear spin angular momentum, the spectrum of the Ne-NO_2

complex has a complicated fine and hyperfine structure. We analysed this via spherical tensor operator algebra, which elegantly enabled us to use the eigenvectors of the dynamics calculations and the experimentally determined fine and hyperfine constants of the NO_2 molecule to calculate the expectation values of the fine and hyperfine operators for each state of the molecular complex. To achieve this, another program was written in MATHEMATICA8 which operated in two stages. At the first stage, the program transformed the NO_2 constants to the complex frame. At the second stage, it uses these values to predict the fine and hyperfine energy level splittings by composing and diagonalising the respective Hamiltonian matrix. Additionally, we derived the very useful expression shown in equation 10.47, which may find more applications in future research that uses spherical tensor algebra.

One insight gained by this analysis was the significance of both the different vibrational states (the radial motion) and of the Coriolis forces. Both contributed to the effective fine and hyperfine constants of the complex, and it was not until these were included that we could fit the calculated fine and hyperfine energy levels using a semi-rigid approach. Yet, once this was done, the two approaches proved compatible, and the predicted fine and hyperfine structure could be fitted to an effective Hamiltonian with an RMSD of only 0.185 MHz. The reason for this is probably that the origins of the interaction (i.e. the fields created by the motions of electrons, either due to their spin or rotation with the molecular complex and the electron distribution around the nitrogen nucleus) are only very slightly (if at all) perturbed by the presence of Ne, and therefore, one must mainly account for the relative orientation of the NO_2 moiety in the molecular complex. This may be done analytically through dynamics or approximately in a semi-rigid perspective. This is an encouraging result, as that part of the calculation was highly demanding in terms of computing requirements, and it is positive that one may still successfully use the semi-rigid approach even in such a floppy complex.

However, there are elements of the analysis that are not accessible through the semi-rigid approach: because by performing the quantum dynamics one obtains all the eigenvalues and eigenvectors of the fine and hyperfine Hamiltonian, the extra information enabled us to calculate all the corresponding constants. This proved significant especially for the spin rotation

around the a-axis (ε_{aa}), which is the dominant contribution for the $K_r = 2^{\pm}$ levels (through second order perturbation theory effects) but which may not be fitted directly from the spectrum. Furthermore, we were able to highlight the Coriolis interaction as the main reason for the spin-rotation splittings. At the same time, a large amount of experimental work was performed which both reproduced the previously recorded spectrum and also found two new transitions.

Using the dynamically predicted spectrum, the new transitions and Dyer's assignment of the $K_r = 0$ spectrum, we were able to finally assign the $K_r = |2|$ transitions of Ne-NO_2. Although the fitted values from the dynamically predicted spectrum did not agree well with the experimental values for the hyperfine structure and ε_{aa} constants, our calculations were able give very good agreement for the decisive $\varepsilon_{bb} \pm \varepsilon_{cc}$, and thus predict the energy ordering of all but three transitions.

Next, we examined the nature of an open-shell open-shell interaction in van der Waals complexes. Intriguingly, there has been no unified view on the ordering of the energy levels when two radicals meet but do not form a bond. For this fundamental chemistry question, there are two possible approaches: The Heitler-London theory (which is part of the Valence Bond theory, VB) which would predict the lowest multiplicity state to be the lowest in energy and actually form a covalent bond. A competing view comes from Hund's first rule of maximum multiplicity (which uses Molecular Orbital theory) and would predict the highest multiplicity state to have the lowest energy. Both of these theories have been stretched outside their original domain by being applied to van der Waals complexes (with the monomers having core electrons) and there has been published work in support of both perspectives [100, 105]. Yet, to the best of our knowledge these studies did not set out to investigate this question, but rather assumed an energy ordering.

To answer this question, we studied the weakly bound complex of NO with O_2, both of which are radical species, relatively stable in room temperature. This system is also interesting as there is the added question of different symmetry states (on top of different spin states) as well as the possibility of forming NO_3. Ironically, forming such a molecule is what chemical intuition would predict! As our hypothesis agreed with the Heitler-London (VB) prediction, we

used supermolecular MO theory in our calculations, as an agreement would signal an answer from both perspectives. We investigated this complex using multireference second order perturbation theory *ab initio* methods. We discovered that indeed the Heitler-London theory does predict the correct energy order, due to a "pseudo-covalent" exchange contribution to the potential energy, which seems to align the molecules to maximise the overlap between molecular orbitals. Hund's first rule seems to correctly predict the energy ordering if the electrons are all part of the same molecule, but in our case they belong to separate molecules and the dominant effect is the exchange interaction rather the consequence of the Fermi hole. Indeed, the Fermi hole argument strictly speaking is valid only if the electrons could potentially have all quantum numbers the same, which is not the case for electrons on different molecules.

Moreover, we were able to model this pseudo-covalent contribution by a Born-Mayer-type term to a good approximation. Also, through our survey of *ab initio* methods we highlighted the strengths and shortcomings of each one, and compared their results to the "golden standard" RCCSD(T) method when appropriate. One surprising insight was the possible contribution of charge transfer, which previous research suggested to be negligible [7, 107] and a wrongly-overestimated induction effect. Yet, using the same previous theory, it was argued that in the case of open-shell open-shell species, there might be an exception to that rule. This was also consistent with the *ab initio* predicted dipole moments.

Finally, all the previous arguments were combined to study one open-shell open-shell van der Waals complex, NO_2-O_2. Like in the case of Ne-NO_2 and NO-O_2, high level *ab initio* calculations were used to obtain the PES of this complex. Similarly to the NO-O_2 complex, the Heitler-London theory correctly predicted the energy ordering of the two spin states, and we demonstrated that again we found a pseudo-covalent contribution to the potential energy. For NO_2-O_2, a combination of *ab initio* methods (RCCSD(T) and RSPT2) was deemed more reliable than a single method for the PES of both possible spin states, mainly due to the intruder state problems of RSPT2. Although we were not able to perform the radial dynamics, we performed the angular dynamics on a composite PES. As the angular part of the potential is the dominant contribution to the shape of the rotational spectrum (as we demonstrated on the

Ne-NO_2 complex) we were able to qualitatively predict the "shape" of the rotational spectrum of the NO_2-O_2 complex and thus settle the question of the effect of the nuclear spin statistics. We determined that the tunnelling motion of NO_2 around its *a*-axis continues but as an accompanying rotation of the O_2 is required to complete the symmetry operation and the bonding between the monomers is stronger, the tunnelling frequency becomes low enough that both the even and the odd K_r transitions fall within our experimental range. At the same time we predicted that the tunnelling motion of O_2 is uncorrelated from the NO_2 tunnelling, and determined (approximately) the tunnelling frequency for NO_2.

While a large number of weak transitions were recorded experimentally in the appropriate spectral region using FTMS, upon closer investigation it became clear that these belonged to another system with a more complex fine and hyperfine pattern. However, we were delighted to hear that another experimental group in the University of Virginia have now recorded the spectrum of NO_2-O_2 in helium clusters, and its appearance is in agreement with our predictions [148]. However, they have not yet released any numerical results that would allow further comparison. Finally, we were able to fit the predicted transitions using a semi-rigid approach in a practically perfect fit, with a RMSD of 0.04 MHz. This demonstrates that in the case of NO_2-O_2, which is more strongly bonded than Ne-NO_2, the semi-rigid theory may be used to analyse the spectrum, although the effects of nuclear spin statistics would have to be included *ad hoc*. Moreover, the value of D_{NK} was, in agreement to our analysis of Ne-NO_2, abnormally large (1.1 MHz) and not in line to the D_N value, again suggesting that this may be used as an indicator of dynamical effects. All the programs mentioned in this work, PESs and recorded FTMS spectra are included in the CD attached to this thesis.

Bibliography

[1] P. W. Atkins & J. De Paula. "Atkins Physical Chemistry". Oxford University Press (2002).

[2] T. G. Starkey. D. Phil., University of Oxford (2007).

[3] I.G. Kaplan. "Intermolecular Interactions". John Wiley and Sons (2006).

[4] Wikipedia.org, Argon dimer potential.png, accessed on 5 Sept 2013.

[5] G. J. B. Hurst, P. W. Fowler, A. J. Stone & A. D. Buckingham. *Intern. J. Q. Chem.*, **XXIX**, 1223-1239 (1986).

[6] P. E. S. Wormer & A. van der Avoird. *Chem. Rev.*, **100**, 4109-4143 (2000).

[7] A. J. Stone. "The Theory of Intermolecular Forces". Oxford University Press (2002).

[8] I. M. Scishchev & R. J. Boyd. *J. Phys. Chem. A*, **102**, 7294-7296 (1998).

[9] K. M. T. Yamada & G. Winnewisser. "Interstellar Molecules". Springer-Verlag Berlin Heidelberg (2011).

[10] R. V. Mikhaylov, A. A. Lisachenko, B. N. Shelimov, V. B. Kazansky, G. Martra & S. Coluccia. *J. Chem. Phys. C*, **117**, 10345-10352 (2013).

[11] S. Tolansky. "Microwave Spectroscopy". Methuen and Co. (1948).

[12] M. C. Heaven. *Annu. Rev. Phys. Chem.*, **43**, 283-310 (1992).

[13] L. N. lamsal, R. V. Martin, D. D. Parrish & N. A. Krotkov. *Environ. Sci. Technol.*, **47**, 7855-7861 (2013).

[14] D. D. Thomas, L. A. Ridnourb, J. S. Isenbergc, W. Flores-Santanab, C. H. Switzerb, S. Donzellib, P. Hussaind, C. Vecolie, N. Paoloccie, S. Ambsd, C. A. Coltonf, C. C. Harrisd, D. D. Robertsc & D. A. Wink. *Free Radic. Biol. Med.*, **45**, 1, 18-31 (2008).

[15] A. Carrington. "Microwave Spectroscopy of Free Radicals". Academic Press (1974).

[16] H. W. Kroto. "Molecular Rotation Spectra". Dover Publication (1992).

[17] J. Brown & A. Carrington. "Rotational Spectroscopy of Diatomic Molecules". Cambridge University Press (2003).

[18] David S. Perry Research Group website. http://gozips.uakron.edu/ dperry/.

[19] D. Kivelson, J. Wilson & E. Bright. *J. Chem. Phys.*, **260**, 4, (1936).

[20] W. Gordy & R. L. Cook. "Microwave Molecular Spectra". John Wiley and Sons (1984).

[21] J. K. G. Watson. *Molec. Phys.*, **5**, 15, 479-490 (1968).

[22] H. M. Pickett. *J. Mol. Spectr.*, **148**, 371 (1991).

[23] http://www.ifpan.edu.pl/ kisiel/asym/pickett/crib.htm, accessed on 10 Aug 2013.

[24] B. Ouyang. D. Phil., University of Oxford (2008).

[25] D. G. Lister, J. N. Macdonald & N. L. Owen. "Internal Rotation and Inversion". Academic Press (1978).

[26] D. M. Bishop. "Group Theory and Chemistry". Dover Publications (1993).

[27] N. R. Zare. "Angular Momentum". John Wiley and Sons (1988).

[28] J. M. Brown & B. J. Howard. *Molec. Phys.*, **31**, 1517 (1976).

[29] A. R. Edmonds. "Angular Momentum in Quantum Mechanics". Princeton University Press (1985).

[30] M. E. Rose. "Elementary theory of Angular Momentum". John Wiley and Sons (1957).

[31] http://www.weisang.com/index/php?id=143&tx0pshtmlhelppi1 accessed on 23 Sept 2013.

[32] D. A. Varshalovich, A. N. Moskalev & V. K. Khersonskii. "Quantum Theory of Angular Momentum". World Scientific Publishing (1988).

[33] Brian J. Howard. D. Phil., Cambridge University (1970).

[34] F. Jensen. "Introduction to Computational Chemistry". John Wiley and Sons (2007).

[35] H. Hettema. "Quantum Chemistry, Classic Scientific Papers". World Scientific (2001).

[36] P. W. Atkins & R. S. Friedman. "Molecular Quantum Mechanics". Oxford University Press (1975).

[37] Gerrit Groenenboom, private communication, 2013.

[38] C. J. Crammer. "Essentials of Computational Chemistry". John Wiley and Sons (2005).

[39] M. W. Schmidt & M. S. Gordon. *Annu. Rev. Phys. Chem.*, **49**, 233-66 (1998).

[40] H. J. Werner. *Mol. Phys.*, **89**, 2, 645-661 (1996).

[41] C. Camachom, R. Cimiraglia & H. A. Witek. *Phys. Chem. Chem. Phys.*, **12**, 5058-5060 (2012).

[42] J. Soto, F. J. Avila, J. C. Otero & J. F. Arenas. *Phys. Chem. Chem. Phys.*, **13**, 7230-7231 (2011).

[43] P. Celani, H. Stoll, H.-J. Werner & P. J. Knowles. *Mol. Phys.*, **102**, 21, 2369-2379 (2004).

[44] C. Angeli, M. Pastore & R. Cimiraglia. *Theor. Chem. Acc.*, **117**, 743-754 (2007).

[45] C. Angeli, R. Cimiraglia & J.-P. Malrieu. *J. Chem. Phys.*, **117**, 9138 (2002).

[46] C. Angeli, R. Cimiraglia, S. Evangelisti, T. Leininger & J.-P. Malrieu. *J. Chem. Phys.*, **114**, 10252 (2001).

[47] F. G. Kalatzis & I. N. Demetropoulos. *Mol. Phys.*, **105**, 17-18, 2334-2343 (2007).

[48] P. E. S. Wormer, J. A. Klos, G. C. Groenenboom & A. Van Der Avoird. *J. Chem. Phys.*, **122**, 244325 (2005).

[49] G. C. Groenenboom, A. V. Fischuk & A. van der Avoird. *J. Chem. Phys.*, **131**, 12307 (2009).

[50] G. S. F. Dhont, J. H. van Lenthe, G. C. Groenenboom & A. van der Avoird. *J. Chem. Phys.*, **123**, 184302 (2005).

[51] M. Bartolomei, M. I. Hernandez, J. Campos-Martinez, E. Carmona-Novillo & R. Hernadez-Lamoneda. *Phys. Chem. Chem. Phys.*, **10**, 5374-5380 (2008).

[52] M. Bartolomei, E. Carmona-Novillo, M. I. Hernadez, J. Campos-Hernadez & R. Hernadez-Lamoneda. *J. Chem. Phys.*, **133**, 124311 (2010).

[53] H.-J. Werner. *Molec. Phys.*, **89**, 2, 645-661 (1996).

[54] J. Stanton and P. Jensen, private communication.

[55] P. Jensen & P. R. Bunker. "Computational Molecular Spectroscopy". John Wiley and Sons (2000).

[56] S. F. Boys & F. Bernardi. *Mol. Phys.*, **19**, 553 (1970).

[57] A. J. Stone & A. J. Misquita. *Intern. Rev. Phys. Chem.*, **26**, 1, 193-222 (2007).

[58] G. D. Truhlar. *Chem. Phys. Lett.*, **194**, 45-48 (1998).

[59] A. Halkier, T. Helgaker, W. Klopper, P. Jorgensen & A. G. Csaszacutear. *Chem. Phys. Lett.*, **310**, 385-389 (1999).

[60] K. Back. Part II Thesis, University of Oxford (2003).

[61] T. J. Balle & W. H. Flygare. *Rev. Scient. Instr.*, **52**, (1), 33-45 (1981).

[62] B. J. Watson. D. Phil., University of Oxford (2004).

[63] B. J. Howard. "The Structure and Dynamics of van der Waals Molecules". Iberdrola Lectures, Consejo Superior de Investigationes Cientificas (CSIC) (2001).

[64] M. J. Hollas. "Modern Spectroscopy". John Wiley and Sons (1992).

[65] J. W. Cooley & J. W. Tukey. *Math. Comput.*, **19**, 297, (1965).

[66] M. J. Frisch, G. W. Trucks, H. B. Schlegel, G. E. Scuseria, M. A. Robb, J. R. Cheeseman, J. A. Montgomery, Jr., T. Vreven, K. N. Kudin, J. C. Burant, J. M. Millam, S. S. Iyengar, J. Tomasi, V. Barone, B. Mennucci, M. Cossi, G. Scalmani, N. Rega, G. A. Petersson, H. Nakatsuji, M. Hada, M. Ehara, K. Toyota, R. Fukuda, J. Hasegawa, M. Ishida, T. Nakajima, Y. Honda, O. Kitao, H. Nakai, M. Klene, X. Li, J. E. Knox, H. P. Hratchian, J. B. Cross, V. Bakken, C. Adamo, J. Jaramillo, R. Gomperts, R. E. Stratmann, O. Yazyev, A. J. Austin, R. Cammi, C. Pomelli, J. W. Ochterski, P. Y. Ayala, K. Morokuma, G. A. Voth, P. Salvador, J. J. Dannenberg, V. G. Zakrzewski, S. Dapprich, A. D. Daniels, M. C. Strain, O. Farkas, D. K. Malick, A. D. Rabuck, K. Raghavachari, J. B. Foresman, J. V. Ortiz, Q. Cui, A. G. Baboul, S. Clifford, J. Cioslowski, B. B. Stefanov, G. Liu, A. Liashenko, P. Piskorz, I. Komaromi, R. L. Martin, D. J. Fox, T. Keith, M. A. Al-Laham, C. Y. Peng, A. Nanayakkara, M. Challacombe, P. M. W. Gill, B. Johnson, W. Chen, M. W. Wong, C. Gonzalez & J. A. Pople. "Gaussian 03, Revision C.02". Gaussian, Inc., Wallingford, CT, 2004.

[67] H. Mouhib, Yueyue Zhao & W. Stahl. *J. Mol. Spectrosc.*, **261**, 59-62 (2010).

[68] B. P. Van Eijck, J. Van Opheusden, M. M. M. Van Schaik & E. Van Zoeren. *J. Mol. Spectrosc.*, **86**, 465-479 (1981).

[69] J. Sheridan, W. Bossert & A. Bauder. *J. Mol. Spectrosc.*, **1**, 80 (2009).

[70] D. Jelisavac, D.C. Cortes Gomez, H. V. L. Nguyen, L.W. Sutikdja, W. Stahl & I. Kleiner. *J. Mol. Spectrosc.*, **257**, 111-115 (2009).

[71] H. Mouhib, D. Jelisavac, W. Stahl, R. Wang, I. Kalf & U. Englert. *Chem. Phys. Chem.*, **12**, 761 764 (2011).

[72] A. J. Stone & R. J. A. Touch. *Chem. Phys. Lett.*, **110**, 2 (1984).

[73] S. L. Price, A. J. Stone & M. Adlerton. *Mol. Phys.*, **52**, 4, 987-1001 (1984).

[74] A. Koide & T. Kihara. *Chem. Phys.*, **5**, 34-48 (1974).

[75] V. Magnasco & G. Figari. *Mol. Phys.*, **67**, 6, 1261-1272 (1989).

[76] A. D. Buckingham, P. W. Fowler & J. M. Hutson. *Chem. Rev.*, **88**, 963-988 (1988).

[77] P. Jankowski, A. R. W. McKellar & K. Szalewicz. *Intern. J. Q. Chem.*, **336**, 1147 (2012).

[78] R. J. LeRoy & J. M. Hutson. *J. Chem. Phys.*, **86**, 2 (1987).

[79] J. M. Hutson. *Adv. Mol. Vibr. Coll. Dyn.*, **100**, 17 (1999).

[80] M. H. Karimi-Jafari, A. Maghari & A. Farjamnia. *J. Phys. Chem. A*, **115**, 1143-1151, (2011).

[81] M. Bartolomei, E. Carmona-Novillo, M. I. Hernadez, J. Campos-Martinez & R. Hernadez-Lamoneda. *J. Chem. Phys.*, **133**, 124311 (2010).

[82] M. Meuwly & J. M. Hutson. *J. Chem. Phys.*, **100**, 17 (1999).

[83] F. Lique. *Chem. Phys. Lett.*, **471**, 54-58, (2009).

[84] G. Economides. Part II Thesis, University of Oxford (2007).

[85] J. Makarewicz. *J. Chem. Phys.*, **132**, 234305 (2010).

[86] J. Lei, Y. Zhou & D. Xie. *J. Chem. Phys.*, **136**, 084310 (2012).

[87] R. A. Aziz & M. J. Slaman. *Z. Phys. S*, **25**, 343-344 (1993).

[88] K. T. Tang & J. P. Toennies. *J. Chem. Phys.*, **66**, 4 (1977).

[89] K. T. Tang & J. P. Toennies. *J. Chem. Phys.*, **80**, 3726, (1984).

[90] B. J. Howard. *Molec. Phys.*, **100**, 1, 219 (2002).

[91] K. Patel, P. R. Butler, A. M. Ellis & M. D. Wheeler. *J. Chem. Phys.*, **119**, 2 (2003).

[92] A. H. Brittain, A. P. Cox & R. L. Kuczkowski. *Trans. Faraday Soc.*, **65**, 1963 (1969).

[93] L. Valachovic, C. Riehn, K. Mikhaylichenko & C. Wittig. *Chem. Phys. Lett.*, **258**, 644-650 (1996).

[94] M. Minissale, E. Congiu, S. Baouche, H. Chaabouni, A. Moudens, F. Dulieu, G. Manico & V. Pirronello. *Chem. Phys. Lett.*, **565**, 52-55 (2013).

[95] C. A. Coulson. "Valence, Second Edition". John Wiley and SonsOxford University Press (1961).

[96] I. N. Levine. "Quantum Chemistry". Prentice-Hall (2000).

[97] G. Herzberg. "Molecular Spectra and Molecular Structure, Vol. 1". D. Van Nostrand Company (1963).

[98] H.-J. Werner, P. J. Knowles, G. Knizia, F. R. Manby, M. Schütz, P. Celani, T. Korona, R. Lindh, A. Mitrushenkov, G. Rauhut, K. R. Shamasundar, T. B. Adler, R. D. Amos, A. Bernhardsson, A. Berning, D. L. Cooper, M. J. O. Deegan, A. J. Dobbyn, F. Eckert, E. Goll, C. Hampel, A. Hesselmann, G. Hetzer, T. Hrenar, G. Jansen, C. Köppl, Y. Liu, A. W. Lloyd, R. A. Mata, A. J. May, S. J. McNicholas, W. Meyer, M. E. Mura, A. Nicklass, D. P. O'Neill, P. Palmieri, D. Peng, K. Pflüger, R. Pitzer, M. Reiher, T. Shiozaki, H. Stoll, A. J. Stone, R. Tarroni, T. Thorsteinsson & M. Wang. "MOLPRO, version 2012.1, a package of ab initio programs" (2012). See http://www.molpro.net.

[99] T. Schwabe. *J. Phys. Chem. A*, **117**, 2879-2883 (2013).

[100] T. G. Wright & E. P. F. Lee. *Chem. Phys. Lett.*, **347**, 429-435 (2001).

[101] T. G. Wright & E. P. F. Lee. *Chem. Phys. Lett.*, **318**, 196-202 (2000).

[102] http://www.molpro.net/pipermail/molpro-user/2004-December/001131.html, accessed on 23 Sept 2013.

[103] E. Carmona-Novillo, M. Bartolomei, M.I. Hernandez, H. Campos-Martinez & R. Hernandez-Lamoneda. *J. Chem. Phys.*, **137**, 114304 (2012).

[104] M. C. Van Hermert, P. E. S. Wormer & A. van der Avoird. *Chem. Phys. Lett.*, **51**, 13, 1167-1170 (1983).

[105] P. E. S. Wormer & A. van der Avoird. *J. Chem. Phys.*, **81**, 1929 (1984).

[106] L. A. Poveda, M. Biczysko & A. J. C. Varandas. *J. Chem. Phys.*, **131**, 044309 (2009).

[107] F. Cozzi, M. Cinquini, R. Annuziata & J. S. Siegel. *J. Am. Chem. Soc.*, **115**, 5330-5331 (1993).

[108] "Mathematica, Version 8.0, Wolfram Research Inc. Champaign, IL" (2010).

[109] T. S. Sears. *Comp. Phys. Rep.*, **2**, 1-32 (1984).

[110] I. C. Bowater, J. M. Brown & A. Carrington. *Proc. R. Soc. Lond. A*, **333**, 265-288 (1973).

[111] C. C. Lin. *Phys. Rev.*, **116**, 4 (1959).

[112] J. R. Low, C. J. Whitham, T. D. Varberg & B. J. Howard. *Chem. Phys. Lett.*, **222**, 443-449 (1994).

[113] M. D. Brookes J. R. Low, C. J. Whitham, T. D. Varberg & B. J. Howard. *J. Chem. Phys.*, **105**, 16 (1996).

[114] C. J. Whitham, J. R. Low & B. J. Howard. *Chem. Phys. Lett.*, **286**, 408-414 (1998).

[115] S. Blanco, C. J. Whitham, H. Qian & B. J. Howard. *Phys. Chem. Chem. Phys.*, **3**, 3895-3900 (2001).

[116] L. A. Dyer. Part II Thesis, University of Oxford (2010).

[117] http://www.pci.tu-bs.de/aggericke/PC4e/Kap$_V$/*Walsh_AB*2.*html*, *accessedon*23*Sept*2013.

[118] Y. Xie, R. D. Davy, B. F. Yates, C. P. Blahous III, Y. Yamaguchi & H. F. Schaefer III. *Chem. Phys.*, **135**, 179-186 (1989).

[119] P. P. Bera, Y. Yamaguchi & H. F. Schaefer III. *J. Chem. Phys.*, **127**, 174303 (2007).

[120] L. Burnelle, P. Beaudouin & L. J. Schaad. *J. Phys. Chem.*, **71**, 7 , 2240-2247 (1967).

[121] V. C. Mota, P. J. S. B. Caridade & A. J. C. Varandas. *J. Phys. Chem. A*, **116**, 3023-3034 (2012).

[122] G. R. Bird. *J. Chem. Phys.*, **25**, 5, (1956).

[123] G. R. Bird, J. C. Baird, A. W. Jache, J. A. Hodgeson, R. F. Curl Jr., A. C. Kunkle, J. W. Bransford, J. Rastrup-Andersen & J. Rosenthal. *J. Chem. Phys.*, **40**, 11, (1964).

[124] A. Cabana, M. L. C. Pepin & W. J. Lafferty. *J. Mol. Spec.*, **59**, 13 (1976).

[125] R. M. lees, R. F. Curl & J. G. Baker. *J. Chem. Phys.*, **45**, 2037 (1966).

[126] R. J. Low. D. Phil., University of Oxford (1995).

[127] W. H. Press, B. P. Flannery, S. A. Teukolsky & W. T. Vetterling. "Numerical Recipes". Cambridge University Press (1986).

[128] Microsoft. (2003). Microsoft Excel [computer software]. Redmond, Washington: Microsoft.

[129] M. Abramowitz & I. A. Stegun. "Handbook of Mathematical Functions". Dover Publication (1972).

[130] M. Frise. Part II Thesis, University of Oxford (2009).

[131] The author(s) would like to acknowledge the use of the EPSRC UK National Service for Computational Chemistry Software (NSCCS) at Imperial College London in carrying out this work.

[132] J. M. Rintelman, I. Adamovic, S. Varganov & S. M. Gordon. *J. Chem. Phys.*, **122**, 044105 (2005).

[133] T. Shiozaki & H.-J. Werner. *J. Chem. Phys.*, **133**, 141103 (2010).

[134] F. G. Kalatzis & I. N. Demetropoulos. *Mol. Phys.*, **90**, 6, 875-888 (1997).

[135] M. J. Frisch, G. W. Trucks, H. B. Schlegel, G. E. Scuseria, M. A. Robb, J. R. Cheeseman, G. Scalmani, V. Barone, B. Mennucci, G. A. Petersson, H. Nakatsuji, M. Caricato, X. Li, H. P. Hratchian, A. F. Izmaylov, J. Bloino, G. Zheng, J. L. Sonnenberg, M. Hada, M. Ehara, K. Toyota, R. Fukuda, J. Hasegawa, M. Ishida, T. Nakajima, Y. Honda, O. Kitao, H. Nakai, T. Vreven, J. A. Montgomery, Jr., J. E. Peralta, F. Ogliaro, M. Bearpark, J. J. Heyd, E. Brothers, K. N. Kudin, V. N. Staroverov, R. Kobayashi, J. Normand, K. Raghavachari, A. Rendell, J. C. Burant,

S. S. Iyengar, J. Tomasi, M. Cossi, N. Rega, J. M. Millam, M. Klene, J. E. Knox, J. B. Cross, V. Bakken, C. Adamo, J. Jaramillo, R. Gomperts, R. E. Stratmann, O. Yazyev, A. J. Austin, R. Cammi, C. Pomelli, J. W. Ochterski, R. L. Martin, K. Morokuma, V. G. Zakrzewski, G. A. Voth, P. Salvador, J. J. Dannenberg, S. Dapprich, A. D. Daniels, . Farkas, J. B. Foresman, J. V. Ortiz, J. Cioslowski & D. J. Fox. "Gaussian 09 Revision D.01". Gaussian Inc. Wallingford CT 2009.

[136] The authors would like to acknowledge the use of the University of Oxford Advanced Research Computing (ARC) facility in carrying out this work.

[137] H. Dachsel. *J. Chem. Phys.*, **124**, 144115 (2006).

[138] M. A. Blancoa, M. Floreza & M. Bermejo. *J. Mol. Str. (Theochem)*, **419**, 19-27 (1997).

[139] E. Anderson, Z. Bai, C. Bischof, S. Blackford, J. Demmel, J. Dongarra, J. Du Croz, A. Greenbaum, S. Hammarling, A. McKenney & D. Sorensen. "LAPACK Users' Guide". Society for Industrial and Applied Mathematics, Philadelphia, PA, third edition (1999). ISBN 0-89871-447-8 (paperback).

[140] C. L. Lawson, R. J. Hanson amd D. Kincaid & F. T. Krogh. *ACM Trans. Math. Soft.*, **5**, 308-323 (1979).

[141] J. J. Dongarra, J. Du Croz, S. Hammarling & R. J. Hanson. *ACM Trans. Math. Soft.*, **14**, 1–17 (1988).

[142] J. J. Dongarra, J. Du Croz, S. Hammarling & R. J. Hanson. *ACM Trans. Math. Soft.*, **14**, 18–32 (1988).

[143] J. J. Dongarra, J. Du Croz, I. S. Duff & S. Hammarling. *ACM Trans. Math. Soft.*, **16**, 1–17 (1990).

[144] J. J. Dongarra, J. Du Croz, I. S. Duff & S. Hammarling. *ACM Trans. Math. Soft.*, **16**, 18–28 (1990).

[145] L. S. Blackford, J. Demmel, J. Dongarra, I. Duff, S. Hammarling, G. Henry, M. Heroux, L. Kaufman, A. Lumsdaine, A. Petitet, R. Pozo, K. Remington & R. C. Whaley. *ACM Trans. Math. Soft.*, **28-2**, 135–151 (2002).

[146] J. Dongarra. *ACM Trans. Math. Soft.*, **16(2)**, 115–199 (2002).

[147] J. Dongarra. *ACM Trans. Math. Soft.*, **16(1)**, 1–111 (2002).

[148] 67th OSU International Symposium On Molecular Spectroscopy (2012).

[149] A. Savitzky & M. J. E. Golay. *Anal. Chem.*, **36**, 8, (1964).

[150] "MATLAB and Statistics Toolbox Release 2010b, The MathWorks Inc., Natick, Massachusetts, United States".

[151] J. M. Hutson, BOUND computer code, version 5 (1993), distributed by Collaborative Computational Project No. 6 of the Science and Engineering Research Council (UK).

Appendix A

Fundamental Constants and Conversion Factors

A.1 Fundamental Constants

Quantity	Symbol	Value
Planck Constant	h	$6.62606876(52) \times 10^{-34}\,\mathrm{J\,s}$
Free electron g factor	g_s	2.0023193043737(82)
Atomic mass constant	$u=m_u$	$1.66053873(13) \times 10^{-27}\,\mathrm{kg}$
Magnetic constant	μ_0	$4\pi \times 10^{-7}\,\mathrm{N\,A^{-2}}$
Bohr magneton	μ_B	$9.27400899(37) \times 10^{-24}\,\mathrm{J\,T^{-1}}$
Nuclear magneton	μ_N	$5.05078317(20) \times 10^{-27}\,\mathrm{J\,T^{-1}}$
Universal Gas Constant	R_u	$8.314472\,\mathrm{J\,mol^{-1}\,K^{-1}}$ [1]
Speed of light (vacuum)	c	$2.99792458 \times 10^{8}\,\mathrm{m\,s^{-1}}$
Avogadro constant	L,N_A	$6.02214199(47) \times 10^{23}\,\mathrm{mol^{-1}}$
Boltzmann constant	k_B	$1.3806503(24) \times 10^{-23}\,\mathrm{J\,K^{-1}}$

A.2 International System (SI) Units Conversion Factors (approximate)

unit	Hartree	eV	cm^{-1}	Hz
Hartree	1	2625.50	27.212	2.1947×10^{5}
6.57966×10^{15}				
eV	3.6749×10^{-2}	1	8065.5	$2.418\,04\times10^{14}$
cm^{-1}	4.5563×10^{-6}	1.2398×10^{-2}	1	$2.997\,93\times10^{10}$
Hz	$1.519\,83\times10^{-16}$	$4.135\,58\times10^{-15}$	$3.335\,65\times10^{-11}$	1

1 J = 1 kg m^2 s^{-2}

1 Pa = 1 N m^{-2} = 10^{-5} bar = 10 dyne/cm^2 = 7.501 μm Hg

1 Pa = 7.501×10^{-3} Torr = 9.869×10^{-6} std atm = 1.450×10^{-4} psi[2]

1 Bohr =0.529177249 Å

1 K = 1 °C=(F-32)/1.8

[2]psi is an abbreviation for the unit pound-force per square inch

Appendix B

Standard angular momentum formulæ

Here are quoted some fundamental formulæ, for reference purposes [1, 27, 96]. All symbols hold their standard meaning.

B.1 Definitions of operators

$$
\begin{aligned}
j^2 &= j_x^2 + j_y^2 + j_z^2 && \text{(B.1)}\\
J_\pm &= J_x \pm i J_y && \text{(B.2)}\\
j^2 \,|jm\rangle &= j\,(j+1)\,|j,m\rangle && \text{(B.3)}\\
j_z \,|jm\rangle &= m\,|jm\rangle && \text{(B.4)}\\
j_\pm \,|jm\rangle &= \left[j(j+1) - m(m\pm 1)\right]^{1/2} |j,m\pm 1\rangle && \text{(B.5)}\\
\left\langle j'm' \mid jm \right\rangle &= \delta_{j',j}\delta_{m',m} && \text{(B.6)}\\
& && \text{(B.7)}
\end{aligned}
$$

In Cartesian axis, the orbital angular momentum operators are defines as:

$$\begin{aligned} l_x &= yp_z - zp_y && \text{(B.8)} \\ &= -i\left(y\frac{\partial}{\partial z} - z\frac{\partial}{\partial y}\right) && \text{(B.9)} \\ l_y &= zp_x - xp_z && \text{(B.10)} \\ &= -i\left(z\frac{\partial}{\partial y} - y\frac{\partial}{\partial z}\right) && \text{(B.11)} \\ l_z &= xp_y - yp_x && \text{(B.12)} \\ &= -i\left(x\frac{\partial}{\partial y} - y\frac{\partial}{\partial x}\right) && \text{(B.13)} \end{aligned}$$

Spherical coordinates correspond to the Cartesian coordinates by:

$$\begin{aligned} x &= r\sin\theta\cos\phi && \text{(B.14)} \\ y &= r\sin\theta\sin\phi && \text{(B.15)} \\ z &= r\cos\theta && \text{(B.16)} \end{aligned}$$

When expressed in spherical coordinates, the angular momentum operators become:

$$\begin{aligned} l_x &= i\left(\sin\phi\left(\frac{\partial}{\partial\theta}\right) + \cot\theta\cos\phi\left(\frac{\partial}{\partial\phi}\right)\right) && \text{(B.17)} \\ l_y &= i\left(-\cos\phi\left(\frac{\partial}{\partial\theta}\right) + \cot\theta\sin\phi\left(\frac{\partial}{\partial\phi}\right)\right) && \text{(B.18)} \\ l_z &= -i\frac{\partial}{\partial\phi} && \text{(B.19)} \end{aligned}$$

Combination of the above gives an overall angular momentum operator, l^2:

$$l^2 = -\left[\frac{1}{\sin^2\theta}\frac{\partial^2}{\partial\varphi^2} + \frac{1}{\sin\theta}\frac{\partial}{\partial\theta}\left(\sin\theta\frac{\partial}{\partial\theta}\right)\right] \qquad \text{(B.20)}$$

Appendix C

More Experimental

C.1 FID Processing

In order to achieve a higher S/N, the signal is also treated by two processes. The first one happens before the Fourier transform and it consists of multiplying the signal by a Gaussian "window" function:

$$G(t) = e^{-\left(\frac{t-t_0}{k}\right)^2} = e^{\frac{2t\times t_0}{k^2}} e^{-\frac{t^2}{k^2}} e^{-\frac{t_0^2}{k^2}} \tag{C.1}$$

where t is the time of the FID, t_0 is a positioning parameter for the Gaussian and k is the decay constant of the function. As it is expanded in the far right hand side, the first exponential will dominate in small t values, while the second at large. The last exponential is independent of t and therefore is a constant that does not influence the shape or S/N ratio of the signal. One can adjust t_0 as to modify the first exponential, but here for clarity we set $t_0 = 1$. If the FID signal is expressed as

$$S(t) \propto e^{-\frac{t}{\tau}} \tag{C.2}$$

where τ is the lifetime of the FID and which is related to the bandwidth of the signal ($\Delta\nu$) as:

$$\Delta\nu = \frac{1}{2\pi\tau} \tag{C.3}$$

Then, by multiplying the $S(t)$ by $G(t)$:

$$S(t) \times G(t) \propto e^{-t\left(\frac{1}{\tau}-\frac{2}{k^2}\right)} e^{-\frac{t^2}{k^2}} \tag{C.4}$$

With this transformation, the lifetime of the emission at small t is artificially increased, while at large t (when there is mainly noise) it is reduced. This helps to distinguish very close frequency

peaks and overlapping signals.

The second process takes place after the Fourier transform and it is an application of the Savitzky-Golay [149] smoothing method. This acts as a filter by performing a local N-th order polynomial regression on the signal using, for each point, ± M neighbouring points. The default settings in the FTMS program are $N = 2$ and $M = 2$. This creates a smoother function, thus reducing the noise. The main advantages of this specific technique is that it maintains the relative maxima, minima and their width, therefore does not alter the position of the peaks or the linewidth. This smoother function is then used to find (by calculating its turning points) the peak positions. For automatic peak searching, a maximum of this function is compared to the background noise, and if its S/N is high enough then it is deemed a peak.

C.2 Signal Generation

If the electric field generated by the radiation is considered classically, the interaction between a molecule and the field can be written as:

$$\widehat{V}(t) = -\hat{\mu}\,\varepsilon_0 \cos(\omega t) \tag{C.5}$$

where ε_0 is the strength of the applied electric field, ω is the angular frequency with which the field oscillates, t is the time variable and $\hat{\mu}$ is the dipole moment operator. This interaction can be regarded as a perturbation to the energy levels of the molecule in absence of the electric field. Then, the Hamiltonian of the species before the radiation (H_0) can be used to solve the time-independent Schrödinger equation (TISE):

$$\widehat{H}^0|\phi\rangle = E|\phi\rangle \tag{C.6}$$

while to find the eigenfunctions of the full Hamiltonian:

$$\widehat{H} = \widehat{H}^0 + \widehat{V}(t) \tag{C.7}$$

One needs to solve the time-depended Schrödinger equation (TDSE):

$$\widehat{H}|\Psi\rangle = \imath\hbar\frac{\partial}{\partial t}|\Psi\rangle \tag{C.8}$$

The eigenvalues of the full Hamiltonian have the form

$$\psi_n = \phi_n e^{-\imath\omega_n t} \tag{C.9}$$

where ϕ_n are the solutions of the equation C.6 and ω_n are related to the energy of the levels at $t = 0$ by

$$\hbar\omega_n = E_n \tag{C.10}$$

$V(t)$ will perturb and mix the energy states of H^0. The overall final state may be written as

$$\Psi(t) = \sum_n c_n(t)\,\phi_n e^{-\imath\omega_n t} \tag{C.11}$$

For a two-state system, $|\phi_l\rangle$ and $|\phi_u\rangle$ with $E_l < E_u$, both the TDSE and the TISE can be written:

$$\begin{aligned}\left(\widehat{H}^0 - \hat{\mu}\,\varepsilon_0\cos(\omega t)\right)|\Psi\rangle &= \imath\hbar\left(\dot{c}_l\phi_l e^{-\imath\omega_l t} + \dot{c}_u\phi_u e^{-\imath\omega_u t}\right) \\ &\quad + E_l^0 c_l\phi_l e^{-\imath\omega_l t} + E_u^0 c_u\phi_u e^{-\imath\omega_u t} \qquad \text{(C.12)} \\ \widehat{H}^0|\Psi\rangle &= E_l^0 c_l\phi_l e^{-\imath\omega_l t} + E_u^0 c_u\phi_u e^{-\imath\omega_u t} \qquad \text{(C.13)}\end{aligned}$$

If we take the difference between TDSE and TISE, and then post multiply by $\langle\phi_l|$:

$$\begin{aligned}- &\left(\underbrace{\langle\phi_l|\hat{\mu}|\phi_l\rangle}_{=0} c_l e^{-\imath\omega_l t} + \langle\phi_l|\hat{\mu}|\phi_u\rangle c_u e^{-\imath\omega_u t}\right)\varepsilon_0\cos(\omega t) = \\ = &\ \imath\hbar\left(\underbrace{\langle\phi_l|\phi_l\rangle}_{=1}\dot{c}_l e^{-\imath\omega_l t} + \underbrace{\langle\phi_l|\phi_u\rangle}_{=0}\dot{c}_u e^{-\imath\omega_u t}\right) \qquad \text{(C.14)}\end{aligned}$$

In above equation, the dipole moment matrix element is zero by symmetry, while the right-hand side of the equation is simplified using the orthonormality of the functions. By repeating the same process and post multiplying by $\langle\phi_u|$, we obtain a pair of coupled differential equations:

$$\begin{aligned}\dot{c}_l &= \frac{-\langle\phi_l|\hat{\mu}|\phi_u\rangle\varepsilon_0 c_u}{2\imath\hbar}\left(e^{\imath(\omega_l-\omega_u+\omega)t} + e^{\imath(\omega_l-\omega_u-\omega)t}\right) \qquad \text{(C.15)} \\ \dot{c}_u &= \frac{-\langle\phi_u|\hat{\mu}|\phi_l\rangle\varepsilon_0 c_l}{2\imath\hbar}\left(e^{\imath(\omega_u-\omega_l+\omega)t} + e^{\imath(\omega_u-\omega_l-\omega)t}\right) \qquad \text{(C.16)}\end{aligned}$$

At near resonance

$$\omega \approx \omega_u - \omega_l = \omega_0 \tag{C.17}$$

and the terms depending on $(\omega + \omega_u - \omega_l)$ or $(-\omega - \omega_u + \omega_l)$ are very rapidly oscillating and can be ignored. Assuming the initial populations:

$$c_l(t=0) = 1 \quad c_u(t=0) = 0 \tag{C.18}$$

According to the Born interpretation of the wavefunction, the squared modulus of these coefficients corresponds to the probability density of finding the system at that state:

$$c_u^* c_u = \frac{\langle \phi_u | \hat{\mu} | \phi_l \rangle \langle \phi_l | \hat{\mu} | \phi_u \rangle^* \varepsilon_0^2}{4\hbar^2} f(\omega_0 \omega t) \tag{C.19}$$

where

$$f(\omega_0 \omega t) = \frac{\sin^2(0.5(\omega_0 - \omega)t)}{(0.5(\omega_0 - \omega))^2} \tag{C.20}$$

The above function peaks sharply at the exact resonance, therefore only then will a transition occur[1]. From equation C.19 it can also be seen that only if there is a non-zero dipole moment will a transition occur. In the case of exact resonance, the time-dependent coefficients become:

$$c_l(t) = \cos\left(\frac{\omega' t}{2}\right) \quad c_u(t) = -\imath \sin\left(\frac{\omega' t}{2}\right) \tag{C.21}$$

where

$$\omega' = \frac{\langle \phi_u | \hat{\mu} | \phi_l \rangle \varepsilon_0}{\hbar} \tag{C.22}$$

The probability of a transition being made to the any state at time t is given by:

$$P_l = |c_l|^2 = \cos^2\left(\frac{\omega' t}{2}\right) \qquad P_u = |c_u|^2 = \sin^2\left(\frac{\omega' t}{2}\right) \tag{C.23}$$

However, a collection of molecules will not all be in the lower energy state, but rather

$$c_l(t=0) = a_m \qquad c_u(t=0) = b_m \tag{C.24}$$

This modifies the expressions in (C.21) to

$$c_l = a_m \cos\left(\frac{\omega' t}{2}\right) + i b_m \sin\left(\frac{\omega' t}{2}\right) \tag{C.25}$$

$$c_u = b_m \cos\left(\frac{\omega' t}{2}\right) - i a_m \sin\left(\frac{\omega' t}{2}\right) \tag{C.26}$$

Transition dipole moment between these states now is:

$$\langle \Psi | \hat{\mu} | \Psi \rangle = c_l^* c_u \langle \phi_l | \hat{\mu} | \phi_u \rangle e^{-\imath \omega_0 t} + c_u^* c_l \langle \phi_u | \hat{\mu} | \phi_l \rangle e^{-\imath \omega_0 t} \tag{C.27}$$

[1]To be precise, the function $f(\omega_0 \omega t)$ becomes a normalised delta function. More details may be found in reference [16].

The macroscopic polarisation of the collection of molecules is related to their dipole moment as

$$\mathbf{p} = \sum_m \langle \hat{\mu}_m \rangle \tag{C.28}$$

where $\langle \hat{\mu}_m \rangle$ is the expectation value of the transition dipole moment (from here on assumed real) and m is a running index for the molecules. When the sample is introduced into the cavity (without any radiation field), the alignment of the dipole moments is random and therefore there is no mass polarization ($\mathbf{p} = 0$).

When the radiation is present, $\widehat{V}(t)$ mixes the states of H_0 as described above. Taking the expectation value of the dipole moment for a molecular assembly, with the time dependence of the coefficients of the wavefunction is as derived, gives

$$\mathbf{p} = (P_l - P_u) \left| \langle \phi_u | \hat{\mu} | \phi_l \rangle \right| \sin\left(\omega' \tau\right) \sin\left(\omega_0 t\right) \tag{C.29}$$

The optimum conditions would be $(\omega' \tau) = \frac{\pi}{2}$, which is referred to as a "$\frac{\pi}{2}$-pulse". Underpowering or overpowering the cavity would actually damage the polarisation, and a π pulse would actually give no signal!

The power emitted[2] from the relaxation of this pulse is

$$\text{Power} \quad \text{emitted} = 2\pi Q \left(P_u - P_l\right)^2 \omega_0 \left| \langle \phi_u | \mu | \phi_l \rangle \right|^2 \tag{C.30}$$

where Q is the quality factor of the cavity, which was explained earlier. One interesting thing to note is that the signal power (power emitted) depends on the square of the population difference.Using a supersonic expansion, as described earlier in chapter, helps to achieve population cooling, which increases the signal.

[2]This equation is taken from electrophysics and its derivation is beyond the scope of this thesis.

Appendix D

More on the Ne-NO_2 Complex

D.1 More Potential Models

D.1.1 The LEAPOT Approach

The first model we attempted was a LEAPOT expansion to represent the potential[1]:

$$V_{tot}(R,\theta) = \sum_i V_{i,radial}(R) V_{i,angular}(\theta,\chi;R) \tag{D.1}$$

where R,θ,χ are the intermolecular coordinates used in the *ab initio* calculations. For the Ne-NO_2 case, there are only two intermolecular angular coordinates so the angular functions may be modelled using a linear combination of spherical harmonics:

$$V_{angular}(\theta,\chi;R) = \sum_{\ell,m} C_{\ell,m}(R)\mathscr{Y}^{\ell}_{m}(\theta,\chi) \tag{D.2}$$

We note that if m was allowed to take any odd values, that would mean there are functions in the potential that differentiate between the two oxygen nuclei, which is unphysical. Therefore, m can only take even values (including zero). Moreover, using equations 3.9, 3.13, 3.14 and 3.8, we can express the potential as the following linear combination, with m only taking positive integer values, and zero:

$$V_{angular}(\theta,\chi;R) = \sum_{\ell,m} C'_{\ell,m}(R)\mathscr{P}^{\ell}_{m}(\cos\theta)\cos(m\chi) \tag{D.3}$$

[1] LEAPOT is the acronym of *Linear Expansion in the Anisotropy of the Potential*, as described in chapter 7.

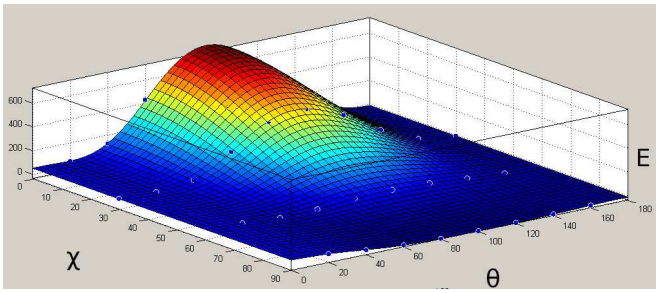

Figure D.1: Fitted angular Ne-NO_2 potential at $R = 3.2$ Å, energy is quoted in cm^{-1} and angles in degrees

As there were only 4 values that the χ variable took, and 10 values that θ took, in the *ab initio* calculations, the maximum value for ℓ was set at 9 and for m at 6. Since at any single R, the PES was only three-dimensional, the fitting could be performed using the *Surface Fitting Tool* of the MATLAB2010b [150] program.

It was found that by using an upper value of $\ell = 7$ and $m = 6$ (20 parameters) and scaling the potential using an arctan function to having values up to 1,000 cm^{-1} relative to the energy minimum, we were able to fit the angular part of the potential with a RMSD=1.8-2.6 cm^{-1} (with the error scaling inversely with distance). A picture of the fitted potential at $R = 3.2$ Å is given in figure D.1. The fit used was a linear least squares fit.

Having fitted the angular part of the potential, the next step was to fit the radial functions to the angular function coefficients. The radial functions used were of the form:

$$V_{radial} = A\exp[-bR] - \sum_{k=6;\ \text{even}}^{12} c_k R^{-k} \tag{D.4}$$

where k only took even values. There were two reasons for this choice: Physically this is a function analogous to the Modified Buckingham potential. The second reason is that the total potential function could be used in conjunction with the program BOUND [151] by Hutson, which could then be used to perform the dynamics. The fitting of the radial part of the potential was performed using the *Curve Fitting Toolbox* of the MATLAB2010b program. The RMSE of this fit was in the range of 3.5-7.1 cm^{-1}.

Unfortunately, the angular coefficients changed significantly with distance. It is worth noting that the relative magnitude of the coefficients of different terms in the fitted potential also changed

What became obvious is that different angular functions were contributing in the fit in different ways at different distances, with little physical meaning. Moreover, there was aliasing between the points, while in total the quality of the fit was still not very good.

Perhaps unsurprisingly, when this potential was used with BOUND, the result was unphysical, with very low Zero Point Energy for the complex. A lot of effort went into finding better radial functions, or iteratively obtaining the angular coefficients for their values to be more

consistent over distance, yet the final results were still not satisfactory.

D.1.2 The Global Potential Approach

The poor quality of the fit obtained using the LEAPOT approach was seen as an indication of the strong coupling between the angular and radial motions. For this reason, the next approach taken was to perform a global fit, where the function is fitted simultaneously to an expression for both the radial and the angular coordinates. Also now we changed our approach from LEAPOT to LEAPAR[2]. This was as to obtain a more physically meaningful potential function, where the coefficients indicate the relative importance of different effects.

The functional form of this potential is the same as in equation 7.30, i.e. it comprises of a Born-Mayer term to represent the exchange-repulsion at short range and a Multipole Moment expansion for the long range forces:

$$V_{Ne-NO_2} = Ae^{-\alpha(\theta,\chi)(R-\rho(\theta,\chi))} + \sum_{n=6}^{8} f_n(R)\frac{C_n(\theta,\chi)}{R^{-n}} \tag{D.5}$$

In comparison to equation 7.30, it is worth noting that we have not included a angular dependence on the pre-exponential factor, as to limit the correlation between it and the parameters in the exponent. Now we will have a quick look at each of the contributions of the potential function. Although various similar potential functions were attempted here we only present the most successful one.

Following from the previous section, the angular dependence of the potential may be modelled by a linear combination as the one in equation D.3. For the $\alpha(\omega)$ the maximum ℓ was set to 3 and m to 2, while for the $\rho(\omega)$, the maximum ℓ and m used were 4. The R dependence of the exponential contribution was represented as a linear series of $\left(bR+\delta bR^{-1}\right)$ type expressions. Therefore, a total of 13 parameters were used to model the short-range part of the potential.

The long-range part comprises of three terms:

- An R^{-6} term which aims to represent mainly the leading effect of dispersion between the two species. For the angular dependence of this term it was multiplied by an expansion with $\ell = 0, 2$

- An R^{-7} term that represents the leading induction contribution (except of the R^{-6} which is absorbed in the previous term) in this complex. Its angular dependence was represented by a linear combination of terms with $\ell = 1, 3$

[2]LEAPAR stands for *Linear Expansion on the Anisotropy of the PARameters*, and was introduced in chapter 7.

- An R^{-8} term that aims to represent the higher order dispersion and induction effects between the two species. Its angular dependence was modelled with a linear expansion with $\ell = 4$

For all the linear expansions above, the m projection took even integer values up to the corresponding ℓ. The functions of $\ell = 0,2$ were not included in the R^{-8} term as to limit the correlations between these parameters and the corresponding one with an R^{-6} dependence.

All terms representing the long range attractive forces were multiplied by damping functions analogous to the Tang and Toennies functions mentioned in chapter 7. For these functions it was explored whether it was necessary to include the whole exponential expression, or even the part corresponding to the angular dependence of the function being damped. However, it was found that as long as $b >> \delta b$ and that both the $\alpha(\omega)$ and $\rho(\omega)$ series were convergent, the $\exp[bR]$ effect was dominant and sufficient for the damping.

Moreover, the value of R_0 was fixed at 3.15 Å. This was chosen by fitting an parabola in the energy minimum geometry of the complex and finding the minimum.

Thus the final expression for the potential was:

$$\begin{aligned} V_{Ne-NO_2} &= A\exp\left[-\left(\sum_{1\le\ell\le3;m}\alpha_{\ell,m}\mathscr{P}_m^\ell(\theta)\cos(m\chi)\right)\right. \\ &\times \left.\left(bR+\delta b\,(R)^{-1}-\sum_{0\le\ell\le4;m}\rho_{\ell,m}\mathscr{P}_m^\ell(\theta)\cos(m\chi)\right)\right] \\ &- \left(1-e^{-bR}\sum_{k=0}^{6}\frac{(bR)^k}{k!}\right)\frac{\left(\sum_{\ell=0,2;m}c_{6,\ell,m}\mathscr{P}_m^\ell(\theta)\cos(m\chi)\right)}{(R)^{-6}} \\ &- \left(1-e^{-bR}\sum_{k=0}^{7}\frac{(bR)^k}{k!}\right)\frac{\left(\sum_{\ell=1,3;m}c_{7,\ell,m}\mathscr{P}_m^\ell(\theta)\cos(m\chi)\right)}{(R)^{-7}} \\ &- \left(1-e^{-bR}\sum_{k=0}^{8}\frac{(bR)^k}{k!}\right)\frac{\left(\sum_{m}c_{8,4,m}\mathscr{P}_m^4(\theta)\cos(m\chi)\right)}{(R)^{-8}} \end{aligned} \tag{D.6}$$

where all m take only even integer values up to the corresponding ℓ. The fitting of the above function was performed using MATHEMATICA8. The main problem met in fitting the potential of equation D.6, was the high degree of correlation between different parameters. As it can be seen from equation D.6, all the parameters are (directly or indirectly) multiplied by each other.

One way to reduce the correlation was to keep the parameters of the damping functions set to the value calculated by the previous iteration. This way the short and long range forces were separated. Then the long range forces were fitted at long distances first, and the short range forces at short distances independently, and then a global fit was performed.

Our best fit had an RMSE value of 5.4 cm^{-1}, using a total of 25 parameters. Yet, even this fit was unsatisfactory, as the correlation between the parameters was high. Another worry was that

the fitting was not natural, as the series were not convergent and the short range forces seemed to contribute to the long range attraction. We could add more parameters to lower the RMSE further, but when this was attempted the fitting became even less physical.

D.2 Vector Model for Spin-Rotation Analysis

Using a vector model, the spin-rotation interaction may be written as the sum of the interactions between the spin and the rotational angular momenta on each of the principle axes of the complex:

$$\hat{H}_{sr,vector} = \varepsilon_{aa}\hat{N}_a\hat{S}_a + \varepsilon_{bb}\hat{N}_b\hat{S}_b + \varepsilon_{cc}\hat{N}_c\hat{S}_c \tag{D.7}$$

where ε_{jj} is the effective spin-rotation constant along the j principle axis of the complex. This is also equivalent to summing the projection of the total spin-rotation interaction ($\hat{N}\cdot\hat{S}$) on the three principle axes:

$$\hat{H}_{sr,vector} = \underbrace{[\varepsilon_{aa}\hat{N}_a^2 + \varepsilon_{bb}\hat{N}_b^2 + \varepsilon_{cc}\hat{N}_c^2]}_{\varepsilon_{aa}\hat{N}_a^2+(\varepsilon_{bb}+\varepsilon_{cc})\frac{\hat{N}_b+\hat{N}_c}{2}+(\varepsilon_{bb}-\varepsilon_{cc})\frac{\hat{N}_b-\hat{N}_c}{2}} \frac{\hat{N}\cdot\hat{S}}{\hat{N}^2} \tag{D.8}$$

The diagonal contribution of the term in the square brackets for the states $K_r = 0$ and $|K_r| = 2$ scales as:

$$\varepsilon_{aa}K_r^2 + (\varepsilon_{bb}+\varepsilon_{cc})\frac{N(N+1)-K_r^2}{2}$$

while still using the vector model we may approximate

$$N\cdot S = \frac{J(J+1)-N(N+1)-S(S+1)}{2} \tag{D.9}$$

where J in this model is given by the vector sum of N and S. Thus the complete expression for the vector model for the even K_r states is:

$$\langle\hat{H}_{sr,vector}\rangle = \frac{[\varepsilon_{aa}K_r^2 + (\varepsilon_{bb}+\varepsilon_{cc})\frac{N(N+1)-K_r^2}{2}](J(J+1)-N(N+1)-S(S+1))}{2N(N+1)} \tag{D.10}$$

Moreover, the 6-j symbol which appears in equation 10.50 has an N, K_r dependence [29]:

$$(-1)^{N-K}\sqrt{N(N+1)(2N+1)}$$

This expression mirrors exactly the trend observed in the spin-rotation constants in table 10.12, when no off-diagonal Coriolis interactions are included.

D.3 The Fine and Hyperfine Predicted Energy Levels

In table D.1, the calculated energy level splittings due to the fine and hyperfine interactions are given. The eigenvectors used for this calculation came from performing the quantum dynamics with four vibrational levels and $n_{NO_2} = 19$.

D.4 The Predicted and Assigned for $K_r = 0$

In table D.2, the $K_r = 0$ spectrum predicted using the eigenvectors from calculation with four and one vibrational levels (all with $n_{NO_2} = 19$) are juxtaposed next to the spectrum as assigned by Dyer [116].

D.5 The Assigned Spectrum

The assigned spectrum for the $|K_r| = 2$ transitions of Ne-NO_2 is given in table D.3. The notation used represents the semi-rigid asymmetric top approach used for the assignment.

Table D.1: Energy level shifts due to fine and hyperfine interactions for Ne-NO_2 with respect to pure rotational energy levels

N	K_r	F	G	Energy level Shift /MHz
0	0	0.5	0.5	-147.2300
0	0	0.5	1.5	73.6150
1	0	0.5	0.5	-141.4800
1	0	1.5	0.5	-151.1740
1	0	0.5	1.5	58.6358
1	0	1.5	1.5	68.3301
1	0	1.5	2.5	82.8440
2	0	1.5	0.5	-140.1860
2	0	2.5	0.5	-154.9160
2	0	0.5	1.5	48.0446
2	0	1.5	1.5	58.0475
2	0	2.5	1.5	72.7774
2	0	3.5	1.5	90.6620
2	2^-	1.5	0.5	-196.3810
2	2^-	2.5	0.5	-155.3990
2	2^-	0.5	1.5	178.1520
2	2^-	1.5	1.5	157.6120
2	2^-	2.5	1.5	116.6300
2	2^-	3.5	1.5	3.9237
2	2^+	1.5	0.5	-195.1130
2	2^+	2.5	0.5	-154.6730
2	2^+	0.5	1.5	175.8730
2	2^+	1.5	1.5	155.5840
2	2^+	2.5	1.5	115.1440
2	2^+	3.5	1.5	5.4427
3	0	2.5	0.5	-139.8030
3	0	3.5	0.5	-157.5930
3	0	1.5	1.5	43.7432
3	0	2.5	1.5	58.7203
3	0	3.5	1.5	76.5099
3	0	4.5	1.5	96.0189
3	2^-	2.5	0.5	-169.2520
3	2^-	3.5	0.5	-143.4150
3	2^-	1.5	1.5	124.0880
3	2^-	2.5	1.5	108.2550
3	2^-	3.5	1.5	82.4185
3	2^-	4.5	1.5	35.7605
3	2^+	2.5	0.5	-165.3800
3	2^+	3.5	0.5	-142.8820
3	2^+	1.5	1.5	116.4480
3	2^+	2.5	1.5	102.4730
3	2^+	3.5	1.5	79.9757
3	2^+	4.5	1.5	41.4903

Table D.2: Predicted and assigned spectrum of $K_r = 0$

Upper State			Lower State			Transition Frequencies/ MHz		
N'	F'	G'	N	F	G	Predicted $v_{max} = 3$	Predicted $v_{max} = 0$	Experiment [116]
1	1.5	0.5	0	1.5	1.5	5628.1275	5621.2581	5883.7997
1	0.5	1.5	0	0.5	0.5	5639.1627	5636.1544	5897.2328
1	1.5	1.5	0	1.5	1.5	5637.8218	5635.4101	5897.5215
1	0.5	0.5	0	0.5	0.5	5648.8567	5649.8434	5906.9672
1	1.5	2.5	0	1.5	1.5	5652.3357	5654.8463	5910.2338
2	1.5	1.5	1	1.5	1.5	11242.3468	11239.8516	11750.6714
2	1.5	0.5	1	1.5	0.5	11242.0382	11239.1600	11752.1486
2	1.5	2.5	1	1.5	2.5	11242.5628	11240.9325	11754.3271
2	0.5	2.5	1	0.5	1.5	11248.8874	11248.0817	11759.0223
2	1.5	1.5	1	1.5	0.5	11252.0411	11254.0036	11764.38
2	0.5	1.5	1	0.5	0.5	11253.9234	11255.3097	11764.5098
2	1.5	2.5	1	1.5	1.5	11257.0767	11260.3687	11767.0335
2	1.5	3.5	1	1.5	2.5	11260.4474	11265.8694	11771.506
2	0.5	1.5	1	0.5	1.5	11263.6174	11268.9987	11774.2408
3	1.5	1.5	2	1.5	1.5	16780.7426	16772.2226	17529.814
3	1.5	2.5	2	1.5	2.5	16780.9898	16774.7542	17530.7705
3	1.5	3.5	2	1.5	3.5	16780.8948	16774.8292	17533.271
3	1.5	1.5	2	1.5	0.5	16790.7455	16787.0662	17542.0741
3	0.5	3.5	2	0.5	2.5	16792.3699	16789.1488	17543.3809
3	1.5	2.5	2	1.5	1.5	16795.7197	16795.2713	17547.1408
3	0.5	2.5	2	0.5	1.5	16795.4299	16794.0708	17547.5094
3	1.5	3.5	2	1.5	2.5	16798.7794	16799.7661	17550.4525
3	1.5	4.5	2	1.5	3.5	16800.4038	16803.9172	17553.7847
3	0.5	2.5	2	0.5	2.5	16810.1599	16814.9878	17562.7233

Table D.3: Assignment and error of the $|K_r| = 2$ $N = 3 \leftarrow 2$ transitions of Ne-NO_2

N'_{K_a,K_c}	G'	F'	N_{K_a,K_c}	G	F	Observed/MHz	Error/kHz	Dynamics Prediction
$3_{2,2}$	1.5	2.5	$2_{2,1}$	1.5	1.5	17587.0399	1.53	16759.2244
$3_{2,2}$	1.5	3.5	$2_{2,1}$	1.5	2.5	17604.8098	1.03	16777.1671
$3_{2,2}$	0.5	3.5	$2_{2,1}$	0.5	2.5	17610.5404	3.74	16824.1264
$3_{2,2}$	0.5	2.5	$2_{2,1}$	0.5	1.5	17626.7665	4.47	16842.0684
$3_{2,2}$	1.5	4.5	$2_{2,1}$	1.5	3.5	17633.6552	1.41	16848.3830
$3_{2,1}$	1.5	2.5	$2_{2,0}$	1.5	1.5	17725.9711	151.00	16882.8952
$3_{2,1}$	1.5	3.5	$2_{2,0}$	1.5	2.5	17746.0386	9.26	16898.0407
$3_{2,1}$	0.5	3.5	$2_{2,0}$	0.5	2.5	17749.8360	97.69	16944.2362
$3_{2,1}$	0.5	2.5	$2_{2,0}$	0.5	1.5	17768.0654	42.22	16959.3812
$3_{2,1}$	1.5	4.5	$2_{2,0}$	1.5	3.5	17776.2563	130.58	16964.0890